Title
Network dynamics: biofilament and neuronal networks

Author
Slepukhin, Valentin

Publication Date
2021

Peer reviewed|Thesis/dissertation

UNIVERSITY OF CALIFORNIA

Los Angeles

Network dynamics: biofilament and neuronal networks

A dissertation submitted in partial satisfaction
of the requirements for the degree
Doctor of Philosophy in Physics

by

Valentin Maximovich Slepukhin

2021

ABSTRACT OF THE DISSERTATION

Network dynamics: biofilament and neuronal networks

by

Valentin Maximovich Slepukhin
Doctor of Philosophy in Physics
University of California, Los Angeles, 2021
Professor Alex J. Levine, Chair

In this dissertation, I study two types of networks: biopolymer filament networks (part I) and biological neural networks (part II).

First, I focus on the most common structural element of the filament networks: bundles of parallel stiff filaments held together by smaller molecules (cross links). The experiment and numerical simulations show that such bundles can have localized regions of high curvature that are long-lived metastable states (kinks). I suggest the mechanism of kink stabilization as a topological defect, with three possible defect types: a difference in trapped length of the filament segments between two cross-links (loop); the braiding of the filaments in the bundle; and the dislocation where the endpoint of a filament occurs within the bundle. I show that the pairs of defects are produced under compressive loading. Loops then get separated, while braids remain coupled. The braid separation requires cycles of compression and tension.

Second, I explore the force propagation in the whole network from the point-like source. Numerical simulations show a particular pattern of stress propagation. In

particular, the force decays exponentially, which I can capture using an analytical model in a particular parameter region.

Third, I study the statistical properties of the filament in the network modeling the rest of the network as a quenched random potential. I compare the average end-to-end distance in this model with one obtained numerically validating it.

Finally, I switch to neural networks and explore the preBötzinger complex which produces rhythm that times inspiration in mammals. We explore the initiation of the activity by external stimulation of a small subset of neurons. In the leaky integrate-and-fire neuron model, I observe that only a small subset of network patterns can produce results resembling experimental data. Using the firing-rate model with dendritic adaptation, we observe that if the system quits the oscillatory phase, it gets separated into two subnetworks: highly firing and low firing one. This separation occurs even for the all-to-all coupled networks thus being a spontaneous symmetry breaking. For the arbitrary network, simplified ("on-off") version of neuronal dynamics the separation is exactly controlled by the topological feature of the network - k-cores.

The dissertation of Valentin Maximovich Slepukhin is approved.

Robijn Bruinsma

Jack L. Feldman

Eric d'Hoker

Alex J. Levine, Committee Chair

University of California, Los Angeles

2021

In memory of my grandfathers, German and Eduard

Table of Contents

List of Figures

Preface

First of all, I would like to thank my advisor. It was great to do science together, but you also cared about my well-being and helped me so much in my year-long job search. Thank you, Alex.

To Wolfgang, Max, and Kei - for your hospitality in Germany and being so wonderful long-term collaborators.

To Jack and Sufyan - for your patience in working with me, a theoretical physicist. It took me such long time to accept that I should change my models to fit reality, not vice versa.

To Elliot and Qingda - for our paper on kinks that definitely costed all the efforts.

To Robijn, for wonderful classes with an excellent sense of humor, and for your questions and feedback during this journey.

To Zvi, for being the reason I applied to UCLA.

To Stephanie, Frank, Randy, and all the stuff - for making UCLA a new home for me.

To Jonny, for being the person who lure me into biophysics and stayed with me in one office all this journey. And of course, for the paper that we published together.

To Krishna and Nina, for being my companions on the road to neuroscience. Well, I ended up not going there, but the experience was great.

To Janaki, for walking the path I was walking one year before me, and giving me all the good hints and advice.

To Andrey, for basically being my mentor.

And of course, to my family. Without your support, I would never make this far.

Chapter 2 is adapted from Ref. [162] with permission from PNAS.

Chapter 3 is adapted from Ref. [166] .

Chapter 4 is adapted from Ref. [165] with permission from MDPI.

Chapter 5 is adapted from Ref. [59] with permission from The Royal Society of Chemistry.

Chapter 6 is adapted from Ref. [164] with permission from APS.

Chapter 7 is adapted from Ref. [161].

Chapter 8 is adapted from Ref. [13] with permission from APS.

Curriculum Vitae

2009 – 2013	B.S. in in Physics and Applied Math (with honors). Moscow Institute of Physics and Technology, Russia. Advisor: Prof. Emil Akhmedov.
2013 – 2015	M.S. in in Physics and Applied Math (with honors). Moscow Institute of Physics and Technology, Russia.
2015 – Present	Ph.D. student in Physics, University of California, Los Angeles (UCLA).

Publications

Braiding dynamics in semiflexible filament bundles under oscillatory forcing VM Slepukhin, AJ Levine arXiv preprint arXiv:2105.12879

Thermal Schwinger Effect: Defect Production in Compressed Filament Bundles. VM Slepukhin, AJ Levine arXiv preprint arXiv:2103.08832

Topological defects produce kinks in biopolymer filament bundles. VM Slepukhin, MJ Grill, Q Hu, EL Botvinick, WA Wall, AJ Levine Proceedings of the National Academy of Sciences 118 (15)

Microcircuit synchronization and heavy tailed synaptic weight distribution in preBötzinger Complex contribute to generation of breathing rhythm VM Slepukhin, S Ashhad, JL

Feldman, AJ Levine arXiv preprint arXiv:2012.12486

Directed force propagation in semiflexible networks. MJ Grill, J Kernes, VM Slepukhin, WA Wall, AJ Levine Soft Matter

Dynamical phase separation on rhythmogenic neuronal networks. M Bibireata, VM Slepukhin, AJ Levine Physical Review E 101 (6), 062307.

The conformation of a semiflexible filament in a quenched random potential. VM Slepukhin, MJ Grill, KW Müller, WA Wall, AJ Levine Physical Review E 99 (042501).

Infrared dynamics of the massive ϕ^4 theory on de Sitter space. ET Akhmedov, FK Popov, VM Slepukhin Physical Review D 88 (2), 024021

CHAPTER 1

Introduction

1.1 Networks around us

The study of complex, many-body systems is one of the forefront questions in modern physics. While such systems have been the subject of intense studies, these investigations have been mostly confined to systems with local interactions, i.e., the situation where only the nearest neighbors can interact. Spatially nonlocal interactions, however, appear in a variety of systems, and are particularly ubiquitous in the living world. For example, genetic and neural networks exhibit interactions controlled by connectivity in an abstract space, not distance. Namely, the strength of the interaction between two neurons depends solely on the strength of the connection between them, not on the distance between two neurons. Such networks can be referred as controlled by topological properties only (i.e., who connects to whom) - the position of elements of the network in the space does not play role in its dynamics.

There are, however, networks where both topology of connections and the geometrical position in space matter. Examples are transport networks and biopolymer filament networks, where long molecules (filaments) are held together by shorter ones (cross-links). The position of the transport route in space, its shape, matters for the dynamics. The same is true for filament networks, where bent filament and straight

filament certainly respond to applied force in a different way.

In this thesis, I consider one example of the solely topology controlled network, and one example of the geometry controlled network. For the geometry controlled, I study the above-mentioned biopolymer filament network (see Section 1.2). For the topologically controlled, I study the particular case of the biological neuronal network, the preBötzinger Complex, controlling breathing of mammals (see Section 1.3).

1.2 Biopolymer networks

Biopolymer filament networks are ubiquitous in the living nature, from the cytoskeleton inside living cells to the intercellular matrix in between cells forming tissues.

The cytoskeleton, the "carcass" of the cell that controls its shape, consists of long (from 100 nm to few microns [86]) molecules of F-actin, called filaments, connected by shorter molecules of different types, called cross links (see Fig. 1.1 for an image of the cytoskeleton). These cross links are physical, or transient: the binding energy is low enough so they can couple and decouple [101]. This property is not a general case; for example, certain types of rubber are created using chemical crosslinking, where the bonds are covalent (which makes their energy significantly higher than the energy of the thermal fluctuations), so the cross links can be considered as constant [179]. For the living cells, however, the bonds are hydrogenic, which makes them much easier to destroy.

There are different types of cross links. Smaller ones, such as α-actinin and fimbrin, are usually participating in forming bundles - groups of filaments aligned together, densely connected by the cross links. The larger, such as filamin, spectrin,

and dystrophin, are less likely to require alignment of the filaments, thus being a crucial ingredient for forming a whole network of the cytoskeleton [172, 1].

The intercellular matrix is made up of collagen bundles, that have a hierarchical structure (see Fig. 1.2 for illustration). On the lowest level of this hierarchy, there is a triple helix of approximately 0.3 micron length, that consists of three polypeptide chains. These triple helices aligned together form fibrils, and fibrils, aligned together, form fibril bundles and fibers, and, finally, fibers form the intercellular matrix [175].

Thus, in both cytoskeleton and intercellular matrix bundles of filaments are one of the most common structural motifs. Naively, such bundles could be considered as coarse-grained thick and stiff filaments. However, the real picture is far more complicated. For example, due to the possibility of sliding one filament relative to the rest of the bundle, the effective collective bending modulus starts to depend on the length of the bundle [11, 68]. Another crucial difference is the presence of the metastable states. Namely, crosslinking can trap a segment of the bundle in a state, different from the straight bundle. We refer to the segment of the bundle in this state as a *defect*. To go from this state to a straight bundle, one needs to remove all cross links either on the left or on the right from the defect, which makes it very stable and long-living. We devote the first three chapters of the manuscript to the study of these defects.

In the chapter 2, we classify the defects on the bundle and explore the conditions when the defect can produce a region of localized curvature, that we name a *kink*. We observe such kinks in the experiment with collagen fibers and in numerical simulations. In the chapter 3, we see how compression of the bundle leads to the production of a particular type of defects, in a way resembling the Schwinger effect

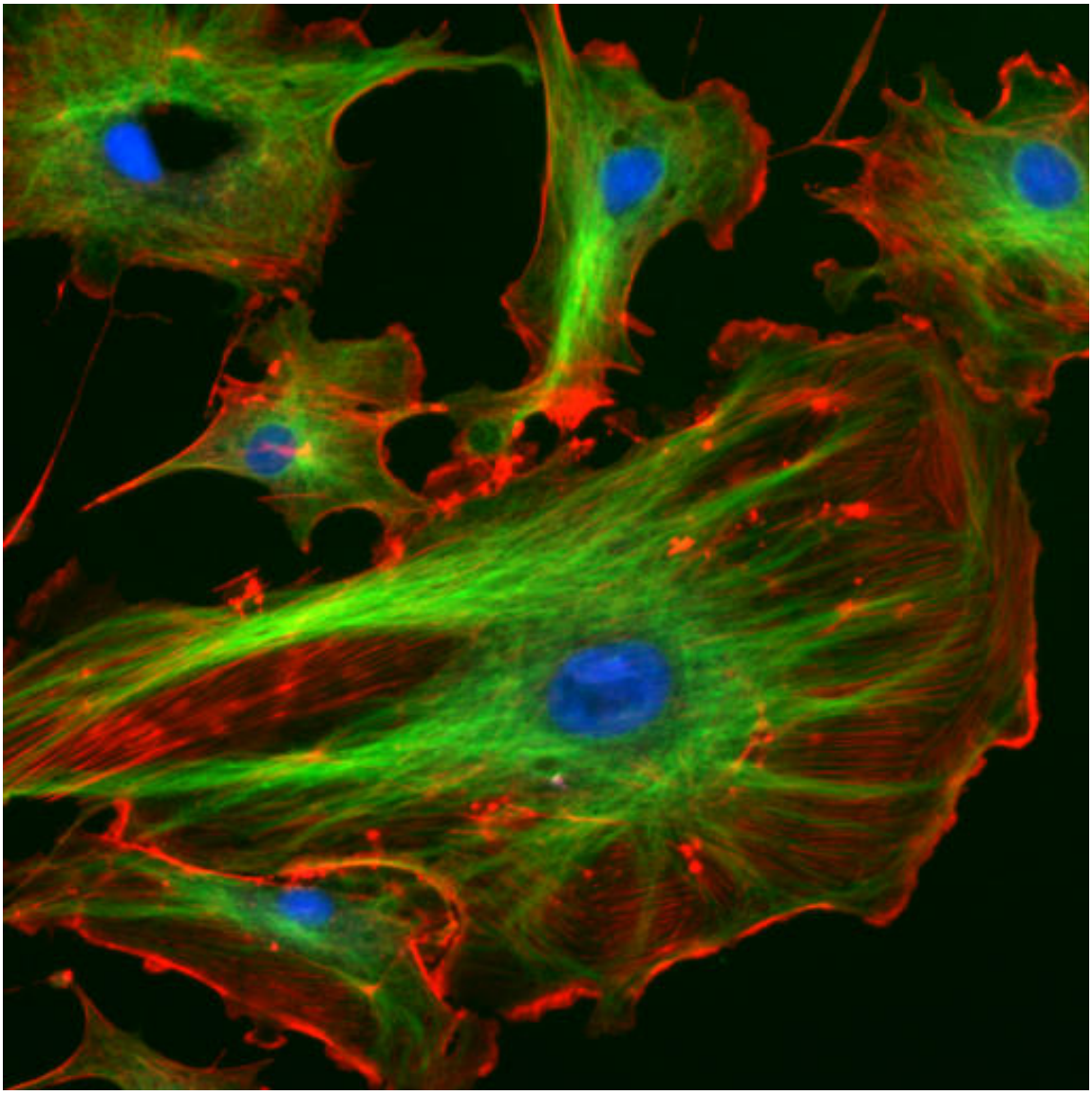

Figure 1.1: Fluorescent image of the cytoskeleton. F-actin filaments are shown in red. Image from [185]

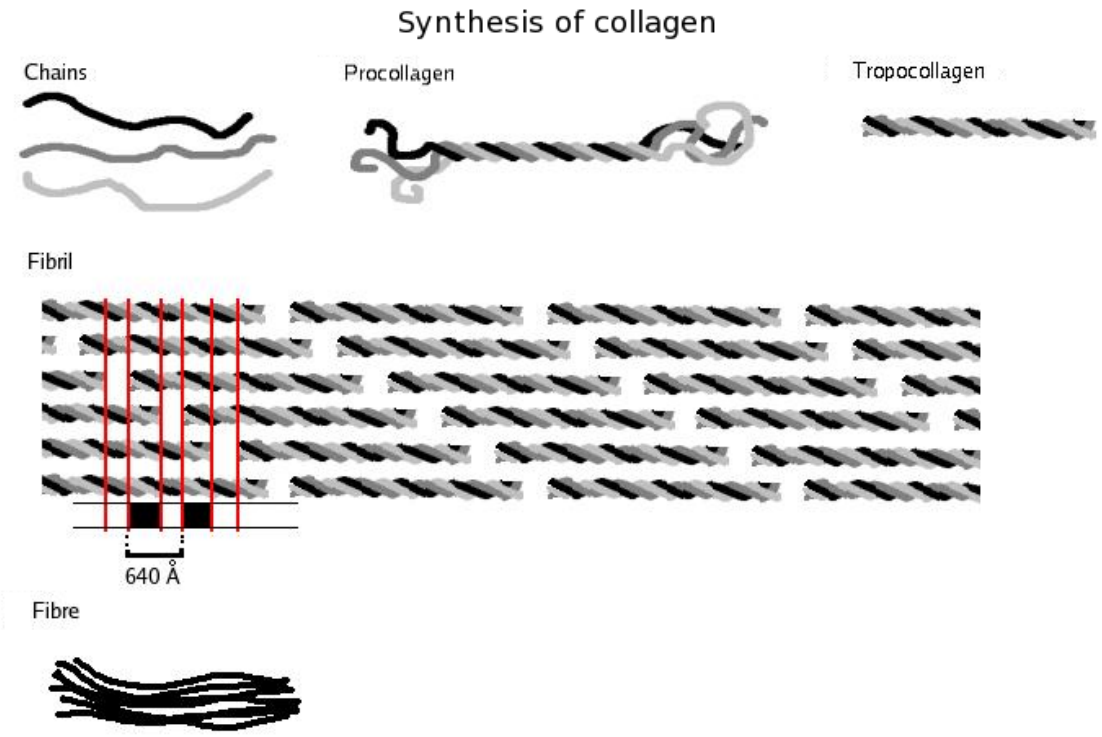

Figure 1.2: Hierarchical structure of collagen. Triplices (on top) form fibrils (middle) that form fibers (bottom). Image from [186]

- the production of electron-positron pairs in the strong electric field. We continue studying the effect of the external field in chapter 4, where we see that oscillatory force enhances the production of another type of defects.

In the next chapter, we change gears and look at the elastic properties of the whole network. Namely, we study numerically and analytically force propagation from the point-like source. We observe that instead of homogeneous stress distribution like in the uniform elastic media the tension propagates in a tree-like way like a lightning. We call these tension pathways *force chains*. This non-homogeneous distribution is crucial for mechanosensing, the force-driven communication between distant cells in a tissue.

We conclude this part with chapter 6, where we change gears once again. Here we look at the single filament, modeling other filaments in the bundle or network as a quenched random potential. Such treatment allows to directly take into account thermal fluctuations of the filament.

1.3 Neuronal networks

Neuronal networks are perhaps the most well-known example of the network in biology. They control almost any complicated animal behavior, including learning, memory, and decision making. Outside of the living world, they inspired artificial neural networks - structures, where the nodes are borrowing particular properties of real neurons to achieve such functions as image recognition, linguistic analysis, and many more that biological neural networks are tremendously capable of.

The main ingredient of the neural network, is, as one may guess, the neuron (see

Fig. 1.3 for an illustration). Neuron is cell that consists of *soma*, *dendrites*, and *axon*. Soma is the compact body of the neuron, often modeled as a point. Dendrites stem from the soma and branch for a few hundred micrometers around it. Single axon also stems from the soma, but can be much longer, even up to 1 meter. It also branches. Axon ends with *axon terminals*, where it synapses to dendrites of another neuron (which means that while neurons remain to be distinct cells, the electric current from the axon of the first neuron will influence the state of the other neuron).

In this picture, dendrites are essentially input terminals, and the axon is the output of the neuron. When the electric potential of soma (called somatic potential) exceeds a certain threshold, the neuron *fires*: it produces a sharp impulse of current that spreads along the axon, called *action potential*. This action potential (sometimes referred to as spike because of its shape as a function of time) reaches dendrites of other neurons, leading to the change of the membrane potential of these neurons, and the magnitude of the effect depends on the synaptic connection between axon terminals and dendrites. If the neuron that fires is *excitatory*, the somatic potential increases; if it is *inhibitory*, somatic potential decreases. Thus, excitatory neurons make their neighbors fire more, while inhibitory suppress their firing.

The crucial feature of this structure is the non-linearity of the input-output function of the neuron. Indeed, the neuron does not increase its firing linearly as the input increases, but demonstrates a sharp threshold behavior, with very low or no firing for below threshold input and noticeable firing above the threshold. It is important to keep this property for the artificial neural network as well - none of them can work with purely linear neurons.

The models of individual neurons can differentiate on the level of complexity

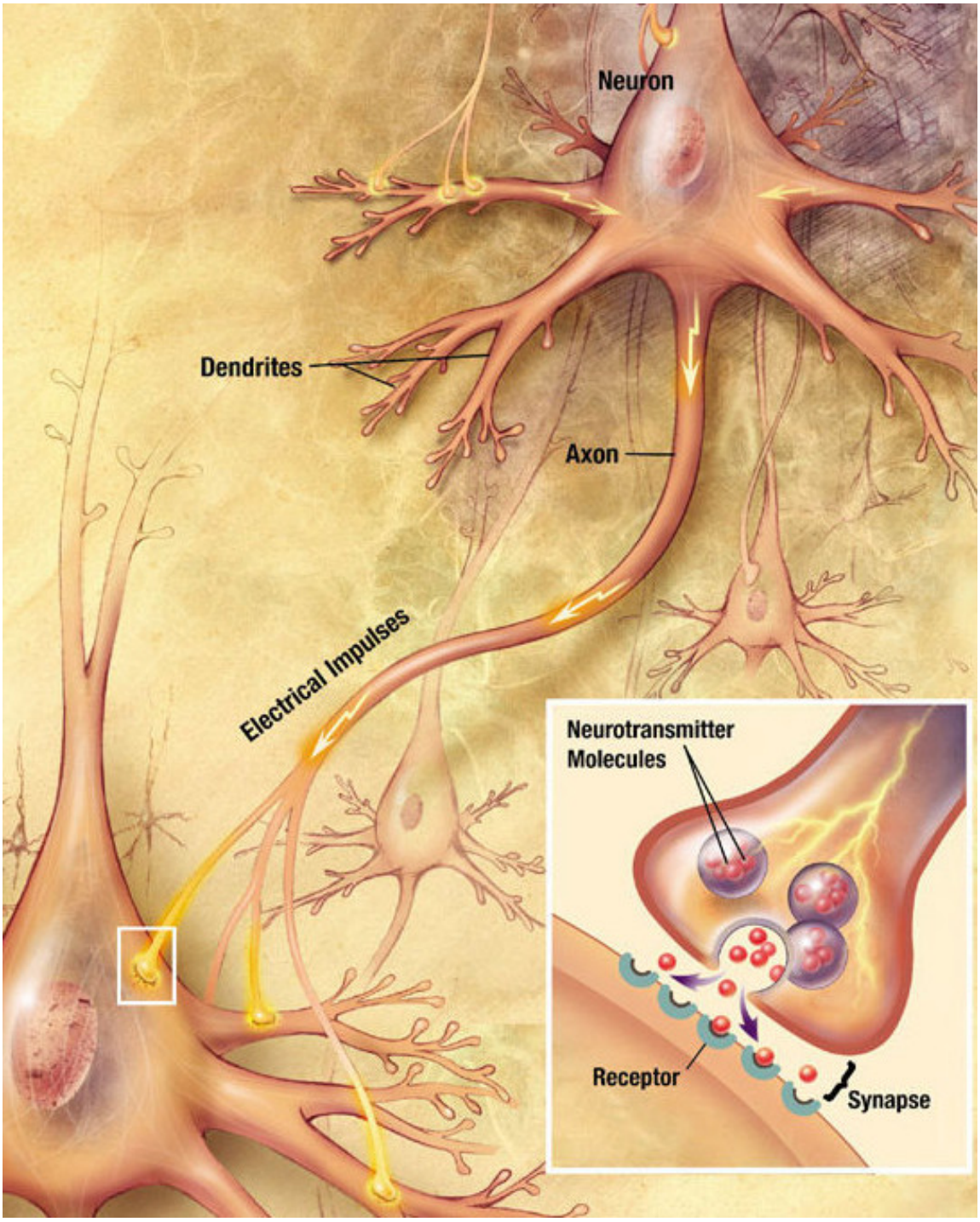

Figure 1.3: The artistic view of the neuron. Image from [184]

and physiological accuracy. There are complicated multi-parameter models such as Hodgkin-Huxley, that aim to create an electrophysiological model of the cell. The significant simplification is the leaky integrate-and-fire (LIF) model, where the somatic potential is controlled by a first-order differential equation of the charging capacitor [92]:

$$RC\frac{dV_i}{dt} = V_{\text{rest}} - V_i(t) + R\sum_j I_{i,j}(t) \tag{1.1}$$

where V_{rest} is the resting potential with no external input, C is the membrane capacitance, R is the membrane resistance, $I_{i,j}$ is the input current from the neuron j to neuron i , the sum is over all input neurons that synapse to neuron i. The current $I_{i,j}$ is a series of sharp pulses with centers around the times when neuron j was firing (and delayed by the time of transmission from neuron j to neuron i that is usually insignificant)". Neuron fires when its somatic potential reaches the firing threshold, and that the somatic potential drops back to the rest value, or even slightly below. This model is perhaps the simplest among the physiological models, yet it is usually still too complicated for the analytical treatment.

A slightly simpler yet still useful model is the firing rate model. In this model, one does not consider the exact time when neuron fires, but rather looks at the average firing rate of the neuron as the function of its somatic potential. In terms of this average firing rate, the somatic potential as a function of time is still controlled by a first-order differential equation

$$\frac{dV_i}{dt} = \frac{1}{RC}(V_{\text{rest}} - V_i) + \Delta V\sum_j r(V_j) \tag{1.2}$$

where the summation is again over the neighbors that synapse to neuron i, $r(V)$

is an average firing rate of neuron j, and ΔV is the average change of the somatic potential of the neuron due to the incoming spike. Different versions of this model are used for artificial neural networks, and it has enough flexibility to capture the dynamics of biological neural networks in cases when only the average firing rate, not the exact moments when neurons spikes, is relevant. However, it is not able to capture the situation when the exact time of the spiking is the crucial ingredient, for example, for the process of synchronization between the neurons. Firing-rate based model is significantly simpler than the LIF model and sometimes allows analytical treatment. When it does not, it is still significantly faster for numerical computations, which perhaps was the main reason for using it in artificial neural networks. There are cases, however, when even the firing rate model is not simple enough, for example, when intense numerical exploration is not feasible due to the generality of the problem and only analytical solution may bring some new ideas.

In this case, one may consider the on-off neurons, where the neuron can be either in "on", or firing state, or "off", or not firing. This is nothing but the limiting case of the firing rate model with the firing rate $r(V)$ being the Heaviside step function. This simple model strongly resembles the Ising model and in many cases is solvable analytically.

The dynamic of the whole network is controlled by two components: the dynamics of the individual neurons, described above, and the way neurons are connected. In the second part of this dissertation, I am primarily interested in how network connectivity patterns influence the dynamics of the system. While the models we consider are quite general and can in principle be applied to different brain regions, to compare with the real data I focus my attention on solely preBötzinger Complex (preBötC). PreBötC is a microcircuit consisting of a few thousand neurons that

produce rhythmic activity, controlling inspiration in mammals [168, 31]. This rhythm consists of short periods of high activity, or bursts, when all neurons fire with high frequency ($\approx$ 40 Hz, [80]), and long periods of low activity, or interburst intervals, when neurons are almost silent (firing frequency 0.5-2 Hz, [7, 58, 147, 137]). During the burst, the signal travels from preBötC to muscles causing inspiration.

This periodic activity is an emergent property of the complex [31, 7, 26, 44, 181, 79, 133, 134]. While there are pacemaker neurons in preBötC, that may produce rhythm on their own, blocking them does not terminate the rhythm [134]. This implies that the rhythmic activity must be a collective property of the network rather than the property of single neurons. Excitation only is not enough to obtain desired oscillations; inhibition is also required. The inhibition can be realized either by adding inhibitory neurons to the network or by introducing internal variable for each neuron, modulating its sensitivity [43, 154]. Here I am going to consider the latter approach.

Specifically, the slow internal variable (identified by experiment to be dendritic calcium concentration [124]) leads to the oscillatory behavior in the following way. The membrane resistance of each neuron is high when the calcium concentration is low, and low when the calcium concentration is high. The calcium concentration grows with the incoming synaptic current. Thus, this calcium mediation plays the role of negative feedback. When the calcium concentration is low, membrane resistance is high, the neurons are sensitive to incoming spikes and, through mutual excitatory interactions, they collectively increase their somatic potential and firing rate, leading to a burst. During the burst, high input synaptic current drives calcium to higher values, making neurons insensitive to further input. Then the somatic potential of the neurons returns to its rest value, and the firing ceases until the calcium

concentration also decays to its equilibrium value, completing the cycle.

In this part of the dissertation, I construct the mathematical model of this process for different neuron's dynamics and different networks and compare the results with experimental data. In chapter 7 I consider the process of external activation of the burst by stimulation of the small subset of neurons (1-10), obtaining for the LIF model quantitative agreement with experimental data and limitations for the possible network connectivity patterns. In chapter 8 I consider how network topology controls the stability of the rhythm, observing for the firing rate model the phase separation onto high firing and low firing subnetworks.

Part I

Filament networks

CHAPTER 2

Topological defects produce kinks in biopolymer filament bundles

2.1 Introduction

As we discuss in chapter 1, the cross linked filament bundles can trap defects dramatically changing their mechanical properties and even shape. We focus on these defected, metastable states and their effect on the low-energy configurations of the bundle. Specifically, we show that there are three types of defects, two of which correspond to topological defects in the bundle's unstressed state – braids and dislocations. These and a third form of trapped length (loops) are all long-lived structures due to cross linking.

As a result of these structural defects within the bundle, the elastic reference state is no longer straight, even though straight filament configurations are individually the lowest energy state of the constituent filaments. Bundles containing these defects can minimize their elastic energy by taking on localized bends, which we call kinks. The presence of kinks allows one to relate the micron-scale contour of kinked filament bundles to their nanoscale structure, specifically the presence of length-trapping defects. We show that the combination of theory and simulation of defected bundles

can account for the distribution of kinks we observe in experiment. Over long times, defects slowly anneal in bundles. This slow relaxation of the bundle's structure can be understood in terms of the diffusion and interaction of the defects on it. Specifically, defects leave the bundle either through diffusion off the bundle's ends, or by the annihilation of defects within it.

Defected bundles not only explain the apparent kinks in collagen fibers, but also the presence of defects have implications for the collective elastic response of the bundle. In particular, we show that kinks are more bending compliant than undefected lengths of a bundle. As a result, we hypothesize that the collective mechanics of a network of defected bundles depends on the number and position of these quenched defects, which act like soft hinges in a three-dimensional network of bundles that behave more like stiff beams.

Topological defects are well known in condensed matter, including e.g., disclinations in nematic liquid crystals and dislocations in crystalline solids [22, 91, 131]. Defect motion plays a dominant role in the plastic deformation of many solids. Dislocations and disclinations are topological defects; their removal requires a system-sized reorganization of interatomic bonds. The defects in filament bundles share this feature. They cannot be removed without breaking a number of cross links proportional to the bundle length (we consider the filaments to always be unbreakable). This feature ensures that the defects are long-lived on the scale of the thermal undulations of the bundles themselves.

In our observations of collagen networks, we observe kinked bundles, whose contour we quantify by measuring their local curvature using light microscopy. Due to their connection to the network, we cannot be certain that these kinks are not in

some way related to elastic stress in the network. To address this question, we used large-scale Brownian dynamics simulations to study kinking in quenched filaments with force- and torque-free boundary conditions, finding that quenched defects produce a statistical distribution of kinks similar to those observed in the experiment. Using the simulations, we are also able to measure the reduction of the bundle's local bending modulus at the location of the defects and observe the motion of the defects along the bundle. Finally, we present theoretical calculations using a simple model of semiflexible filaments that demonstrate the relationship between defects and kinks in the bundle. Moreover, we analytically determine (and test via simulation) the time evolution of the number of defects in a bundle as they slowly anneal through defect-defect annihilation or by diffusion off the ends.

We first report our observations from light microscopy of kinks in collagen bundles and compare these kinks with those from numerical simulations. We then present a general discussion of the three types of defects and demonstrate that the minimum energy state of the defected bundle can be kinked. We explore defect dynamics, estimating the life time of a kink and the number of kinks in a bundle as a function of time, which we compare to simulation. To properly describe interaction of braiding type defects, we use the theory of the braid group; some relevant background is provided in the Appendix A.

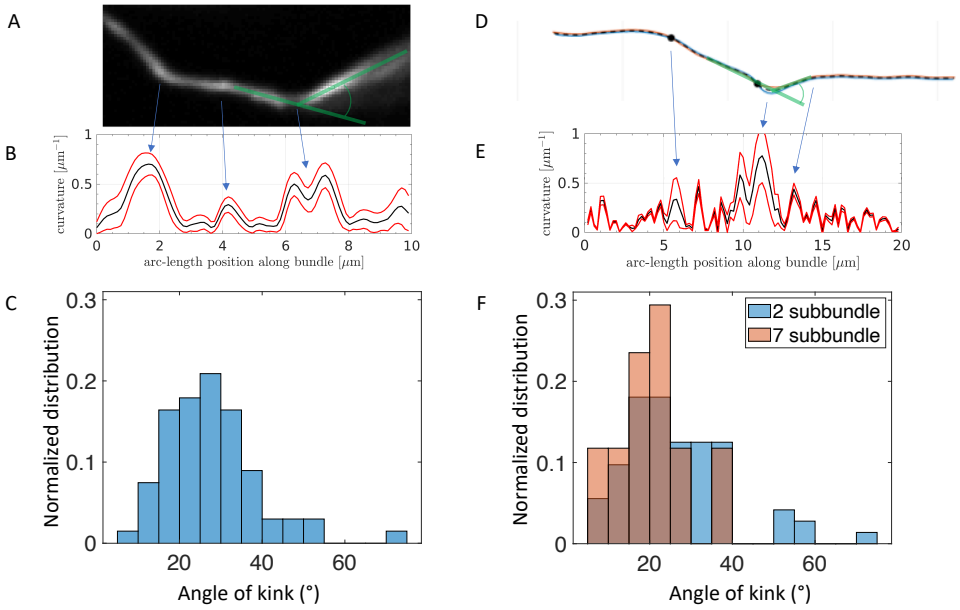

Figure 2.1: Measurements of collagen bundles using fluorescence microscopy (left column) and simulations (right). A) Fluorescence image of a collagen bundle with noticeable kinks. Green traces show a measurement of the kink angle, given as angular deviation from straight. B) Mean curvature (black) of a collagen bundle over 50 images. Red lines show the spread of curvature in time (1 std). Blue arrows mark the locations of high curvature. C) Histogram of mean kink angles for all measured bundles ($n = 74$). D) 2D simulation of bundles with reversible cross linkers showing the bundle centerline (black dashed line), individual filaments (blue and red) and braids (black dots). E) Mean of the curvature over 100 configurations (black). Red lines indicate one standard deviation. F) Kink angles from simulation for 2 filament bundles in 2D and 7 filament bundles in 3D measured in the same way as in (C).

Results

2.1.1 Experiment[1]

The nanoscale structure of collagen is quite complex [159, 18]. Small fibrils bind together to form larger fibrils, which, in turn, bind together to form fibers, which we observe in light microscopy. Given that these fibers associate rapidly and strongly with local bonds, collagen fibers are a good place to look for quenched defects in bundles and kinks, if such sharp bends of the bundle indeed result from those defects [83]. In fact, kinked collagen bundles have been observed previously [48, 144, 60] using electron microscopy. These observations leave the possibility that the kinks observed in a single snapshot of a dynamic, flexible structure may be consistent with thermal undulations about a straight equilibrium state, rather than long-lived sharp bends [178]. To address this question, we made multiple observations of collagen bundles in an aqueous environment to determine if the time-averaged state of the bundles includes kinks.

We reconstituted pepsin-extracted type I bovine collagen and fluorescently labelled and imaged individual bundles. In Fig. 2.1A we show fifty superimposed images of a single bundle (White on a black background) taken 0.5s apart and showing three persistent kinks, which confirms that they are indeed long-lived structures. Green lines indicate the measurement of a kink angle. We measure the 2D projection onto the microscope's focal plane of the physical kink angle in three dimensions. We accept kink observations only when at least about three microns of bundle is observable on either side of the kink. In order for the image of the bundle to extend away

[1] **Experiment was performed by Qingda Hu and Elliot Botvinick, UCI**

from the kink on both sides, our reported kinks must lie in a plane making at most a small angle with respect to the focal plane. As a result, the discrepancy between our observed kink angle distribution and physical one is quite small. We find less than ten percent discrepancies between the projected and three-dimensional, physical angle distribution when testing this procedure with simulated data – see Appendix A Sec. 1D.

74 kink angle measurements from 43 bundles are summarized in Fig. 2.1C. The trace of the local curvature versus arc length along the bundle shown in Fig. 2.1B quantifies the points of high persistent curvature as indicated by the blue arrows. These local curvatures were computed by discretizing the contour using the intensity pixels in each image and computing the curvature from a cubic spline fit to these data. More details are given in Appendix A Sec. A.1A.1.2. Repeating this procedure for other bundles, we observed kinks and determined their mean kink angles by averaging again over up to fifty repeated measurements of each kink angle. They showed temporal fluctuations with a nonzero mean. We present the distribution of kink angles for 74 bundles in Fig. 2.1C. There were larger variations between kink angles measured across multiple bundles than in the thermal fluctuations of a given kinked bundle. The distribution of these time-averaged kink angles has a mean at 26 degrees and includes a range of typical angles between 7 and 55 degrees. We observed one high-angle kink with a bend of 74 degrees.

Many of the experimentally observed kinks appeared to be flexible. As typical example, the kink angle of the bundle shown in Fig. A.1 had a mean of 29 degrees, but fluctuated between 21 and 38 degrees. Because the bundle's ends were constrained by the network, we cannot use these thermal fluctuations of the kink angle as a true measure of the kink's bending compliance.

2.1.2 Numerical simulation[2]

To better explore both the nanoscale structure of the cross section of the kinked bundles and to study the system with simpler, free boundary conditions, we turn to Brownian dynamics, finite-element simulations. Our numerical model describes

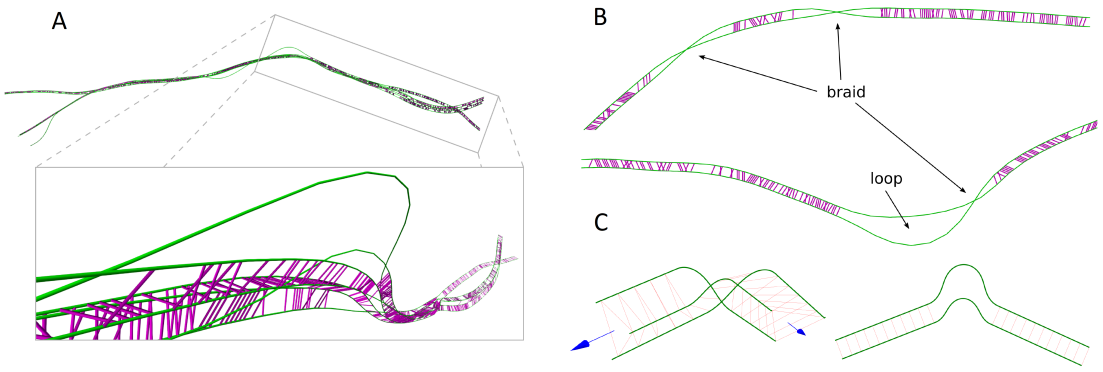

Figure 2.2: Typical bundle shape and defects observed in numerical simulations of the bundle formation process, starting from initially straight and parallel filaments without any initial cross links. (A) Example images show the entire bundle consisting of 7 filaments (green) in 3D and approximately 1600 cross links (pink). A magnified part is shown in the inset. (B) Braids and loops observed in simulations with a minimal setup of two filaments (green) and transient cross links (pink) in 2D. (C) Schematic of a braid (left) and a loop (right) as described in our analytical model.

the semiflexible filaments as elastic objects via geometrically exact beam theory, and includes viscous dissipation (local drag), thermal forces, and the random binding and unbinding of cross links [28, 29, 129]. Bound cross links are treated as short elastic beams making locally normal connections to the filaments to which they are

[2]**The numerical simulations were performed by Maximillian Grill and Wolfgang Wall**

bound. As a result they act like so-called bundling cross linkers that elastically constrain the angle between the bound filaments. Such linkers are well-known in F-actin networks [117, 188, 139]. The details of collagen intra-bundle cross linking are more poorly understood. In the absence of detailed models for these cross linkers, we chose this simple linker model to promote bundling. Initially, all filaments were straight and parallel without any cross links. To form bundles, a fixed concentration of cross linkers was added to the finite-temperature (stochastic) simulation. The interaction of the thermally undulating filaments with transient cross linkers lead to rapid bundle self-assembly (see Fig. A.4) with a number of quenched defects. Further details of the model and the setup of the computational experiments are provided in the methods section below and in Appendix A Sec. A.2.

2.1.2.1 Observation and characterization of defects

A 7-filament bundle is shown in Fig. 2.2A from a simulation in three dimensions. Its contour deviates quite drastically from the trivial equilibrium shape of straight and parallel filaments, which are regularly cross linked along their entire length. These metastable configurations of the bundle with localized bends – kinks – persist over long times as compared to the typical time scale of the angular fluctuations of the mean local tangent of the bundle. Over still longer times, the locations of the kinks move along the bundle, as described below.

We observe two distinct classes of defects in the quenched bundles, which are all related to a mismatch between amount of filament arc length taken up per fixed unit length of the bundle. These are (1) *braids*, i.e., rearrangements of filaments within the bundle, and (2) *loops* where one filament stores excess length by looping out of the

bundle and then reattaching to it. Both braids (actually pseudo-braids, as described below) and loops are shown in Fig. 2.2B from a two-dimensional simulation of two filaments where the filaments are allowed to cross each other but cannot untwist. This special setup is motivated by the fact that it is the smallest system capable of supporting a loop or a pseudo-braid. The pseudo-braid is a projection of a braid onto two dimensions and is the mechanical analog of a true braid in 3D. As will be shown in Sec. 2.1.3, the two-filament pseudo-braid is energetically equivalent to the case of a true braid of three filaments in 3D when the two filaments making up the pseudo-braid in 2D have different bending moduli. The simplest system that supports true braiding defects is a three-filament bundle in three dimensions, shown in Fig. 2.2C. The inset of Fig. 2.2A shows the typical structure of a loop in a larger bundle. There is also a third type of defect, (3) a *dislocation* in which a filament end appears within the bundle. This defect was not created in our simulations due to the fact that we started the system with equal length filaments whose ends were initially aligned at one end of the simulation box. In the simulations, we concentrate on braids and loops. We first analyze the curvature of the bundle center line as well as the kink angles resulting from such defects, and then investigate the dynamics of the defects, i.e., how they move along the bundle and potentially interact with each other.

2.1.2.2 Curvature and kink angles of defected bundles

Fig. 2.1D shows a typical configuration of the minimal bundle setup with two filaments (blue and red) in two dimensions. The bundle centerline (black dashed line) is computed as the average of the two filament centerlines, and braids (black dots) are

detected by the crossings of the filament centerlines. The curvature of the bundle's centerline as a function of centerline arc length is plotted in Fig. 2.1E, showing both the mean (black) and the standard deviation range (red lines) of the curvature computed from 100 simulation snapshots with a time interval of 1s. Close to the midpoint of the bundle in the range of arc lengths $10\mu\text{m} < s < 12\mu\text{m}$, we observe two peaks in the curvature that are clearly visible as a double kink in the bundle configuration shown in Fig. 2.1D. These can be explained by the braid and loop defects there. The standard deviation of the curvature is increased by about one order of magnitude in this defected region, indicating a local increase in angular fluctuations at this point. This is a direct measure for the decreased effective bending modulus of the bundle in these defected, non-cross-linked regions. Using the relation between the thermal fluctuations of the local curvature and the bending modulus, we estimate a decrease in the effective bending modulus of about two orders of magnitude. Apart from the locally decreased bending modulus, such a defect most likely also leads to an anisotropy in the bundle's bending mechanics, which breaks another basic assumption of the ideal bundle as a single, thick filament. Similar features in the curvature data are observable for the second braid of this bundle at approximately $s = 6\mu\text{m}$ of this bundle. More examples are found in the other simulation runs. Additional results showing the curvature along the bundle at different time points are provided in Fig. A.5.

The histogram of measured kink angles over a total of 12 simulations is shown in Fig. 2.1F. Here, we applied the same procedure for the angle measurements as described for the experimentally obtained microscopy images in Appendix A Sec. A.1A.1.2. The 3D simulation results were rotated such that the bundle centerline tangents left and right of the kink lie within the image plane. The distribution of

72 kink angles for the two-filament bundle has a mean of 27 degree, with a standard deviation of 14 degrees and values ranging from 4 to 77 degrees. The kink angle distribution for larger bundles with 7 filaments in three dimensions demonstrate a trend towards smaller angles and a more narrow distribution with 20±8 degrees (mean ± standard deviation). Big bundles with up to 225 filaments will be investigated in more detail below.

2.1.2.3 Dynamics and interactions of defects

We now use our simulations to study dynamics on longer time scales, where we expect to see the motion of defects along the bundle and their annealing as the metastable, defected bundle slowly relaxes. To facilitate these observations, we need to speed up the motion of the defects by doubling the linker unbinding rate in our simulations to $k_{\text{off}} = 6\text{s}^{-1}$. At this rate the motion of defects is still much slower than the undulatory fluctuations of the bundle, but now defect motion is moved into a time scale accessible by simulation, which covers 1000 seconds.

Fig. 2.3 shows an example of how the (defected) configuration of a two-filament bundle evolves over time. We plot the position (measured by arc length) of braids (red dots) and cross links (blue dots) along the bundle horizontally, with time increasing vertically. The resulting red tracks record the world-lines of the braids over a simulated period of 500 seconds. The white vertical scars show cross-linker gaps in the otherwise densely cross-linked bundle. Due to a small off-set between the filaments, there is a nearly persistent gap in cross linking at the left end of the bundle where one filament stops. Cross linkers appear in this gap because one filament slid far enough past the other to wrap around and briefly cross link to the other one

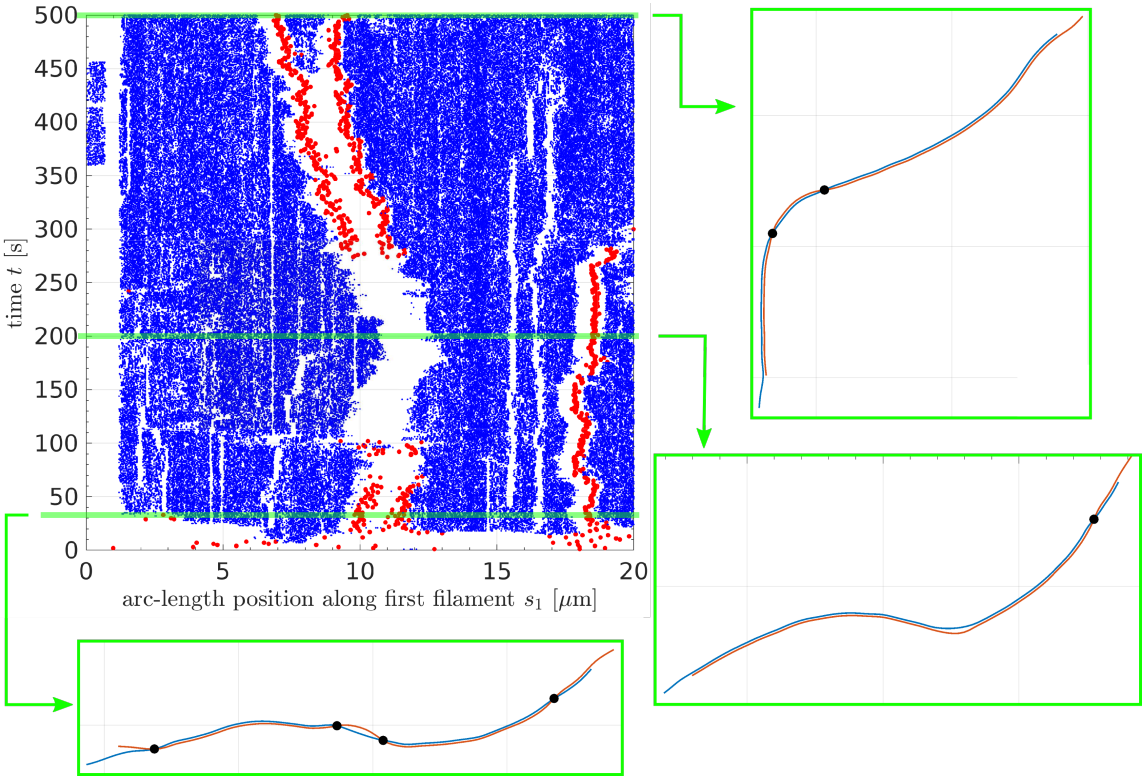

Figure 2.3: Dynamics and interactions of defects observed in 2D numerical simulation. The position of braids (red dots) and cross links (blue dots) along the (first, i.e., blue) filament is tracked over time. The inset images (green frames) show the corresponding configuration of the two filaments (blue and red lines) and the braids (black dots) in the bundle at three different time points.

due to the periodic boundary conditions of the simulation box. We observe a pair of braids located near the bundle midpoint first emerge after $\sim$ 20s during the initial quench of the bundle. This timescale for the formation of the quenched bundle is typical and consistent with observation of the initial growth of the number of doubly bound cross linkers; that number rapidly increases from zero at the beginning of a simulation and plateaus around 20s, indicating the maturation of the defected bundle – see Fig. A.4 for further details on bundle self-assembly. Once the bundle has formed, the two braids in the middle approach each other and appear to annihilate, leaving a low-cross-linker density region within the bundle during the time period of 100s $< t <$ 270s. After that time, a new pair of braid defects form. These slowly separate as more and more cross links are formed between them.

The single braid close to the bundle's right end diffuses until it approaches the far right end of the bundle at $s \approx 19\mu$m and at time $t \approx$ 280s. Here it vanishes by diffusing off the open end. The filaments simply uncross and new cross links are established between the unbraided filaments. Looking more carefully, one may observe a similar phenomenon on the left edge of the bundle. Immediately after the quench there are actually four braids on the bundle, as indicated by the picture of the system at timeslice $t =$ 34s. Almost immediately after this time and long before the next bundle configuration image at $t =$ 200s, that leftmost braid diffuses off the left end of the bundle. The final state of the bundle at $t =$ 500s shows a bent configuration where the localized bend near the center of the bundle is due to the two interacting braids that remain in the system. For these parameter values, the typical lifetime of a defect is 100s of seconds.

2.1.2.4 Bundles with large number of filaments

Motivated by the fact that the number of filaments in a biopolymer bundle is likely to vary from $\mathcal{O}(1)$ to $\mathcal{O}(10^3)$, we explored simulations of bundles with significantly larger than in previous sections number of filaments in three dimensions. Fig. 2.4A shows a self-assembled bundle with 225 filaments (white) and approximately 16000 cross links (pink). To rule out the influence of the initial arrangement of filaments in plane perpendicular to the bundle's mean tangent, we ran simulations with filament endpoints placed on a square grid in addition to the hexagonal grid. We observed no significant differences.

The large bundle's structure is hierarchical; one can identify more tightly bound sub-bundles that form loops and braids with each other along the bundle's length. As observed already in 25-filament bundles, its centerline remains rather straight, while the sub-bundles show the characteristic kinks observed in the smaller bundles. One possible explanation for the rather straight form of the big bundles is the smaller aspect ratio as compared to the small bundles; in other words, very large bundles may well show kinks over longer distances, since such kinks require higher energy and thus statistical less probable, defects. Simulations of big bundles with the same aspect ratio as the smaller ones remain computationally prohibitive. We observe in the large bundle a large hole created by a sub-bundle loop defect. Its appearance is strikingly similar to our experimental images of collagen bundles in Sec. 2.1.1 (Fig. 2.4B). Those parts of the images showing the hole defect are magnified and compared side-by-side in the center panel of Fig. 2.4.

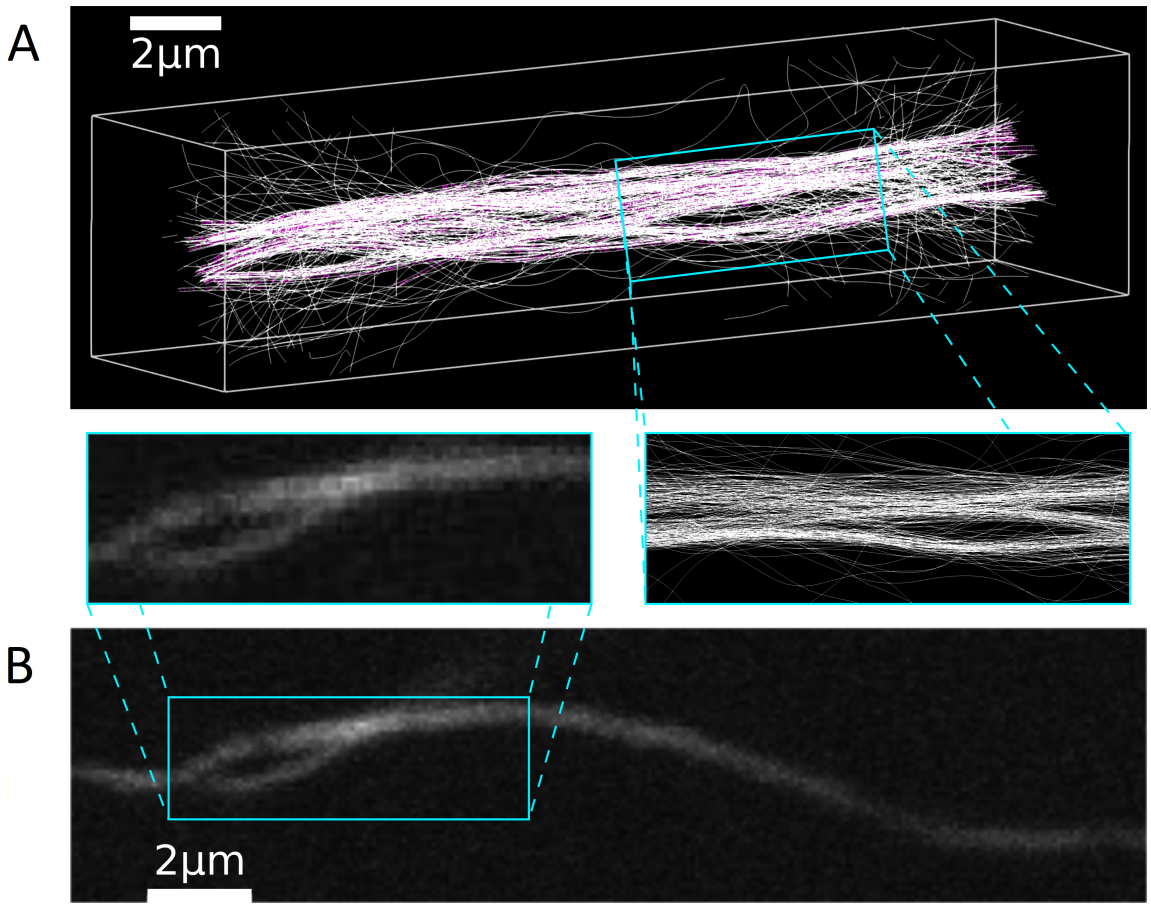

Figure 2.4: Hole defect observed in simulation and experiment. (A) 3D simulation of a bundle with 225 filaments (white) and approximately 16000 cross links (pink). (B) Fluorescent confocal laser scanning image of a collagen bundle. Those parts of both images showing the hole defect are magnified and compared side-by-side in the center panel of this figure.

2.1.3 Kinking Theory

2.1.3.1 The model

We now examine the energetics of kink formation using a a simple model consisting of a bundle of N inextensible, semiflexible filaments connected by cross links. The filaments' elasticity is controlled by a single bending modulus κ. The filaments are arranged so that their mean tangent directions are parallel along the $\hat{x}$ axis. In a cross section normal to this direction (the yz plane) the filaments' centers lie on a triangular lattice with a lattice constant equal to the size of the cross linkers. The cross linkers are assumed to locally constrain both the distance between the cross-linked filaments and their crossing angle so that the cross links are normal to the filaments to which they bind. We further assume that the cross linking is reversible, i.e., they bind and unbind from the filament bundle so that the cross linker density within the bundle remains in chemical equilibrium with a solution of free cross linkers at a fixed chemical potential. Previous work has shown that thermal undulations of the filaments induce Casimir forces between cross links [76, 77] and cause the transition between states of free filaments and a densely cross-linked bundle to be a discontinuous, or first-order phase transition rather than a smooth crossover. Here we work at chemical potentials above this transition so that we may assume dense cross linker coverage; hereafter we neglect Casimir interactions and other fluctuation-induced effects.

If all the bundle's filaments have the same length, the energetic ground state is a straight bundle with as many cross links as possible. However, if, at least one of the filament's length differs from those of others, the straight bundle configuration will necessarily have a defect where a filament's end occurs within the bundle. That

dislocation defect may, in fact, be unstable towards forming a kink in the bundle's interior, leading to a kink in the elastic ground state of the system (we explore this point in Sec. 2.1.3.4).

When we consider metastable states, there are many more options. If removing a defect in the structure of cross-linked straight filaments requires uncoupling a large number of cross links, the lifetime of that defect may exceed the time of the experiment. We divide such defects into two groups: defects due to the deviation of the filament from its straight state (loop), and the effects due to the permutations of the filaments (braiding). We study the simplest cases of these effects in Sec. 2.1.3.2 and Sec. 2.1.3.3 respectively.

In all these cases, the energy of the bundle can be written as the sum of two terms: the bending energies of the (n) constituent filaments and energy of their chemical interactions with the cross links

$$E = \sum_{i=1}^{n} \int ds \left\{ \frac{\kappa_i}{2} \left(\partial_s \hat{t}_i \right)^2 + \mu \right\}, \tag{2.1}$$

where $\hat{t}_i$ is unit tangent vector of filament i. The integral is taken over the piece of the filament ℓ without cross links, which generates the term $\mu\ell$ equal to the work of unbinding the cross links in this piece, where μ is a linker binding energy per unit length. Eq. 2.1 implicitly assumes a linear elastic response of the material to bending deformation in that the bending torque is proportional to the bending angle. The parameterization of local curvature, however, is exact even for large bending. In essence, we use the usual assumption [99] that, due to the thinness of the filaments, there are no large strains within the filament cross section even at large curvatures, so constitutive bending nonlinearities may be neglected even for highly deformed filaments.

Since we assume that the cross links completely fix both angle and positions of the filaments, the piece of the filament with cross links is straight and parallel to the whole bundle. We now minimize the bundle's energy subject to boundary conditions that enforce the presence of one or more defects. If a kinked configuration minimizes this energy, we conclude that elasticity theory predicts a kink. This calculation will also determine the optimal size (length) and bending angle of the kink, which we report below. All such calculations assume that the defects do not trap filament torsion. We note from simulation that typical defects include some torsional deformations. As a result, our calculations represent the minimum energy configurations of each defect. We anticipate there to be a continuous spectrum of excited defect states associated with increasing torsional energy. We now perform this minimization for the three different types of defects.

2.1.3.2 Loops

We start with the simplest case of a two-filament bundle, forming a loop defect by demanding that the filaments have disparate lengths $L_1 \neq L_2$ between consecutive cross links. What results is the bending of the whole bundle to form a kink – see Fig. 2.2B. This approach generalizes to N-filament bundles, and can be adapted to large bundles in which two sub-bundles form a loop. To simplify this calculation, we take the size of the cross links and the filaments' diameter (whose sum is a) to be zero. In case of loops, the excess trapped length in the defect is not principally controlled by that length so in this case the $a = 0$ limit is both reasonable and simplifies the calculation. Then the boundary conditions for the position of the ends

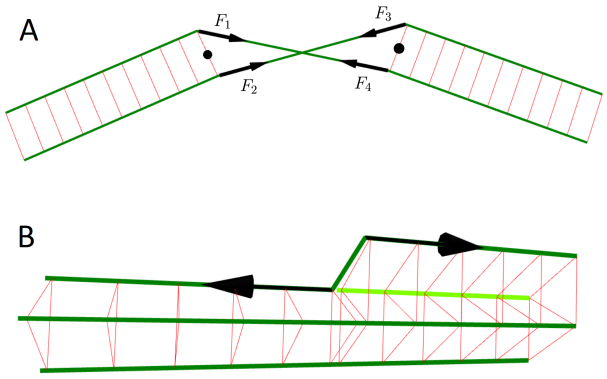

Figure 2.5: (A) Braid in the limit of zero bending. Forces F_1, F_2, F_3, F_4 (black arrows) have equal magnitude, but F_2 and F_4 create a larger torque (relative to the middle of the corresponding cross link, black dots). This torque leads to the rotation of the left piece of the bundle counterclockwise and right piece clockwise, i.e., increases the angle of the kink. (B) Dislocation in the limit of zero bending. The least energy configuration is a straight bundle, with one filament rearranging at the right angle when filament 4 (chartreuse) stops, immediately taking its place. However, if we increase the bending to nonzero, this segment under the right angle tries to straighten, producing repulsive forces (black arrows). These forces create an uncompensated torque at the left and right part of the bundle, leading to a kink.

of the filament are integral conditions on the tangent vector:

$$\int_{-L_1/2}^{L_1/2} ds\hat{t}_1(s) = \int_{-L_2/2}^{L_2/2} ds\hat{t}_2(s), \tag{2.2}$$

and boundary conditions for the tangent vector determine the kink angle ϕ, which is the total bend of the tangent across the structure. We pick a reference frame so that these boundary conditions are symmetric:

$$\hat{t}_1(\pm L_1) = \hat{t}_2(\pm L_2) = \begin{pmatrix} \cos(\phi/2) \\ \sin(\phi/2) \end{pmatrix}. \tag{2.3}$$

Minimizing the energy from Eq. 2.1 in the limit of small filament bending ($\hat{t}_y \ll 1$) we obtain a lengthy self-consistent equation for the angle ϕ (see Appendix A Sec. A.3A.3.1), which can be simplified in the case of the equal bending moduli $\kappa_1 = \kappa_2 = \kappa$ to

$$\phi = \gamma \left(\Delta L \sqrt{\frac{\mu}{\kappa}} \right)^{1/3}, \tag{2.4}$$

with the numerical constant $\gamma \approx 0.93$, and $\Delta L = L_2 - L_1 \neq 0$. We verified these results by minimizing the energy numerically – see Fig. 2.6A. Loops produce a continuous spectrum of kink angles that grow as the cube root of their length mismatch. As expected, an increase in the bending modulus suppresses this kink angle, while an increase in the linker binding energy increases it by shrinking the extent of the gap in the cross linking. We now turn to braids.

2.1.3.3 Braids

The simplest model of braiding in 3D requires three filaments. Braiding of two filaments in 3D can be undone by twisting the bundle about its long axis; it is not topologically protected (the relationship between braiding and rotation is discussed in

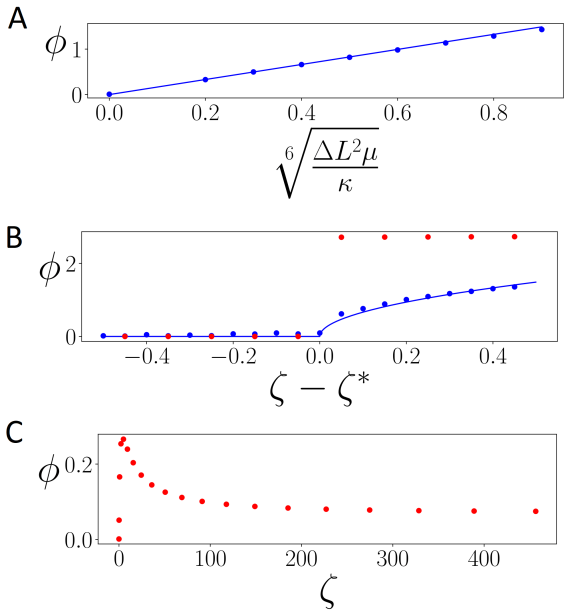

Figure 2.6: Kink angle ϕ as a function of a dimensionless parameter for (A) loops, (B) braids and (C) dislocations showing both numerical solutions to the energy minimization (circle), and the analytic predication (solid line). We show two cases $\kappa_1 = \kappa_2$ (blue) and $\kappa_1 = 2\kappa_2$ (red). (A) Numerical results agree with the small angle theoretical prediction even up to $\phi \approx \frac{\pi}{2}$. (B) For the symmetric case $\kappa_1 = \kappa_2$, the angle ϕ produced by the braid grows as $\sqrt{\zeta - \zeta^*}$ with $\zeta^* = 2$. The coefficient of proportionality for the analytical curve was chosen to best fit the data. For the asymmetric case, there is a discontinuous (first order) jump in ϕ at $\zeta^* \approx 12.25$. (C) For dislocations, the angle reaches a maximum at a finite value of ζ and goes to zero at $\zeta = 0$ and $\zeta = \infty$.

more detail in the Appendix A Sec. A.3A.3.3). The minimum energy configuration of three cross-linked filaments with the same length will be a right prism with an equilateral triangle as its base. We choose a coordinate system so that the x-axis lies parallel to the filaments, filaments 2 and 3 are in xz-plane, and filament 1 is above that plane. To introduce a braid we require filament 1 to go from above to below the xz-plane – see Fig. 2.2(C). This configuration is metastable since we need to decouple all the cross links on one side to get to the minimal energy configuration. There is no rotation of an end of the bundle that will eliminate the braid.

Since the cross links fix both relative angle and position of the filaments, filament 1 can not be connected to the filaments 2 and 3 by the cross links in the defect core, however, filaments 2 and 3 can remain cross linked. Thus, filaments 2 and 3 behave as one combined filament 2' with double the bending stiffness, and remains in the xy plane like filament 1. The true three-filament braid in 3D is thus energetically equivalent to a two-filament pseudo-braid, as introduced in our simulations.

The boundary conditions on the vector $\hat{t}$ are the same as in the previous case, Eq. 2.3, but the displacement boundary condition differs, incorporating the finite cross linker length a, which is necessary for the braid to trap excess length. We find

$$\int_{-L_1/2}^{L_1/2} ds\hat{t}_1(s) = \int_{-L_2/2}^{L_2/2} ds\hat{t}_2(s) + 2a\cos(\phi/2)\,\hat{y}, \tag{2.5}$$

Unlike in looping, we do not fix the filament length mismatch $\Delta L = L_2 - L_1$, but instead allow it to vary to relax the braid's energy. It is conceivable that one may encounter higher-energy braids in which braiding and an excess of trapped length (looping) coexist. We do not study this case here.

We observe that braids should generate local bending, at least in the limit of a sufficiently soft bending modulus. The binding free energy (chemical potential

difference between free and bound linkers) acts as an effective tension on the bundle. Setting the bending modulus to zero and fixing the length of the braided region, the solution for the filament contours inside the braid will be straight lines. In this configuration, linker-induced tension generates a torque that increases the kink angle of kinked configurations – see Fig. 2.5A. To stabilize this angle at a finite value we must including finite bending compliance. We do so now, turning to the full calculation.

Calculating the energy of the braid as a function of the kink angle ϕ, we find that kinking is controlled by the dimensionless parameter

$$\zeta_i = \frac{\mu a^2}{\kappa_i}, \tag{2.6}$$

where μ is the cross-linker binding energy per unit length, κ_i is the bending modulus of filaments of type i, and the length a is the normal distance between the center lines of a pair of bound filaments. This length can be interpreted to be the sum of the radii of the filaments and the length of the cross-linking molecule. ζ is the ratio of the linker binding energy per unit length μ to an energy per length set by bending on the scale of the inter-filament separation, κ/a^2. In general, we expect larger ζ values to lead to kinking. Below we verify this intuition. Larger values of the linker binding energy and inter-filament separation increase filament bending in the defected region. This bending, which is opposed by κ provides the torques necessary to produce the kinks. The nonphysical limit of zero inter-filament distance ($a \to 0$) implies that braids involve no filament bending and thus generate no bending moments necessary for kinking.

We prove in the Appendix A (see Appendix A Sec. 3B.1.) that for small values of ζ_i, the energy is minimized at $\phi = 0$, i.e., there are no kinks. For large values of

ζ_i, the minimum energy states are kinked ($\phi > 0$). We examine this transition in more details for the case $\kappa_1 = \kappa_2$. We assume symmetric bending, $\alpha_1(s) = -\alpha_2(-s)$ noting that numerical solutions of the minimization show that the symmetric solution based on this ansatz indeed identifies the global energy minimum. We obtain (see Appendix A Sec. 3B.2.):

$$\lambda^2 \sin^2(\phi/2) = \frac{8\kappa^2}{a^4}(\zeta - 2), \tag{2.7}$$

where we introduced a Lagrange multiplier λ to enforce the $\hat{y}$ component of Eq. 2.5, which plays the role of the tensile force in $\hat{y}$ direction. When ζ increases to 2, there is a second order transition at which the kink angle grows continuously from zero as ζ increases. Near the critical point $\zeta = 2 + \epsilon$, $\phi \sim \sqrt{\epsilon}$. Numerical minimization of the energy from Eq. 2.1 leads to the same result (see Fig. 2.6B). In that figure, we also see (red dots) that when the two filaments have differing bending moduli, there is a first order kinking transition where the kink's angle jumps discontinuously from zero at the critical value of ζ.

2.1.3.4 Dislocations

The simplest dislocation requires a bundle of four filaments in 3D where one of the four ends within the bundle. The stable state of four filaments is a right prism formed by a base of two equilateral triangles sharing one edge, as shown in Fig. 2.5B. We label these triangles as 1-2-4 and 2-4-3; only filaments 1 and 3 are not cross linked to each other. If either filament 1 or 3 ends within the bundle, the configuration remains stable because the other three form a stable three-filament prism. But if another filament ends, e.g., filament 4, the remaining filaments must deform to recreate a cross section with an equilateral triangle – see Fig. 2.5B. Due to cross-

linker constraints, the distortion associated with the defect must locally remove cross linkers between two of the filaments. Without loss of generality, we demand that filaments 2 and 3 remain cross linked. Calculating the energy associated with this defect is complicated by the fact that there is no mapping to a 2D version of the distortion. To gain immediate insight, it is helpful to consider momentarily the unphysical case of zero filament bending modulus. Then filaments 2 and 3 remain straight, but filament 1 makes two right-angle bends at the defect to move to the location of the missing filament 4 and thereby maximize cross linking. If we now reintroduce a finite bending modulus, this localized dislocation will spread out along the bundle to decrease bending energy at the expense of reducing the maximal cross linking shown in the figure. A force pair is also introduced by filament 1's bending (shown in the figure as black arrows) which produce a torque causing the entire bundle to kink. We perform numerical minimization of the energy assuming that filaments 2 and 3, being cross linked everywhere, form a ribbon that can bend in the direction perpendicular to its plane with bending modulus $\kappa_{ribbon} = 2\kappa$, but is absolutely rigid in the direction parallel to its plane. The results are consistent with the qualitative study (see Fig. 2.6C) – the maximum of the kink angle is observed at a finite value of parameter ζ, while zero and infinite values lead to zero kink angle.

2.1.4 Defect dynamics

Over times significantly longer than those associated with the undulations of the bundle, defects can move along the bundle and interact. These dynamics require multiple cross linker binding/unbinding events. As a result of these events, defects move diffusively and may eventually fall off the ends of the bundle. In the case of

dislocations and braids, defects may combine or annihilate. For the latter type, these interactions are controlled by the structure of the braid group.

Consider two braids – a braid/anti-braid pair – separated by N cross links. Since these defects would annihilate if the intervening cross links were removed, we may expect this pair might vanish if their separation becomes sufficiently small. The braids are motile with a diffusion constant set by the linker detachment rate k_{off} and do not strongly interact when separated by lengths greater than the defect core size. The probability density $p(n,t)$ of there being n cross links separating the two defects at t then obeys a diffusion equation

$$\frac{\partial p(n,t)}{\partial t} = 2k_{off}\frac{\partial^2 p(n,t)}{\partial n^2} \tag{2.8}$$

Using a well-known result for the first mean passage time [81], the mean lifetime of this braid/anti-braid pair is

$$T = \frac{3N^2}{k_{off}}. \tag{2.9}$$

For the simulations presented in Fig. 2.3 we have $k_{off} = 6\text{s}^{-1}$, $N \approx 15 - 35$. Then Eq. 2.9 predicts $T \approx 100 - 500$s, while in Fig. 2.3 we obtain $T \approx 200$s, within the predicted range.

For a three-filament bundle the dynamics of N braids is equivalent to the diffusion of N particles (braids) of three types, which are randomly distributed after a quench. The braid group (see Appendix A Sec. A.3A.3.3) requires that a particle of one type can annihilate only with particles of one other type. If particles encounter each other and cannot annihilate, we assume they stick, since, by merging their defected regions, the net number of cross linkers on the bundle increases. Using these dynamical rules, we studied the annealing of braided bundles using Monte-Carlo simulations – results are shown in the Appendix A.

Simple combinatorics shows that annihilation events are less common than braid combination (sticking) since the former requires braid/anti-braid adjacency. Since the number of different braid group operators grows linearly with the number of filaments in the bundle, the probability for braid/anti-braid adjacency decreases with increasing braid size. When considering large bundles we can neglect annihilation. Doing so and using a mean-field approximation, we let $\rho(x,t)$ be the braid density, implying that the average distance between neighboring braids is $\frac{1}{\rho}$. The time to halve the number of braids will then be $t_{1/2} \propto \frac{1}{\rho^2 k_{off}}$ according to Eq. 2.9. The same logic implies that the continuous rate of decrease of the braid density will obey

$$\frac{d\rho}{dt} = -\alpha\rho^3 \tag{2.10}$$

where α is a phenomenological parameter accounting for the probability of braids combining upon close approach. Solving Eq. 2.10, we find $\rho \propto t^{-1/2}$, which is a general result for sticky (or annihilating) random walkers [20]. The predictions of this mean-field model are consistent with our Monte Carlo simulations and with the Brownian dynamics simulations of the full bundle model - see Fig. A.6.

We briefly mention the dynamics of loop and dislocation defects. Complete annihilation of loop defects is highly unlikely as it would require the amount of trapped length in the two loops to match. We expect loop defects to diffuse along the bundle and, in larger bundles, to pass through each other. Dislocations should also diffuse by a type of reptative motion (as in polymer melts) in which the filament end detaches within the bundle, forms a loop and reattaches. Thus, dislocations in an otherwise ordered bundle should retract towards the bundle edge with more filaments in it. After loops are formed the dislocation should perform a biased random walk due to the fact that the energy of loop defects will suppress further retractions of the

dislocation core towards the bundle's end.

Discussion

Biopolymer filament bundles are kinked in spite of the fact that the elastic ground state of their constituent filaments is straight, as clearly seen in our experiments on collagen bundles. In this article, we quantified these kinks and proposed that their existence can be attributed to defects quenched into the bundles during cross linking. These defects come in three classes: loops, braids, and dislocations. This proposal is supported by both analytic calculations of the energy-minimizing contour of bundles containing these defects and by finite-element Brownian dynamics simulations of the quenched bundles of two to two hundred filaments. The mechanical connection between these defects and kinks (high curvature regions) of the bundle is straight forward – defects generate a local distortion of the filaments driven by cross linking. The entire bundle may bend producing a kink in order to compensate for that distortion. This mechanism is reminiscent of the relaxation of a flexible hexatic membrane in the vicinity of a disclination [135]. There a topological defect relaxes local strain via a puckering of the membrane that produces long-ranged Gaussian curvature. Here the distortion of the bundle may be entirely localized in a sharp bend.

In our experiments we found that 4% of the observed collagen bundles had one or more kinks and that these kink angles had a mean of 26 degrees, but were quite varied ranging up 74 degrees in the sample of 74 kinks studied. When we consider that loop defects can produce a continuous distribution of kink angles, it seems natural to suppose that this defect is the predominant cause of kinking. The number

of observed kinks is likely an underestimate of the real system, due to the limitations of our imaging that shows only those bundles lying in the imaging plane. Only kinks oriented so that the bundle bends within the imaging plane are observable.

The kinks associated with both braids and dislocations are expected to be narrowly distributed at angles set by the number of filaments in the bundle since these defects produce fixed kink angles that depend only on that number, the cross-linker binding energy, and bending moduli of the filaments. For a fixed number of filaments, both dislocations and braids produce kink angles that depend on only a single dimensionless number $\zeta = \mu a^2/\kappa$. In the case of braids, the kink angle grows from zero at a critical value of ζ, which depends on the number of filaments but is roughly of order unity. Looking at stiff F-actin cross linkers like α-actinin, we find that $\zeta \sim 0.1$; it is too small for braids to generate kinks. We do, however, expect braids to be associated with kinks in softer filament systems such as DNA condensed by polyvalent counter ions [111, 142] or cross-linked intermediate filaments [24, 61] where $\zeta \sim 10 - 100$. Currently, our understanding of collagen bundle cross linking is less precise; our estimate in this system is that $\zeta \sim 1$ (see Appendix A Sec. A.1A.1.5). This suggests that loops certainly should produce kinks, but that braids are also potentially kink-generating defects since our estimate for ζ is near the threshold where such braid-induced kinking should occur. Of course, even if braids do not produce kinks, we expect them to be present and to produce high flexible "hinges" in the bundle. Dislocations always generate kinks, but the kink angle is appreciable only when $\zeta \sim 1$. We surmise that dislocations may also be responsible for some of the experimentally observed kinks in the collagen bundles.

Another argument for loop controlled defects in collagen is a presence of z-shaped double kinks (see Fig. A.7 for the examples), which can be attributed to slippage

between two filaments in a bundle such that they produce a pair of loops. The lengths stored in this pair are such that, after the two loops, the filaments once have no length mismatch.

The life time of these defects appears to be significantly larger than the characteristic time of thermal undulations of the filaments and longer than the typical observation time in experiment. This is supported by the experimental data, where kink annihilation or diffusion to the ends is never observed. When we study kink dynamics via simulation on the timescales significantly longer than those covered by experiment, we observe their diffusion, sticking, and annihilation, which one expects from the theory. Specifically for braids, we find that their motion is consistent with particles diffusing in 1D with interactions obeying the rules of the braid group. We speculate that bundles under compression may relieve stress by the pair production of braid/anti-briad pairs in a manner resembling the Schwinger effect [155, 156].

Examining Fig. 2.4 leads us to speculate that very large bundles of many filaments might be considered to be smaller bundles composed of more weakly bound sub-bundles, which are themselves composed of the original filaments. If we may consider this hierarchical approach, we can replace a in ζ's by the sub-bundle radius and write the bending modulus in terms of that radius as well using $\kappa \sim Ea^4$, where E is the Young's modulus of the material (typically in the 1GPa range for proteins). In that case, we see that $\zeta \sim (\mu/E)a^{-2}$, so that as the radius of the sub-bundles increases, ζ decreases rapidly. As a result, we expect that kinks in larger bundles will be dominated by loop defects regardless of the value of ζ for the original filament system. When considering very large bundles, one may ask whether cross linkers deep in the bundle's interior remain in equilibrium with the cross linker concentration in the surrounding fluid. Due to steric hindrance, these internal linkers may diffuse

slowly out of the bundle, leading to a linker chemical potential gradient across the bundle's radius on measurable time scales. We do not incorporate such effects in our simulations, and we do not expect them to be relevant in the case of our collagen bundles where we do not have exogenous linkers. But this nonequilibrium effect, where relevant, may introduce intriguing viscoelastic effects in the bending dynamics of very large bundles.

Many biopolymer filaments are chiral and their chirality is known to affect their packing into tight bundles [56]. In particular, chirality introduces a form of geometric frustration in these tightly packed bundles. We suspect that these defects may play a role in reducing the elastic stress associated chirality-induced packing frustration, and thus may be important for understanding the long length scale structure of such chiral bundles.

We note that defects rather generally produce weak links in the bundle where, due to the absence of cross linking, the effective bending modulus of the bundle is reduced by at least an order of magnitude. This suggests that the collective mechanics of a rapidly quenched bundle network might be dominated by these defects, which introduce a set of soft joints into the otherwise quite stiff bundles. As a result, rapidly quenched bundle network may be anomalously compliant as compared to their annealed state. It is interesting to note that these defects provide soft hinges in the network (rather than universal joints) and that there may well be many more such soft hinges than there are kinks, since not all defects generate kinks, but all disrupt the local cross linking. Currently, there are no kinetic theories of bundling that allow us to estimate the number of such soft hinges in a network of filament bundles and then attempt to predict the mechanics of the defected network. Of course, filament bundle networks produced by transient cross linkers have a complex

rheological spectrum, including a low-frequency power-law regime [14, 127]. Understanding the mechanical effect of these soft hinges on that low-frequency rheology remains an interesting direction for future studies.

2.2 Materials and methods

Experiments

Type I Bovine pepsin extracted collagen (PureCol 5005-100ML lot 7503, Advanced BioMatrix) was reconstituted according to Doyle, 2016 [38]. Reconstituted collagen solution was diluted to 0.2mg/mL with PBS and was incubated at 37°C over night. The collagen was fluorescently labelled (Atto 488 NHS ester 41698-1MG-F lot BCBW8038, Sigma-Aldrich) and then imaged with Olympus Fluoview1200 laser scanning confocal microscope using a 60x 1.45NA oil immersion objective. To construct a trace of the bundle, Matlab was used to determine the position of bundle in each row of the image defined as the mean of the Gaussian fit of the pixel intensity across each row. A cubic spline is used to estimate the curvature along the bundle. The kink angles were measured using imageJ. Further details can be found in Appendix A Sec. A.1.

Simulations

In our numerical model, the individual semiflexible filaments are described via nonlinear, geometrically exact, 3D Simo-Reissner beam theory [145, 160] and discretized in space by suitable finite element formulations [74, 118]. Their Brownian dynamics is modeled by including random thermal forces and viscous drag forces along the

filament [28, 29]. We apply an implicit Euler scheme to discretize in time, which allows us to use relatively large time step sizes [28, 29]. Cross links are modeled as additional, short beam elements between distinct binding sites on two filaments, which bind and unbind randomly based on given reaction rates and binding criteria [129]. In particular, the latter include a preferred distance between binding sites and a preferred angle between filament axes that need to be met such that a linker molecule switches from the free to the singly bound state or from the singly to the doubly bound state. Altogether, this finite element Brownian dynamics model turns out to be a highly efficient numerical framework, which enables large-scale simulations with hundreds of filaments over hundreds of seconds and has been used in several previous studies [27, 126, 129, 109, 78, 164]. We used the existing C++ implementation in our in-house research code BACI [2], which is a parallel, multi-physics software framework. In addition, we used self-written Matlab [174] scripts for the data analysis and Paraview [88] for the visualization of the system. Further details about the numerical model including all parameter values and the detailed setup of the computational experiments can be found in Appendix A Sec. A.3.

CHAPTER 3

Thermal Schwinger Effect: Defect Production in Compressed Filament Bundles

Stiff rods under compression are known to undergo a mechanical instability called Euler buckling, leading to a symmetry-breaking event. Upon compression directed along its long axis, a circular elastic rod first shortens its length, bearing the external loading via compression. But at a critical compressive strain, the rod buckles, supporting the compressive stress via bending on the length scale of the entire rod, and thereby breaking the rotational symmetry (when viewed down the long axis of the undeformed rod) of the deformed state [99, 54]. When I consider the response to compressive loading of biopolymer filament bundles bound by transient cross linkers, I find that Euler buckling is precluded in such composite objects at finite temperature by another type of instability: at compressive stresses lower than the Euler buckling threshold, the bundles shorten by the thermally-activated production of defects, considered in chapter 2. While dislocations cannot be produced without breaking the filament, braids and loops can be produced in pairs. See Fig. 3.1C and D for schematic diagrams of pairs of loops and braids respectively. Forming these defects from a quench by adding cross linkers is commonplace, but since the addition or removal of these defects requires a system-sized rearrangement of cross linkers, one cannot expect them to form spontaneously. Rather, they form in defect

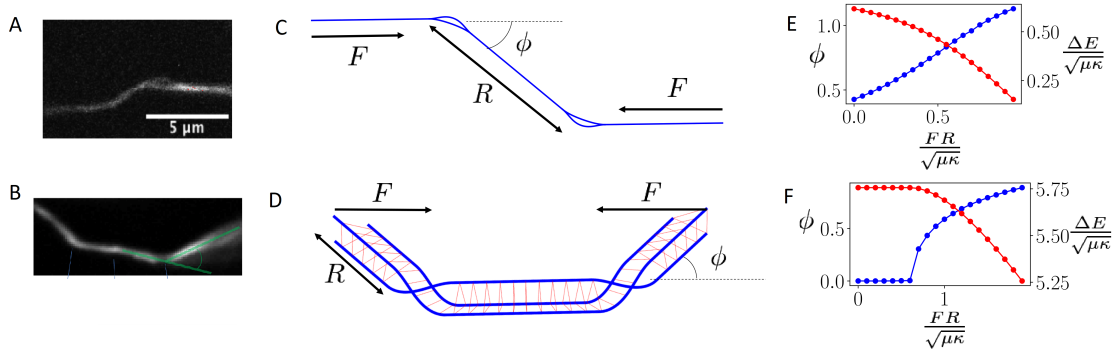

Figure 3.1: Fluorescence microscopy images of a z-bend (A) and a u-bend (B) in a collagen bundle. (C) Two loops under compression form a z-bend. (D) Two braids under compression form a u-bend. (E) Angle produced by a loop pair and energy difference between the looped and straight bundle as a function of dimensionless torque. (F) Angle produced by a braid pair and the energy difference between braided and straight bundles as the function of dimensionless torque. [Images courtesy of E. Botvinick and Q. Hu]

– anti-defect pairs, which require only local cross-linker rearrangements. Since these defect pairs are associated with kinks, compressive loading suppressed the energy barrier associated with defect pair production. As a result, at a critical compressive stress, I expect the proliferation of these defect pairs once the energy cost of pair production is reduced to the thermal energy.

Pair production of defects is analogous to the Schwinger effect, in which electron-positron pair production was predicted in a sufficiently strong static electric field [155, 156]. The forces due to the large electric field on the charged particle pairs pulls them apart, stabilizing these quantum fluctuations of the vacuum. In the same way, it is energetically favorable for thermally-generated defects to separate under the

compression of the bundle. I term this mechanism the *thermal Schwinger effect*.

We first consider the energetic cost of the production of loop and braid defects in a compressed bundle. I then use these results to compute the loop pair production rate at temperature T in a calculation reminiscent of the Kramers' escape problem [95, 81]. We also analyze the critical stress for defect pair production in a few biopolymer systems including F-actin, DNA, and collagen bundles.

To compute the minimal energy configuration for stable and metastable states of the N-filament bundle under a compressive force F, I introduce the energy

$$E = -F\Delta L + \mu\ell + \sum_{i=1}^{N} \int ds \frac{\kappa_i}{2} \left(\partial_s \hat{t}_i\right)^2 . \tag{3.1}$$

The first term gives the energy reduction due to the shortening of the bundle's end-to-end distance ΔL. The cross linkers have binding energy μ per unit length. Since the defect(s) disrupts cross linking over a distance ℓ, their presence increases the system's energy as reflected by the second term on the right hand side of Eq. 3.1. The third term gives the bending energy stored in the bundle, where κ_i and $\hat{t}_i(s)$ are the bending modulus and tangent vector of the i^{th} filament. s is the arc length along the bundle. I neglect torsion, so all defect energies are actually lower bounds. There will be a continuous spectrum of excited states due to trapped torsion.

We examine first a pair of loop defects. I assume the compressive load to be sufficiently weak so the characteristics of a loop, i.e., the dependence of its kink angle and energy as a function of its size can be taken from our previous calculations in the zero-compression limit in the previous chapter 2. The kink angles generated by neighboring loops are equal and opposite, since the amounts of their trapped length have to be equal and opposite (which makes the loop sizes also equal, see Appendix B). The pair of loops produce a *z-bend* where parts of the bundle not

lying between the loop pair are parallel and offset in the normal direction to the undeformed bundle – Fig. 3.1A,C. This result holds even for bundles having filaments of differing bending moduli, as long as the excess trapped length in the loop is much smaller than the total length of the defected region. For simplicity, I focus on the case of equal bending moduli. Then the total energy of configuration with two loops of size $\ell/2$ each, generating kink angles ϕ, and separated by a distance R is

$$E_{\text{tot}} = g_1 \mu \ell - FR(1 - \cos\phi). \tag{3.2}$$

The first term in the Eq. 3.2 is the energy of the pair of loops of length $\ell/2$, with coefficient $g_1 \approx 1.48$ (see Appendix B). The second term is the decrease of energy due to the compression (see Fig. 3.1C. As long as $F \ll \mu$, it is not important whether I define R to be the distance between centers of loops or their edges, since the difference will be small in comparison with the first term. However, I pick R to be the distance between closest edges, so it is equal to zero when loops are not yet separated.

There is a continuous distribution of loop sizes, leading to a continuous distribution of angles of the z-bends produced by loop pairs and a similar distribution of energy reductions associated with them as shown in Fig. 3.1E. Observed loop pairs are the result of a stochastic process of pair production, which is related to the classic problem of the thermally-activated escape from a potential well.

We investigate the energetics of pair production and escape. Loop formation involves cross linker removal and filament bending leading to an energy increase of $g_1 \mu \ell$ as the loop size ℓ increases. At some loop size ℓ_0, the two growing loops separate due to random fluctuations. Once separated, the loops can no longer exchange trapped length so their lengths are now fixed at $\ell_0/2$ each (see Appendix B). As the distance R between the loops of the resulting z-bend grows, the energy of the

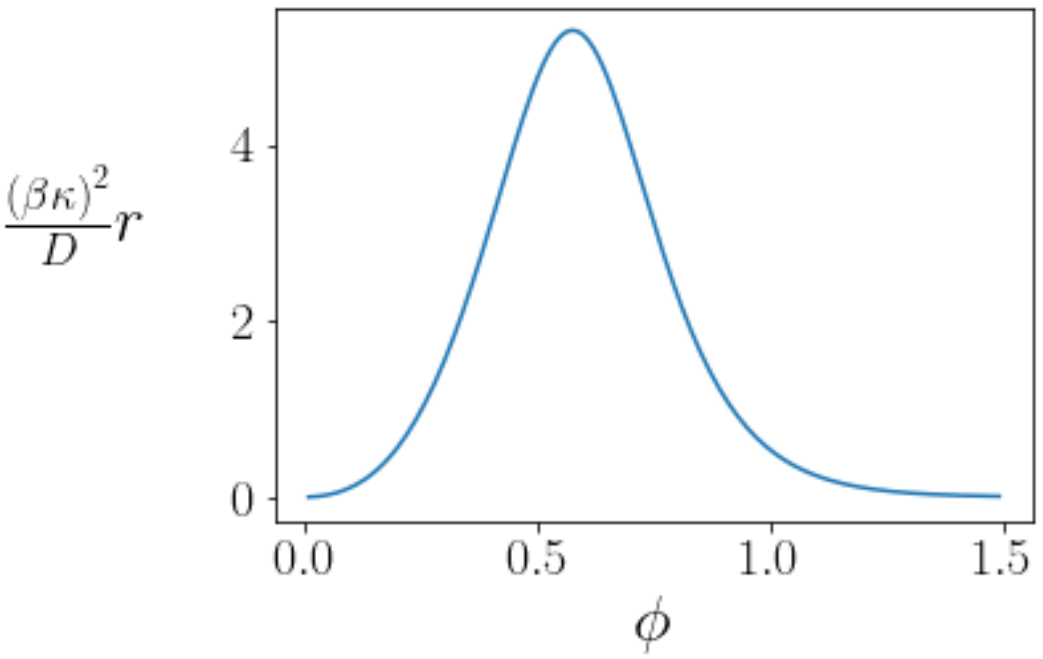

Figure 3.2: Dimensionless loop pair production rate with $\eta = 10$, $\tau = 0.1$ (see Eq. 3.5)

compressed bundle decreases due to shortening along the direction of the compressive load. I can consider this process as an escape from the potential well using x as a single reaction coordinate that describes the growth of the loop size while they overlap and then their separation afterwards:

$$U(x) = \begin{cases} g_1 \mu x, x < \ell_0 \\ g_1 \mu \ell_0 - F(1 - \cos\phi)(x - \ell_0), x > \ell_0, \end{cases} \tag{3.3}$$

x grows with the sizes of the loops $x = \ell$ before separation (upper equality), and then describes the distance between the separated loops $x = R$ (lower equality). The effective potential for the growing loops increases linearly with loop size up to the final loop size ℓ_0 and then decreases linearly due to the shortening of bundle along the direction of the applied force.

Treating this process as a Kramers' escape problem [95] in the potential Eq. 3.3, I compute the escape rate r, the rate of loop pair production in thermal equilibrium at a fixed compressive stress. I compute this rate as the inverse of the mean time to escape using the standard Kramers' approach for an overdamped system:

$$r^{-1} = \frac{1}{D} \int_0^{x_0} dy e^{\beta U(y)} \int_0^{y} dz e^{-\beta U(z)}, \tag{3.4}$$

where x_0 is defined such that $U(x_0) = 0$ and $\beta = 1/k_{\mathrm{B}}T$. The reptative motion of the defects is heavily overdamped; I introduce a loop diffusion constant $D \propto k_{\mathrm{off}} \Delta x^2$ in terms of k_{off} the rate of cross-linker unbinding and the distance between consecutive binding sites of those cross linkers along the filament Δx.

Performing the integral in Eq. 3.4 in the limit of small F/μ and ϕ (see Appendix B), I obtain

$$r^{-1} = \frac{4}{D\beta^2 F^2 \phi^4} \left(\frac{\tau \phi^2}{2 g_1} e^{\eta\phi} + \eta\phi - 1 + e^{-\eta\phi} \right), \tag{3.5}$$

where I introduce the dimensionless parameters $\tau = F/\mu$, $\eta = g_1 g_2 \beta \sqrt{\kappa\mu}$, with $g_2 \approx 4.8$ relating defect size to the kink angle it produces: $\ell = g_2 \sqrt{\frac{\kappa}{\mu}}\phi$ (see Appendix B). The pair production rate r vanishes as ϕ goes to zero since the potential barrier width diverges as $1/\phi^2$. Conversely, very large angle kink production is also suppressed ($r \to 0$ as $\phi \to \infty$) due to the increasing energy of the loop. The rate of pair production has a maximum at a finite angle – see Fig. 3.2. I obtain a prediction for the most commonly produced kink angles in z-bends as a function of material parameters of the bundle and the applied compressive load. In the limit of weak compression, the maximum loop pair production rate $r_{\max}$ (z-bend formation rate) occurs at angle $\phi^\star$ (see Appendix B for details):

$$\phi^\star = \eta^{-1} \log\left(\frac{6 g_1 \eta^2}{\tau}\right) \tag{3.6}$$

$$r_{\max} = \frac{D}{3}\left[\frac{\tau \log\left(\frac{6 g_1 \eta^2}{\tau}\right)}{2\beta\kappa}\right]^2 \tag{3.7}$$

The production rate of the z-bends increases as the compressive force squared and is rather sharply peaked – Fig. 3.2 – as a function of angle, suggesting that, for fixed material parameters, including bundle sizes, one expects to observe a narrow range of z-bending angles. The most probable z-bend angle scales roughly as $k_{\mathrm{B}}T/\sqrt{\kappa\mu}$; the binding energy of the linkers determines the typical observed angles for bundles of a fixed number of filaments. Finally, as the bundle size grows, the effective κ increases, driving the z-bend angles to zero.

We now examine the production of braid/anti-braid pairs in a three-filament system. Within the lowest energy configuration of the braid, two of the filaments follow the same trajectory, allowing us to reduce the problem to that of studying two filaments in 2D. We call the case of two filaments with equal bending moduli

a pseudobraid, reserving the name braid for the more physical but analytically less tractable case unequal bending moduli $\kappa_1 = 2\kappa_2$. See Ref. [163] for further details.

Unlike in the case of loops, only the magnitude of the kink angles produced by the braid pair must be equal. The kink angles generated by braids thus do not have to form z-bends; in fact, the lowest energy state will be a *u-bend* as shown in Fig. 3.1B. This energy is minimized when the two defects are close to each other and localized in the middle of the bundle, since this provides the greatest shortening in response to the force. I speculate that braid defect co-localization is the primary reason for the rarity of u-bend observations as compared to z-bends (see Ref. [163]). The u-bends could be easily misinterpreted as a single defect with a larger kink angle.

In minimizing the total energy of the bundle (see Appendix B), it is convenient to introduce a dimensionless parameter $\zeta = \frac{\mu a^2}{\kappa}$, where a is the spacing between the centerlines of the filaments enforced by the cross linkers. We expect this distance to be the sum of the linker size and twice the radius of the filament's cross section. Using the same parameters, I also introduce a dimensionless applied force $f = \frac{FRa}{\kappa}$. We find that, up to a critical compression $f^\star(\zeta)$, implicitly determined by

$$\int_0^1 \frac{\frac{(\zeta-\sqrt{2\zeta})^2}{f^2} t dt}{\sqrt{1-\frac{(\zeta-\sqrt{2\zeta})^2}{f^2}t^2}\sqrt{1-t}} = \sqrt{\zeta/2}, \tag{3.8}$$

the minimum energy configuration of the braid/antibraid pair remains that of an unkinked bundle as shown in Fig. 3.1F. This is distinct from the case of loop pairs where low-angle loops can form at any compressive load. For $f > f^\star(\zeta)$, the defect pairs produce finite-angle kinks – Fig. 3.1F – resulting in a u-bend whose angles grow with f.

Solving Eq. 3.8 numerically (which agrees with the numerical minimization of

the energy Eq. 3.1), I obtain a phase diagram spanned by compressive loading f and ζ shown in Fig. 3.3. Above and to the right of the boundary, u-bends are present. One can interpret the diagram as a graph of the critical loading versus linker binding energy μ at fixed κ and a. The non-monotonic behavior of the curve can be understood as follows. For sufficiently large μ, kinks appear at braids even at zero compressive stress, but as the linker binding energy decreases, kink formation is energetically unfavorable unless the shortening of the bundle under load produces a sufficient energy reduction. For small enough linker binding energy, the defected regions extend in arc length, thereby becoming more bending compliant so that there is a re-entrant kinking regime at small μ. The behavior of the more physical, asymmetric case (green circles) is similar to that of the pseudobraid (red circles and blue line), but the transition is shifted to higher compressive loads due to the increased bending rigidity of the system.

Upon increasing the compressive load, I predict that bundles should first shorten by producing loop pair defects creating z-bends, as found in the collagen bundles seen in Fig. 3.1A. Assuming the size of the bundles is known and controlled the resulting z-bends will be generated with reproducible angles, due to the peak in stochastic defect production rate with angle as shown in Fig. 3.2. We expect the high polydispersity of typical biopolymer filament bundles to spread out the distribution of z-bend angles. But since the angle of maximum production $\phi^\star \sim k_\mathrm{B}T/\sqrt{\kappa\mu}$, for a bundle of N filaments so that $\kappa \sim N^2$, I expect $\delta\phi^\star \sim \delta N N^{-2}$. The peak in the z-bend angle distribution may be hard to observe without some bundle control unless N is large. If the cross-linking energy is sufficiently large, the z-bend angles will vanish as $\phi \sim 1/\mu^{1/2}$. However, as the distance R between the two loops increases, I cannot continue to neglect the increase of the equilibrium loop angle shown in Fig. 3.1E,

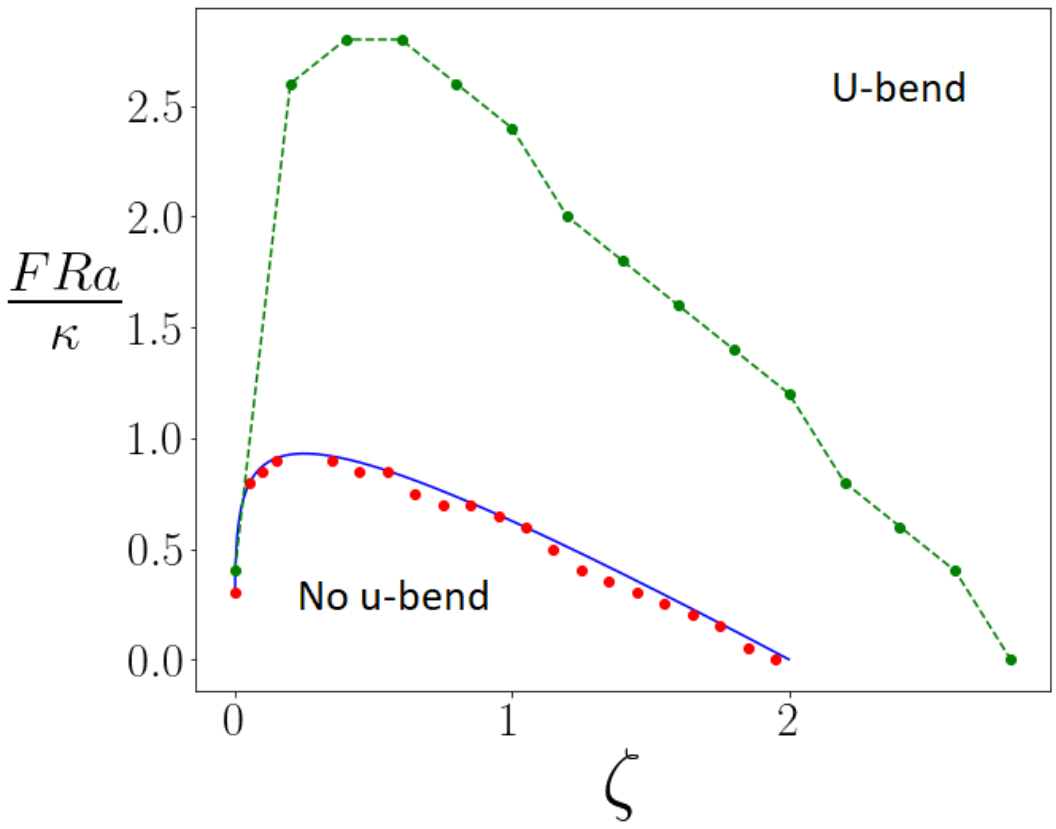

Figure 3.3: Numerical minimization of the energy (red dots) and analytical prediction implicitly given by Eq. 3.8 for a symmetric pseudobraid $\kappa_1 = \kappa_2$. The numerical solution of the more complex, three-filament braid with $\kappa_1 = 2\kappa_2$ (green circles, green dashed line is a guide to the eye) shows that the transition is shifted to higher compression.

which may lead to observable angles at large R, even if they were unobservably small angles at formation.

At higher compression, the u-bends seen in Fig. 3.1B will also be created when braid pair production is reduced to thermal energy. Using estimates of ζ for various filament bundle systems, I find F-actin and collagen to have $\zeta \sim 0.1$, so uncompressed bundles support unkinked braids. Braid pair production leading to u-bend formation should occur for compressive forces on the order of 10 pN based on the phase diagram shown in Fig. 3.3. DNA condensed by polyvalent ions and cross-linked intermediate filaments have $\zeta \sim 100$ suggesting that there will be a number of kinked braids quenched into the bundle. As a result, I expect these bundles to collapse by bending at the preexisting braids, which introduce more bending compliant regions via cross linker reduction. Finally, I note that under sufficiently large forces, Euler buckling can take over from braid-generated u-bend formation. We estimate that Euler buckling should be found for $FRa/\kappa \approx 5$ (see Appendix B) for $\zeta \approx 0.1$ (and this value only grows for larger ζ) which is well above the region shown in the u-bend phase diagram, Fig. 3.3.

The most direct test of the theory should be found in compression experiments on individual bundles. For collagen and F-actin the necessary compressive forces are on the order of 10pN, suggesting laser trapping experiments should probe the relevant force scales.

CHAPTER 4

Braiding dynamics in semiflexible filament bundles under oscillatory forcing

4.1 Introduction

While in the previous chapter I considered only static external force, the situation with time-dependent drive is more complicated. Namely, bundles possesses a viscoelastic response – their stress relaxation has a complex time dependence and these systems dissipate work not only through viscous dissipation in the surrounding fluid but also by linker unbinding. As a result, the collective mechanical response of networks of filament bundles has a nontrivial low-frequency viscoelastic response at frequencies below a characteristic linker unbinding rate [15, 128].

I explore here particular type of stress relaxation through the production and movement of defects in cross-linked bundles. Previously, I have shown that bundles support a set of topological defects – loop, braids, and dislocations [162]. The lifetime of these defects is quite long, growing with the length of the bundle, since they cannot be removed by local rearrangements of the cross linking on the bundle. Defects, however, can be produced in defect/anti-defect pairs by local rearrangements, and defect pair production is predicted to be enhanced by applied compressive loads [166]. In

this chapter, I report on theoretical studies of defect pair production under reciprocal mechanical deformations and consider how the proliferation and motion of defects affects the force-extension relation of a bundle in constant applied force experiments. I point out that there is a range of bundle mechanical parameters that allows for a nonmonotonic extension versus time curve at constant force.

The motion of topological defects plays a critical role in the long-time plastic deformation of crystalline solids under mechanical loading. I suggest here that defect motion plays a similar role in the slow relaxation of bundles under load. Mechanical loading can also generate defect pair production. I first consider pair production in cycles of compression and extension of one bundle. I then examine the force extension relation of defected bundles by examining the extension of the bundle as a function of time for fixed force.

4.2 Materials and Methods

To study the conformation of the bundle under the external load, I look at the minimal energy configuration of the N-filament bundle under a force F. The energy has three contributions:

$$E = -F\Delta L + \mu\ell + \sum_{i=1}^{N} \int ds \frac{\kappa_i}{2} \left(\partial_s \hat{t}_i\right)^2 . \tag{4.1}$$

The first term is work of the force F, extending the bundle by distance ΔL. Note that, unlike in Ref. [166], I pick positive sign for the extensive force; a compressive force takes a negative sign. The second term is the missing binding energy of the cross links. Namely, if cross links are absent on the interval of bundle of length ℓ, I assume that the energy of the bundle is larger by $\mu\ell$ where μ is binding energy

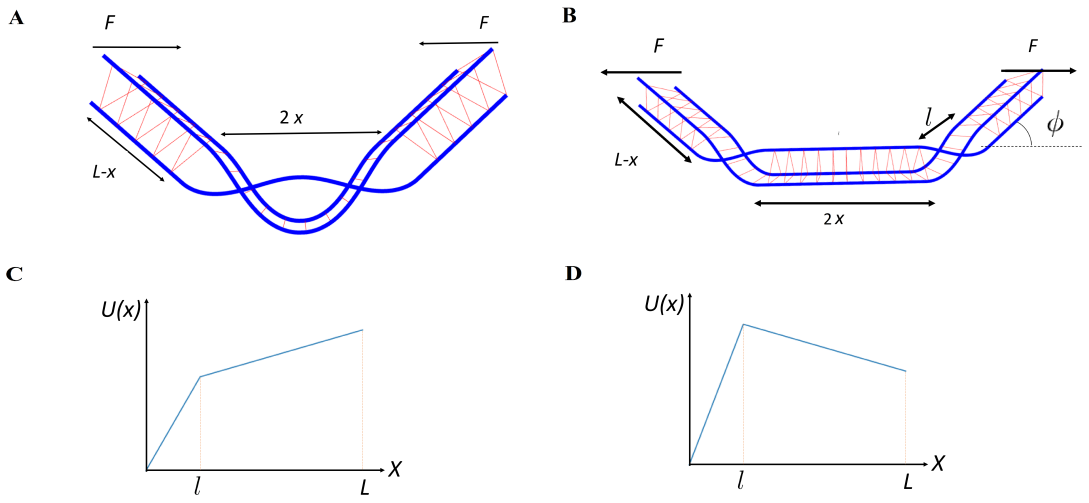

Figure 4.1: Schematic illustration: (A) A pair of braids produced under compression force F on a semiflexible filament bundle of length $2L$ (and comprised of three filaments), but not separated. $2x$ is the size of the defected region. The filaments are shown in blue, while the cross links are shown in red. (B) A pair of braids is now separated under applied tension. The braids produce a kink with angle ϕ. $2x$ is the distance between braids (including their own size – the total excess length stored within the braid). In the lower figures I show the piece-wise linear potential $U(x)$ under compression (C) and under extension (D) . The left part of the potential $x < l$ corresponds to the production of defects, the while right $x > l$ controls the separation of the defects.

per unit length. Here and throughout this work, I assume that the cross linkers are highly inextensible so where the filament have the inappropriate spacing within the braid, the cross linkers must be missing. I do not consider more elastically compliant cross linkers here. The third term is the bending energy of all the filaments in the bundle, where $\hat{t}_i(s)$ and κ_i are the tangent vector and the bending modulus of the i^{th} filament. The integral is over the whole bundle; however, in the minimal energy state, the part of the bundle without defects is perfectly straight, so the expression under the integral is zero at this part – only the defected part of the bundle contributes to the bending energy.

In this chapter, I study three-filament bundle, and a particular type of defect, braids. Each braid can be envisioned as a permutation of the filaments within the bundle with the understanding that the product of two such permutations does not restore the bundle to its undefected state as the filaments remain wound about it other. For a more complete description of the group of braid operations, please see Ref. [162] and the references therein. The case of a single braid, or a braid/anti-braid pair is particularly simple to analyse because in these configurations, two filaments within three-filament bundle remain cross-linked everywhere, while the third filament passes back and forth in between them as shown in Fig. 4.1(A,B). As a result the equilateral triangle formed by the filaments in the plane perpendicular to their local tangent flips by π as one moves through a single braid. The anti-braid simply flips this triangle back to its original orientation. The simplicity of this structure allows one to treat the two everywhere-cross-linked filaments as a single effective filament having twice the bending rigidity of the single filaments. Then the problem effectively maps on two filaments in two dimensions, one of which has bending modulus twice as big as the other. I write the boundary conditions for this problem in terms of the

tangent vector $\hat{t}$. First, I have a condition that at the ends of the braid the filament should be parallel to each other

$$\hat{t}_1(\pm L_1) = \hat{t}_2(\pm L_2) = \begin{pmatrix} \cos(\phi/2) \\ \sin(\phi/2) \end{pmatrix}. \tag{4.2}$$

where ϕ is the angle that the braid forms (see Fig. 4.1B). Notice that here I have also specified the direction of coordinate axis. The second boundary condition fixes the position of the ends of the filaments:

$$\int_{-L_1/2}^{L_1/2} ds\hat{t}_1(s) = \int_{-L_2/2}^{L_2/2} ds\hat{t}_2(s) + 2a\cos(\phi/2)\,\hat{y}, \tag{4.3}$$

where $L_{1,2}$ is the length of the filament in the braid, and a is the size of the cross-link plus two the radii of the filament (the distance between the center lines of the cross linked filaments). In these boundary conditions, ϕ, L_1 and L_2 are subject of variation. Since the braid/anti-braid pair is produced from undeformed state, I should have a length conservation condition:

$$L_1^{\text{braid}} + L_2^{\text{anti-braid}} = L_2^{\text{braid}} + L_1^{\text{anti-braid}} \tag{4.4}$$

I minimize the energy Eq. 4.1 subject to the conditions Eqs. 4.2, 4.3, 4.4. The results shown here were obtained using the SciPy package in Python [75]. I discretize each filament into 50 elements. The numerical results coming from this discretization is previously validated by their comparison to analytic results as shown previously in Ref. [166].

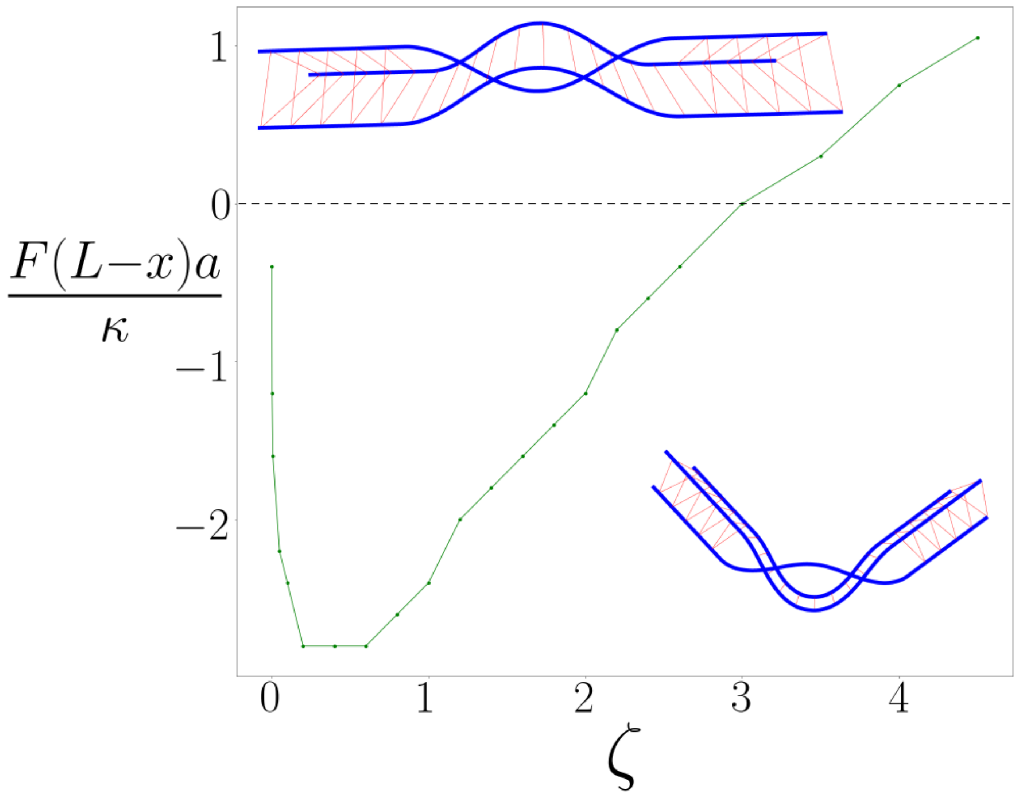

Figure 4.2: The phase boundary in the parameter space of dimensionless torque (vertical axis) and the dimensionless material parameter $\zeta = \frac{\mu a^2}{\kappa}$ (horizontal axis). The positive values of the torque (above the dashed line) correspond to extension, the negative (below the dashed line) to compression. Above the curve, the angle formed by braid is zero, and below it is nonzero. The pictures represent straight, or unkinked braid pair (upper) and a bent, kinked braid pair (lower).

4.3 Results

4.3.1 Braid configuration under external force

Minimizing the energy Eq. 4.1, I obtain a phase diagram, which is shown in Fig. 4.2 spanned by the applied torque $F(L-x)a/\kappa$ and the dimensionless parameter $\zeta = \frac{\mu a^2}{\kappa}$ that quantifies the propensity of the braided bundle to form a kink. The kink angle is given by ϕ. Depending on ζ and the applied torque, the braid may or may not cause a localized bend of the filament or *kink*, as can be seen in the figure where, at large applied torques, I predict straight, braided bundles, as is intuitively reasonable. If the braids move outward along the bundle, or if I decrease the applied force, the torque acting on the kinks is reduced. In the first case this is due to the decreasing moment arm produced by the kinked bundle while in the second case it is simply due to the reduced applied force.

The nonmonotonic behavior of the phase boundary is perhaps the most striking feature of the phase diagram, which was also discussed in Ref. [166]. If ζ is small, the binding energy of the linkers is also small, allowing the braid to extend along the bundle and thereby reduce its effective bending modulus. As ζ is increased the braids become shorter and stiffer. When ζ is sufficiently large, however, the braid will now kink even in the absence of an applied force in order to minimize the energy of the bundle. Because of this effect, the large-ζ limit also exhibits kinks. I note that this large-ζ limit occurs around $\zeta \sim 3$, which I believe is obtainable in some biopolymer systems, including condensed DNA [111, 142], cross-linked intermediate filaments [24, 61] and perhaps for collagen [143, 189, 144, 162]. I should note that I introduced the torque with the opposite sign from that used here in Ref. [166], i.e.,

extension is positive, compression is negative.

When I consider the case of sufficiently large values of the ζ parameter, so that kinks exist even under non-zero tensile force, I may then investigate how the kink angle changes in response to that loading by determining the energy-minimized configuration of each kinked braid. As expected, the kink is straightened – the kink angle ϕ decreases – under tension. The dependence of the kink angle ϕ versus applied tension is shown in Fig. 4.3 for a fixed $\zeta = 4$ I observe that the angle versus torque of the kinked bundle is nonlinear; the torque response of the bundle is non-Hookean. I understand this effect to occur because the structure of the energy-minimizing braid itself changes with applied torque so the braided bundle does not bend simply like an effectively thicker filament.

I will later see that the force-induced straightening of the kinks allows for the nonmonotonic behavior of the bundle's extension versus time under a constant tensile loading. This is discussed in more detail in Section 4.3.4. But first, in the following section, I assume the torque to change weakly, so I can assume the kink angle to be constant, which sufficiently simplifies the study of the braid/anti-braid pair production for our analysis.

4.3.2 The piece-wise linear defect potential and the defect distribution

I have shown that the production of braid/anti-braid pairs in a compression bundle can be mapped onto the Kramers escape problem in one dimension using a single reaction coordinate [95, 166]. The two defects must be first produced together in the form of defect/anti-defect pairs, which requires energy E_{defect}. The formation of one defect introduces a length mismatch between the filaments involved that is

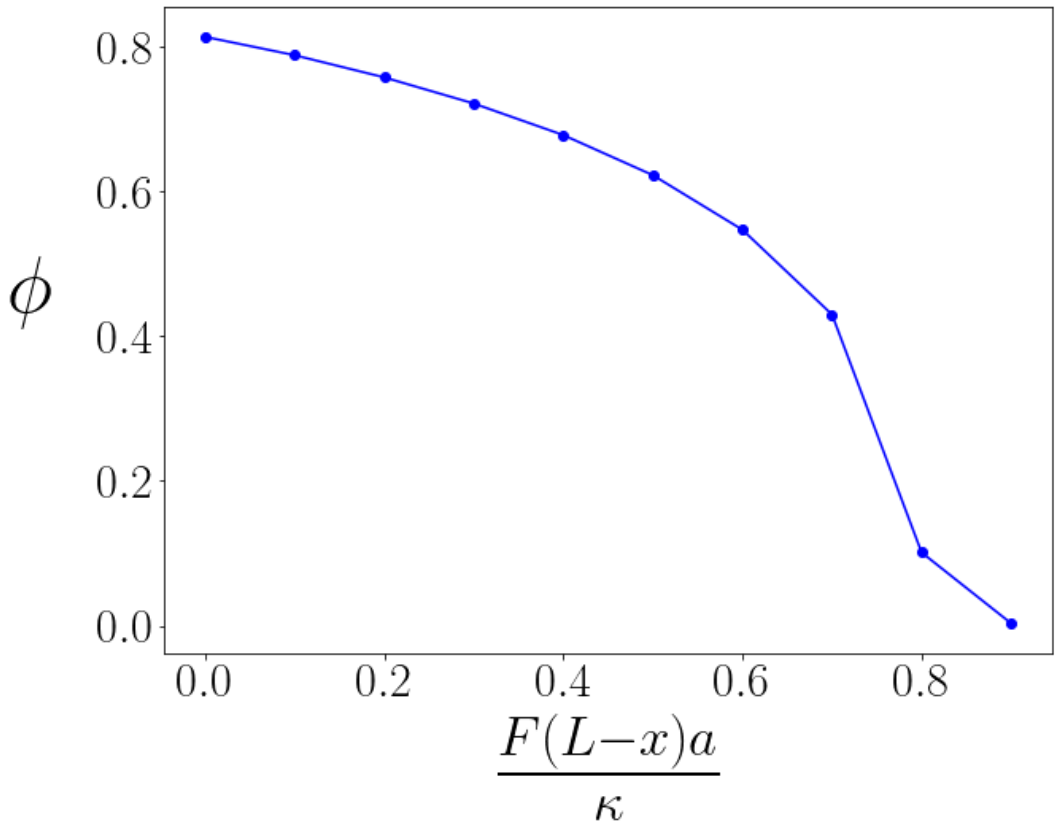

Figure 4.3: Angle produced by braid under extension as function of the value of the torque. Dimensionless parameter $\zeta = 4$. The angle versus torque curve shows that the bending response of the braid is nonlinear, unlike the linear or Hookean response of the individual filaments.

then compensated by the second, anti-defect. As a result, defect pair production entails only local rearrangements of cross linkers. During this point in the thermally-activated production of the defect pair, I may take the single reaction coordinate to represent the total length "exchanged" between defects. Once the defects separate so that a region of cross-linked bundle appears between them, the defects can no longer exchange length, but they may separate along the bundle by reptative motion. Most importantly, since the defects generate localized bends or *kinks* under external loading, the motion of the defects changes the end-to-end distance of the bundle under load. By separating the braids, the energy of the system decreases in response to applied tension and increases in response to applied compression. During this separation (under external loading) the distance between the defects plays the role of the reaction coordinate.

Taking these two aspects of the problem together, I may consider the stochastic pair production process as the thermal escape of a single fictitious particle, representing the reaction coordinate x, in an approximately piece-wise linear potential. Before defect pair separation $x < l$, where l is the size of the defect at the moment of the separation, the potential increases linearly as more length is exchanged between the defect pair and thus more cross links are removed. Understanding the exact form of this potential would require taking into account all different pathways leading from the properly cross-linked bundle to the bundle with braids. I make the simplest approximation, i.e., a linear potential, motivated by the fact that I need to remove number of cross links proportional to the size of the uncross-linked region. Then the effective potential is $U(x) = Ax$, with $A = E_{\text{defect}}/l$. The energy of the defect incorporates bending energy of the filaments, the missing binding energy of

the cross links absent in the defected region, and the work of the applied force:

$$E_{\text{defect}} = E_{\text{bending}}(\phi) + E_{\text{binding}}(\phi) - 2F(L-x)\cos(\phi) - 2Fx, \tag{4.5}$$

where ϕ is the angle formed by a single braid (see Figure 4.1), F is a force acting on the ends of the bundle (positive sign is chosen for the extension), $2L$ is a length of the bundle. The angle ϕ is determined by energy minimization with respect to it. As defects separate, x grows. The angle also changes, but as soon as $x \ll L$, this change contributes to the energy at the next order in the small parameter x/L. I address the explicit dependence of the angle on interbraid separation in the Section 4.3.4. Omitting this effect, I can again write an effective potential $U(x) = Al + B(x-l)$ with $B = 2F(\cos\phi - 1)$. Thus, I may explore the pair production process using the potential

$$U(x) = \begin{cases} Ax, x < l \\ Al + B(x-l), l < x < L \\ \infty, x > L \end{cases} \tag{4.6}$$

Before considering dynamics, I use this potential to consider the equilibrium distribution of defects on a bundle of length L. Specifically, I consider the equilibrium separation of two defects. Using Eq. 4.6 it is trivial to write the probability distribution in this potential: $p(x) = \frac{1}{Z}e^{-\beta U(x)}$ where the partition function Z is given by

$$Z = \int_0^L e^{-\beta U(x)} dx, \tag{4.7}$$

and $\beta = 1/k_{\text{B}}T$ is the inverse temperature. A straightforward calculation arrives at the partition function written as the sum of two parts corresponding to the two pieces of the potential

$$Z = Z_1 + Z_2. \tag{4.8}$$

with

$$Z_1 = \frac{1}{\beta A}(1 - e^{-\beta A l}) \tag{4.9}$$

and

$$Z_2 = \frac{1}{\beta B} e^{-\beta(A-B)l}(e^{-\beta B l} - e^{-\beta B L}). \tag{4.10}$$

Taking the ratio of these partition sums I obtain the ratio of observable separated braid pairs to strongly interacting and co-localized braids:

$$Z_2/Z_1 = \frac{A e^{-\beta(A-B)l}(e^{-\beta B l} - e^{-\beta B L})}{B(1 - e^{-\beta A l})} \tag{4.11}$$

From the above I see that in thermal equilibrium I expect there to be a low density of separated braids, at least at low temperatures ($T \approx 300$K). Specially, if the thermal energy is much lower than the cross-linker binding energy (which is typically true in biopolymer filament systems) I expect an exponentially small density of braids ($\propto e^{-E_{\text{braid}}\beta}$, where for known filaments $\beta E_{\text{braid}} \gg 1$. In fact, it appears that the smallest value of βE_{braid} is found for DNA bundles condensed by polyvalent ions where $\beta E_{\text{braid}} \approx 50$ [111, 142, 166]. Braid pairs, however, can be generated either during bundle formation or via cycles of compression and expansion, as would be expected in a bundle network under reciprocal shear.

4.3.3 The nonequilibrium braid distribution in a time-dependent potential

When one applies a time-varying force, the effective potential controlling the production and motion of the braids also changes in time. As a result, I cannot rely on the equilibrium distribution discussed in the previous section. Instead, I have to

solve the Smoluchowski diffusion equation for defect density $\rho(t,x)$:

$$\partial_t \rho(t,x) = D\partial_x \left[(\partial_x - \beta F(t,x))\, \rho(t,x) \right], \tag{4.12}$$

where the force now takes the form

$$F(t,x) = \begin{cases} A(t), x < l \\ \\ B(t), l < x < L. \end{cases} \tag{4.13}$$

During compression $A(t) = A_c$ and $B(t) = B_c$. During expansion $A(t) = A_s$, $B(t) = B_s$ (note that B_s is negative). In the above, D is the defect diffusion constant. I cannot solve this equation analytically, however, I can provide a qualitative analysis. To simplify, I assume that A and B are fixed during each period of compression and expansion. I explore how the defect production rate depends on the lengths of these periods of compression and extension. I also estimate the maximal defect production rate.

The transport time from 0 to l in the potential is controlled by the constant A. This is the braid pair production rate when the braids have stored length of l. This problem is simply the first passage time [95] to reach l in the linearly increasing potential, which I may estimate to be

$$T_{0l} = \frac{1}{D} \frac{e^{\beta A l}}{\beta^2 A^2}. \tag{4.14}$$

Similarly, I estimate the transport time from L to l. This gives an approximate value of the lifetime of the braid pair, since when their separation returns to l they will likely annihilate. Here I must distinguish between two limiting cases. In the first case, I consider purely diffusive braid motion and in the second, I look at the deterministic transport of the braids under an applied force using a mobility set by

the diffusion constant and the Einstein relation. I find

$$T_{Ll} = \begin{cases} L^2/D, B\beta > 1/L \\ L/(B\beta D), B\beta < 1/L. \end{cases} \tag{4.15}$$

In general, where I expect there to be both diffusive and advective defect motion, I find that the time for defects to recombine is

$$T_{Ll} = \frac{L^2}{D(1+\beta BL)} \tag{4.16}$$

In the limit of large L, $T_{Ll} \gg T_{0l}$ so that the time for distant defect pairs to come together and potentially annihilate is much greater than their production time. If braids are able to separate sufficiently, I expect this ordering of time scales to be valid and thus predict braid proliferation on the bundle.

Because the production time T_{0l} has an exponential dependence on A,

$$T_{0l}^{\text{compression}} \ll T_{0l}^{\text{stretching}}, \tag{4.17}$$

since the A parameter is much larger under stretching than it is under compression: $A_c < A_s$. If I choose the time-dependence of the applied force so that the stretching time τ_s and compression τ_c satisfy the inequalities

$$T_{0l}^{\text{compression}} \ll \tau_c \ll \tau_s \ll T_{0l}^{\text{stretching}} \ll T_{Ll}, \tag{4.18}$$

I may analyse the dynamics of the system using a few approximations.

Since the braid production rate during compression is small compared to the compression time: $T_{0l}^{\text{compression}} \ll \tau_c$, then, during the compression period, the density on the left $0 < x < l$ equilibrates. Since $\tau_s \ll T_{0l}^{\text{compression}} \ll T_{Ll}$, during the stretching period, the probability density $\rho(x)$ decreases near the potential maximum at $x = l$,

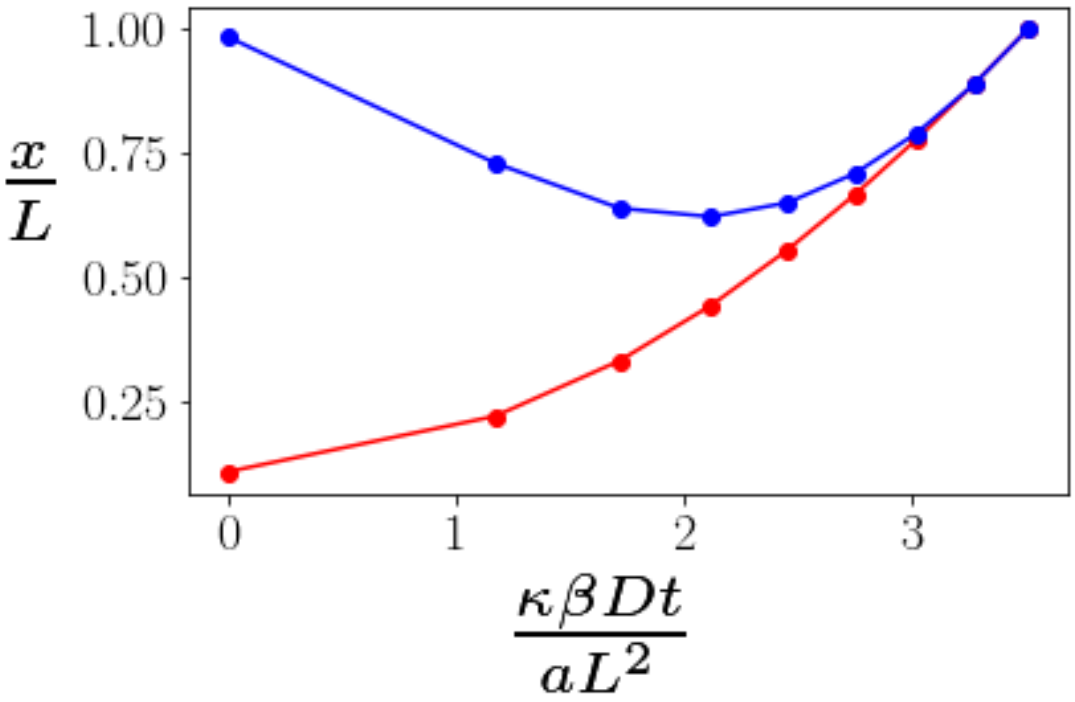

Figure 4.4: The time evolution of the distance between two defects (red) and the end–to-end distance of the bundle (blue) under a constant applied tensile force $F = 0.9\frac{\kappa}{aL}$ plotted as a function of non-dimensionalized time. The cross linker binding energy is $\mu = 4\frac{\kappa}{a^2}$.

but it is highly unlikely that thermally excited hopping over the barrier at l occurs. Since $\tau_c \ll \tau_s \ll T_{0l}^{\text{compression}} \ll T_{Ll}$, the applied force is changing sufficiently fast that the density of the right of of the potential $x > l$ may be replaced by its time-averaged value. Moreover, since $\tau_c \ll \tau_s$, density on the right of the potential is effectively determined by the dynamics during the stretching period. Because the compression period is shorter, the already produced braids are unlikely to be driven together and annihilate. As a result, I conclude that the density distribution on the left is effectively determined by the compression period and the density on the right by the stretching period. Finally, I note that the Smoluchowski diffusion equation requires the continuity of both the probability density and its current at the boundary $x = l$. From these conditions, I obtain a value of the averaged density on the right as a function of the equilibrium density on the left. This implies that with this sequence of inequalities, the braid production and separation may be considered to take place in a time-averaged, effective potential where the production part is set by the compression forces and braids separate under a force related to extension. Specifically, I consider

$$U(x) = \begin{cases} A_c x, x < l \\ A_c l + B_s(x - l), l < x < L \\ \infty, x > L. \end{cases} \tag{4.19}$$

In this potential, the probability of braids on the left $x < l$ will be proportional to

$$Z_1 = \frac{1}{\beta A_c}(1 - e^{-\beta A_c l}), \tag{4.20}$$

while on the right

$$Z_2 = \frac{1}{\beta B_s} e^{-\beta(A_c - B_s)l}(e^{-\beta B_s l} - e^{-\beta B_s L}). \tag{4.21}$$

The ratio is

$$Z_2/Z_1 \approx -\frac{A_c}{B_s} e^{-\beta(A_c - B_s)l} e^{-\beta B_s L} \gg 1, \tag{4.22}$$

which exceeds the case of only compression by a factor of $e^{\beta|B_s|L}$, and the case of only expansion by a factor of $e^{\beta(A_s - A_c)l}$ – see Eq. 4.11.

4.3.4 Constant force stretching dynamics of a braided bundle

I now consider an experiment in which one stretches a previously compressed bundle (by laser tweezers or other means) at a fixed force and determines the time rate of change of the bundle's length. This is akin to a step force rheological measurement, and is closely related to determining the force-extension curve of a filament or filament bundle. Typically, in such force extension measurements, one considers the limit of slow extension so that the observed length corresponds the thermal equilibrium prediction under a fixed force [106]. In this case, however, the extension of the bundle will be time dependent even though the force is constant.

To study this problem, I minimize the energy of the bundle under a fixed stretching force. By doing so, I assume that bending of the kink angles at the braids is fast compared to the time scale of measurement of the end-to-end distance. I do not, however, assume that the advection and diffusion of the braids is similarly fast. Doing this energy minimization numerically, I obtain the time dependence shown in Fig. 4.4. The time dependence of the bundle's extension is nonmonotonic: as defects diffuse from each other, the bundle initially becomes shorter. This happens due to the fact that as x grows, the $L - x$ becomes smaller, hence, the moment of the force decreases as well. Since the stretching force decreases, kinks become less stretched and their angles increase (see Fig. 4.3), decreasing end-to-end distance

$\Delta L = 2(x + (L - x)\cos\phi)$.

4.4 Discussion

Semiflexible filament bundles admit three classes of topological defects: loops, braids, and dislocations. These defects are all likely to be produced in the formation of bundles from solutions of semiflexible filaments by the introduction of cross-linking agents. They are, however, unlikely to form spontaneously in thermal equilibrium when the filament bundles are also chemically equilibrated with a reservoir of cross linkers. Here I have pointed out that reciprocal compression and extension of filament bundles, however, is capable of producing a higher nonequilibrium density of braid defects within a bundle. The key insight is that bundles under compression can locally buckle producing braid, anti-braid pairs. Upon subsequent extension, these braid pairs will be driven to separate, as long as they do not immediately annihilate. In order to ensure that braid pairs produced in the previous compression cycle (and separated during the previous extension part of that cycle) do not annihilate during the subsequent compressive cycle, one needs to introduce an asymmetry between the period of compression (short) and the period of extension (long). Other cycles of compression and extension will also produce braid, anti-braid pairs, but at lower density. I predict that the short compression period following long extension one will result in the maximum possible defect density.

I also examined the extensional dynamics under a fixed tensile load of semiflexible bundles containing a braid defect pair. Here one does not observe the standard worm-like chain force extension relation at very low frequencies. The extension of the bundle is not controlled by the depletion of the length reservoir associated with

the thermally-generated undulations of the bundle, but rather by the motion of the braid defects and the bending of the kinks associated with these defects. In essence, our predictions refer to the analog of plastic deformation in solids associated with defect motion rather than the (entropic) elastic response of the bundle, which, due to cross linking, is suppressed. I note that the end-to-end distance of the bundle varies nonmonotonically with time under a constant tensile load. This somewhat counter-intuitive result occurs due to the combination of two effects: braid separation, which lengthens the bundle, and kink angle relaxation, which shortens it.

For experimental verification of these predictions, there is no more direct measurement than compression/extension experiments on individual semiflexible filament bundles using laser or magnetic tweezers to manipulate the bundle's stress state [171]. In addition, one expects that the imagining experiments on compressed semiflexible filament bundles should produce observable kinks (localized bending defects) rather than the uniform curvature of the entire bundle, as would be expected from classical Euler buckling. Although less direct in testing the predictions made here, standard shear measurements and studies of stress relaxation in networks of filament bundles with transient cross linkers at long times or low frequencies are particularly relevant to the present work. I imagine that, at sufficiently long times, stress relaxation will be dominated by plastic deformation of network comprised of both tearing and reattachment of bundles from each other, and the plastic deformation of the individual bundles themselves, presumably following the mechanisms discussed here. I do not, as yet, understand how to distinguish these dynamics in rheological data, and this remains one of the principal open questions related to this work.

Other open questions involve the the mechanical compliance of the cross linkers

and their binding kinetics. In this work, I have considered the cross linkers to be essentially inextensible so that when they must fall off the defected regions where the inter-filament spacing is no longer equal to the cross linkers' length. I imagine that cross linker redistribution and defect energies will be affected by the elastic compliance of the cross linkers. In fact, sufficiently compliant cross linkers may even allow for Euler buckling of the bundle under compression. Lastly, I point out that I have assumed that cross linkers are able to bind and unbind on short time scales compared to the observation time for both defect pair production and motion along the bundle. When investigating bundle mechanics at sufficiently short time scales, one must consider the possibility that the cross linker distribution is no longer in equilibrium with the bundle in its current stress state. I leave these open questions to future work.

CHAPTER 5

Directed force propagation in semiflexible networks

5.1 Introduction

As we discussed in chapter 1, the transmission of force through filamentous networks on the mesoscale is a complex problem that cannot be directly addressed by appeals to continuum elasticity. Understanding that, at sufficiently large length scales, a filamentous network must act like a continuum elastic solid is not helpful in predicting how that force is supported at mesoscopic length scales in the network immediately surrounding the point of force application. The complexities associated with this question are reasonably clear; they are related both to the spatial heterogeneity and geometric complexity of filament interconnections and the inherent nonlinearity of the filaments' force extension relations. Biopolymer filaments are generically strongly strain hardening under tension, but quite soft under compression, due to Euler buckling.

A well-known system that combines both geometric heterogeneity of force-transmitting contacts and strong mechanical nonlinearity is granular piles [103, 21, 72]. In a sand pile, one has a complex network of force-transmitting contacts that are elastically

nonlinear – the contacts support large compressive loading and essentially no tensile loading. These granular systems generically exhibit long and quite ramified force chains, spanning large numbers of intergrain contacts. Although the bending stiffness of the filaments makes the analogy between filamentous networks and granular media imperfect, one might expect similar force chains in such networks in the response to point forces. This expectation seems to be supported by previous simulations [65, 67] of the point force response of mikado networks and experiments on force-based interactions of cells with the fibrous extracellular matrix (ECM) [105, 150]. In the former, one sees the breakdown of the continuum elastic response on scales much larger than the mesh size. In the latter, one observes intercellular force transmission over long lengths, but only along particular, directed paths. Intriguingly, numerical studies of three-dimensional filament networks subjected to large shear strains [71] reveal the appearance of percolating tensed subnetworks that may also be related to force chains.

In the ECM experiments, it is not clear if these long tracks of force transmission are a generic consequence of isotropic random networks, or due, in part, to some filament anisotropy or heterogeneity either in the form of stiffer filament bundles or spatial variations in the networks density. Such heterogeneity may well be important. In even slightly anisotropic networks, previous work [120, 47, 110] has shown that there exist long-ranged buckling scars forming in the network's response to even uniform shearing.

Another consequence of the mesoscopic failure of continuum elasticity (by which we mean on scales greater than several mesh sizes is that the collective point-force response of the network is remarkably heterogeneous. Active microrheology experiments [94, 87] have shown that the linear response of a bead embedded in the network

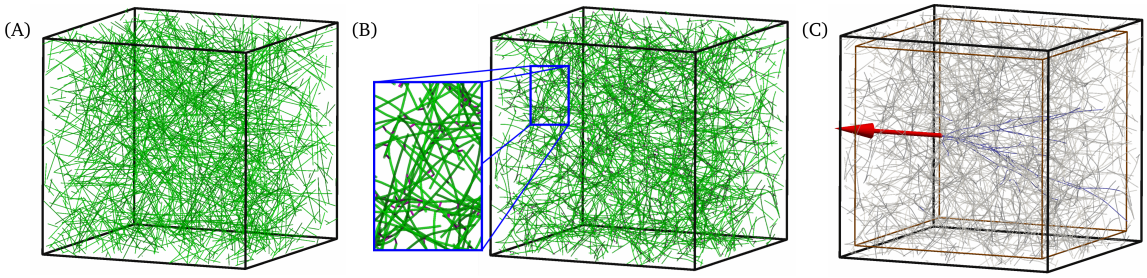

Figure 5.1: Schematic of the setup and protocol of the numerical experiments. (A) Pre-processing: Random placement of straight filaments (green) and free linker molecules (not shown) in a cubic box with periodic boundaries. (B) Simulation of the network assembly driven by Brownian motion and random formation of cross links (pink). Subsequent equilibration of the system considering permanent cross links and zero temperature. (C) Simulation of the quasi-static network response to a point force (red arrow), applying zero displacement boundary conditions in the thin outermost shell of the network (between brown and black box).

to force varies from location to location within the network by one order of magnitude. Similarly, recent experiments [70] have shown that the response of the network to a force acting on one filament is also highly heterogeneous. The displacement of the surrounding network depends critically on which filament is pulled, and in which direction. These complexities of the point force response are not attributable to large-scale spatial gradients in either the density of cross links or filaments. Instead, the experiments suggest that the inherent mesoscale structure of a network, whose density and connectivity is, at least, statistically homogeneous or self-averaging on long length scales, is responsible for these effects.

To better understand the peculiarities of the response of these seemingly simple systems, we examine in this manuscript the question of force chains and the elastic response of isotropic and homogeneous filament networks to point forces. These choices allow us to assess the complexity of force propagation in the most simple form of a random filament network. In this work, we combine the results of large-scale, finite-element simulations with theoretical modeling to determine how a force applied to a single point on a filament spreads out through the network. We confine our studies here entirely to the static response of the system. We show via simulation that tensile force chains exist in the vicinity of the point of force application. We use these simulations to further characterize both the spatial structure of the force chains and the forces they carry, paying particular attention to how the force applied to a particular filament bleeds off into the surrounding network through cross-linked junctions. In addition, we examine the collective response of the network to applied point forces by determining the point force response that is measured by low-frequency microrheology experiments in fibrous materials like the ECM.

We then turn to the theoretical approach to understanding force chains and

the point force response of the network. We develop a self-consistent approach to calculating the point-force response function. Finally, we compare simulation and theory, as well as discuss our results in the broader context of intercellular force propagation in tissues in our summary. There we address the question of whether one can account for the observations of both long force chains and the dramatic spatial heterogeneity of the collective response of the network to point forces within a statistically isotropic and homogeneous filament network.

5.2 Simulations[1]

This section covers the large-scale, finite-element simulations we performed to study the point force response of randomly assembled 3D networks of semiflexible filaments. After a brief description of the conducted numerical experiments and the underlying computational model in Sec. 5.2.1 and 5.2.2, respectively, we present the simulation results in Sec. 5.2.3.

5.2.1 Computational experiments

A schematic overview of the setup and protocol of the performed experiments is given in Fig. 5.1. In a pre-processing step, a number of straight filaments and free linker molecules are randomly distributed inside a cubic simulation box with periodic boundary conditions (Fig. 5.1(A)). We chose the filament concentration so that we end up with 834 filaments in a box with edge length of 10μm. The number of linker molecules is chosen as $N_\ell = 10^4$. During the first simulation phase of $t =$

[1]**The numerical simulations were done by Maximillian Grill and Wolfgang Wall, Technical University of Munich**

1.5s, the filaments experience stochastic, thermal undulations, and cross links are established, such that we obtain a random 3D network geometry (Fig. 5.1(B)). The final number of (doubly bound) cross links in these assembled networks varies from 2998 to 3097 over the ten random realizations that have been considered in our study. A subsequent relaxation phase of 1s allows the network to release some of the prestress that has been trapped during the assembly in order to start the subsequent force application from an equilibrium state. For this purpose, the thermal energy $k_{\mathrm{B}}T$ and the binding and unbinding rates k_{on} and k_{off} of the linkers are set to zero after the assembly phase.

Finally, a point force is applied in order to investigate the quasi-static response of the network (Fig. 5.1(C)). The point of force application is chosen close to the box center in order to restrict the influence of the boundary conditions. Specifically, the filament nodes in the outermost shell of the network sample (the volume between the brown and black box in Fig. 5.1(C)) are pinned via zero displacement Dirichlet boundary conditions. The thickness of this shell is chosen to be 0.5μm, which corresponds to 5% of the edge length. The direction of the applied force is chosen either tangentially to the filament axis or transverse to it. It is important to note, however, that the point force direction is kept constant, i.e., it will not follow the filament's deformation. The force magnitude is increased linearly until it reaches its maximum $F = 100$pN after another 1s of simulation. This is sufficiently slow to ensure a quasi-static response of the system. At the smallest forces recorded, we do observe viscous effects dependent on the rate of force increase, which perturb our results for pulling forces around 1pN. Note that the third phase of the simulation, consisting of the actual force application, is run independently several times in order to generate our complete data set, and to observe the influence of the direction of

force application. Starting from the identical equilibrated network configuration, the network is thus probed along three mutually orthogonal axes with two directions each, which leads to six numerical pulling experiments for each network geometry.

5.2.2 Numerical model

We employ the numerical model developed and applied in our previous work [28, 29, 27, 126, 129, 109, 78, 164], describing semiflexible filaments via geometrically exact beam theory, subjected to Brownian dynamics. Thermal excitations and the presence of cross-linker molecules give rise to network self-assembly, which produces isotropic and uniform random 3D networks, which are to be probed by applying a point force later on. Further details including the parametrization of the model are given as follows.

5.2.2.1 Filament model

Each filament is modeled by nonlinear, geometrically exact, 3D Simo-Reissner beam theory and discretized in space using beam finite elements. In terms of the structural rigidity of the filament, we thus account for axial, torsional, bending, and shear deformation. All filaments are chosen to be initially straight with a length of $L_0 = 4\mu$m and persistence length $L_p \approx 7\mu$m. The geometrical and material parameters resemble F-actin, which is a key constituent of the cytoskeleton. A complete specification is given by the cross-section area $A = 1.9 \times 10^{-7}\mu\text{m}^2$, area moment of inertia $I = 2.85{\times}10^{-11}\mu\text{m}^4$, polar moment of inertia $I_p = 5.7{\times}10^{-11}\mu\text{m}^4$, Young's modulus $E = 10^9\text{pN}/\mu\text{m}^2$, and Poisson ratio $\nu = 0.3$. By default, we discretized each filament with four beam finite elements of the Hermitian Simo-Reissner type,

which has been presented in our recent contribution [118].

As described above, once the networks have been created by the Brownian diffusive dynamics of cross links and filaments, we explore force propagation in the network in zero temperature simulations. Other computational approaches to forming filament networks starting from individual filaments have been pursued [71], leading to similar networks without resorting to this Brownian dynamics approach to network construction. Force propagation in these networks depends only on the relative size of two length scales, the filament length and the distance between consecutive cross links along the filament. As a result, our studies of force propagation under static loading apply equally well to filament networks at all scales including cytoskeleton and ECM.

5.2.2.2 Brownian dynamics

To model the Brownian motion, we include viscous drag as well as thermal forces, each distributed along the entire filament length as in previous work [29]. Viscous forces and moments are computed assuming a quiescent background fluid and individual damping coefficients for translations parallel and perpendicular to the filament axis, as well as rotation around the filament axis. Thermal forces are determined from the stochastic Wiener process in accordance with the fluctuation-dissipation theorem. Finally, an implicit Euler scheme is used to discretize in time and a Newton-Raphson algorithm solves the resulting nonlinear system of equations. Further details on this simulation framework including all formulae can be found in Ref. [29].

Here, temperature is set to $T = 293\text{K}$ and the dynamic viscosity of the quiescent background fluid to $\eta = 10^{-3}\,\text{Pa}\,\text{s}$. The base time step size is chosen as $\Delta t = 0.01\text{s}$,

which is augmented by an adaptive time stepping scheme that reduces the time step size whenever necessary.

5.2.2.3 Cross-link model

Our numerical model tracks linker molecules explicitly as they switch between three possible states: free, singly bound, or doubly bound. All details on the linker model can be found in the original publication [129]. Free linker molecules experience Brownian motion until eventually all binding criteria are met and they establish a first, and later possibly a second, connection to a filament. In the doubly bound state, *i.e.*, a cross-link spanning two filament binding spots on different filaments, each linker is treated as an additional, very short beam element, which can transmit forces and moments between the filaments. We do not prescribe a preferred binding angle between the filament axes that needs to be met for binding. However, due to the rigid connection to the filaments, the cross links act to maintain the specific angle(s) that were present at the time of binding. As such, these short filaments (the cross linkers) behave more like α-actinin or other bundling cross linkers than they do act like filamin, which is known to form quite flexible hinges. The binding decision is made based on a given binding rate and a distance criterion that takes into account the spatial extent and thus action range of the linker molecule. Here, the length of the linker is chosen to be $L_\ell = 0.1\mu\text{m}$ (with a tolerance of $\Delta L_\ell = 2\text{nm}$) and binding spots are assumed to be located equidistantly along the filament with a spacing of $\Delta s_{\text{bs}} = 0.1\mu\text{m}$. During the assembly of the networks, the binding and unbinding rates are set to $k_{\text{on}} = 10^5\text{s}^{-1}$ and $k_{\text{off}} = 0\text{s}^{-1}$ in order to speed up the network generation process.

5.2.3 Simulation results

All the simulations were performed by means of the parallel, multi-physics, in-house research code BACI. [2] The following simulation results aim to characterize the collective point force response of the system, the resulting deformation and the stress state inside the system. In particular, we explore how the applied external force propagates through the system.

5.2.3.1 Force-displacement curves and effective spring constants

Fig. 5.2(A) shows the measured force-displacement curves for 10 different network geometries with two axial and four transverse pulling directions each, *i.e.*, for a total of sixty numerical pulling experiments. The response from both the axially (red) and transversely (blue) applied point forces reveal a highly nonlinear, hyperelastic behavior. Generally, we observe significantly smaller local stiffness in the regime of low forces (see magnified part on the left of Fig. 5.2(A)) as compared to the high-force regime, which yields a pronounced strain hardening behavior. To further characterize and investigate the system response, we compute the local, effective spring constant as the slope of each curve, both for the low- and high-force regime as indicated by the green and orange triangles, respectively. Specifically, we use the first two data points of each curve to compute the slope at zero force and the two data points with largest force values of each curve to compute the slope in the high-force regime.

The resulting distributions of the effective spring constants in both regimes are shown in Figs. 5.2(B) and 5.2(D). On average, the effective stiffness for high forces is approximately one order of magnitude higher than for low forces. In addition, the shape of the distribution changes from a bell shape with fat right tail for low

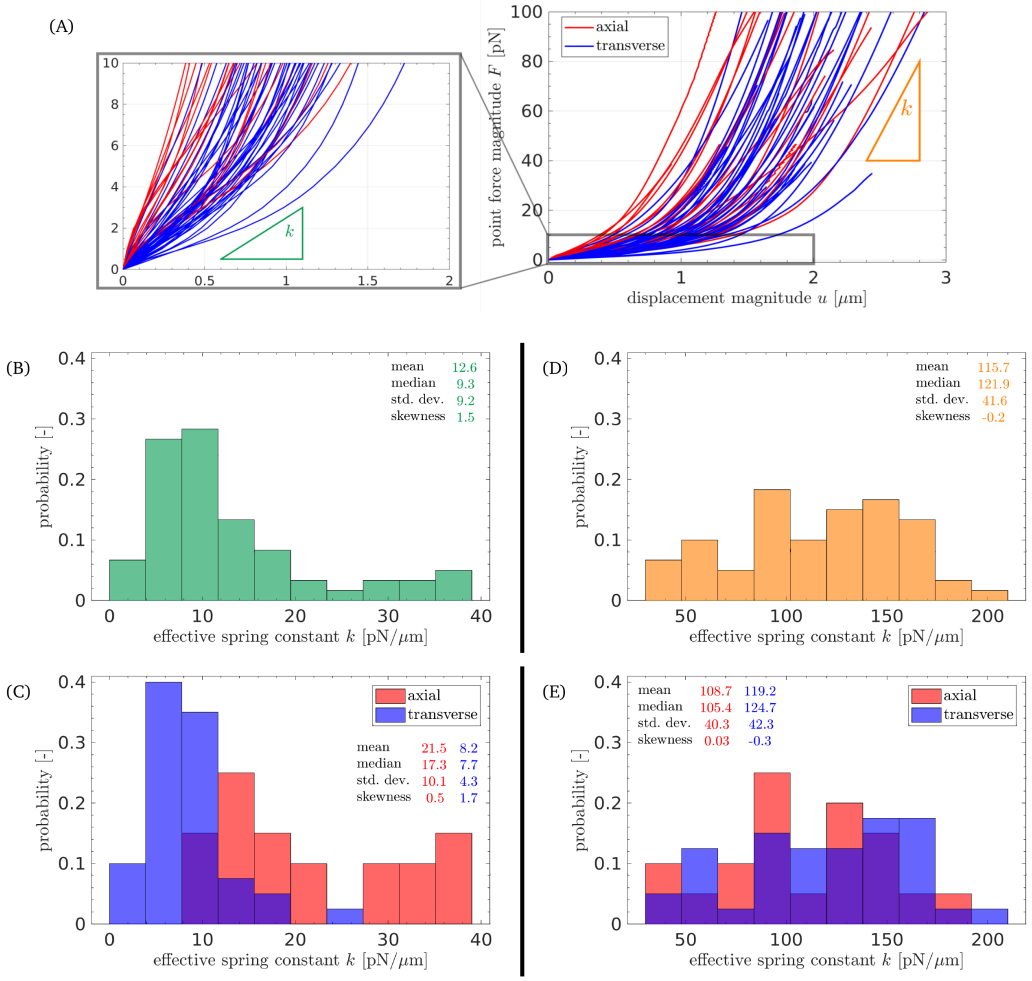

Figure 5.2: (A) Force-displacement curves for 10 different network geometries with 2 axial (red) and 4 transverse (blue) pulling directions each, i.e., a total of 60 numerical pulling experiments. The inset on the left shows the magnified low-force regime. The green and orange triangle indicates the calculation of the effective spring constants for the low- and high-force regime, respectively. (B,D) Histogram of effective spring constants for the low-force and high-force regime respectively and (C,E) the same data broken down into axial (red) and transverse (blue) pulling.

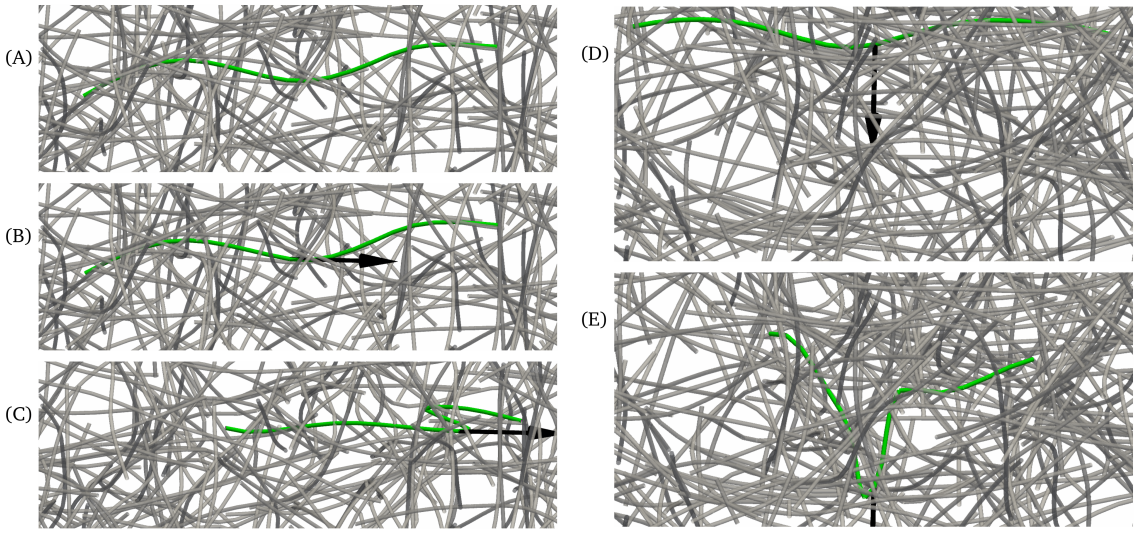

Figure 5.3: Close-up views of the filament being pulled at (green) by a point force (black arrow). All other filaments in the network are shown in gray. (A) Equilibrated state, i.e., point force magnitude $F = 0$. (B) Axial loading at $F = 1$pN. (C) Axial loading at $F = 100$pN. (D) Transverse loading at $F = 1$pN. (E) Transverse loading at $F = 100$pN.

forces, to a rather broad and uniform distribution for high forces. Breaking this down into axial and transverse pulling experiments results in the histograms shown in Fig. 5.2(C) and (E). In the low-force regime (Fig. 5.2(C)), this clearly reveals a strong dependence on the pulling direction relative to the filament orientation. On average, the stiffness values observed for tangentially applied point forces are a factor of 2.6 higher than for transverse point forces. This is an expected result, because slender, semiflexible filaments typically have a significantly larger axial stiffness than (effective) bending stiffness, making them much more compliant under transverse loading. In the high-force regime (Fig. 5.2(E)), the picture is less clear and the difference between both cases is reversed. A close look at the deformed states of the network (see Fig. 5.3 for an example) suggests a reason for this change. When a filament is pulled transversely, it deforms as shown in Fig. 5.3 (E). In effect, at high force the pulled filament (green), after becoming sharply bent, might be thought of as two axially-tensed filament halves, each of which may generate its own tensile force chains and thus becoming stiffer to further pulling. When the filament is pulled axially, however, this effect is weaker – see Fig. 5.3 (C). In that case, we surmise that the load is imperfectly transferred to two tensile force chains, leading to a smaller increase in the collective stiffness of the system to these large forces. We speculate that the reversed effect of slightly higher mean effective stiffness in the case of transverse loading might originate from the fact that the load is distributed more evenly on both branches and thus involves a larger fraction of the entire network for high forces.

5.2.3.2 Comparison of the resulting displacement field to the analytical solution for a linear elastic continuum

In this section, we characterize the resulting displacement field in the filament network, and compare it to the analytical solution for an infinite homogeneous, isotropic, linear elastic continuum. For an isotropic elastic continuum, the displacement u_i of each point x_i of the medium with Young's modulus E and Poisson ratio ν under the action point force F_i at the origin obeys the equation [99]

$$(u_i x_i)|\vec{x}| = \frac{1+\nu}{2\pi E}(F_i x_i). \tag{5.1}$$

Fig. 5.4 characterizes the resulting displacement field in the network at a point force magnitude of (A) $F = 2$pN, (B) $F = 10$pN, (C) $F = 20$pN, and (D) $F = 100$pN. Each scatter plot contains the data of 2000 nodes in the filament network. These plots show the correlation between the scalar products $(u_i x_i)$ and $(F_i x_i)$, where $\vec{F}$ denotes the applied point force vector acting at the origin and $\vec{u}$ and $\vec{x}$ denote the displacement and position vector of a particular point in the network. Whereas the analytical solution for a homogeneous, isotropic, linear elastic continuum would be a straight line with the slope equal to $(1+\nu)/(2\pi E)$ (see Eq. 5.1), the simulation results for the filament network show an entirely different behavior.

Irrespective of the force's magnitude, there is a high concentration of points around zero displacement, indicating that a large fraction of the network is barely influenced by the applied point force. The remaining data points become distributed more widely upon increasing the force magnitude. Only for the smallest force value of $F = 2$pN (Fig. 5.4(A)) can one find a linear feature consistent with the solution from continuum elasticity. We show this as a guide to the eye with a black, dashed line. Note also the asymmetry of the data with respect to the origin, which again increases

with the force magnitude. It may be explained by the strong asymmetry of the filaments to bear tensile versus compressive loads. Altogether, one may conclude – on the mesoscale considered here – the point force response of a semiflexible filament network is conceptually different to the response of a continuous elastic medium, even in the regime of small forces. We now consider other ways to characterize the distribution of forces within the network.

5.2.3.3 Distribution of axial force in the network

To characterize the stress state of the entire filament network as a result of point force application, we report the distribution of axial force measured at the center of each finite element. Fig. 5.5 compares, on a semi-log scale, the distribution obtained after the equilibration phase (blue) with the one obtained for an applied point force magnitude of $F = 100$pN (red). In order to obtain more data points in the long high-force tail of the distribution, we have included data from thirty numerical pulling experiments.

As expected, the reference distribution of axial forces in the equilibrated state has a sharp peak near zero force, with mean value and standard deviation -0.006 ± 0.1pN. Applying the point force significantly broadens and shifts the distribution towards tensile, *i.e.*, positive force values with mean value and standard deviation 0.3 ± 1.9pN. Also, the skewness increases by more than two orders of magnitude, reflecting the well-known, strong asymmetry between tensile and compressive force transmission in semiflexible filaments. The median, however, of that distribution changes only very little from -0.003pN to 0.007pN when compared to the significant increase of the mean value. This indicates, once again, that the vast majority of the filaments in

the network remain almost unaffected by the applied point force. Together with the long tail of the distribution, it provides evidence for the existence and importance of tensile force chains.

5.2.3.4 Force propagation via force chains

Fig. 5.6(A) shows the concept of force chains to be used for the characterization of force propagation in filament networks. Filament segments with a total elastic energy per finite element above 0.75aJ, 0.25aJ, and 0.075aJ are highlighted in red, blue, and green respectively, while all other filaments are depicted as thin, gray lines. Choosing and varying this threshold value allows one to track force transmission from the point of force application to the support at the boundaries. The resulting force-chain structures are typically connected, and span cone-shaped subregions of the network volume. To get a clearer picture, all other untensed filaments are hidden in Fig. 5.6(B). Cross links supporting a force greater than a threshold of 8pN are also shown in pink to demonstrate that the tensile force chains pass between filaments via such highly loaded cross links. Finally, Fig. 5.6(C) shows an overlay of three different pulling directions and the resulting force chains distinguished by color. All the simulation snapshots shown in Fig. 5.6(A)-(C) correspond to the highest point force magnitude $F = 100$pN used in the numerical experiments.

Since the threshold value is fundamentally arbitrary, it is helpful to look at changes of force-chain-related quantities as function of that threshold. The most basic quantity associated with the force chains is the fraction of the total filament length with tensile loading above the chosen threshold. This quantity, which can be computed at the level of individual finite elements, simply measures how much of

the network (by filament length) is sufficiently tensed to reach the chosen force-chain criterion. Specifically, we calculate the total length of those finite elements whose tensile loading exceeds the threshold and divide that by the total length of all finite elements in the network. Fig. 5.6(D) shows a double-logarithmic plot of that fraction of the total filament length making up the force chains as a function of the applied point force magnitude for three different threshold values (dotted, dashed, and solid lines). The colors indicate six pulling experiments with different point force directions. The smallest threshold value 0.01aJ is chosen such that it is exceeded by a small fraction of filaments already for small point force magnitudes (dotted lines). We observe that the corresponding filament length fraction approximately increases with the square root of the point force magnitude in the high-force regime. A second threshold of 0.1aJ is exceeded only for intermediate to high point force magnitudes and the corresponding filament length fraction seems to increase linearly for high force values. The highest threshold value of 1aJ is exceeded only for very high point force magnitudes and only in a very small fraction of the filament length.

Fig. 5.6(E) gives the complementary picture, where the fraction of filament length is plotted as a function of the threshold value for three different values of the applied point force magnitude (dotted, dashed, and solid lines). Again, the colors indicate six pulling experiments with different point force directions. Naturally, as the elastic energy threshold approaches zero, the entire network is activated, and so all curves collapse to unity. For the smallest chosen force magnitude 2pN, we observe a rapid decrease of the filament fraction decaying approximately $\sim E^{-6}$ at large E. This behavior changes for higher applied force magnitudes, where the fraction of filament length falls off much slower, especially in the regime of intermediate threshold values. For the largest threshold values E observed for a given force magnitude, there seems

to be a similar behavior with $\sim E^{-6}$ decay for all three force magnitudes considered here.

Finally, we note that the topology of the observed force chains was that of a branching network – see Fig. 6(A,B,C). In the sixty simulations we performed, we did not observe any loops in these force-chain networks, suggesting that such structures are quite rare. Moreover, the force chains (at the higher threshold values) were generally connected; as the threshold force was lowered, we did observe occasional disconnected pieces of force chains arising in the vicinity of the main, connected chains.

5.2.3.5 Decay of axial tension along force chains

For a detailed study of the decay of the axial force along the filaments and force chains, we use a slightly modified setup, which is shown in Fig. 5.7(A). In addition to all the filaments with (initial, stress-free) length $L_0 = 4\mu$m (gray), one long filament with $L_0 = 20\mu$m (green) is placed along the axis of an elongated simulation box of size $25 \times 6 \times 6\mu$m. The central filament is discretized with 100 beam finite elements to ensure a fine spatial discretization. Instead of the filament midpoint, the point force is now applied to one of the filament endpoints and we only consider tangential tensile loading. All other parts of the setup and protocol of the numerical experiments as described in Sec. 5.2.1 and 5.2.2 remain unchanged. In particular, once again 10 different network geometries have been generated by random initial placement of the straight filaments, simulating the dynamic assembly driven by Brownian motion, and a subsequent equilibration simulation.

Fig. 5.7(A), (B), and (C) show simulation snapshots of the same pulling exper-

iment at three different point force magnitudes of $F = 100\text{pN}$, $F = 50\text{pN}$, and $F = 2\text{pN}$, respectively. All filaments in the force chains for an elastic energy threshold (per finite element) $E_{\text{el,ele}} = 0.1\text{aJ}$ are highlighted in blue. This already reveals that the perturbation of the network in form of the applied point force is transmitted along a few paths of cross-linked filaments in the vicinity of the location of force application. From the persistent wavy form of the left half of the central filament even for very high point force magnitudes, it becomes obvious that the perturbation is absorbed quite rapidly. Note in this respect that the force chains reaching from the central filament to the pinned boundaries typically include a couple of cross links and thus different filaments such that the pathological edge case of one filament reaching from the central filament to the pinned boundary is typically not observed in this simulation setup.

For a quantitative analysis of the tension decay along the filaments, we look at the axial force along the central filament. The semi-logarithmic plot in Fig. 5.8(A) shows the mean values over all twenty numerical pulling experiments obtained for 5 different point force magnitudes. In addition, the data for all twenty individual realizations at the lowest ($F = 2\text{pN}$) and highest ($F = 100\text{pN}$) force magnitude is plotted (with linear scale on the vertical axis) in Fig. 5.8(B) and (C), respectively. Most importantly, Fig. 5.8(A) reveals an approximately exponential decay of the average axial tension with increasing distance from the location of force application – more or less irrespective of the applied force magnitude. Second, the slope of the curves and therefore also the characteristic decay length, varies slightly over the five different applied force magnitudes with the fastest decay being observed for the smallest force magnitude. Finally, from looking at the data for each individual realization in Fig. 5.8(B) and (C), a characteristic step-wise decay behavior is revealed. This

can be explained by the fact that tensile force is transmitted to other filaments at the (randomly distributed) discrete locations of cross links along the filament axis. To conclude, this analysis confirms the rapid absorption of tension along the filaments in a quantitative manner, and reveals an exponential decay, which is consistent with the theoretical calculations presented in the following section.

5.3 Analytical model

We adopt a simple model of semiflexible filament networks that is often referred to in the literature as a mikado model [64, 66, 65]. This class of network models imagines that the system is composed of initially straight, stiff filaments cross linked by permanent bonds that allow for free rotation of the filaments at these connections. Typically such models are treated in two dimensions. We do so as well, except in specific instances where we consider three dimensional extensions; these are explicitly noted. Inextensible filaments are placed one by one in a cube of volume L^3, truncating at the boundaries. Intersecting filaments are then cross-linked together, creating a collection of filament *s*egments that form the network. The lower coordination number of our model differs from those of previous studies on force chains on lattices [103, 25]. As mentioned above, we study this model in two dimensions. We believe that this choice is not important for our analysis of force balance at a given cross-linked node in the network. Dimensionality is important when discussing the isostaticity condition in the network [170, 114, 82]. It is also likely to be important in its effect on how branching force chains interact with each other. In three dimensions, we expect them to more rarely intersect than in two. We briefly comment on these points in the conclusions.

The mechanics of each filament is controlled by its bending rigidity κ and its longitudinal modulus μ. In thermalized networks of effectively inextensible filaments, these two elastic constants are actually connected. The filaments bend and therefore contract under thermal fluctuations, leading to an entropic effective longitudinal spring constant $k_{entropic} \sim \kappa^2/(k_B T \ell^3)$ [107]. Here we treat the longitudinal compliance μ as a simple phenomenological constant. For a large number of regular filament networks, one can compute the collective elastic constants in terms of these filament-level elastic quantities [112, 113], as well as for random elastic gels [107].

The Hamiltonian density for a filament segment (directed along $\hat{x}$ axis) spanning two cross linked sites on that filament is given by

$$\frac{\delta \mathcal{H}}{\delta s} = \frac{\mu}{2}\left(\frac{\delta \ell}{\delta s}\right)^2 + \frac{\kappa}{2}\left(\frac{\delta \theta}{\delta s}\right)^2, \tag{5.2}$$

where $\delta\ell(s)$ is the extensional deformation of the filament as a function of arclength s, and $\delta\theta(s)$ the change in angle of local filament tangent with respect to the x-axis. In the presence of an applied force f, a length scale $\sqrt{\kappa/f}$ emerges in the system, which may be relevant at high forces. In the absence of applied force the system admits an inherent length scale:

$$\ell_{\text{bend}} = \sqrt{\kappa/\mu}, \tag{5.3}$$

governing the competition between bending and stretching in the network. The length ℓ_{bend} sets a tension absorption length, to be confirmed later. Incidentally, ℓ_{bend} also represents the crossover length for ensemble-averaged semiflexible networks to shift from non-affine to affine elasticity [66, 65]. The lowest energy modes of the mikado model involve filament bending. In one limit where this bending energy is taken to be zero, these result in so-called *floppy modes* [69], or zero-energy deformations of the network.

Force propagation within the network depends strongly on the boundary conditions imposed at the ends of the filaments. To illustrate this point, consider a situation where, in the undeformed state, the central filament (along the x axis) is crossed by a number of filaments normal to that central filament. If one were to pull on the left end of the central inextensible filament, while leaving the right end free, one would expect that the displacement of the network would resemble a sort of "bow and arrow" configuration, in which each crossing filament bends and that bending transfers the tensile loading on the central filament to these crossing ones. The displacements of each of these cross-linked points would be equal but nonzero. On the other hand, if one were to pin the right end of the central filament, these displacement would all vanish and the tensile load would be perfectly transmitted along the central filament. Another way that the connection to the boundary can play a role is in the excitation of topologically protected surface modes of the network [191]. We do not consider such surface states here. In our calculations, we assume that the filament is not directly pinned to the boundary, except where explicitly noted. As long as the tension applied to the filament in question has been transferred to the rest of the network before coupling to the boundary, we expect that the effect of the boundary condition should be small.

5.3.1 Self-consistent theory of tension propagation within linear response

We begin by treating the filaments as linear elastic elements, but accounting for their different responses to longitudinal and bending deformation. The bending rigidity of the filaments eliminates the *floppy modes* of the network. We now apply a tension τ along a particular filament within the network at an arbitrary point of the filament.

The point where this force is applied is displaced by Δx along the $\hat{x}$ axis. In the following, we use a self-consistent approach to compute the collective linear response of the network to this force by computing

$$k_{\parallel} = \frac{\tau}{\Delta x}. \tag{5.4}$$

The self-consistency condition is invoked by demanding that the effective spring constant of the particular filament to which we apply the force, called the *central* filament hereafter, is equal to the one of all other filaments cross-linked to it. The validity of this approximation rests on the assumption that the tension in the crossing filaments are all selected from the same distribution, and that there are no correlations in those tensions. The former seems reasonable for a statistically homogeneous network. The latter is not obviously valid, especially if there are a large number of closed paths, or loops, in the network along which tensions may propagate. Thus, we do not expect the self-consistent approach to remain valid for the case of regular lattices, where such loops abound.

Now, we consider force balance at one node on the central filament labeled i – see Fig. 5.9. As shown in the inset of that figure, there are six forces acting on the node on the central filament, shown in blue and green. We treat these forces as being linearly related to the displacements of the nodes. Specifically, the longitudinal springs associated with the extension of the crossing filaments (shown in black) have an effective Hookean spring constant $k_{\parallel}$, which takes into account both the longitudinal compliance of that filament and the displacement of other nodes in the network. This spring constant will be determined self-consistently in the following calculation. This Hookean spring generates the forces $T_i^{\times}$ and $\tilde{T}_i^{\times}$ shown in green in the inset of Fig. 5.9.

In addition to this force, there is a force associated with the bending of the filament crossing the central one at node i. This spring constant, $k_\perp \sim \kappa/\ell_c^3$, is proportional to the bending modulus of the filaments and inversely proportional to the distance between consecutive cross links along a given filament, ℓ_c [187]. The movement of the neighboring nodes can be taken into account by a diminishing of this constant: $k_\perp \to \epsilon k_\perp$ for $0 < \epsilon < 1$. This bending spring generates the force $F_i^\times$ (shown in blue). The central filament may also bend, generating a displacement of node i in the vertical direction Δy_i. Using the same $k_\perp$, this produces the force $F_i^c = k_\perp \Delta y_i$. We expect that the bending modulus of the central filament will not be affected by the motion of the surrounding nodes, so that $k_\perp > \epsilon k_\perp$ is fixed.

We now apply tension T_i^c to the filament segment to the left of the node and in the left direction. Writing down the force-balance conditions along the X and Y axes, we obtain:

$$-T_i^c + T_{i+1}^c + (\tilde{T}_i^\times - T_i^\times)\cos\theta_i + F_i^\times \sin\theta_i = 0, \tag{5.5}$$

$$(T_i^\times - \tilde{T}_i^\times)\sin\theta_i - F_i^\times \cos\theta_i - F_i^c = 0. \tag{5.6}$$

The forces, written in terms of displacements of node i, are given by:

$$F_i^c = -k_\perp \Delta y_i, \tag{5.7}$$

$$\tilde{T}_i^\times - T_i^\times = -k_\parallel(\Delta x_i \cos\theta_i - \Delta y_i \sin\theta_i), \tag{5.8}$$

$$F_i^\times = -\epsilon k_\perp(\Delta x_i \sin\theta_i + \Delta y_i \cos\theta_i). \tag{5.9}$$

After some algebra we obtain

$$T_i^c - T_{i+1}^c = \frac{\epsilon k_\parallel k_\perp + (k_\parallel \cos^2\theta_i + \epsilon k_\perp \sin^2\theta_i)k_\perp}{(k_\parallel \sin^2\theta_i + \epsilon k_\perp \cos^2\theta_i + k_\perp)}\Delta x_i. \tag{5.10}$$

To connect the displacements of the i^{th} and $(i+1)^{th}$ nodes (counting to the left), we include the Hookean extensibility of the central filament segment between these

nodes to write

$$T_i^c = k_s(\Delta x_{i-1} - \Delta x_i). \tag{5.11}$$

For many biopolymers, at low forces the longitudinal compliance is dominated by the pulling out of thermally generated undulatory modes. In that case, the Hookean spring constant introduced above in Eq. 5.11 can be related to the bending modulus and temperature via $k_s = 6\kappa^2/k_{\mathrm{B}}T\ell_c^4$ [107]. However, nothing in the following analysis requires this, and the calculation applies equally well to athermal systems. We solve Eqs. 5.10 and 5.11 numerically to find the self-consistent solution for $k_{\|}(k_s)$.

This solution is shown in Fig. 5.10, where we plot the effective longitudinal response $k_{\|}$ of the network as a function of the segment longitudinal spring for different numbers of cross links N and for pinned (solid) and free (dashed) boundary conditions. Both spring constants are scaled by the underlying bending spring constant of the network $k_{\perp}$. On the log-log plot, we observe that for small longitudinal spring constants, the collective longitudinal spring constant of the network grows $\sim k_s^{3/4}$. In this region the behavior of $k_{\|}$ does not depend on the number of cross links or the boundary conditions on the filament. For larger k_s we observe the transition of $k_{\|}$ to a plateau for free end boundary condition. There is linear growth in the case of a pinned end boundary condition. This transition occurs at a characteristic spring constant that depends on the number N of crossing filaments, as shown in Fig. 5.10.

In addition to this numerical solution of the self-consistent equations, there are two particular cases that admit a straight-forward analytic solution. It is instructive to look at them to directly observe in detail how tension propagates along the central filament. The first case applies to perfectly inextensible filaments, $k_s \to \infty$. The

second is a scale-free solution, *i.e.*, one that is independent of the total number of filaments cross linked to the central one, N. We refer to this solution as a critical point. The case of the inextensible filament leads to a constant $\Delta x_i = \Delta x$ for all i. Summing Eq. 5.10 for all i we obtain

$$T_0^c - T_N^c = \Delta x \sum_{i=1}^{N} \frac{\epsilon k_\parallel k_\perp + (k_\parallel \cos^2\theta_i + \epsilon k_\perp \sin^2\theta_i)k_\perp}{(k_\parallel \sin^2\theta_i + \epsilon k_\perp \cos^2\theta_i + k_\perp)}. \tag{5.12}$$

Imposing self-consistency for $k_\parallel$ forces that spring constant to satisfy

$$k_\parallel = \left\langle \sum_{i=1}^{N} \frac{\epsilon k_\parallel k_\perp + (k_\parallel \cos^2\theta_i + \epsilon k_\perp \sin^2\theta_i)k_\perp}{(k_\parallel \sin^2\theta_i + \epsilon k_\perp \cos^2\theta_i + k_\perp)} \right\rangle. \tag{5.13}$$

Note that the random angle θ_i at each node is assumed to be uncorrelated with the other angles , so each average is independent of the others. Thus, we find

$$k_\parallel = \frac{N}{2\pi} \int_0^{2\pi} d\theta \frac{\epsilon k_\perp k_\parallel + k_\perp(k_\parallel \cos^2\theta + \epsilon k_\perp \sin^2\theta)}{k_\parallel \sin^2\theta + \epsilon k_\perp \cos^2\theta + k_\perp}. \tag{5.14}$$

After performing the integral and solving the self-consistent equation we obtain

$$\begin{aligned} k_\parallel &= \frac{1}{2}\left(-2k_\perp N + k_\perp N^2 + \epsilon k_\perp N^2\right) \\ &+ \frac{1}{2}\left(\sqrt{(2k_\perp N - k_\perp N^2 - \epsilon k_\perp N^2)^2 + 4N^2 \epsilon k_\perp k_\perp}\right). \end{aligned} \tag{5.15}$$

In the limit of large N, this simplifies to

$$k_\parallel = (k_\perp + \epsilon k_\perp)N^2. \tag{5.16}$$

The effective spring constant is proportional to N^2.

The other case that allows for an analytical solution results from the assumption that the displacements decay exponentially from node to node, *i.e.*, $\Delta x_{i+1} =$

$(1/q)\Delta x_i$ for all i and for $q > 1$. Substituting this ansatz into Eqs. 5.10, 5.11 gives, after some algebra,

$$(q-1) - \left(1 - \frac{1}{q}\right) = \frac{1}{k_s} \frac{\epsilon k_\perp k_\parallel + k_\perp (k_\parallel \cos^2\theta_i + \epsilon k_\perp \sin^2\theta_i)}{k_\parallel \sin^2\theta_i + \epsilon k_\perp \cos^2\theta_i + k_\perp}. \tag{5.17}$$

This is consistent with our assumptions if, and only if, the right hand side of the above equation is also independent of i. This requires that the dependence on the random angles θ_i vanishes. The necessary condition for this is $\epsilon k_\perp = k_\parallel$, which leads to:

$$q^2 - \left(2 + \epsilon \frac{k_\perp}{k_s}\right) q + 1 = 0. \tag{5.18}$$

The solution of this quadratic equation defines the allowed values of q consistent with our assumption of an exponential decay of displacements and the spring constant relation $k_\parallel = \epsilon k_\perp$. Depending whether we apply tension (a) between nodes or (b) directly on the node, we get (a) $k_\parallel = T_0^c/\Delta x_1$, or (b) $k_\parallel = T_1^c/\Delta x_N$. Thus, in the first case (a)

$$k_\parallel^{(a)} = k_s \left(1 - \frac{1}{q}\right), \tag{5.19}$$

and in the second case (b)

$$k_\parallel^{(b)} = k_s (q-1). \tag{5.20}$$

We obtain two equations for roots of the polynomial $q_{1,2}$. One for case (a)

$$q_a^2 - \left[2 + \left(1 - \frac{1}{q_a}\right)\right] q_a + 1 = 0, \tag{5.21}$$

and one for case (b)

$$q_b^2 - (2 + q_b - 1)\, q_b + 1 = 0. \tag{5.22}$$

The first (a) gives us the roots

$$q_a = 1, 2. \tag{5.23}$$

The second (b) gives us a linear equation for q_b, having the single root

$$q_b = 1. \tag{5.24}$$

These roots are now independent of the number of crossing filaments, which means that the decay of tension and displacement along the central filament is independent of filament length at this critical point. This ansatz provides an analytic solution. To test whether that solution is unique, we can compare it to the results of our numerical solutions of Eqs. 5.10 and 5.11. We did not find other numerical solutions at or near the critical point that differed substantially from the analytic one. In fact, it appears that the exponential tension decay is a robust result in this region.

The solution $q = 1$ corresponds to the previously considered case of inextensible filaments, which have equal displacements at each node. The other solution, $q = 2$, is consistent with the assumed exponential decay of those displacements. At every node, the magnitude of the tension falls by a factor of 2, i.e., $T^c_{i+1} = T^c_i/2$. Substituting this tension relation into the force balance equation for the $\hat{x}$ direction, we obtain

$$(\tilde{T}^\times_i - T^\times_i)\cos\theta_i + F^\times_i \sin\theta_i = T^c_i/2, \tag{5.25}$$

which means that the tensile force exactly splits between the crossing filament and the central filament at each node.

5.4 Conclusions

Experiments on the force propagation between cells in a filamentous extra-cellular matrix suggest that forces are transmitted over long distances along particular pathways. This observation raises the question: do these force pathways arise naturally

in randomly structured filament networks, or does the ECM contain particular structural heterogeneities, such as system-spanning subnetworks of filament bundles, that prescribe these force-transmitting paths? In our work, we make a preliminary investigation of this question by addressing the first possibility.

Our simulations of random homogeneous and isotropic networks do indeed show weakly branching force chains over scales of many mesh sizes in the network. Based on the imperfect analogy between force propagation in filament networks and force chains in granular media, such structures are not entirely surprising. We believe that the high-force pathways observed in simulation are sufficiently similar to those seen in granular media, so as to warrant using the same terminology. The principle distinction between the two types of mechanical systems is that filament bending in the network provides (typically) highly compliant elastic degrees of freedom, which, in some sense, absorb the tensile loading on a highly tensed filament. In this way, filament-based force chains naturally terminate over some finite distance.

The simulations demonstrate that the point-force response of the network is highly heterogeneous. It depends on both the point of loading and the direction of that applied force. This is, again, in qualitative agreement with the results of active microrheology experiments in fibrin gels. In particular, we observe that the microscopic geometry of the network near the point of loading has a large effect on the collective point-force response of the system. Based on the numerical data presented here, we believe that the wide distribution of linear response observed in experiment is qualitatively consistent with our numerical results. In short, our distribution appears to be narrower than that seen in experiment. There may be multiple causes for this quantitative difference including necessarily smaller system sizes explored in our numerical work. An alternative potential cause is that the fibrin

networks used in experiment are more structurally heterogeneous on the microscale, either due to bundle formation, or simply length polydispersity.

We also show the expected asymmetry between pushing and pulling on a filament. This is evident in our simulations, which show force chains propagating only in the direction associated with tension (rather than compression) in the filaments. The importance of buckling in limiting the propagation of compressive loading is clear. This buckling-controlled case seems to correspond to the non-affine bending regime [67], where force chains were observed, while the linear case fits the affine-stretching regime [67] with more a homogeneous distribution. In our theoretical analysis of the collective mechanical response of the network, we treated the crossing filaments as linear elastic objects, but we did not include compressive loading of the filament to which the force was applied. In the self-consistent analysis of the mechanical response functions, these imposition of the elastic nonlinearity affects the mechanical properties of the entire network through the self-consistently determined spring constants. In this way we partially included the elastic nonlinearity that is evident in the simulations. The semi-quantitative agreement of that simplified analysis with the simulation data suggests that improvements in handling the elastic nonlinearity of the filaments should be explored in future work.

The effect of this nonlinearity may be weakened in highly tensed networks, where the applied forces do not typically reach the threshold for Euler buckling. Such tensed networks may, in fact, behave more like continuum elastic solids with regard to their point-force response. We do not, as yet, have numerical data to test this supposition. The recent work on a strain-induced rigidity transition in disordered elastic networks and athermal filament networks without bending interactions [176, 158, 5, 6] points to the idea that, quite generally, loading may push the network towards elastic behavior

consistent with continuum elasticity. In addition, we observe in simulations that the collective point force response depends quite strongly on the direction of pulling with respect to the local filament tangent and that there appear to be two distinct types of response corresponding to a low-force regime and a high-force regime where the pulling changes the local structure of the network.

We also approached the problem of force propagation in the network through a simple analytic model of the system using harmonic springs (of two classes: bending and stretching) and rather simple assumptions of how forces propagate through the network (which are supported by simulation), *i.e.*, they do not form closed loops. By invoking self-consistency for the collective longitudinal compliance (which takes into account the motion of other nodes in the network) of the filament, we obtain an analytic prediction for the point-force response measured in our numerical experiments.

These calculations qualitatively agree with the simulated results in that they predict the decay of tension along the filament of force application due to those tensile forces being transmitted into a combination of bending and tensile loading on the filaments cross linked the filament of force application. In one analytically tractable limit, the self-consistent calculation predicts that tensions decay exponentially along the filament of force application. Numerical solutions away from this point suggest that the exponential behavior is more broadly applicable.

To quantitatively compare the predicted and observed tension decay lengths, we need to use parameters from the numerical simulations. Using the average filament segment length $\ell_c = 0.56\mu$m and filament rigidity $\kappa = 5.6 \times 10^{-2}pN\mu$m^2, and making the seemingly reasonable estimate of $k'_\perp = \kappa/\ell_c^3$, we obtain a value of ≈ 0.33pN/μm.

This value is much smaller than the average of $k'_{\perp} \approx 8.2\text{pN}/\mu\text{m}$ observed in the low-force regime of our simulations – see Fig. 5.2(D). If we also use the same analysis to determine $k'_{\parallel} \approx 3.4 \times 10^2 \text{pN}/\mu\text{m}$, we obtain a prediction for the tension decay length $\xi \sim 18\mu\text{m}$, which is an order of magnitude greater than the $\xi = 2.2\mu\text{m}$ observed for the lowest magnitude force simulation – see Fig. 5.8(A). There are, however, reasons to be skeptical of these approximations, particularly in the case of $k'_{\perp}$, since one expects the boundary conditions imposed on the other end of these crossing filaments to significantly change the estimates. Recognizing this, we instead can take our value of $k'_{\parallel}$ and $k'_{\perp}$ directly from the numerical data – see Fig. 5.2(C). We now obtain a much more reasonable prediction of $\xi \sim 0.9\mu\text{m}$. One might suggest that this discrepancy between the first estimate of the local bending spring constant and the measured one is attributable to prestress in the numerically simulated networks. If the filaments are under tension $T = 0.1\text{pN}$ (from the standard deviation of observed tensions in the equilibrated networks – see Fig. 5.5) then, $k_{\perp} = 4T/l_c \approx 1\text{pN}/\mu\text{m}$, but this alone is not sufficient. We suspect that the aforementioned uncertainties associated with the boundary conditions within the network have an important effect.

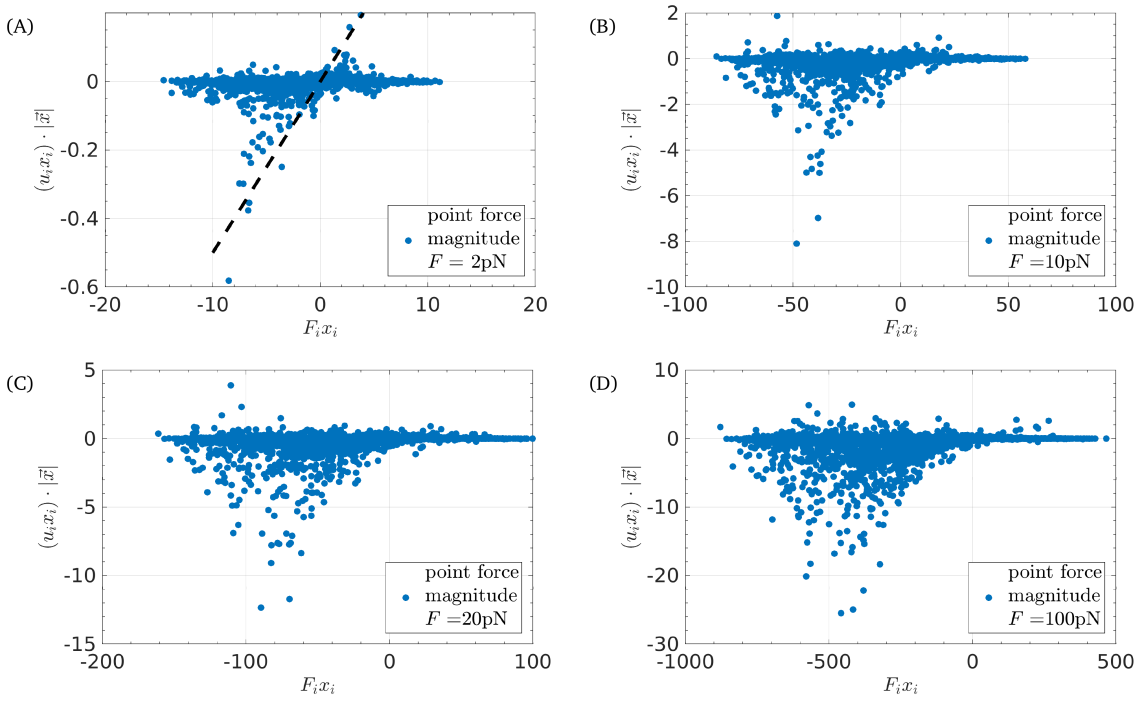

Figure 5.4: Scatter plots showing the correlation between the scalar products $(u_i x_i)$ and $(F_i x_i)$, where $\vec{F}$ denotes the applied point force vector acting at the origin and $\vec{u}$ and $\vec{x}$ denote the displacement and position vector of a particular point. The data contains approx. 2000 nodes in the filament network for one (axial) pulling experiment at a point force magnitude of (A) $F = 2$pN, (B) $F = 10$pN, (C) $F = 20$pN, and (D) $F = 100$pN.

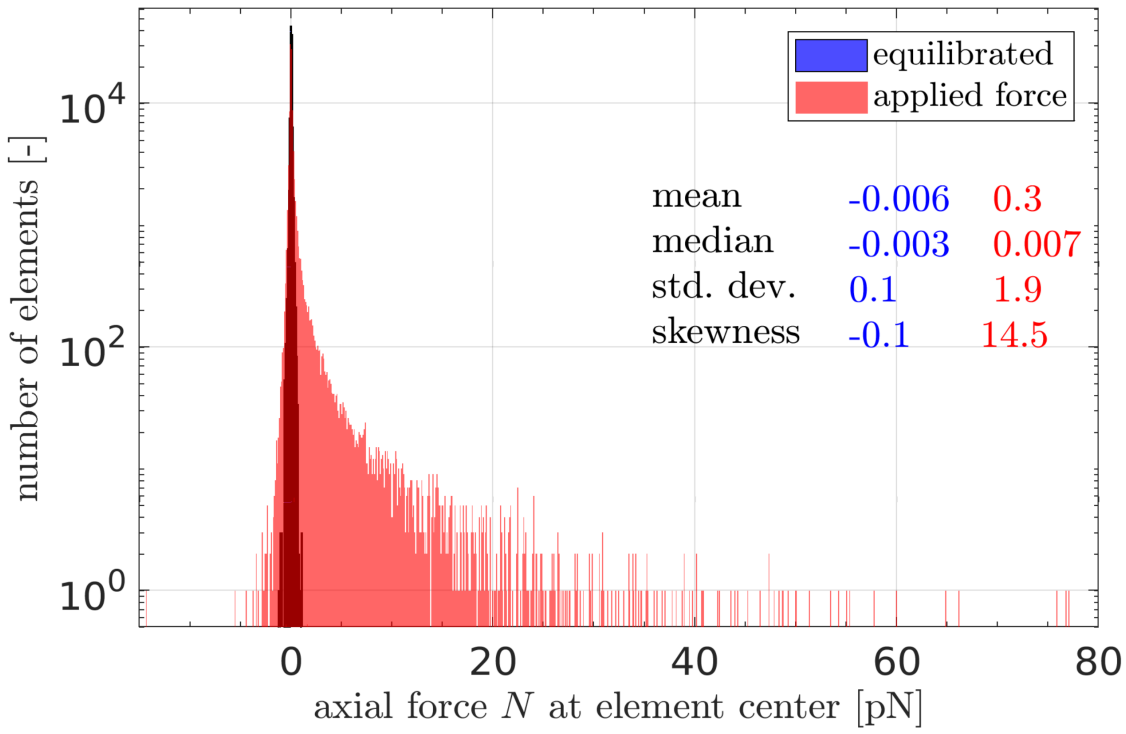

Figure 5.5: Histogram of axial forces at the element center in the entire network for 30 numerical pulling experiments and an applied point force magnitude of $F = 100$pN. Note the logarithmic scale on the vertical axis.

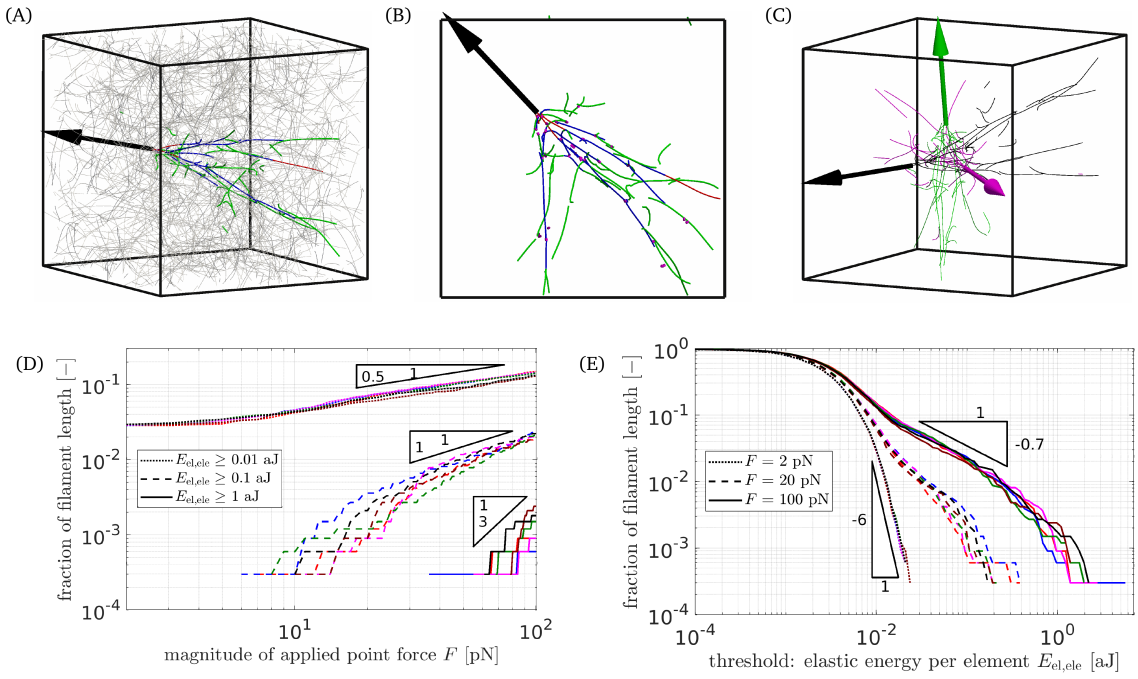

Figure 5.6: Analysis of force chains. (A) Force chains resulting for an elastic energy threshold (per finite element) of 0.75aJ (red), 0.25aJ (blue), and 0.075aJ (green) among all other filaments in the network (gray, thin lines). (B) Top view hiding all other filaments for clarity and showing also all cross links with a force magnitude above 8pN (pink). (C) Overlay of three different pulling directions and the resulting force chains (for an elastic energy threshold of 0.1aJ) in one color each. The simulation snapshots in (A)-(C) show the state for the highest considered point force magnitude $F = 100$pN. (D) Fraction of filament length exceeding a certain elastic energy threshold (per finite element) over the magnitude of the applied point force for three different threshold values. Colors indicate 6 different pulling experiments. (E) Fraction of filament length exceeding a certain elastic energy threshold (per finite element) over the threshold value for three different force magnitudes. Again, colors indicate 6 different pulling experiments.

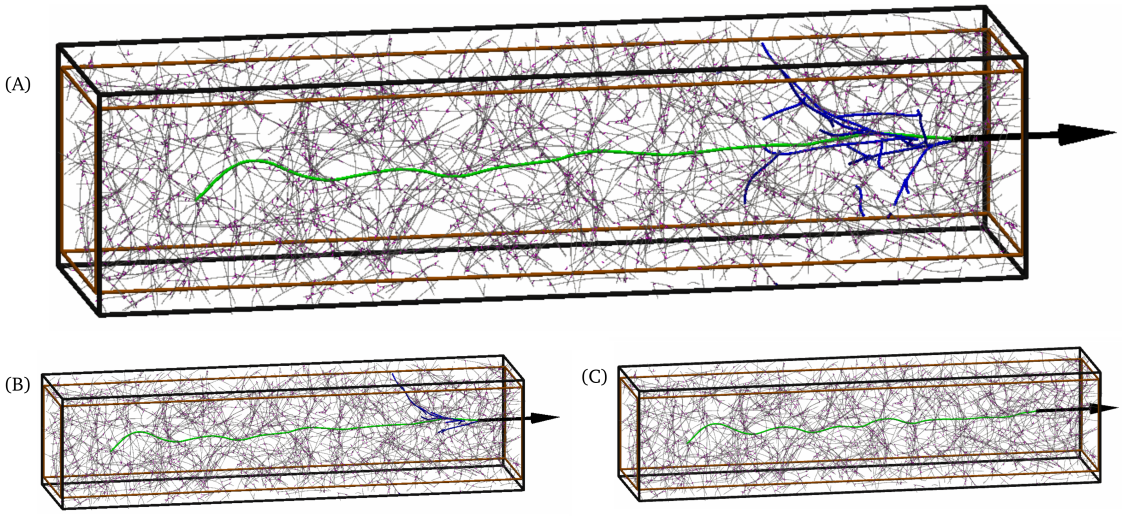

Figure 5.7: Simulation snapshots for an applied point force of magnitude (A) $F = 100$pN, (B) $F = 50$pN, or (C) $F = 2$pN. The central, long filament is highlighted in green in the middle of the network of all other filaments (thinner, gray lines) and cross links (pink). All filaments in the force chains for an elastic energy threshold (per finite element) $E_{\text{el,ele}} = 0.1$aJ are highlighted in blue. The black arrow indicates the applied point force and the thin shell outside the brown box represents the region where filaments are pinned.

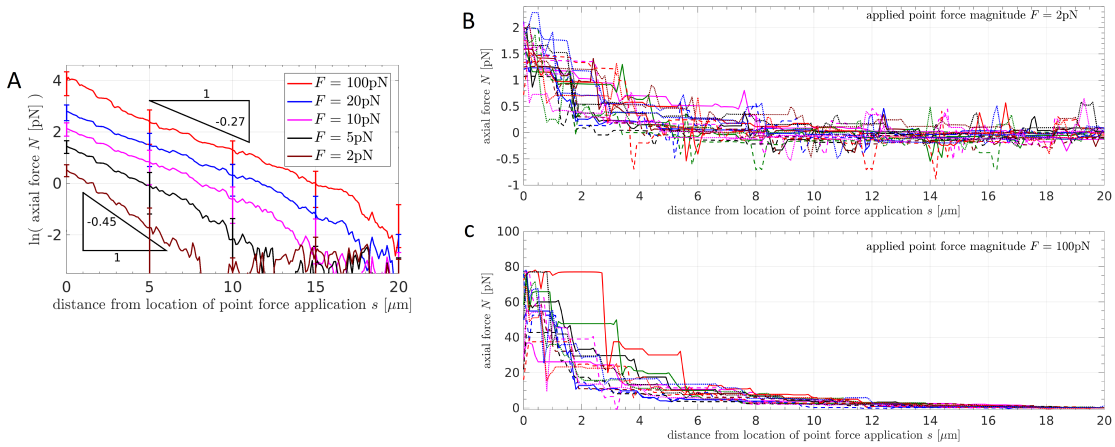

Figure 5.8: (A) Semi-logarithmic plot of the axial force N along the central filament for 5 different point force magnitudes F, using the average over 20 pulling experiments. The error bars indicate the standard deviation at five exemplarily chosen, equidistant points along the filament. The curves for all individual pulling experiments at a point force magnitude of $F = 2$pN and $F = 100$pN are shown in (B) and (C), respectively. Each pulling experiment is indicated by a different combination of color and line style. Performing a linear fit to the mean tension decay in (C), we obtain decay lengths $\xi = 2.24, 2.99, 3.55, 3.80,$ and 3.67μm, in order of increasing applied force.

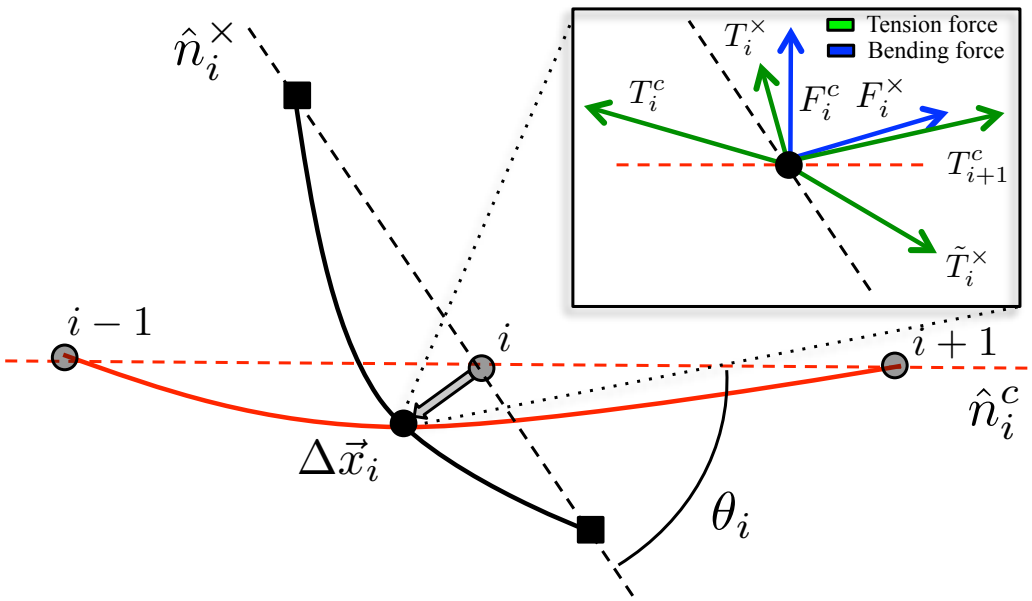

Figure 5.9: Schematic representation of forces and displacements at a single node. The central filament (deformed, red; undeformed, dashed), pointing in the $\hat{n}_i^c$ direction, is aligned along the x-axis. The crossing filament (black), in the direction $\hat{n}_i^{\times}$ makes an angle θ_i with the central filament. The network is pulled in the $-\hat{x}$ direction, leading to two incoming tensions T_i^c and $T_i^{\times}$, and two outgoing tensions T_{i+1}^c, $\tilde{T}_i^{\times}$ at node i (see inset). In the self-consistent model of sec. 5.3.1, displacements (wide gray arrow) $\Delta\vec{x}_i$ are with respect to the undeformed state. We show in the inset the free-body diagram of forces at node i including the effects of tensions T (green) and bending F (blue) associated with the semiflexible filaments.

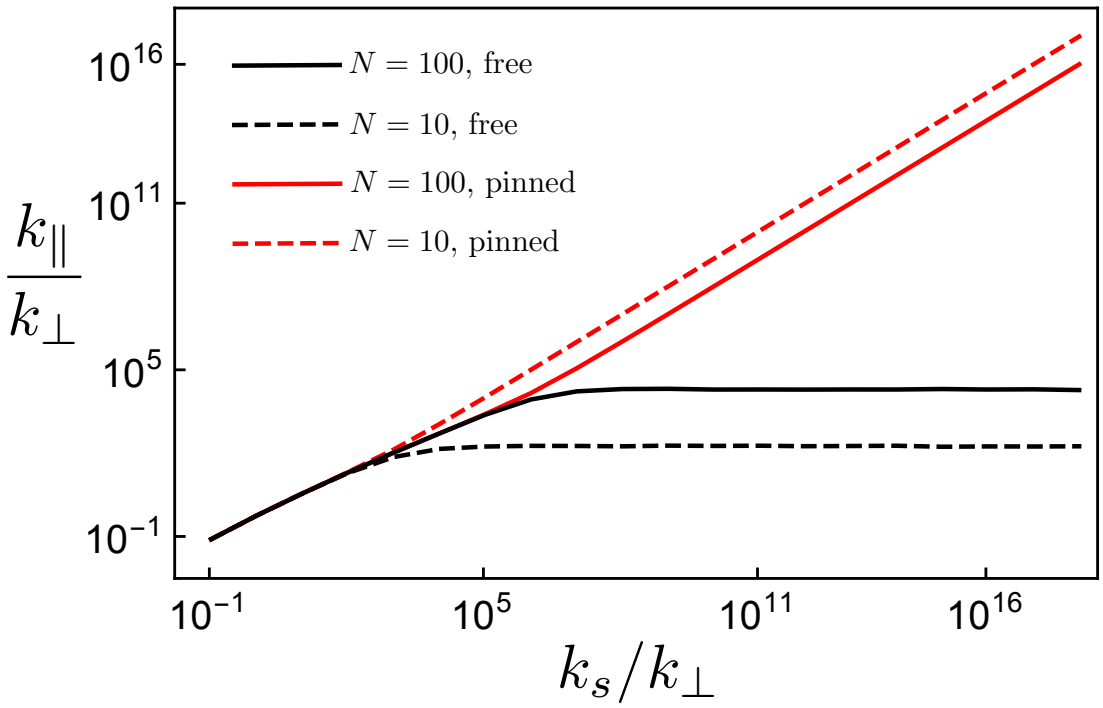

Figure 5.10: Numerical solution of the self-consistent Eqs. 5.10 and 5.11 for both free (black) and pinned (red) boundary conditions, for a total number of crossing filaments $N = 100$ (solid curves) and $N = 10$ (dashed curves). We set $\epsilon = 1$. For small longitudinal spring constants k_s the behavior of $k_{\|}$ is independent of the number of cross links N and the boundary conditions. The transition to a regime where boundary condition affect the result occurs at higher k_s for larger N.

CHAPTER 6

The conformation of a semiflexible filament in a quenched random potential

6.1 Introduction

Semiflexible polymer networks are well known to trap *prestress* in their formation. Cross linking molecules typically lock-in curved and thus elastically stressed states of the filaments. As a consequence of this being an out of equilibrium process, the cross linkers may, however, trap more thermal energy – $k_{\mathrm{B}}T$ – per bending mode. The result is that cross-linking during network formation typically traps excess free energy, which then slowly bleeds out of the system. That relaxation process appears to lead to large, nonequilibrium stress fluctuations, and is associated with the glassy power-law rheology of the network at very low frequencies. Such low-frequency power-law rheology has been observed in both simulation [127] and experiment [14]. Living cells are similarly observed to have soft, glassy, power-law rheology [169], albeit with a distinctly different power law exponent [100, 19]. The large nonequilibrium stress fluctuations have currently been observed solely in simulation and we suggest that they should make an intriguing target for future experiments.

The underlying dynamics of transiently cross linked semiflexible networks is likely to be fundamental to the mechanics of both the active biological and passive *in vitro* systems. Simulations suggest that both the stress fluctuations and this characteristic power-law rheology of transiently cross linked networks are associated with the reorganization of progressively larger sections of the network occurring on progressively longer time scales. Understanding these dynamics presents a theoretical challenge.

In an effort to better understand the excess free energy trapped in such networks, we consider the problem of a single semiflexible filament at temperature T interacting with a quenched random potential. We hope that, in this single filament model, the quenched pinning potential mimics the effect of random cross linking sites that mechanically couple the filament in question to the surrounding network. In particular, we will examine the role of spatial correlations in the pinning potential, which, at least loosely speaking, introduces an effective mesh size of the surrounding network. We analyze the disordered-averaged conformational fluctuations of the filament and the elastic energy stored in the system as a function of persistence length of the filament and the correlation length of the potential. We compare these predictions to the results of large-scale finite element Brownian dynamics simulations of such a semiflexible filament in a random potential.

The study of the statistical mechanics of a single stiff filament in a random potential recalls a number of related systems in which a low-dimensional elastic object interacts with a quenched pinning potential. Examples include disorder-pinned domain walls between symmetry-equivalent ground states [97], vortex lines in superconductors [115, 73, 42], and the three-phase contact line associated with the spreading of fluids as they wet a disordered substrate [130, 153]. The key distinction between these systems and the one of current interest is the presence of a bending

term in the elastic Hamiltonian of the filament. In cases where this term dominates the statistical weights of various filament conformations, *i.e.*, when filament tension is sufficiently small or when examining bends on short enough lengths, we expect to obtain results distinct from those obtained for these previously studied systems.

A filament interacting with a quenched random potential can be characterized by three lengths: the filament length L_0, the thermal persistence length $\ell_{\rm P}$, and the correlation length ξ of the potential. We will focus on the case of stiff filaments (although we introduce alternatives) in which the persistence length is typically longer than that of the filament itself: $L_0 < \ell_{\rm P}$. In this case, there are still two distinct limits. One might imagine that either $\ell_{\rm P} \ll \xi$, in which case the filament should be flexible enough to follow the twists and turns of the local minima of the random potential. Alternatively one may consider the case where $\ell_{\rm P} \gg \xi$ and the filament is so stiff that the elastic energy cost for following the valleys of the potential becomes prohibitive.

Similarly, the problem is endowed with two energy scales: the thermal energy T (we work in units where Boltzmann's constant is set equal to unity) and the typical energy scale of the pinning potential V_0. The potential has dimensions of energy per length. The inverse length scale $\nu = V_0/T$ must control the states of the filament, allowing one to examine both "strongly pinned" on scales where $L_0\nu \gg 1$ versus "weakly pinned" $L_0\nu \ll 1$ cases. The former is more interesting for the system under consideration.

There are two quantities that will provide insight into the ensemble of filament configurations. These are the effective persistence length of a filament in the pinning potential. This length differs from the usual tangent vector correlation length of

the filament due to its interaction with the pinning potential. It also provides a clear target for experimental studies of labeled filaments in networks. The effect of this extra filament bending imposed by the pinning potential (or the network in experiment) is that the filaments store excess elastic energy. We propose that this excess free energy is a prediction for the prestress in networks. The single filament model thus makes two predictions for nonequilibrium networks.

The remainder of this chapter is organized as follows. In section 6.2 we describe the filament Hamiltonian. We then provide in section 6.3 an analytical calculation of the averaged free energy of the filament in the strong-pinning limit of a random potential, described above. We start with the case of the completely flexible filament, i.e., the filament without bending energy, and then move forward to the more general case of the semiflexible filament. We then turn in section 6.5 to numerical simulations of the system using finite element Brownian dynamics of a geometrically exact Simo-Reissner beam model. We then summarize our results and their implications for pre-stress in networks in section 6.6, where we conclude with a proposal for new experiments. Finally, we provide an appendix addressing the applicability of the replica method to the problem explaining that it provides unphysical results for many of the measurable quantities.

6.2 The model

We consider a filament in two dimensions that is anchored at both ends. We introduce a coordinate system in which these anchoring sites are at positions $(0, 0)$ and $(L_0, 0)$ respectively. The anchoring sites are assumed to be able to generate arbitrary constraint forces necessary to hold the filament at these points, but to provide no

constraint torques. The directed filament is further assumed to be free of overhangs, allowing its configuration to be described by a function $y(x)$. A representation for a numerical simulation (to be described in section 6.5) of a few filaments (green lines) interacting with the potential (heat map) is shown in Fig. 6.1. We will allow the arclength of the filament between these two anchoring points to vary. In short, the anchoring points are reservoirs of extra length. A simple mechanical model of this situation can be thought of as follows. The filament fluctuates on a table whose height topography in a uniform gravitation field gives the pinning potential. The anchoring points may be thought of as holes in this table through which more filament may enter or exit the table's surface. Weights may also be added below the table to enforce a fixed tension on the filament. We should notice that for the simulation we use a slightly different model, with one end fixed and the other free to move in one direction (see section 6.5). We assume that for the small conformation the difference between these two models is negligible.

In the small bending limit ($\frac{dy}{dx} \ll 1$), which should be valid for filaments much shorter than their persistence length, we can write the filament's energy functional as

$$E[y(x)] = \int_0^{L_0} dx \left\{ \frac{1}{2}\kappa \ddot{y}^2 + \frac{1}{2}\tau \dot{y}^2 + V\left(x, y\left(x\right)\right) \right\}, \tag{6.1}$$

where κ is the filament's bending modulus defining a thermal persistence length $\ell_{\mathrm{P}} = \kappa/T$. τ is the tension imposed on the filament. $V(x, y)$ is the quenched random potential (with dimensions of energy per length), described in more detail below. We have introduced the notation $\dot{y} = \frac{dy}{dx}$. Then the classical partition function for such a filament at temperature $T = 1/\beta$ is given by the path integral over all trajectories

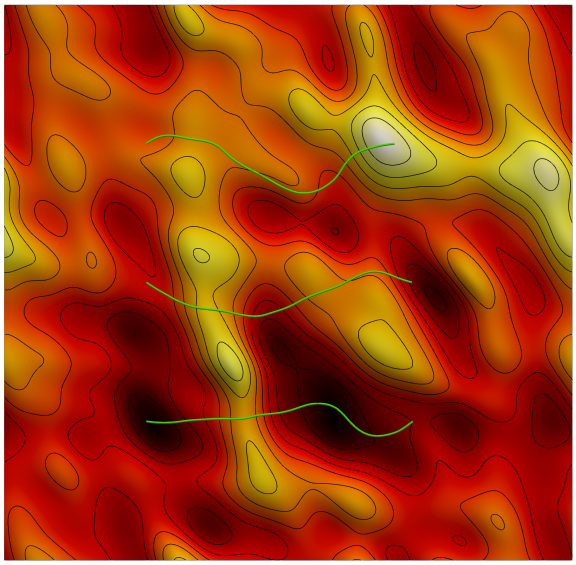

Figure 6.1: (color online) Three tensed filaments interacting with the pinning potential, shown as a heat map with brighter colors representing higher potential energies. The lowest filament traverses a saddle between local potential maxima. On the right of that saddle point it curves into a deep potential minimum (dark). Similar features may be seen in the other filaments. This is a snapshot from our Brownian dynamics simulations, discussed in section 6.5.

of the filament weighted by a Boltzmann factor obtained from Eq. 6.1:

$$Z = \int \mathcal{D}y(x)\, e^{-\beta E[y(x)]}. \tag{6.2}$$

We will later consider averages of the free energy, obtained from Eq. 6.2 in the usual way: $F = -T \ln Z$, over an ensemble of random potentials.

Turning to the pinning potential, we can consider two rather simple forms for its probability distribution that allow for a finite spatial correlation length, but do not break rotational invariance. The first is inspired by the massive scalar field Lagrangian

$$\mathcal{P}_{\mathrm{V}}(V) = \frac{1}{P_0} \exp\left\{ -\frac{1}{2V_0^2} \int d^2x \left[(\nabla V)^2 + \xi^{-2} V^2 \right] \right\}. \tag{6.3}$$

Here ξ sets the correlation length and V_0 the energy scale of the potential. It is straightforward to see that this model generates an ensemble of random potentials in which the amplitude of each Fourier mode is selected as an independent Gaussian random variable from a distribution with zero mean and a width that depends on the magnitude of the wavenumber $k = |\mathbf{k}|$.

We may also consider a related problem in which the correlation length is assigned to the force rather than to the potential. Since the force is the (negative) derivative of the potential, one can obtain the necessary Gaussian probability distribution for force by introducing another derivative in Eq. 6.3. We obtain

$$\mathcal{P}_{\mathrm{F}}(V) \sim \exp\left[-\frac{1}{2V_0^2} \int d^2x\, \xi^2 (\nabla^2 V)^2 + (\nabla V)^2 \right]. \tag{6.4}$$

The first version of the potential in which the Fourier amplitudes of the scalar potential are Gaussian distributed generates quite large pinning forces at short correlation lengths since the slope of the potential is V_0/ξ. We speculate that the second version of the potential in which the spectrum of *pinning forces* on the filament is

Gaussian distributed is a better approximation of the physical problem since one may then manipulate the correlation length of the potential (which is our approximation to the mesh size of a filament network) without changing the scale of forces to which the filament is subjected. We return to this point in our discussion. Hereafter we refer to the first type of random potential as the *energy controlled* distribution while the second will be called the *force controlled* distribution.

These distributions can also be expressed in terms of a probability distribution for the Fourier components of the potentials. Working in terms of those Fourier modes, we can also introduce another distribution with an exponential suppression of the higher Fourier modes:

$$P(V_{k_x,k_y}) \propto \exp\left\{-\frac{L_x L_y}{\xi^2}\frac{V_{k_x,k_y}^2}{8V_0^2}\exp\left(\xi^2(k_x^2+k_y^2)\right)\right\}, \tag{6.5}$$

where the rectangular system has an area $A = L_x L_y$. This particular form of the random potential is not convenient for analytic calculations, but generates more numerically stable simulations. See Fig. 6.2 for examples of random potentials selected from these distributions. The pinning forces generated from these potentials are shown in Fig. 6.3. The energy controlled potential produces a complex force landscape with very short ranged correlations. We do not reproduce that vector field here.

6.3 The Valley Approximation

There is a considerable simplification to be found if we assume that $L\nu \gg 1$. In this strong pinning limit, the ensemble of filament configurations is dominated by states where the filament is confined to the valleys of the pinning potential. We indeed

observe this in simulations. There we also see instances in which filament crosses from one valley to another over a saddle point of the potential. We will address escapes from one valley to the next over saddle points later. Excluding such saddle points for now, we assume that the potential is roughly constant along the bottom of the valley and that the curvature of the potential in the direction orthogonal to the path along the valley floor is also constant. Thus, the local form of the pinning potential is given by

$$V(x,y) = \frac{\tilde{k}}{2}\left[y - y_0(x)\right]^2 . \tag{6.6}$$

We have introduced a curvature (spring constant) scale $\tilde{k} = \frac{V_0}{\xi^2}$. The path of the valley minimum $y_0(x)$ remains a random curve. To analyze the effect of the quenched distribution of such paths, we may either calculate physical quantities of interest for an arbitrary curve $y_0(x)$ and then average, or use the replica trick to handle the average over the potential simultaneously with the thermal averaging. The replica trick, however, provides unphysical results as we explain in appendix C.

6.3.1 Flexible filaments with the energy controlled distribution

We now explore the valley approximation first for a flexible polymer by setting $\kappa = 0$. We require a finite tension so the polymer's path can be considered to be nearly straight. In this limit the energy of the polymer in the random potential may be written as

$$\frac{E_{flexible}}{T} = \int_0^{L_0} dx \left\{ y(x)\mathcal{O}y(x) + ky(x)y_0(x) + \frac{ky_0^2(x)}{2} \right\}, \tag{6.7}$$

where we have scaled the parameters by temperature T: $m = \beta\tau$ and $k = \beta\tilde{k}$. We have also introduced the differential operator

$$\mathcal{O} = \frac{m}{2}\partial^2 + \frac{k}{2}. \tag{6.8}$$

The partition function is given by the integral

$$Z_{flexible} = \int \mathcal{D}y e^{-E_{flexible}[y(x)]}. \tag{6.9}$$

Calculating this partition sum is equivalent to performing the Euclidean path integral (with x being the time-like coordinate) for a quantum particle with a mass m in a harmonic potential with spring constant k. In the analogous quantum problem the effect of the pinning potential is to introduce a time-dependent force $-ky_0(x)$. Since the integral is Gaussian, we can obtain a closed form solution for the partition function for a particular path of the valley floor:

$$Z = \frac{1}{\sqrt{\det \mathcal{O}}} \exp\left[-\int_0^{L_0} dx \left(-\frac{k^2}{4} y_0(x)\mathcal{O}^{-1}y_0(x) + \frac{ky_0^2}{2}\right)\right]. \tag{6.10}$$

If we choose $y_0(x) = 0$ everywhere, Eq. 6.10 reduces to the partition function of an unforced oscillator. From this we obtain the prefactor, leading us to write

$$\frac{Z}{Z_{SHO}} = \exp\left[-\int_0^{L_0} dx \left(-\frac{k^2}{4} y_0(x)\mathcal{O}^{-1}y_0(x) + \frac{ky_0(x)^2}{2}\right)\right], \tag{6.11}$$

where Z_{SHO} is the well-known result for the simple harmonic oscillator [90]. It is then straightforward to compute the free energy F of the flexible chain in a particular realization of the random potential, the one whose valley follows the path $y_0(x)$. This free energy is given by

$$F = F_{SHO} + T\int_0^{L_0} dx \left(-\frac{k^2}{4} y_0(x)\mathcal{O}^{-1}y_0(x) + \frac{ky_0(x)^2}{2}\right). \tag{6.12}$$

We now average the free energy in Eq. 6.12 over a distribution of the paths of the valley floor that is consistent with our previous random potential distribution given by Eq. 6.3. To obtain this we weight the paths of the valley floor $y_0(x)$ by

$$\mathcal{P}\left[y_0(x)\right] \sim \exp\left[-\frac{1}{2\xi}\int_0^{L_0} dx \dot{y}_b^2\right] = e^{-\int_0^{L_0} y_0 \mathcal{G} y_0 dx}, \tag{6.13}$$

where differential operator

$$\mathcal{G} = -\frac{1}{2\xi}\partial^2 \tag{6.14}$$

incorporates the correlation length of the pinning potential ξ. This weight is analogous to the Euclidean path integral of a free particle. The distribution of quenched potentials determined by Eqs. 6.6 and 6.13 is not identical to that given by Eq. 6.3. But the statistical weight associated with valley floors of these potentials has the same spatial correlations as those valley floors determined by the original potential distribution in Eq. 6.3.

The averaging over the distribution of these valley floors we obtain a correction to the simple harmonic oscillator (SHO) free energy

$$[F] = F_{SHO} + \Delta F, \tag{6.15}$$

where

$$\Delta F = -\frac{Tk^2}{8}\mathrm{Tr}(\mathcal{O}^{-1}G^{-1}) + \frac{Tk}{4}\mathrm{Tr}G^{-1}. \tag{6.16}$$

Here and throughout this article, we use the squared brackets $[\cdot]$ to indicate averages with respect to the quenched random potential. The angled brackets $\langle\cdot\rangle$ represent thermal averages. We compute these traces by diagonalizing the two relevant operators – see appendix C.1. We find that for long filaments (see appendix A) the disorder-averaged free energy is

$$[F] = \frac{L_0\sqrt{V_0\tau}}{4}\left[1 + \frac{2T}{\xi\tau}\right]. \tag{6.17}$$

The correlation length of the quenched potential and the tension set a natural energy scale that controls the free energy correction. When that potential is sufficiently heterogeneous so that its valleys are quite tortuous on the scale of a Pincus blob [138] $\xi < T/\tau$, the pinning potential has a significant effect on the free energy. The result above – Eq. 6.17 – cannot be extended to arbitrarily small tensions $\tau \to 0$ since our assumption that $x(y)$ is a well-defined function breaks down. In effect our use of the Monge gauge fails to adequately represent the polymer's shape.

Finally, we compute the contribution to the length, as compared with the length of the filament in the absence of the pinning potential. We recall that the contour length of the filament

$$L = \int_0^{L_0} dx \sqrt{1 + \dot{y}^2} \approx L_0 + \frac{1}{2} \int_0^{L_0} dx \, \dot{y}^2. \tag{6.18}$$

where the Taylor expansion of the integrand is justified by the fact that the filament is nearly straight when under sufficient tension. The quantity of interest is thermal average $\langle L \rangle$. As the integrand is nonnegative, this average $\langle L \rangle$ is necessarily longer than the separation of the end points L_0. In fact, in the absence of a bending modulus (as assumed here), $\langle L \rangle$ is divergent; there is an infinite amount of contour length trapped in the high wavenumber modes of deformation. It is thus useful to define the change in the contour length of the polymer due to the quenched pinning potential. We introduce

$$\Delta L = [\langle L \rangle] - \langle L \rangle|_{V_0=0} \tag{6.19}$$

as the difference between the thermal average of the filament's contour length when averaged again over ensemble of pinning potentials at fixed V_0 and ξ and the same quantity with no pinning potential, *i.e.*, the problem obtained by setting $V_0 = 0$.

This difference remains finite. We find that

$$\frac{\Delta L}{L_0} = \frac{1}{8}\sqrt{\frac{V_0}{\tau}}\left[1 - \frac{2T}{\tau\xi}\right]. \tag{6.20}$$

Once again we see that the corrections due to the pinning potential enter through the dimensionless ratio of the Pincus blob length to the correlation length of the potential. The negative sign in Eq. 6.20 may appear to be counterintuitive. One might imagine that a shorter correlation length would, in fact, create more transverse undulations in the filament as it tries to follow the more sinuous potential minimum. A shorter correlation length ξ would then be expected to increase ΔL. It does not. The tensed *flexible* polymer has large undulations on length scales below that of the Pincus blob. The effect of a decreasing potential correlation length at fixed V_0 is to increase the curvature of the potential, making the harmonic constraint forces on the filament stronger. These larger forces straighten out the filament on scales below the Pincus blob length, *decreasing* ΔL by straightening it out on these small scales.

The first term in Eq. 6.20 increases the ΔL of the filament with increasing potential (or decreasing τ). This reflects the expected effect of the potential. In a stronger potential the filament is forced to follow more precisely the tortuous valley of the potential minimum and thereby use more arclength. We return to this idea in the case of semiflexible filaments. From this analysis, we see that one may wish to consider an ensemble of random potentials for which the typical scale of the pinning forces remains fixed even as the correlation length is changed.

6.3.2 Semiflexible filaments: energy controlled distribution

We now include the bending modulus in the filament Hamiltonian. Using the same valley-based approximation for the random potential, the energy of the *semiflexible*

filament takes the form

$$\frac{E}{T} = \int_0^{L_0} dx \left[\frac{\ell_{\rm P} \ddot{y}^2}{2} + \frac{m\dot{y}^2}{2} + \frac{k(y(x) - y_0(x))^2}{2} \right]. \tag{6.21}$$

We introduce $\ell_{\rm P} = \beta\kappa$, the normal thermal persistence length of the filament. The partition sum is then given by

$$Z = \int \mathcal{D}y(x) e^{-E/T}. \tag{6.22}$$

In Eq. 6.22 we restrict the paths by imposing boundary conditions such that the filament begins and ends at $x = 0, L_0$ respectively. Moreover, it starts and ends at zero tangent angle with respect to the mean direction (along the x axis): $\dot{y}(0) = \dot{y}(L_0) = 0$.

Following our previous procedure, we may formally integrate over all paths $y(x)$ by introducing the inverse of the differential operator

$$\mathcal{O}_\kappa = \frac{\ell_{\rm P}}{2}\partial^4 - \frac{m}{2}\partial^2 + \frac{k}{2} \tag{6.23}$$

and write the partition function as

$$Z = \frac{1}{\sqrt{\det \mathcal{O}_\kappa}} e^{-\int_0^{L_0} dx (-\frac{k^2}{4} y_0(x) \mathcal{O}_\kappa^{-1} y_0(x) + \frac{k y_0(x)^2}{2})}. \tag{6.24}$$

The prefactor in the above equation is the partition function of a modified harmonic oscillator (MHO), previously discussed in Ref. [89]. Leaving the details of that aside for the moment, we write free energy of the system as

$$F = F_{MHO} + T \int_0^{L_0} dx \left(-\frac{k^2}{4} y_0(x) \mathcal{O}_\kappa^{-1} y_0(x) + \frac{k y_0(x)^2}{2} \right). \tag{6.25}$$

We must now average this free energy over the ensemble of paths taken by the local potential minimum. We average over $y_0(x)$ in an ensemble where we weight

each such path by Eq. 6.13. Doing so, we obtain

$$[F] = F_{MHO} - \frac{Tk^2}{8}\mathrm{Tr}(\mathcal{O}_\kappa^{-1}G^{-1}) + \frac{Tk}{4}\mathrm{Tr}G^{-1}, \tag{6.26}$$

where G is defined by Eq. 6.14. Once again, we are required to compute the traces of the relevant operators, defined by Eqs. 6.14 and 6.23. The analogous exercise for the flexible filament was relegated to appendix C.1. We expand on that discussion for the case of semiflexible filaments here.

First we note that one can factor $\mathcal{O}_\kappa$ into two commuting operators

$$\mathcal{O}_\kappa = \frac{\ell_\mathrm{P}}{2}\left[\partial^2 - \omega_1^2\right]\left[\partial^2 - \omega_2^2\right], \tag{6.27}$$

where we have introduced the (potentially complex) frequencies:

$$\omega_{1,2}^2 = \frac{m}{2\ell_\mathrm{P}}\left[1 \pm \sqrt{1 - \frac{4\ell_\mathrm{P}k}{m^2}}\right]. \tag{6.28}$$

Expanding in a complete eigenbasis of the two operators those product make up $\mathcal{O}_\kappa$, we obtain a form of the disorder averaged free energy in terms of an infinite sum over the (discrete) eigenvalues of $\mathcal{O}_\kappa$ indexed by

$$z_n = n\pi/L_0, \tag{6.29}$$

where $n = 0, 1, \ldots$. The resulting free energy is

$$[F] = F_{MHO} - \frac{\xi k^2}{2\ell_\mathrm{P}}\sum_{n=0}^{\infty}\frac{1}{z_n^2}\frac{1}{(z_n^2+\omega_1^2)}\frac{1}{(z_n^2+\omega_2^2)} + \frac{\xi k}{2}\sum_{n=0}^{\infty}\frac{1}{z_n^2}. \tag{6.30}$$

The MHO free energy is given in the appendix C.2. If we take the limit of a vanishing bending modulus ($\ell_\mathrm{P} \to 0$), we find that $\omega_1 \to \infty$ and $\omega_2 \to \sqrt{k/m}$. This returns us to the previous calculated free energy (up to a constant) for the flexible

filament in the disordered potential – see appendix C.1. As the bending modulus increases from zero, the two frequencies become complex when $\ell_{\mathrm{P}} \geq m^2/4k$ – see Eq. 6.28 . The free energy, however, remains real since $\omega_{1,2}^2$ are complex conjugates.

Finally, we note that the product of fractions in the above summation can be broken up into a set of three independently convergent sums. This allows one to write the disorder-averaged free energy in terms of a sum of cotangents of $\omega_{1,2}^2 L_0$. We consider that solution in the limit of long and stiff filaments $\omega_{1,2} L_0 \gg 1$, obtaining a simple algebraic expression

$$[F] = F_{\mathrm{MHO}} + \frac{1}{2}\frac{kL_0}{2q}\frac{(\omega_2^2 + \omega_1\omega_2 + \omega_1^2)}{\omega_1\omega_2(\omega_1 + \omega_2)}. \tag{6.31}$$

Using Eq. 6.28, we reintroduce the original model parameters. That result is most succinctly expressed in terms of the dimensionless parameter

$$\phi = \sqrt{\ell_P \nu}\frac{T}{\xi\tau}. \tag{6.32}$$

In terms of ϕ we find the disorder-averaged free energy to be

$$[F] = F_{\mathrm{MHO}} + \frac{\sqrt{km}L_0}{4q}\frac{1+\phi}{\sqrt{1+2\phi}}. \tag{6.33}$$

Physically, we see that this dimensionless quantity ϕ is the ratio of the Pincus blob size to the correlation length (as was observed in the flexible polymer case) multiplied by a correction factor that incorporates the strength of the random potential. Specifically, we see that this correction factor is given by the square-root of the ratio of two length scales in the problem: the persistence length ℓ_P of the filament and the arclength of the filament $\nu^{-1} = T/V_0$ required for the potential energy of pinning to equal thermal energy. We may interpret the effect of a finite persistence length as extending the size of the underlying Pincus blobs. This result extends the

disorder-averaged free energy of a flexible polymer to the semiflexible regime, and may be compared to the previous result found in Eq. 6.17. The effect of the finite bending modulus enters in both the difference between F_{SHO} and F_{MHO} in the first term on the right hand side of Eq. 6.33 and in second term on the right hand side of the above equation, where the filament's bending modulus enters solely through the persistence length incorporated into the dimensionless parameter ϕ defined in Eq. 6.32.

We can now calculate the effect of the pinning potential on the length of the chain between the two pinning points. Following the same approach and using the same definitions as used for the flexible filament, we now find

$$\Delta L = L_{MHO} + \frac{\xi\sqrt{\frac{k}{m}}L_0}{8}\frac{1+3\phi}{(1+\phi)^{3/2}} \tag{6.34}$$

The pinning potential always increases the arclength, but its contribution becomes smaller as the filament's bending modulus is increased, *i.e.*, for larger ϕ. Using the result for the MHO and reintroducing the original model parameters, we write

$$\frac{\Delta L}{L_0} = \frac{T}{4\sqrt{\tau\kappa}}\left(\frac{1}{\sqrt{1+2\phi}} - 1\right) + \frac{1}{8}\sqrt{\frac{V_0}{\tau}}\frac{1+3\phi}{(1+\phi)^{3/2}}. \tag{6.35}$$

The first term in the above expression is proportional to the ratio of the Pincus blob size $\zeta = T/\tau$ to the *bending length* $\ell_b = \sqrt{\kappa/\tau}$, which sets the cross over length between a regime where tension dominates the statistical ensemble of filament configurations at longer lengths and the bending modulus at shorter lengths. The second term in the above expression is proportional to the ratio of the same Pincus blob size and the length scale set by the pinning potential $\nu^{-1} = T/V_0$. In the limit of very stiff filaments so that $\ell_P\nu \gg 1$ and $\phi \gg 1$ we see that the first term provides a negative change in length, as observed for the flexible polymer, but the

second term increases the filament arclength with a contribution $\sim \sqrt{\zeta\nu}\phi^{-1/2}$. The interpretation is similar to that given regarding the flexible polymer. The first term produces filament straightening as discussed there. The second term provides for the increase of the arclength due to the tortuosity of of the potential minima.

6.3.3 Semiflexible filaments: force controlled distribution

We now consider the semiflexible filament to be interacting with the smoother, force controlled distribution. The calculation proceeds in a manner analogous to the previous two sections. The key difference is that the differential operator appearing in the statistical weight of valley paths $\mathcal{G}$ is replaced by a new one accounting for the fact that the typical curves along bottom of the valleys of the potential now have their own persistence length. Thus the differential operator $\mathcal{G}$ is replaced by

$$\mathcal{G}_{\mathrm{F}} = \frac{\xi}{2}\partial^4 - \frac{1}{2\xi}\partial^2. \tag{6.36}$$

Following the methods outlined above, we arrive at an expression for the free energy of the filament in the quenched potential, written in terms of a sum over the eigenvalues of the differential operators $\mathcal{O}_\kappa$ and $\mathcal{G}_{\mathrm{F}}$. We find that the disorder-averaged free energy is given by

$$[F] = F_{MHO} + \Delta F, \tag{6.37}$$

where the first term is the free energy of the modified harmonic oscillator, as discussed in appendix B. The second term is the correction due to complex geometry of the valleys of the potential. It is given by

$$\Delta F = \frac{Tk}{2\xi}\sum_{n=0}^{\infty}\frac{z_n^2+\omega_2^2+\omega_1^2}{\left(z_n^2+\Omega^2\right)\left(z_n^2+\omega_1^2\right)\left(z_n^2+\omega_2^2\right)}, \tag{6.38}$$

where $\Omega = 1/\xi$. The frequencies $\omega_{1,2}$ are defined in Eq. 6.28 and z_n is defined in Eq. 6.29. This result simplifies considerably when we examine the limit of very short or very long filaments. If the former case, where $\omega_{1,2}L_0 \ll 1$, only zeroth term survives and we get

$$\Delta F = \frac{Tk}{2\xi}\frac{\omega_2^2+\omega_1^2}{\Omega^2\omega_1^2\omega_2^2}. \tag{6.39}$$

In the latter case, where $\omega_{1,2}L_0 \gg 1$, we may change the summation to an integration over $z = \frac{\pi n}{L_0}$, obtaining

$$\Delta F = \frac{TkL_0}{2\xi\pi}\int_0^\infty dz \frac{z^2+\omega_2^2+\omega_1^2}{(z^2+\Omega^2)\,(z^2+\omega_1^2)\,(z^2+\omega_2^2)}. \tag{6.40}$$

The summation for the general case can also be performed, producing a quite lengthy expression that we do not reproduce here. Performing the integral in Eq. 6.40, we find

$$\Delta F = \frac{TkL_0}{4\xi}\frac{(\omega_1^2+\omega_2^2)(\omega_1+\omega_2)+\Omega(\omega_1^2+\omega_2^2+\omega_1\omega_2)}{\Omega\omega_1\omega_2(\omega_1+\omega_2)(\omega_1+\Omega)(\omega_2+\Omega)}. \tag{6.41}$$

We now wish to compute the average arclength of the filaments to observe the effect of the pinning potential upon their ensemble of conformations. This calculation involves taking the derivative of the free energy with respect to the tension, which is conjugate to the length. First, we write the free energy difference in terms of two auxiliary functions f and g whose argument is $r = m/\ell_{\rm P}$:

$$\Delta F = \frac{T\sqrt{k\ell_{\rm P}}L_0}{4}\frac{f(r)}{g(r)}, \tag{6.42}$$

where

$$f(r) = \Omega(r+s) + r\sqrt{r+2s} \tag{6.43}$$

$$g(r) = \sqrt{r+2s}(\Omega^2 + \Omega\sqrt{r+2s} + s) \tag{6.44}$$

and $s = \sqrt{\frac{k}{\ell_P}}$. Then taking the appropriate derivative, we compute the difference in excess arclength between the filament in the confining potential and the same filament without it

$$\Delta L = \Delta L_{MHO} + \frac{L_0}{4}\sqrt{\frac{k}{\ell_P}}\frac{f'(r)g(r) - g'(r)f(r)}{g^2(r)}. \tag{6.45}$$

The first term, which is the excess arclength of the semiflexible filament in a uniform harmonic potential, is calculated in appendix C.2.

We plot the ΔL versus applied tension in Fig. 6.4. There we see the decrease in excess arclength of the filament with increasing tension τ. There are two regimes characterized by a different power laws $\Delta L \sim \tau^a + \text{const}$ (there is a finite constant in the low tension regime) in the low and high tension regimes, referred to as *weak* and *strong* in the figure caption. In the weak tension regime, the filament is better able to track the valley of the potential minimum. As the applied tension is increased, the ensemble of filament configurations becomes restricted to straighter ones that cannot follow these valleys with high fidelity.

In comparing the theoretical calculation to the numerics, we freely adjusted the curvature and correlation length of the valley to obtain the fit.

6.4 Prestress and excess free energy of the pinned filament

From the results for the excess free energy, we have a prediction for the increase of the energy density of a network due to the effect of pinning. This enhancement of the energy density should be interpreted as the observed *pre-stress* found in biopolymer networks. Pre-stress can be considered to be stored in at least two separate manners. First, there should be excess bending and stretching energy of the filaments as they

are pinned by the network (represented by the quenched potential in our analysis) into configurations that store more than $T/2$ per bending mode – the amount of energy storage consistent with the equipartition theorem. Secondly, there may be excess energy stored in the strain associated with the cross links themselves. We cannot directly measure this quantity in our model. To obtain the excess energy stored in the filament due to the pinning potential, we simply compute the disorder average of the thermal expectation value of the squared amplitude of each Fourier mode of the filament.

6.4.1 Strong tension

First we work under the assumption of strong tension in which the filament is nearly straight. We start by expanding the undulations of the filament

$$y(x) = \sum_{n=1}^{\infty} u_n \sin(z_n x). \tag{6.46}$$

In terms of these Fourier modes the energy in a particular realization of the force-controlled pinning ensemble is

$$E = \frac{L_0}{4} \sum_{n=1}^{\infty} \left\{ \left(\kappa z_n^4 + \tau z_n^2 \right) u_n^2 + 2 f_n u_n \right\}, \tag{6.47}$$

where f_n are the Fourier modes of the pinning force so that

$$f(x) = \sum_{n=1}^{\infty} f_n \sin(z_n x). \tag{6.48}$$

In this Fourier expansion of the pinning force, we assume that the potential is defined in a box of size $[L_x \times L_y]$ with periodic boundary conditions and we set $L_x = L_0$. Now, we may use the equipartition theorem to demand that each Fourier

mode stores $T/2$ energy. This leads to

$$\langle u_n^2 \rangle = \frac{2T}{L_0\left(\kappa z_n^4 + \tau z_n^2\right)} + \frac{{f_n}^2}{\left(\kappa z_n^4 + \tau z_n^2\right)^2}. \tag{6.49}$$

We now average the above result using the force-controlled distribution for the potential from Eq. 6.4 in Fourier representation

$$P(V_{k_x,k_y}) \propto \exp\left\{-L_x L_y V_{k_x,k_y}^2 \left(\frac{\xi^2}{8V_0^2}(k_x^2+k_y^2)^2 + \frac{1}{8V_0^2}(k_x^2+k_y^2)\right)\right\}. \tag{6.50}$$

where Fourier modes are defined in a standard way

$$V(x,y) = \sum_{k_x,k_y} V_{k_x,k_y} \sin(k_x x) \sin(k_y y). \tag{6.51}$$

We now express f_n from Eq. 6.48 in terms of the gradients of V_{k_x,k_y}

$$f_n = \sum_{k_y} k_y V_{k_x,k_y} \tag{6.52}$$

with $k_x = \frac{\pi n}{L_0} = z_n$ Using Eq. 6.52 and Eq. 6.50 we obtain

$$[f_n^2] = \sum_{k_y} \frac{k_y^2}{2L_x L_y \left(\frac{\xi^2}{8V_0^2}(k_x^2+k_y^2)^2 + \frac{1}{8V_0^2}(k_x^2+k_y^2)\right)}. \tag{6.53}$$

Taking L_y to be large we replace the summation with integration to obtain

$$[f_n^2] = \frac{2V_0^2}{L_x \xi^2 \left(\sqrt{z_n^2 + \frac{1}{\xi^2}} + z_n\right)}. \tag{6.54}$$

Since only the second term in Eq. 6.49 depends on the pinning potential the average over the quenched disorder yields an expression for the mean excess bending energy of the filament

$$E_n^{bend} = \frac{T\kappa z_n^4}{2(\kappa z_n^4 + \tau z_n^2)} + \Delta E_n^{bend}. \tag{6.55}$$

in which the second term contains all the information about the filament's interaction with the pinning potential. That second term is

$$\Delta E_n = \frac{\kappa z_n^4 V_0^2}{2(\kappa z_n^4 + \tau z_n^2)^2 \xi^2 \left(\sqrt{z_n^2 + \frac{1}{\xi^2}} + z_n\right)}. \tag{6.56}$$

The first term is merely the standard result from the equipartition theorem for a semiflexible filament [108]. It follows similarly that contribution from the potential to the mean energies stored in filament tension and in the pinning potential are given by

$$\Delta E_n^{ten} = \frac{1}{\ell_t^2 z_n^2} \Delta E_n^{bend} \tag{6.57}$$

$$E_n^{pot} = \frac{k}{\kappa z_n^4} \Delta E_n^{bend}. \tag{6.58}$$

In Fig. 6.5 we plot the bending energy stored in the filament as a function of dimensionless wavenumber $q = \xi z_n$ for a variety of pinning potential strengths (at fixed external tension) (upper panel A) and a variety of tensions at a fixed value of the strength of the pinning potential (lower panel B). From dimensional analysis we note that there is a single scale that sets the strength of the pinning potential

$$\tilde{E} = \frac{V_0^2 \xi}{T\tau}. \tag{6.59}$$

When this quantity is large $\tilde{E} \gg 1$ we expect the pinning potential to control the statistical ensemble of the filament configurations. Conversely, we expect high tension to straighten out the filament so that it cannot follow the local potential minima. Higher tension leads to both straighter typical filament configurations and configurations for which the effect of pinning becomes harder to distinguish against a background of thermal undulations. This transition between pinning dominated states of the filament and thermally dominated ones is wavenumber dependent. At sufficiently high

wavenumbers $q = \xi z_n > q^\star$ the modes of the filament are generically freed from the pinning potential.

In Fig. 6.6 we observe this transition from strongly pinned modes, where the pinning contribution to the bending energy E^{pin} is greater than the thermal component E^{T} for $q < q^\star$ to effectively unpinned ones.

Since the work done by tension to extend the filament is $\tau \Delta L$, we can use Eqs. 6.56,6.57 to compute the excess length

$$\Delta L = \sum_{n=1}^{\infty} \frac{V_0^2}{2(\kappa z_n^2 + \tau)^2 z_n^2 \xi^2 \left(\sqrt{z_n^2 + \frac{1}{\xi^2}} + z_n\right)}. \tag{6.60}$$

The sum is rapidly convergent so the first terms will dominate. In the limit of a short correlation length $\xi/L_0 \ll 1$, $L_0\sqrt{\frac{\tau}{\kappa}} \gg 1$ we get

$$\Delta L = \sum_{n=1}^{\infty} \frac{V_0^2}{2\tau^2 z_n^2 \xi}. \tag{6.61}$$

The summation results in

$$\Delta L = \frac{V_0^2 L_0^2}{12\tau^2 \xi}. \tag{6.62}$$

If instead we consider the case of the large bending we should take the limit $L_0\sqrt{\frac{\tau}{\kappa}} \ll 1$ and

$$\Delta L = \sum_{n=1}^{\infty} \frac{V_0^2}{2\kappa^2 z_n^6 \xi} = \frac{V_0^2 L^6}{1890\kappa^2 \xi} \tag{6.63}$$

For the case of large correlation length, $\xi/L_0 \gg 1$, large tension $L_0\sqrt{\frac{\tau}{\kappa}} \gg 1$ we get

$$\Delta L = \sum_{n=1}^{\infty} \frac{V_0^2}{2\tau^2 z_n^3 \xi^2}, \tag{6.64}$$

which results in

$$\Delta L = \frac{V_0^2 L_0^3}{4\pi^3 \tau^2 \xi^2} \zeta(3) \tag{6.65}$$

where $\zeta(x)$ is Riemann ζ-function. Since the correlation length is much larger than that the filament, we expect that the filament feels an essentially uniform force field, much like that of a hanging rope in a gravitational field. Indeed, the result for the excess length in this classical problem is $\Delta L = \frac{g^2 L_0^3}{6\tau^2}$, which demonstrates the same power law dependence on tension τ and the separation of the end points L_0.

6.4.2 Weak tension

For case of weak tension where the filament can better follow the potential minima, we are free to use the valley approximation. In this case the filament's energy is given by Eq. 6.21. Doing the same calculation for the variance of each Fourier mode of the filament in a valley whose bottom curve is described by the Fourier modes of $y_0(x)$, y_0^n, we find

$$\langle u_n^2 \rangle = \frac{2T}{L_0 \left(\kappa z_n^4 + \tau z_n^2 + \frac{V_0}{\xi^2} \right)} + \frac{V_0^2 (y_0^n)^2}{\xi^4 \left(\kappa z_n^4 + \tau z_n^2 + \frac{V_0}{\xi^2} \right)^2}. \tag{6.66}$$

Once again, the first term is independent of the disorder in the valley, but does depend on the curvature of the potential. This result corresponds to the case of a semiflexible filament in a straight parabolic potential [167]. The second term corrects this result for the tortuosity of the valley. To compute this correction we note that

$$\left[(y_0^n)^2 \right] = \frac{1}{\frac{L}{2\xi} z_n^2 + \frac{L\xi}{2} z_n^4}. \tag{6.67}$$

From this result and from energy function – see Eq. 6.21, we immediately find that

$$\left[E_n^{bend}\right] = \frac{T\kappa z_n^4}{2\left(\kappa z_n^4 + \tau z_n^2 + \frac{V_0}{2\xi^2}\right)} + \frac{\kappa V_0^2 z_n^4}{4\xi^4 \left(\kappa z_n^4 + \tau z_n^2 + \frac{V_0}{\xi^2}\right)^2 \left(\frac{1}{2\xi} z_n^2 + \frac{\xi}{2} z_n^4\right)}. \tag{6.68}$$

Again the first term represents the bending energy associated with the semiflexible filament in a straight parabolic potential. The potential decreases the bending energy, as is physically reasonable. The potential suppresses the normal thermal undulations of the filament. The second term, however, represents an increase in the mean bending energy associated with the curvature of the potential valleys. For a fixed local mean curvature of the pinning potential, $V_0/\xi^2 = \text{const}$, the dependence of this tortuosity correction is nonmonotonic in wavenumber. We examine this in Fig. 6.7. There we see that the wavenumber dependent bending energy goes through a local maximum at the scale of the potential's correlation length,*i.e.*, where $z_n\xi = 1$.

6.5 Simulations[1]

The established computational framework for the Brownian dynamics of semiflexible filaments proposed in [29] and used e. g. in [127] has been extended to account for forces resulting from the random potential field.

6.5.1 The finite element Brownian dynamics simulation framework

A single filament is modeled by nonlinear, geometrically exact, 3D Simo-Reissner beam theory and discretized in space using finite elements [74]. In terms of the

[1]**The numerical simulations were performed by Kei Müller, Maximillian Grill and Wolfgang Wall, Technical University of Munich**

structural rigidity of the filament, we thus account for axial, torsional, bending, and shear deformation. To model the Brownian motion, we include viscous drag as well as thermal forces, each distributed along the entire filament length. More precisely, viscous forces and moments are computed assuming a quiescent background fluid and individual damping coefficients for translations parallel and perpendicular to the filament axis as well as rotation around the filament axis, respectively. Thermal forces are determined from the stochastic Wiener process in accordance with the fluctuation-dissipation theorem. Finally, an Implicit-Euler scheme is used to discretize in time and a Newton-Raphson algorithm solves the resulting nonlinear system of equations. Further details on this simulation framework including all formulae can be found in [29].

6.5.2 Incorporation of the background potential field

As described in section 6.1, the potential field V acting on the filament has dimensions of energy per length. Its contribution to the virtual work required for the weak, variational formulation of the problem can be stated as

$$\delta\Pi = -\int_0^{L_0} ds \left\{ \left(\nabla V(\mathbf{r}(s))\right)^T \, \delta\mathbf{r}(s) \right\} \tag{6.69}$$

where $\mathbf{r} \in \mathbb{R}^3$ is the centerline position and $s \in [0, L_0]$ denotes the arclength coordinate in the stress-free reference configuration of the filament. Subsequent discretization of the admissible centerline variations $\delta\mathbf{r}$ according to the finite element method yields the contributions to the discrete element force vector. We apply the trapezoidal rule on each finite element to numerically evaluate the integral along the filament. Regardless of the fact, that we only consider planar problems throughout this article, the entire simulation framework as well as Eq. 6.69 is capable of model-

ing arbitrary filament configurations in 3D. Note that the potential exerts forces on the filament, however, as it models a surrounding network, it is independent of the filament motion. This is commonly denoted as one-way coupling.

To mention the most important algorithmic details: In a pre-processing step, we use a random number generator, apply a discrete Fourier transformation, and finally a finite difference scheme to arrive at the force field $-\nabla V$ on a sufficiently fine grid in the entire simulation domain. In each iteration, we then interpolate these grid values to compute $-\nabla V$ at the current position of each node and evaluate Eq. 6.69 element-wise.

6.5.3 Simulation setup and results

The simulation setup consists of a single filament of length $L_0 = 20\mu\text{m}$ and persistence length $L_p \approx 14\mu\text{m}$. Its initial, stress-free reference configuration is chosen straight and parallel to the global x-axis, as shown in Fig. 6.8 (A). By means of Dirichlet boundary conditions, the filament is constrained to the xy-plane and simply supported, i. e., free to rotate at both ends, however only free to move in x-direction at one endpoint. Its circular cross-section is specified by the area $A = 1.9 \times 10^{-5}\mu\text{m}^2$, area moment of inertia $I = 4.3{\times}10^{-12}\mu\text{m}^4$ and polar moment of inertia $I_p = 8.6{\times}10^{-12}\mu\text{m}^4$. The material is defined by the Young's modulus $E = 1.3 \times 10^{10}\text{pN}/\mu\text{m}^2$ and the Poisson ratio $\nu = 0.3$. Temperature is set to $T = 293\text{K}$ and the dynamic viscosity of the quiescent background fluid to $\eta = 10^{-3}\,\text{Pa}\,\text{s}$. The filament is discretized in space using 400 linear beam finite elements and the time step size is chosen as $\Delta t = 0.01\text{s}$.

Two variants of the potential field have been considered in simulations. First,

the potential with exponential suppression of high Fourier modes defined by Eq. 6.5 and second, the force controlled distribution defined by Eq. 6.4.

6.5.3.1 Results for the potential with exponential suppression of high wavenumber modes

For the results presented already along with the theoretical prediction in Fig. 6.4, we applied the potential from Eq. 6.5, using 3096 Fourier modes, a correlation length of $\xi \approx 1.6\mu$m and $V_0 = 0.175$pN. In addition, a single point force $\tau = 10^{-2} \ldots 50$pN was applied in global x-direction to the (right) endpoint of the filament that is free to move in this direction. Each simulation was run for 5×10^4 time steps. To speed up simulations, we made use of parallelization and simulated systems of five filaments at a vertical spacing much larger than ξ and without any interactions between the filaments. Each data point in Fig. 6.4 results from the statistical ensemble of 70 to 100 such systems with five filaments each, depending on the deviation in results that was higher for the small tension values. Finally, the excess arclength ΔL is obtained from simulation data as the negative displacement of the (right) filament endpoint in x-direction.

6.5.3.2 Results for the force controlled distribution

While the simulations using the potential with the exponential suppression of the high wavenumber modes are more robust, the theory assumes a force controlled distribution. Therefore, unlike for the previous variant of the potential distribution, there are no adjustable parameters necessary to directly compare these numerical results to the theory. We consider two parameter sets: one representing the case of

large tension and another one representing the case of large bending and zero tension.

The first parameter set is given as $V_0 = 1/256^2$ pN, $\tau = 0.006$ pN, $\xi = 1\mu$m, $L_0 = 5\mu$m. The simulation gives us $\langle \Delta L \rangle = 2.0 \pm 0.6 \times 10^{-5}\mu$m, while Eq. 6.61 predicts $\Delta L \approx 1.3 \times 10^{-5}\mu$m. The second parameter set is $V_0 = 1/256^2$ pN, $\tau = 0$, $\xi = 1\mu$m, $L_0 = 5\mu$m, $\kappa \approx 0.0125\,\mathrm{pN}\,\mu\mathrm{m}^2$. Here, the result from our simulations is $\langle \Delta L \rangle = 2.2 \pm 0.4 \times 10^{-5}\mu$m, while Eq. 6.63 predicts $\Delta L \approx 1.2 \times 10^{-5}\mu$m. We performed sixteen simulation runs for each parameter set.

6.6 Discussion

We have examined the statistical mechanics of a single semiflexible filament in a quenched pinning potential as a model for studying how the network environment changes the typical stored elastic energy of filaments and leads to prestress. Based on these calculations we propose that there are two experimental quantities for which we may make predictions even with our single filament model. The first is that we expect the pinning environment of the network to impose a different (and nonequilibrium) statistical weight to filament configurations. One way to parameterize this difference between the ensemble of filament configurations in a network and of a filament in isolation is that the effective persistence length of the network filament will no longer be $\ell_{\mathrm{P}} = \kappa/T$.

Using our results for the disordered-averaged Fourier modes of the filament's undulations, we may directly compute the tangent tangent correlations. We find that

$$G(x_1, x_2) = \langle \dot{y}(x_1)\dot{y}(x_2) \rangle \propto e^{-|x_1 - x_2|/\tilde{\ell}_{\mathrm{P}}}, \tag{6.70}$$

where the *nonthermal* persistence length $\tilde{\ell}_{\rm P}$ is given by

$$\tilde{\ell}_p = \max\left\{\frac{1}{\mathrm{Re}(\omega_1)}, \frac{1}{\mathrm{Re}(\omega_2)}, \xi\right\}, \tag{6.71}$$

where $\omega_{1,2}$ are the eigenvalues introduced in Eq. 6.28. We examine the dependence of the effective, disorder-influenced persistence as a function of tension and potential correlation length in Fig. 6.9.

For the case of sufficiently strong tension or weak pinning potential $\tau \gg V_0$, we find that the tangent correlations do not decay exponentially with separation along the filament. Instead they decay as a polylogarythmic function of the separation: $\mathrm{Li}_2(e^{i\pi|x_1-x_2|/L})$. In that case, no persistence length can be defined. See Fig. 6.10 for the behavior of the correlation function

Turning to the case of prestress, we offer a prediction for the mean excess free energy density of the network due to trapped elastic deformations of its constituent filaments. To arrive at this prediction within our one filament model, we assume the excess free energy density may be computed by summing the excess bending and tension energy $\Delta E^{bend} + \Delta E^{ten}$ of a filament due its interaction with the pinning potential and then dividing that quantity by the area occupied by that filament. In our two dimensional calculation this is simply $L_0 \times \xi$. To make a prediction for a three dimensional network we assume that there are two independent polarization states of the filament's undulations (which is reasonable for small bending angles) resulting in a prediction

$$\Delta F \simeq \left(2\Delta E^{\rm bend} + \Delta E^{ten}\right) L_0^{-1} \xi^{-2}. \tag{6.72}$$

We expect that this quantity should set the scale for the anomalous nonequilibrium stress fluctuations observed in transiently cross linked networks of semiflexible filaments.

There are limits to the single filament description of the collective phenomenon of network structure and excess free energy. Following the example of mean field models of magnets, one might imagine finding a self consistent description of network structure in which the statistics of the pinning potential are determined by the calculated properties of a filament in that potential in a sort of Weiss molecular field description. We leave such self-consistent calculations to future work.

We also note that our description of a single filament is inadequate for studying the crumpling of filaments in a even stronger pinning environments. States of larger deformation, as might be expected in flexible polymers without sufficient tension, cannot be described by our framework; their description requires more complex and inherently nonlinear elasticity. Fortunately, nature provides numerous examples of semiflexible protein filaments for which our analysis should be sufficient. Transiently cross linked networks of such stiff filaments are an arena for the study of the role of quenched disorder on their ensemble of shapes and elastic energy storage.

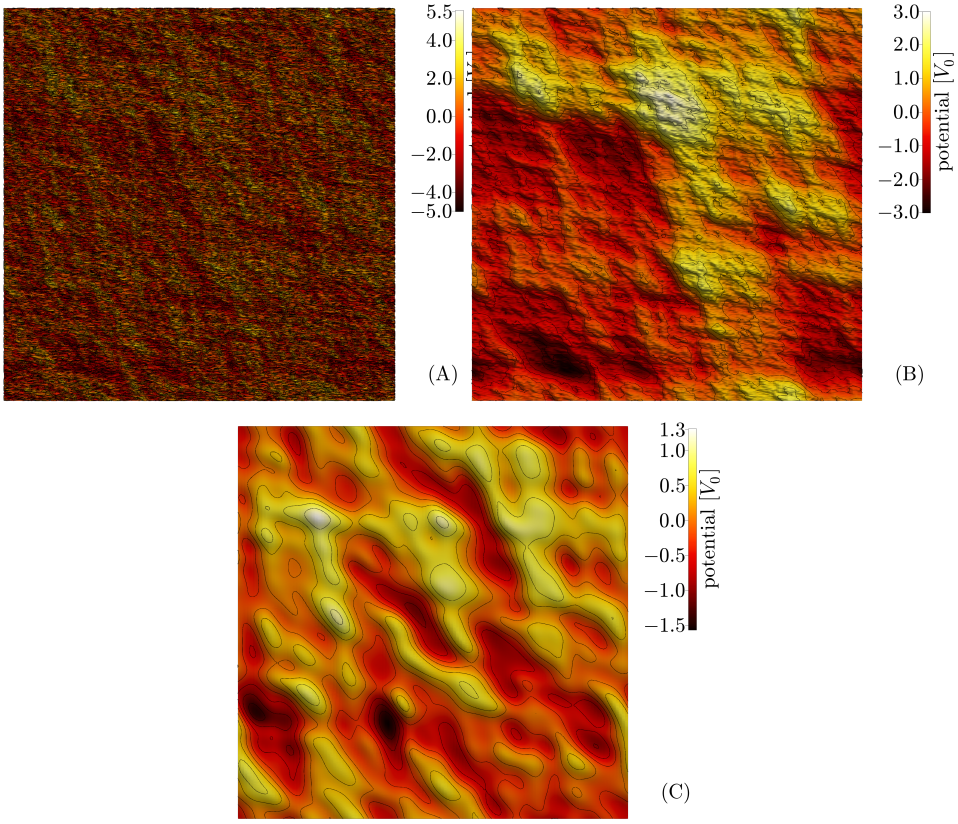

Figure 6.2: Examples of the random potentials $V(x, y)$ (shown as a heat map with contour lines) selected from different distributions: (A) Energy controlled distribution. (B) Force controlled distribution. (C) Exponential suppression of high modes. The correlation length is fixed in all three so that $L_x/\xi = 20$.

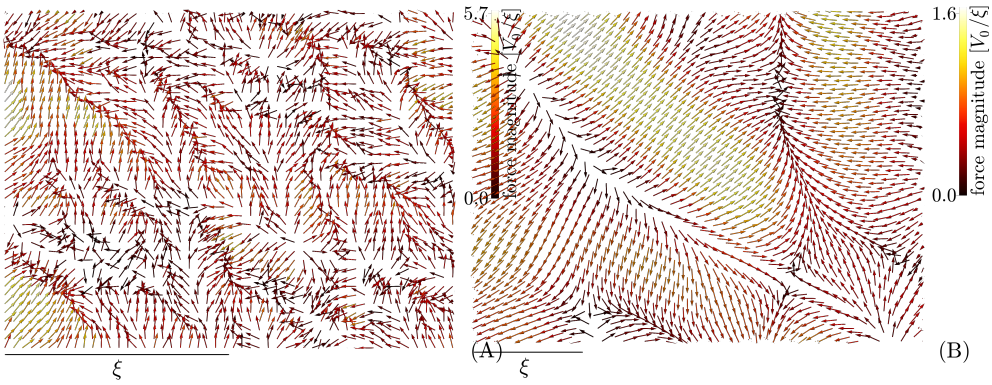

Figure 6.3: (color online) Detail views of the force fields resulting due to the random pinning potentials shown in Fig. 6.2. (A) Force controlled distribution. (B) Exponential suppression of high modes.

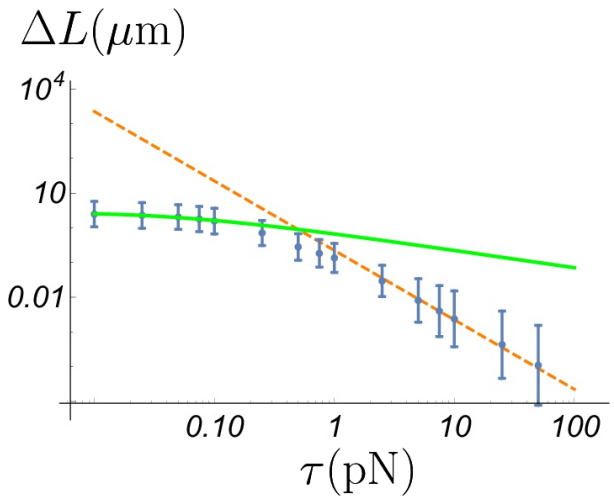

Figure 6.4: (color online) The excess arclength ΔL – see Eq. 6.19 of a semiflexible filament in the quenched pinning potential (with persistence length $\ell_P \approx 14\mu m$) as a function of tension τ. At high tension (orange, dashed) the filament cannot track the bottom of potential valleys, while at low tension (green, thick) or small bending modulus the filament does track the potential valleys with higher fidelity. The (blue) dots with errorbars represent simulation results and the errors show the standard deviations of about five hundred filaments. The pinning potential is defined by $V_0 = 0.175pN$, $\xi \approx 1.6\mu m$.

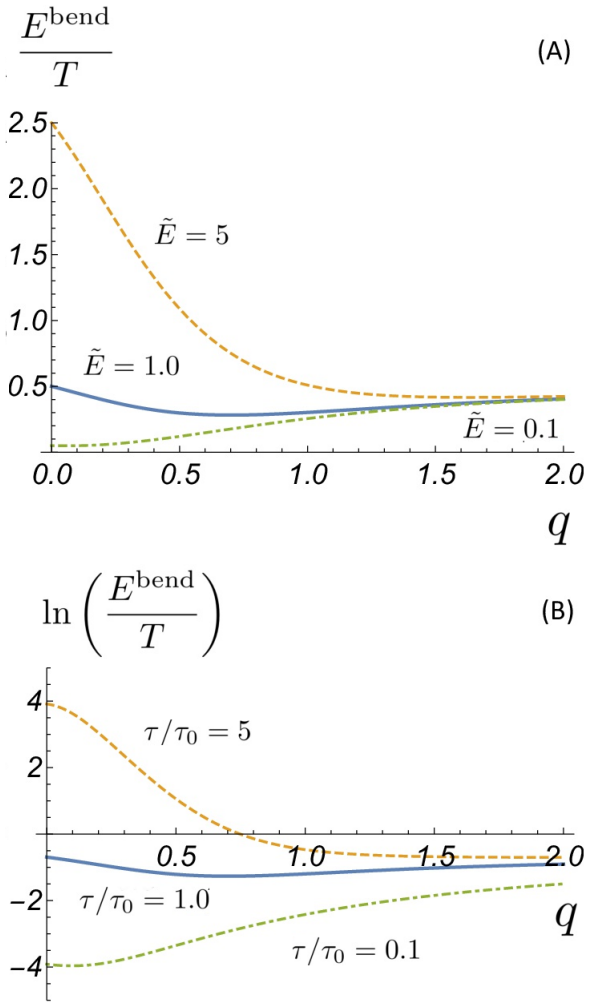

Figure 6.5: (color online) (A) $E^{bend}(q)$, the energy energy per mode of a tensed, pinned filament (in units of T) as a function of $q = \xi z_n$. The pinning potential strength is set by dimensionless $\tilde{E} = V_0^2\xi/T\tau$ using the exponential potential distribution. The small q modes typically have more bending energy than expected for a thermalized filament without the pinning. The high q modes are effectively unpinned. (B) The effect of changing tension on bending energy: $\tau = 0.1, 1, 5\tau_0$ where $\tau_0 V_0^2\xi/T$. We set $\kappa = \xi^2\tau_0$.

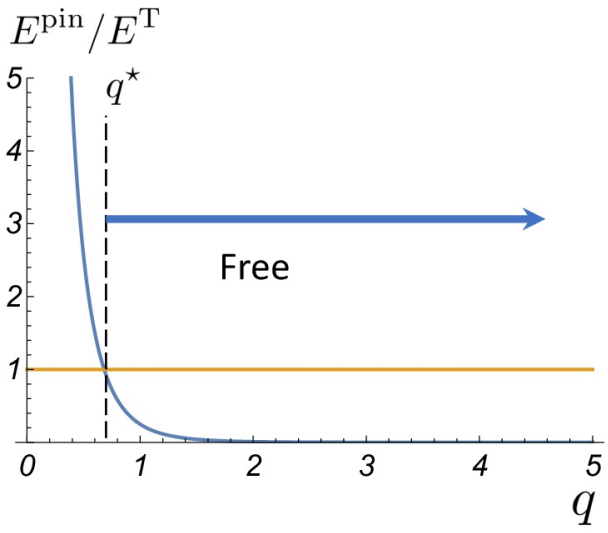

Figure 6.6: (color online) For a given value of the pinning strength and tension, there is a transition at $q^\star$ between pinned modes $q < q^\star$, which trap a significant excess energy as compared to the free filament and free modes $q < q^\star$, which do not. We examine this transition by plotting the ratio of the excess bending energy resulting from the pinning potential E^{pin} to the energy of that mode without the pinning potential $E^{\rm T}$. The pinning potential and the tension are $T/(2\xi)$ and $\sqrt{2\kappa V_0}/\xi$. The figure is qualitatively the same for other values of these parameters.

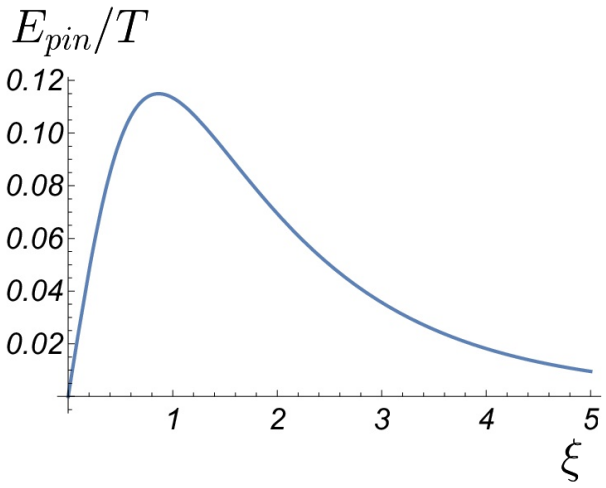

Figure 6.7: The maximum value for the energy stored in the potential is reached at $\xi = 1/z_n$ which resembles the resonance absorption spectrum. Here ξ is measured in the units of $1/z_n$, $V_0 = 20(\tau + \kappa)$ in these units.

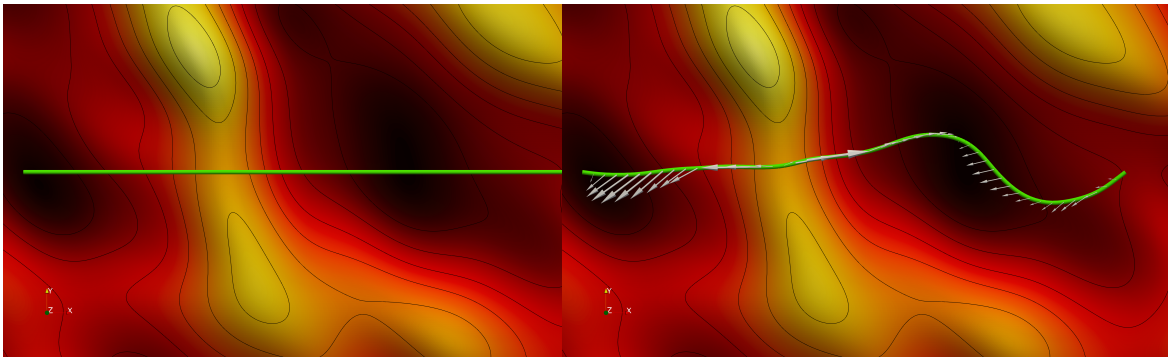

(A) (B)

Figure 6.8: (A) Simulation snapshot of the initial setup. An initially straight, stress-free filament is constrained to the xy-plane and simply supported at its end-points. It interacts with a random potential $V(x, y)$ that is shown as a heat map with contour lines. (B) Simulation snapshot of a deformed configuration showing the forces on the filament resulting from the pinning potential.

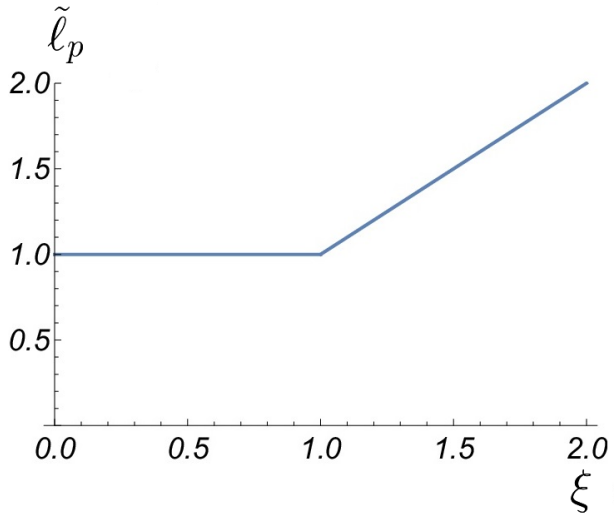

Figure 6.9: Weak tension persistence length

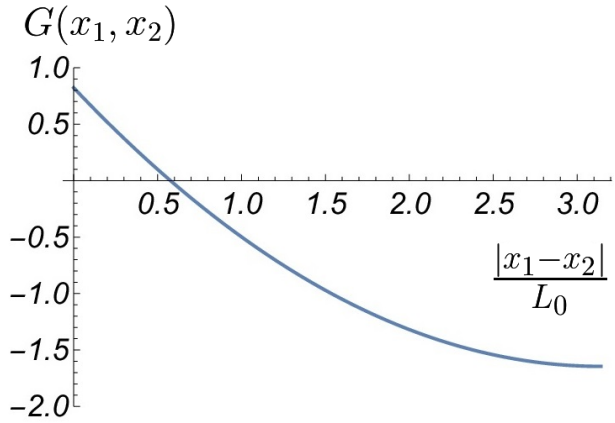

Figure 6.10: Strong tension correlation function

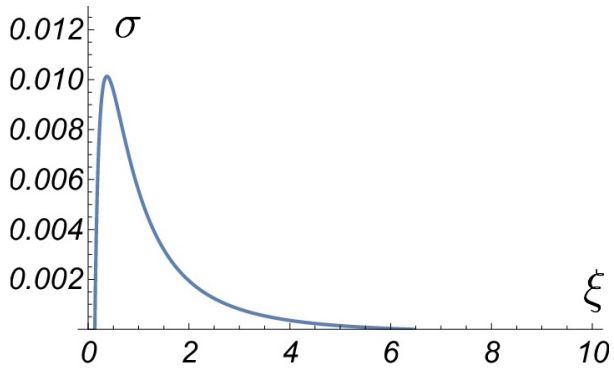

Figure 6.11: Prestress

Part II

Neural networks

CHAPTER 7

Microcircuit synchronization and heavy tailed synaptic weight distribution in preBötzinger Complex contribute to generation of breathing rhythm

When one studies a physical system, mere observation is good starting point. However, a significantly richer understanding of the system can be obtained by looking at the response of the system to external perturbation [46]. For the case of the system at hand, the preBoötC, the external perturbation in living animals is highly non-trivial, because the Complex is deep in the brainstem. However, one can study the behavior of the system *in vitro, i.e.*, on the slices of preBötC outside of the animal.

A useful perturbation of the dynamics of the preBötzinger Complex is the external photostimulation of a small subset of neurons, performed in Ref. [80] (Figure 7.1). This external activation may trigger an ectopic burst (i.e., the burst occurs earlier that it was supposed to following the rhythm). This exogenously induced burst happens with some probability. When it happens, there it occurs with some delay time after the intervention. Both the bursting probability and the latency time depend on the number of activated neurons. To understand this process in more detail and

analyze how the network's connectivity influences it, we constructed the simplest possible model that still accounts for the temporal sequence of neuronal spiking by considering leaky integrate-and-fire (LIF) neurons on a network with various connectivity patterns and synaptic strengths. We set the dynamical properties of the model neurons to be consistent with known dynamics of preBötTC Type I neurons; these parameters are listed in Table 7.1. We demonstrate that this model indeed reproduces the results of the above mentioned experiment with the neuronal parameters taken from the physiological range. Moreover, the model is very sensitive to the network's connectivity, which allows us to use the experimentally observed collective dynamics of the network to constrain the putative types of connectome of the preBötC.

We organize the rest of the chapter as follows. In the section 7.1, we review the LIF neuron model, as well as the physiologically motivated network connectivity patterns we explored. In addition, we introduce a quantity derived from the connectome, *senderness*, that quantifies the information about the network and choice of initially activated neurons into a single class of scalar variables. We show that some of these scalars are good predictors of burst initiation. In the section 7.2, we explore how different connectivity patterns affect the probability of bursting and the burst latency time as a function of the number of initially stimulated neurons using senderness to provide insight into why some stimulation experiments succeed or fail in eliciting a burst. We also see, both by direct observation of the networks and by exploring senderness, the critical effect of the non-linearity in the neuron activation function, which leads to tremendous differences between network dynamics having lognormal and uniform synaptic weight distributions. We discuss experimental tests of these ideas and speculate implications of our findings for the physiological system in the Discussion.

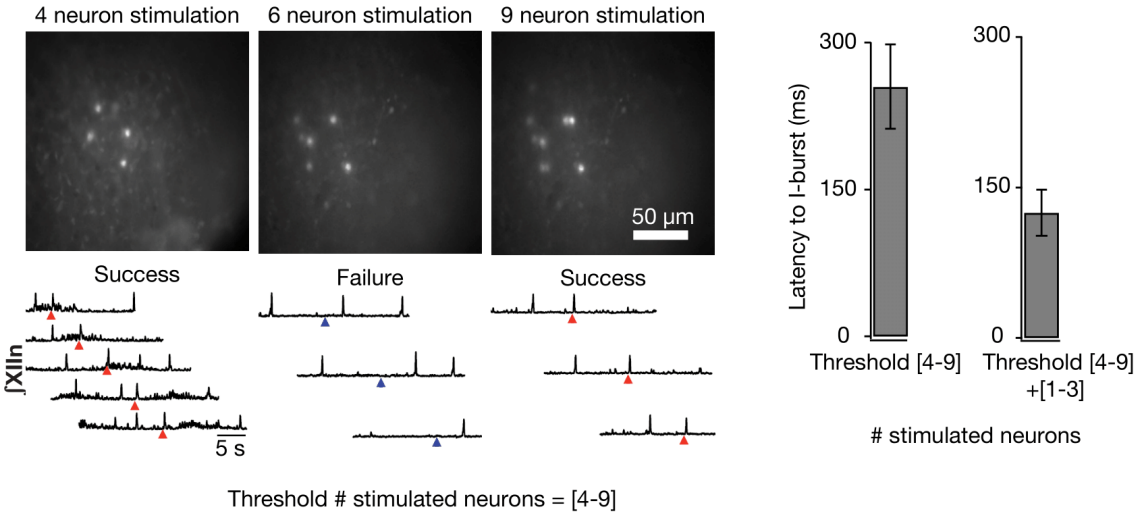

Figure 7.1: Left: Examples of 3 different experiments of multiple trials with holographic photostimulation (top frames) of 4, 6 or 9 neurons with XIIn recording (bottom) in rhythmic slice preparations; photostimulation onset indicated by triangles: red triangles indicate success and blue triangles indicate failure to elicit an ectopic I-burst. Middle: Latency to induce I-burst after the onset of photostimulation in minimum number (threshold) of stimulated inspiratory-modulated neurons, ranging between 4-9, required to induce an I-burst (h). Right: Same as middle but with additional 1-3 stimulated neurons. For (H-I), n=4 experiments with 5-10 trials each. All data expressed in mean±SEM.

7.1 Model

We modeled the preBötC by treating its constituent neurons as low dimensional, nonlinear dynamical systems interacting on a quenched (and frequently random) directed graph, an approach pioneered in other neural networks [41, 51, 50, 136]. In such studies, neuronal models fall into two distinct classes: (i) firing rate models that treat neuronal output in terms of a single firing rate variable but ignore the temporal structure of the underlying spike trains, or; (ii) spiking models that consider the timing of each spike in the network where neuronal interactions depend on the temporal coincidence of discrete excitatory postsynaptic potentials (EPSPs) rather than on their rate-based, highly smoothed temporal summation [96, 36, 12, 102, 180]. The majority of preBötC models are based on firing-rate models [9, 154, 62, 32, 8, 13], which are computationally simpler, but are incompatible with recent findings suggesting that inspiratory burst initiation is a consequence of the progressive synchronization of neuronal spiking within the rhythmogenic microcircuit [7]. Firing-rate models also cannot account for the observation that the simultaneous stimulation of a small subset of neurons (4-9) can induce a global response, i.e., a network burst, at considerable delay, ∼60-400 ms in vitro [80]. Consequently, we focus solely on spiking models.

7.1.1 Neuronal Dynamics

In the leaky integrate-and-fire (LIF) model for point neurons, the change of somatic potential V_i of the i^{th} neuron at time t is controlled by [51]:

$$\tau_{\text{m}} \frac{dV_i}{dt} = V_{\text{rest}} - V_i(t) + R \sum_j I_{i,j}(t), \tag{7.1}$$

where V_{rest} is the resting potential, τ_{m} is the membrane time constant, R the input resistance, $I_{i,j}$ the input current from the j^{th} to i^{th} neuron, and the sum is over all neurons that synapse onto i^{th} one. V_{rest} was set at either at –60 mV or –65 mV depending on the simulated experimental conditions. The current is defined as in Ref. [16]:

$$I_{i,j}(t) = \begin{cases} \frac{W_{i,j}}{R}\,(t - t_j - \Delta t_{ij})\,e^{-\frac{t-t_j-\Delta t_{i,j}}{\tau_{\text{s}}}} & t \geq t_i + \Delta t_{i,j} \\ 0 & t \geq t_j + \Delta t_{i,j}. \end{cases} \tag{7.2}$$

Here t_j is time of spike initiation in the j^{th} neuron. The synaptic weight W_{ij} controls the magnitude of the effect of the spike going from the j^{th} to the i^{th} neuron, while τ_{s} sets the temporal width of the spike. $\Delta t_{i,j}$ is the spike's transmission delay time.

For single spikes, these equations can be solved analytically. Assuming neuron i to be at its resting potential before the arrival of a spike, the solution for its potential (which is the waveform of the resulting EPSP) is

$$V(t) = \frac{\gamma_1 W_{i,j}}{\gamma_3^2}\left[e^{-\gamma_1 t'} - (1 + \gamma_3 t')\,e^{-\gamma_2 t'}\right] \tag{7.3}$$

with $t' = t - t_j - \Delta t_{ij}$, $\gamma_1 = 1/\tau_{\text{m}}$, $\gamma_2 = 1/\tau_{\text{s}}$, and $\gamma_3 = \gamma_2 - \gamma_1$. We discuss the choice of the parameters, shown in Table 7.1, in more detail in the Appendix

The deterministic neuronal spike generation was controlled as follows. When the neuronal potential exceeds the threshold V^*, the neuron fires and its potential instantaneously returns to V_{rest}, with the boundary condition that the neuron cannot again fire during a refractory period of $\tau_{\text{refractory}} = 3$ ms [7, 41, 51]; the potential then once again obeys Eq. 7.1. The initial stimulation was modeled by raising the potential of chosen neurons above threshold multiple times (see Appendix D.1 for details). For some studies we allowed spontaneous stochastic firing (Figure 7.5 only), which is known to occur due to inherent neuronal excitability regardless of potential.

Table 7.1: Model parameters

Parameter	Value
V_{rest}	-60 mV, -65 mV (figure 7)
V^*	-48 mV
τ_m	25 ms
τ_s	0.5 ms
Δt_{ij}	1.3±1.1 ms
W_{ij}	300±160 (mean ± SD) mV/ms =15±8 in step size (0.05 ms)
τ_{delay}	20±3 ms
T_{laser}	39±5 ms
n_{spikes}	7
f_{noise}	0.5-2 Hz

In that case, baseline firing was modeled as a Poisson process with the frequency $0.5\text{Hz} < f_{\text{noise}} < 2.0\text{Hz}$, creating background uncorrelated network activity [58].

7.1.2 Network Structure

We considered four distinct ensembles of random directed graphs: (i) Erdős–Rényi (ER) [40, 52] directed graphs; (ii) directed graphs with an increased number of directed 3-simplicies (small world; see definition below); (iii) localized graphs, and; (iv) hierarchical graphs. In the ensemble of directed ER graphs, the probability for any two rhythmogenic preBötC neurons to be unidirectionally connected was the same $p = 0.065$ based on experimental data [148]. Bidirectional connections, which were not observed experimentally [148], were not forbidden, although their

probability of occurrence p^2 was negligible.

To create small-world networks [182] having a preponderance of directed 3-simplices over that expected in a typical ER network, we used the following technique: we added 3-simplicies to ER networks to exceed the average number of simplices in the ER network by approximately 11% by taking ER networks and adding directed synaptic connections to create directed 3-simplicies. A directed 3-simplex consists of three neurons A,B, and C such that neuron A synapses onto both neurons B and C, while neuron B synapses to neuron C. While for the ER network the number of directed 3-simplices is $N_s = (pN)^3$, for some neuronal networks, including neocortex, the number of directed 3-simplices is significantly higher [50, 136].

The localized networks formed as follows: we placed ~ 1000 neurons in a planar, square array with neighboring neurons separated by unit distance. We then added directed edges to form a network, such that the probability for two nodes to be connected decayed exponentially with distance (measured in the usual way), i.e., the probability of a direct connection between neurons i and j was given by $p_{ij} \propto \exp(-d_{ij}^2/\lambda^2)$, where d_{ij} is the distance between them and λ is the mean connection length. The case $\lambda \gg 1000$ corresponds to the ER network. The motivation for exploring this sort of network is based on the fact that synaptic connections in some compact neural microcircuits decrease with interneuronal distance [136]. This model may be generalized to higher dimensional networks, but we did not pursue that here.

Finally, we considered the ensemble of (c, q)-hierarchical networks of N neurons with c central groups of at least q neurons each, and one large peripheral group containing the almost all neurons of the network – $N \gg cq$; q was chosen such that q simultaneous EPSPs incident on a neuron was required to produce a spike. Each

neuron in the peripheral group synapsed onto each neuron in the first central group. Each neuron in the first central group synapsed onto each neuron in the second central group, & etc. Neurons in central groups were all-to-all connected, while neurons in the peripheral group were not connected to each other. Finally, each neuron from the last central group synapsed onto each neuron in the peripheral group. We introduced multiple central groups in order to avoid bidirectional connections between pairs of neurons, as these have not been observed experimentally [148]. These hierarchical networks were the most likely to produce a burst. Indeed, in this network, the synchronous firing of q peripheral neurons, which make up the vast majority of the neurons, was sufficient to initiate a burst. For any network, the synchronous firing of q neurons was a necessary condition for the activation of the next neuron, but in the other network ensembles this condition was generally not sufficient. Therefore, there is no network we studied that was more likely to synchronize than the hierarchical one.

7.1.3 Generalized Senderness

To introduce more general network quantities related to the efferent synaptic connectivity and neuronal activity, we first denote the initial state of the network by the vector $\mathbf{X_{(0)}}$, where its i^{th} component is one if the i^{th} neuron was initially stimulated and zero otherwise; the number of these stimulated neurons is $\sum_i X_{(0)i}$. The quenched random matrices of synaptic weights $\mathbf{W}$ with matrix elements W_{ij} completely defines an instance of a network draw from one of the four ensembles discussed above. These matracies are generally sparse and have nonnegative (excitatory) entries, which can be selected from any distribution, although we focussed on lognormal

distributions.

With these definitions, matrix multiplication generates a new vector

$$\mathbf{X_{(1)}} = \mathbf{W} \cdot \mathbf{X_{(0)}}, \tag{7.4}$$

which gives the list of neurons that receive inputs from the initially stimulated ones, weighted by the appropriate synaptic strength. This vector essentially encodes the effect of the initially stimulated neurons on the rest of the network. However, it has no information about next order neighbors of the initially stimulated neurons. To include this information about higher order neighbors, one may simply iterate this procedure multiple times introducing

$$\mathbf{X_{(n+1)}} = \mathbf{W} \cdot \mathbf{X_{(n)}}. \tag{7.5}$$

While this formally takes into account next-nearest and higher-order neighbors, using this the expression Eq. 7.5 to investigate how the initial stimulus propagates through the network implicitly assumes a linear weighting of neuronal active propagating from one order to the next via a simple synatpic weight multiplication. In reality, we face an extra complication when we consider that the activation function of the neuron is non-linear, having a threshold. If this were not the case, the continuous activation level of neurons in the n^{th} generation of nearest neighbors would simply follow from $\mathbf{W}^n$. Assuming $\mathbf{W}$ to be diagonalizable, one then immediately observes that the emerging activation pattern of the n^{th} generation of nearest neighbors will be dominated by the (right) eigenvectors of $\mathbf{W}$ corresponding to the eigenvalues having the largest amplitudes. As n increases the relative importance of these particular eigenvectors grows exponentially.

To account for the nonlinearity, we propose a nonlinear generalization of the

above quantity:

$$\mathbf{X}(\mathbf{n})^{\mathbf{i_1 i_2 \ldots i_n}} = \left[\mathbf{W} \cdot \left(\mathbf{W} \cdot \left(\mathbf{W} \cdot \mathbf{X_{(0)}}^{\mathbf{i_1}}\right)^{\mathbf{i_2}}\right)^{\mathbf{i_3}} \ldots\right]^{\mathbf{i_n}}, \tag{7.6}$$

where $\mathbf{X^i}$ is *element-wise* i^{th} power of the vector $\mathbf{X}$, i.e., each component is independently raised to that power. Finally, to obtain a single scalar quantity, we sum over the elements of the vector $\mathbf{X}$, to obtain our definition *generalized senderness*

$$S(n)^{i_1 i_2 \ldots i_n} = \sum \mathbf{X}(\mathbf{n})^{\mathbf{i_1 i_2 \ldots i_n}}. \tag{7.7}$$

We emphasize that we have defined an infinite set of increasingly complex measures of neuronal activity propagation through the network. We note that the index n counts the number of generations of neighbors that $S(n)^{i_1 i_2 \ldots i_n}$ covers, while the superscripts list the (element-wise) exponentiation of the evolving vector $\mathbf{X_n}$ at the n^{th} generation. Higher exponents increase the effect of nonlinearity of the neuronal response function. In the following we will consider both low order (small n) and weakly nonlinear (small integer i_k for all $1 \leq k \leq n$) versions of generalized senderness. We later address the question of which of these quantities is predictive for burst initiation using a machine-learning based filter.

7.2 Results

7.2.1 Burst probability and latency time after stimulation: The effect of network structure

The principal quantities accessible to current experiments on the exogenous stimulation of the preBötC [80] are the burst probability after stimulation, and, where bursts occur, the latency time, measuring delay between stimulation and bursting.

Both quantities are measured as a function of the number of stimulated neurons. In experiments we defined a burst by a voltage criterion that corresponds roughly to the simultaneous stimulation of the entire network. In simulations, we used the criterion that the potential averaged over all neurons in the network was above the individual neuron's firing threshold as the definition of the burst. Our results depended only weakly on this threshold because typically the entire network becomes active in a burst. Having the criterion allowed us to distinguish bursts from burstlets, which are transient maxima in activation of the neuronal population that subside rather than progressing to a true burst. These are also seen in the experimental system.

We demonstrate a typical process of the burst generation in our simulations using Fig. 7.2. In five separate runs the same set of seven randomly chosen neurons in the same network was activated. Due to different spiking times of initially activated neurons, each run produces dynamics with different burst delay times, and, in one case (red curve), no burst at all. In these representative trials, network activity growth due to spiking synchronization can be divided into two epochs. During the first, the activity growth is insignificant (Figure 7.2C), the activity of stimulated neurons appears to be insufficient to initiate a burst. In fact, in some cycles, spikes from activated neurons did not induce any substantial spiking in their downstream (postsynaptic) neurons, e.g., the first set of spikes for R1-R3 in Figure 7.2A. Consequently, network activity died down to baseline once these neurons stopped firing in response to their initial stimulus (Figure 7.2B-C first set of spikes between 0-50 ms). With repeated activation of stimulated neurons, their spikes bore higher coincidence in certain intervals due to the inherent jitter in activation times so that temporal summation of synaptic potentials in their postsynaptic neurons activated of a sufficiently large group of neurons to drive synchronization, which initiated the second

epoch. During this epoch, the transient network activity continued and spread synchronous activity that fueled a rapid and sudden amplification of network activity, i.e., a burst. At this point, the simulations were terminated. For a run that did not end with network synchronization (Figure 7.2A-C, R2), the simulation trial ended with the last spike of initially activated neurons (Figure 7.2A) and quenching of the whole system (Figure 7.2B-C, red trial).

In experiment, one does not know how these stimulated neurons are connected to the rest of the microcircuit. In the simulations, we choose the exogenously stimulated neurons randomly with equal probabilities, but can use our measures of senderness *post facto* to understand why the stimulation of equal numbers of neurons do not always lead to the same bursting outcome, as described below. In order to address the probabilistic nature of eliciting a burst, each numerical experiment was performed 5 times (each curve on the Figure 7.3). A second source of stochasticity in the simulations is random neuronal firing, which we allow in some simulations. We return to this point later.

Ensembles of networks with differing connectomes demonstrate different patterns of behavior (see Fig. 7.3). Each colored curve is the different network from the same ensemble; grey rectangles show the range of experimental results reported in Ref. [80]. The ER network has the largest variability of the mean delay time as one changes the number of initially stimulated neurons. Moreover, the probability curve for the ER networks is smooth, especially when compared to abrupt jumps in probability observed in the other network connectivities tested. This can be understood from the point of view of *clusterization*. An ER network does not cluster. In an ER network, if neurons A and B have both synapse onto a third neuron C, the probability that they have additional common output neurons other than C remains same as for any

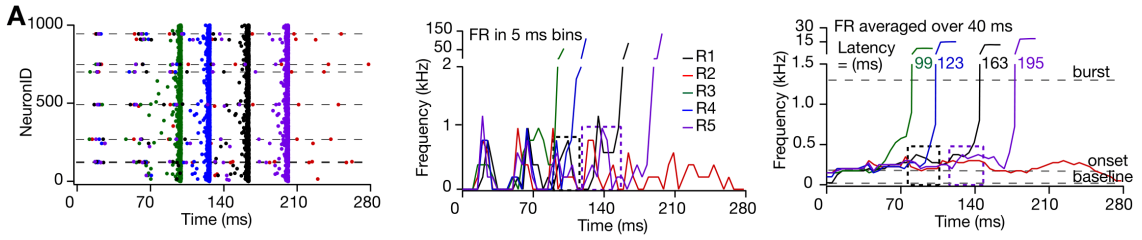

Figure 7.2: ER graphs with lognormal synaptic weights reproduced the robustness of preBötC synchronization and trial to trial variability in the latency to synchronize seen in experiments. A. Model output when the same set of randomly selected 7 neurons (on the dashed lines) was stimulated to fire seven spikes each as in ([80]). Spike times for all neurons represented by circles color coded for 5 trials (green, blue, black, purple, red). Y-axis represents arbitrary order of 1000 neurons. In 4 trials (green, blue, black and purple), the network synchronized, indicated by temporal alignment of spikes in all neurons, but at various latencies. In the 5th trial (red), the network did not synchronize, i.e., no vertical alignment of red dots. B. firing rate (FR) of stimulated neurons and their postsynaptic activated neurons in A (color coded as in A) in 5 ms bins showing waxing and waning of their activity during and poststimulation. C, average firing rate of network computed by averaging network activity in a moving window of 40 ms with 5 ms step increment. Dashed boxes in (B) and (C) represent unusual intervals where despite of relatively high synchronous activity, emerging from stimulated and their recruited neuronal firing, the network did not synchronize fully.

two neurons, regardless of the first criterion. Due to connectivity correlations, this is not the case for neurons in the other three networks. All of them has property of clusterization, i.e., if two neurons have common output, they are likely to be close to each other (localized), or, in general, to be parts of the same cluster, which necessarily leads to a higher probability for them to have more common output neurons. Clusterization is crucial for sharp, nearly discontinuous behavior of the probability and delay time curves in the non-ER networks we studied. Indeed, if the network is clustered, then it is more likely that neuronal activation inside one cluster leads to the burst, while activation of neurons in different clusters will not. The synchronization between activated neurons plays a marginal role in this picture. As a result the bursting probability in these other networks rapidly jumps between zero and one. While this does not prove that ER networks are uniquely consistent with the extant data, we infer that any connectome with clustering will produce synchronization dynamics inconsistent with the data.

Similar reasoning rationalizes the observed latency time as the function of the number of activated neurons. When small numbers of neurons are stimulated, it is likely that the number of spiking neurons will initially grow one by one in the ER network (see Appendix for more detailed analysis and analytical calculations of this process for the ER network), allowing for relatively long latency times when the number of initially stimulated neurons is small. Moreover the latency time will decrease continuously as growing shortly as the number of initially stimulated neurons is increased. In clustered networks, however, neuronal simulation is more likely to lead to subsequent activation of clustered groups of neurons, which significantly reduces the latency time. Of course, the outliers are possible, e.g., the red trace for the localized matrix in Fig. 7.3C where the long delay time reflects many synchro-

nization attempts between the initially stimulated neurons where only the last met with success. Since the experimental data suggests that the delay time smoothly NO I MEAN STRONGLY NOT SMOOTHLY varies as one changes the number of activated neurons, we observe this further supports our inference that clustering-free networks (such as the ER) are necessary to reproduce consistently all of the dynamical data on synchronization and bursting.

7.2.2 The non-linearity of neuronal activation and the synaptic weight distribution.

The spiking output of the simulated neurons is a nonlinear function of the (linear) sum of input EPSPs. Here we address the implications of this essential nonlinearity on the collective dynamics of microcircuit in two ways. First, we compare the dynamics of the network with two different distributions of synaptic weights: lognormal and uniform. If the neuronal nonlinearities are relevant for understanding bursting, the change in the synaptic weight distribution will play an important role. Conversely, as long as we choose the mean synaptic weight to be the same between the two distributions, the collective dynamics of networks with lognormal and uniform synaptic weight distributions will remain similar as long as the inherent neuronal nonlinearity plays a minimal role in the network's collective dynamics (when averaged over many realizations of the network).

ER networks (see Fig. 7.4) with a uniform distribution of synaptic weights were significantly less likely to produce a burst - we needed more than double the number of initially activated neurons in comparison with the lognormal one. This indicates that the main drive for the burst initiation is not related to the mean synaptic weight,

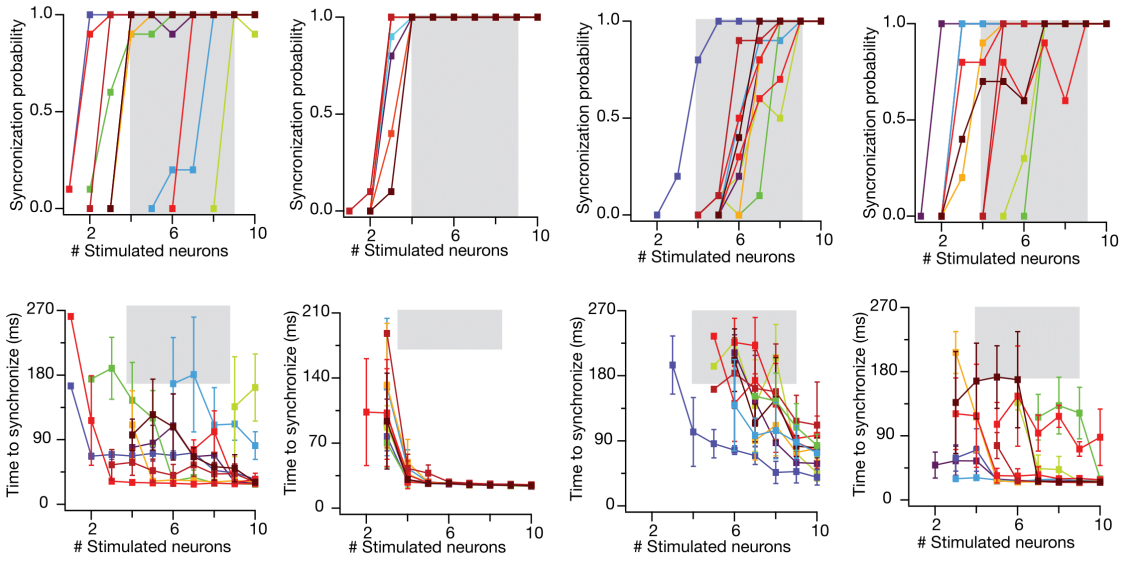

Figure 7.3: Synchronization probability (A,B,C,D) and mean latency to synchronize (E,F,G,H) for localized, hierarchical, ER and small world network respectively as a function of number of initially activated neurons. Each colored trace represents a different network from the same ensemble where synchronization probability and the mean latency to synchronize was computed over 10 trials; error bars show standard deviations; grey boxes span the parameter space that lie within the experimental range (170 ms-370 ms) ([80]) for threshold number of stimulated neurons to induce preBötC bursts.

but is due to those neurons with anomalously strong synaptic connections in the "fat tail" of the lognormal distribution. This is a strong indicator of the importance of the non-linearities.

A second way to explore the nonlinearities in the system is by comparing the predictive efficacy of linear ($i_k = 1$ for all k in Eq. 7.7) and nonlinear senderness variables (see section 7.1). If the nonlinear measures of senderness ($i_k > 1$ for some k in Eq. 7.7) are uniformly more predictive of global networks synchronization leading to a burst, then senderness incorporates information about the choice of initially activated neurons and the network connectivity into a single scalar quantity, that can be either linear or non-linear with respect to the synaptic weights. If non-linear senderness possesses more information about the dynamics of the system, we see another confirmation of the crucial role of non-linearities in the system.

To assess and compare the predictive power of the various linear and non-linear measures of senderness, we used the CatBoost machine learning algorithm (MLA) [141] as follows. We trained the model to predict whether a burst will occur based solely on the value of a particular subset of generalized senderness quantities $S(k)^{i_1 i_2 \ldots i_k}$. The networks used for training and subsequent studies of the predictive power of the MLA were constructed so that their synchronization probability was close to 50% in order to make the classification problem as difficult as possible [1]. By focusing on the incremental change in MLA prediction accuracy as function of the choice of the senderness variables $S(k)^{i_1 i_2 \ldots i_k}$, we produced a measure of the relative information content of these quantities as measured by their utility in providing an accurate classification of bursting and non-bursting trials using the fixed classification algo-

[1] 53% of the networks in the training and test sets synchronized

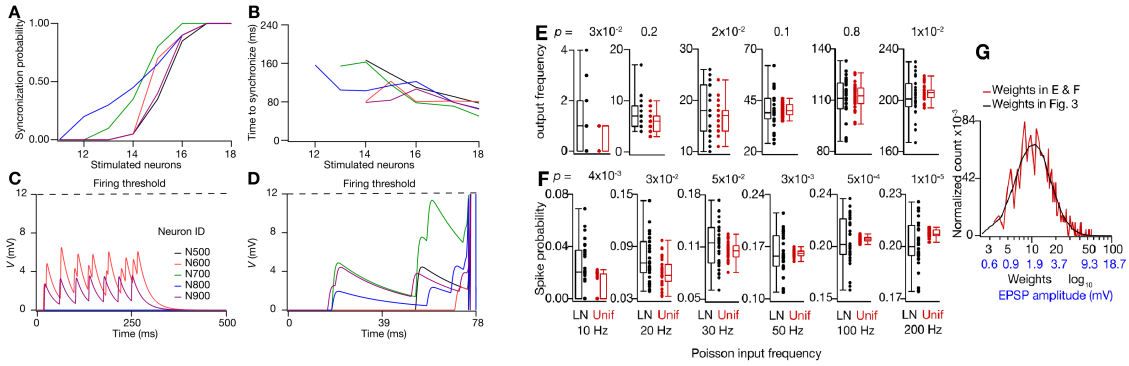

Figure 7.4: A-B, Synchronization probability (A) and latency to synchronize (B) for 5 different ER networks with uniformly distributed synaptic weights that were equal to mean weight used in Figures 2-3. C, Voltage of 5 randomly selected neurons from an ER network with uniform weights when a different set of randomly selected 7 neurons was stimulated like simulations in Figure 3A. D, Same as (C) when the same network connectivity was incorporated with lognormal weight distribution. The network synchronized at ∼78 ms and voltage traces reveal better coincidence detection in this network; vertical lines ∼78 ms represent action potentials. E-F, Average firing frequency (E) and spike probability (F) of individual neurons when 10 randomly selected synaptic inputs (out of 50) were activated at 6 different Poisson frequencies (10-200 Hz; indicated at bottom of F), with either lognormal (LN) or uniform (Unif) synaptic weight distributions; these are composite results from 3 trials each of 10 different neurons at each stimulation frequency; p values for KS test. G, Histogram of LN weights used (E) and (F) (red) compared with the distribution of weights of Figure 3; corresponding EPSP amplitudes for the weights are indicated in blue.

rithm. We interpreted the subset that provided the greatest increase in the MLA's predictive power as indicating the class or classes of active network motifs that were the strongest determinants of network synchronization (see Table 7.2). Looking at these results, one sees that all linear measures of senderness, or senderness where information enters into the next-order neighbors linearly (i.e., $i_1 = 1$), are uniformly poor predictors. Specifically, the worst predictor among the non-linear senderness measures generated a 66% accuracy for the classification algorithm, while the best prediction coming from the exclusive use of linear senderness provided a less accurate 59% success rate (see Table 7.2). Among nonlinear quantities, the one that had information about next-nearest order neighbors demonstrated slightly better prediction accuracy, but the difference was not as pronounced as that between all the linear and all non-linear senderness quantities. We infer that the non-linear properties of the neuron activation function are indeed crucial for the system dynamics.

These results gives us an additional tool to set conditions on possible network architectures, and to form an hypothesis regarding the principal features of the connectome necessary to achieve synchronization and bursting. We first note that (with the exception of $S(1)^4$, all of the more predictive senderness measures involve next nearest neighbor couplings. The inclusion of higher order neighbors, at least up to third order, did not improve the predictive success of senderness. Based on these results, we propose that network motifs involving high senderness (many and high synaptic weight) efferent connections of next nearest neighbors greatly enhances the efficacy of the exogenously stimulated neurons to produce a global synchronization event. Moreover, ER networks naturally generate the requisite number of such motifs to reproduce the sensitivity of the experimental system.

But, for chosen neuron parameters (that are taken from the physiological range)

Table 7.2: Prediction accuracy of various generalized S quantities for network burst.

Parameter	Accuracy
S^2_{32}	0.73±0.01
S^2_{41}	0.72±0.02
S^2_{33}	0.72±0.006
S^2_{42}	0.72±0.009
S^1_4	0.72±0.01
S^2_{43}	0.71±0.01
S^1_6	0.7±0.01
S^2_{31}	0.7±0.01
S^1_3	0.7±0.01
S^2_{23}	0.7±0.01
S^1_9	0.69±0.008
S^1_8	0.69±0.008
S^2_{22}	0.68±0.009
S^2_{21}	0.66±0.009
S^1_2	0.66±0.01
S^2_{13}	0.59±0.008
S^1_1	0.57±0.02
S^2_{12}	0.57±0.01
S^2_{11}	0.56±0.01

ER networks with uniform synaptic weight distributions clearly are less sensitive to the external stimulation than those observed in experiment. ER networks with lognormal weight distributions, however, have an increased sensitivity consistent with experiment. Combined with the previous argument regarding the observed latency time distribution, we propose that only networks with a low degree of clusterization, and having a fat-tailed synaptic weight distribution can simultaneous reproduce all of the currently measured dynamical properties of bursting in the preBötC. In addition, the feature of these networks generating bursting is related to the strength of the efferent connections of the second nearest neighbor neurons to the initially stimulated ones.

7.2.3 Noise-driven burst and burstlet generation

So far we have considered a purely deterministic version of our model in which the only source of initial spiking activity was derived from the external stimulation. The in vitro preBötC, however, in the slice preparation produces bursts even in the absence of such external activation. To explore self-driven bursting, we observe that, even during the interburst intervals, neurons are not absolutely silent, but fire at approximately 0.5 - 2 Hz rate. We model this spontaneous firing as random Poisson process fixing only the mean firing rate (see section 7.1). This distribution implies that there are no temporal correlations between spikes in a given neuron. We recall then that the mean firing rate completely characterizes firing probability density, and emphasize that interneuronal spiking correlations are driven only by synaptic connections. To incorporate the fact that not all neurons in preBötC can fire without stimulation, we allow only a fraction of them (randomly chosen on each

network) to fire stochastically, while the rest can fire only under stimulation, but we also explored networks in which that fraction reaches one. We often observed a noticeable rise in spiking activity across the network that did not lead to a burst – a burstlet, as indicated in Fig. 7.5A by $*$. This is appears to be consistent with observed burstlets in experiment. Burstlets had higher overall spiking frequency across the network than would be expect from the typical fluctuations of the stochastically firing neurons. This is demonstrated by looking at the integrated firing activity of a network with no synaptic couplings (Fig. 7.5A black curve). Such networks cannot produce identifiable burstlets, which indicates that the observed burstlets in synaptically coupled networks resulted from chains of activation of other neurons initiated by the the stochastically spiking neurons, and that these chains failed to achieve a sufficiently global level of synchronous firing to push the burstlet into a full-fledged burst. Bursts were also observed – see Fig. 7.5A, green trace.

We now return to our basic question of how the connectome of the network influences both the reliability of the network to burst in response to endogenous stochastic stimulation and the dependence of bursting on the mean firing rate of the neurons. By comparing dynamics on networks with lognormal synaptic weight distributions (Fig. 7.5B, red traces) with uniform distributions (Fig. 7.5B, black traces), one sees that the former are clearly more sensitive to endogenous spiking. Since there is no exogenous stimulation to set an initial time, we cannot compute the latency to burst, but we can compute the time to burst for a quiescent network. The results are shown in Figs. 7.5C. It is clear that global spiking synchronization and bursting occurs at lower mean spiking frequency of the neurons in lognormal synaptic weight distributions, showing, once again, that such lognormal ER neurons are significantly more sensitive to endogenous spiking. These networks are both

easier to entrain to an external signal and more sensitive to internal spiking, making them more robust bursting circuits.

Comparing network dynamics of systems in which differing fractions of the network are capable of spontaneous stochastic activity, we see in Fig. 7.5D that as the number of spontaneously firing neurons is reduced, the network generates more burstlets before producing a true burst. Eventually, when that fraction falls below $\sim 40\%$, both burstlets and bursts were not observed. If the lognormal synaptic weight distribution is replaced with a uniform one (Fig. 7.5E), one observed the same trends, but generically more burstlets occur before a true burst. This shows, once again, that the network is less liable for global synchronization when the synaptic weight distribution does not have a fat tail.

7.3 Discussion

The rhythmogenic dynamics of the preBötC is currently understood to rely on two distinct features. Spiking synchronization of excitatory typeI neurons leads to the progression of global excitation of the network, followed by a period of activity suppression thought to be due to dentritic adaptation. In this manuscript, we focused on the former property synchronization dynamics by constructing a simple yet predictive numerical model that illuminates how the connectivity of the underlying network influences bursting dynamics. We looked for three specific emergent features in our model. First, we expected to observe global spiking synchronization of the network – bursting – in response to the exogenous stimulation of less than one percent of the network. Based on experiment, bursting should be an inherently stochastic process, leaving a observable of the probability that stimulation induces a burst. Second,

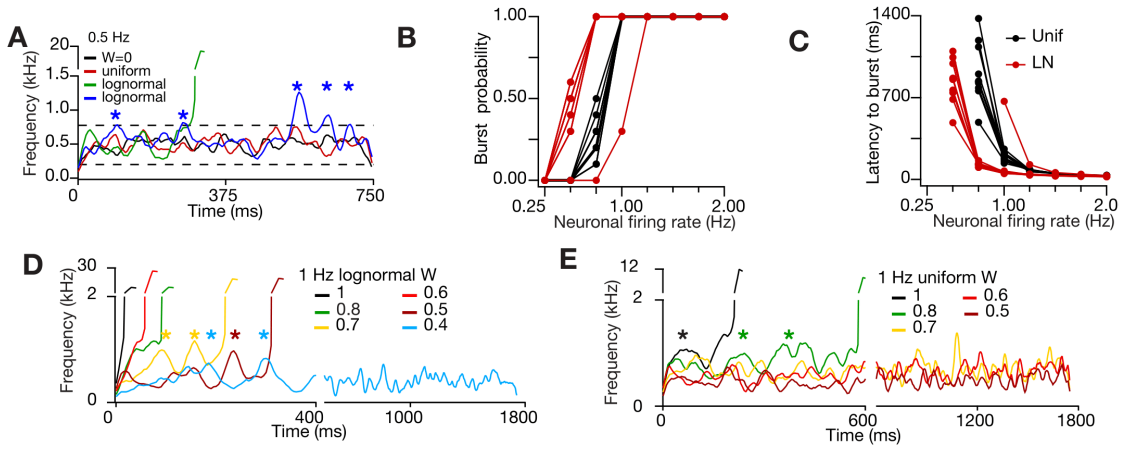

Figure 7.5: A. Average firing rate of ER networks with zero weights (black), uniform (red), lognormal (green and blue), when all neurons stochastically fire at 0.5 Hz. Dotted lines mark 99.75% range of firing rate for the network with zero weight. For lognormal note the partial synchronization and subsequent desynchronization of network activity (*) is similar to experimentally observed burstlets [80]. B-C. Probability (B) and mean latency to burst (C) of 10 ER networks with uniform (black) and lognormal weight distribution (red) when all neurons were made to fire at various Poisson distributed frequencies (Neuronal firing rate) indicated. D. Firing rate of an ER network with lognormal weight distribution when various fractions of its neurons (as indicated in color-code) stochastically fire at a frequency around 1 Hz. E, Same as (D) but with uniform weight distribution; note that the partially synchronized network activity (burstlets), preceding the full network burst, are more prominent and can be generated with a lesser fraction of randomly spiking neurons in networks with LN weights (D) as compared to the ones with uniform weight (E).

there is a reproducible distribution of time delays or latency times between the initiation of the stimulus and the induced burst. Finally, when one examines a network that is driven not by exogenous perturbations, but by the stochastic spiking by some or all of the network's constituent neurons, one should also observe induced bursts; these mimic the endogenous rhythmogenic activity of the microcircuit.

One of the open questions regarding the structure of the preBötC is its connectome. For the specific case of the preBötC, there is reliable data on the mean number of synaptic connections, and there is strong evidence that the circuit's connectome shows large variables amongst individuals. Its detailed structure is not unique, but appears to be drawn from a statistical ensemble of networks, whose topology remains poorly understood. To better identify the physiological ensemble of preBötC connectomes in a population, we consider a variety of random graphs drawn from ensembles that were selected based on previous work on brain microcircuits. To further reduce the space of potential numerical models, we used neuronal parameters consistent with the spiking behavior of typeI neurons in the preBötC.

This reduction of the search space in let of all network of $\mathcal{O}(10^3)$ is necessary as the space is combinatorially large and thus unsearchable. However, when we focused on classes of networks previously suggested to be physiologically plausible, we found that both the burst probability and latency time to bursting as a function of the number of stimulated neurons were quantitatively consistent with the data only for ER networks with both the physiological mean number of synapses and lognormally distributed synaptic weights. Secondly, we observed that, when we included temporally uncorrelated (beyond a refractory period) spiking of some or all of the constituent neurons, the system not only produced bursts, but also its dynamics included burstlets – periods of incipient spiking synchronization across the

network that reached a subthreshold maximum before decaying. Both bursts and burstlets are experimentally observed on conditions without exogenous stimulation.

This ignorance of the detailed structure of the preBötC microcircuit is not unique in neurophysiology and teasing out the detailed structure of circuits of thousands of neurons is not currently feasible. This presents an intriguing challenge for modeling: if one can strongly constrain the statistical properties of ensembles of connectomes by studying their simulated dynamics, one can strongly constrain the features of the hard to measure network structure using more accessible voltage dynamics of either selected neurons of the collective output of the circuit itself. Indeed, we observed that the dynamics of the system were extremely sensitive to both the connetome and to the distribution of synaptic weights within it. This sensitivity allows us to conclude that, amongst the plausible network ensembles explored, only ER graphs with fat-tailed distributions produced dynamics consistent with both the observed stimulated and stochastic dynamics of the circuit. It remains for future work to more precisely quantify how precisely one can make predictions regarding network structure and synaptic weight distribution based solely on the observed collective dynamics, but the present work comparing the ER and small-world graphs containing an only slight higher density of three-simplices suggests that dynamics alone provides a sensitive measure of the statistical properties of the underlying network.

A second line of analysis presented here considers how one can understand more mechanistically why certain exogenous stimulation events were more likely to elicit a burst. To address this question, we explored which features of the network's structure and the selection of stimulated neurons more reliably lead to a burst using a set of scalar measures of senderness, which incorporate both the network structure of a particular network (including its fixed stochastic weights), the particular stim-

ulated neurons, and their nonlinear response. To evaluate the predictive power of these various measures of senderness, we used a machine learning algorithm (MLA) to classify simulated experiments into those that lead to a burst and those that did not using a training set of numerical experiments. To make the classification problem as difficult as possible, we chose an ensemble of networks for which the bursting probability was near to one half. Using the assumption that the most predictive measure of senderness, when solely given to the MLA, incorporates the most information about the subsequent network dynamics after stimulation, we showed that only nonlinear measures of senderness using both the initially stimulated neurons and their nearest neighbors provided the uniquely best predictor. From this we infer two things, the nonlinearity of the senderness measure implies that the fat tail of the synaptic weight distribution dominates the network's response. Secondly, we note that input convergence at second order neighbor plays and important (but not as important and the fat tail) role in eliciting a burst. We suggest that this short of MLA-enabled search for predictive measures of senderness might be a more broadly useful tool to extract the important features of network topology and interactions associated with emergent collective phenomenon, with application to other neural circuits and perhaps more broadly.

We note that there remain a number of open questions. For instance, since we have studied here only the dynamics of burst initiation, clearly the same sorts of questions discussed here apply to burst termination. Burst termination is believed to be driven by dendritic depression associated with the number of EPSPs received by the dendrtic arbor during a period much longer than the temporal width of an individual spike. As a result, precise spike timing probably does not play as important a role in burst termination as it does in initiation. Understanding what

new constraints one can place on network structure by modeling burst termination remains an intriguing, related question, and one that may help to elucidate how relaxing the important of spiking synchrony will change the complex interplay of neuronal dynamics and network structure.

CHAPTER 8

Dynamical phase separation on rhythmogenic neuronal networks

8.1 Introduction

As we discussed in the Chapter 1, we need to add the inhibition to the model of the preBötzinger Complex [43, 154] to obtain the rhythmic behavior. In [154] such model was explored, with simplification of the neuron dynamics model to firing-rate based model. This simplification is reasonable, because the characteristic time of oscillation is significantly larger than inverted firing rate of neurons, so the averaging is well justified.

In addition to the stably oscillating phase of the network, this model was shown to admit two other phases: a quiescent phase, characterized by steady-state low-firing rate throughout the network, and a high-activity phase, characterized by a high firing-rate [154]. A dynamical phase diagram of this system was obtained as a function of network size and basal (low calcium) neuronal excitability both in a mean-field analysis and numerically on a set of Erdős-Rényi (ER) graphs [154]. Intriguingly, the numerically obtained phase boundary between the stably oscillating and high activity phases demonstrates significant deviations from the mean-field

theory predictions, with discontinuous "jumps" whose position on the phase diagram corresponds to numbers of neurons at which the highest k k-core [37] of the network vanishes [154].

In this chapter, we continue to explore the rhythmogenic properties of the model. In order to understand the underlying mechanism leading to the breakdown of mean field behavior and the emergence of k-cores affecting the dynamical phase boundaries, we study broadly the phase behavior of the model over a wide parameter range that includes the current best understanding of physiological preBötC. As a result, we observe a type of dynamical permutation symmetry breaking in which neurons dynamically separate into high- and low- firing rate groups on a network that maintains the permutation symmetry of the neurons' connectivity. This dynamical symmetry breaking - *s*pontaneous activity phase separation - is responsible both for the unexpected roughness of the phase boundaries and for the emergence of k-cores in locating the steps in those boundaries. Moreover, we observe that the dynamical phase space of the model is much richer than previously thought. In particular, we find that region of phase space consistent with stable oscillations is bounded in both network size and neuronal basal excitability. This is inconsistent with the mean-field predictions. We analyze activity phase separation on random networks both numerically and analytically, showing that the connectivity disorder of the random networks guides the separation process. After having broadly investigated the model over a wide range of parameters, we present results for systems with the expected physiological parameters. We note that the current bonds on these physiological parameters are rather large. Consequently, we mention which of our results are robust with respect to changing those parameters. Finally, we note that the model system is, remarkably robust to point (i.e., neuron) damage; this robustness is in

semi-quantitative agreement with experimental observations.

We organize the rest of the manuscript as follows. In section 8.2, we demonstrate spontaneous activity separation using small network to elucidate the process. We show how activity phase separation generates the observed roughness of the phase boundaries, a feature not captured by mean field theory. For the special case of an all-to-all coupled network, one can analytically derive activity phase separation. We do so, and compare these results to numerical simulations on all-to-all coupled networks in section 8.3. From that analysis, we learn that the steepness of the neuronal firing rate function (as a function of somatic potential) controls this spontaneous symmetry breaking on the network. In section 8.4, we move to the case of more sparsely connected networks, chosen from the ensemble of ER networks, where we prove that the activity separated solution, if it exists, is stable for sufficiently sharp neuronal firing-rate functions. The cases where such activity separated solutions do not exist is reminiscent of converse symmetry breaking [132], where symmetric solutions can be paradoxically stabilized by system asymmetry.

In section 8.5, we consider the role of k-cores in determining which neurons fall into the high-activity state in sparsely connected networks. We prove that, when setting the low somatic voltage firing rate to zero, activity phase separation is exactly controlled by the k-cores. We suggest that k-cores remain relevant in controlling the phase boundary between the quiescent and high activity phases of the disordered system, but these topological features cannot alone account the roughness of the high-activity/stable oscillation phase boundary.

In section 8.6, we summarize our main results on activity phase separation, and discuss the implications of our analysis for the physiological preBötC. The reader

primarily interested in our predictions for the *in vitro* preBötC system may choose to turn to that section. Reader interested in simulations will find a reference to our software and appropriate parameters in Appendix E.5.

8.2 The Feldman Del Negro model

Following Ref. [154], we describe the two-compartment neuron model of preBötC neurons. The i^{th} neuron is characterized by two dynamical variables, its somatic potential V_i and its dendritic calcium concentration C_i. Their dynamics are controlled by the equations

$$\frac{dV_i}{dt} = \frac{1}{\tau_V}(V_{eq} - V_i) + \Delta V(C_i)\sum_j M_{ij} r(V_j) \tag{8.1}$$

$$\frac{dC_i}{dt} = \frac{1}{\tau_C}(C_{eq} - C_i) + \Delta C\sum_j M_{ij} r(V_j), \tag{8.2}$$

where $\Delta V(C)$ and $r(V)$ are defined by

$$\Delta V(C) = \Delta V_{max}\sigma\left(\frac{C^* - C}{g_C}\right) \tag{8.3}$$

and

$$r(V) = (r_m - r_b)\sigma\left(\frac{V - V^*}{g_V}\right) + r_b. \tag{8.4}$$

In Eqs. 8.3, 8.4 we have introduced the standard sigmoid (Fermi) function

$$\sigma(x) = \frac{1}{1 + e^{-x}}. \tag{8.5}$$

Here and throughout the manuscript we work in dimensionless calcium concentration units obtained by setting $C_{eq} = 0$ and $C^* = 5$.

Eq. 8.1 is typical of a leaky integrate and fire model for an excitatory neuron. The principal addition in the two-compartment model is dendritic adaptation, which is

built into $\Delta V(C_i)$ defined in Eqs. 8.3 and 8.5. An incoming EPSP produces both an increase in dendritic calcium concentration ΔC and somatic potential $\Delta V(C)$. But above a threshold concentration C^*, $\Delta V(C)$ becomes small, rendering the neuron insensitive to subsequent EPSPs. In the absence of incoming EPSPs, the dendritic calcium concentration returns to C_{eq} on a time scale of τ_C at which point the neuron is once again sensitive to EPSPs.

The parameter space of the neuron model is controlled by a small set of physiological constants. There are the steady-state dendritic calcium concentration and somatic potential C_{eq} and V_{eq} respectively. The voltage-dependent firing rate is determined by the basal and maximal firing rates r_b and r_m as well as g_V, which controls the steepness of the transitions around the threshold voltage V^*. Dendritic adaptation is parametrized by the maximum voltage increment associated with an EPSP ΔV_{max}, a calcium concentration threshold C^* and a steepness parameter g_C, analogous to g_V discussed above. In addition to the two time scales $\tau_V < \tau_C$ for the relaxation of somatic potential and dendritic calcium, there is a fixed calcium concentration increment ΔC associated with the response to an EPSP. Table 8.1 provides the currently available values of the model parameters.

The model also depends on the size and connectivity of the underlying network of synaptic connections between the neurons. The network's structure can be encoded by an adjacency matrix $\mathcal{M}$ whose matrix elements $M_{ij} = 1$ if neuron i synapses on neuron j, and equal to zero otherwise. In this manuscript, we consider only networks built from uncorrelated stochastic connections – Erdős Rényi directed graphs [40]. An ensemble of such networks is determined by a single probability p that any non-diagonal matrix element is equal to one. We exclude the possibility of a neuron synapsing on itself. The all-to-all network is simply the case of such an ER graph

Table 8.1: Model parameters known from experiment

Parameter	**Approximate value**	**References**
V_{eq}	-65 mV	[92]
V^*	-50 mV	[92]
τ_V	20 ms	[146],[7]
r_m	40 Hz	[146],[7]
r_b	0.1 Hz	[7]
ΔV_{max}	2.8 mV	[146],[7]
p	0.065	[146]
N	10^3	[146], [57]

with $p = 1$.

8.2.1 Dynamical phase diagram

For a given set of parameters and given network of N neurons, the dynamical system evolves deterministically from a set of $2N$ initial conditions leading to either a fixed point, limit cycle, or chaotic dynamics at long times. We find multiple fixed points, which can be further distinguished as quiescent (Q) where the somatic potential averaged over the network of neurons $\langle V \rangle$ lies below the transition to the high-firing state V^*, or high activity (HA), where $\langle V \rangle > V^*$ [154]. Similarly, we can distinguish three classes of stable limit cycle oscillations: below threshold oscillations (BTO) where the oscillatory average voltage remains below the threshold for high firing rate, above threshold oscillations (ATO), where the oscillatory average voltage remains above the threshold for high firing rate, and true metronomic activity

(TMA), where the stable limit cycle oscillations carry the system between high and low firing rates, producing the physiologically observed inspiratory rhythm. While these three oscillatory phases were not distinguished in [154] we do so here to give more precise picture of the model's dynamical states.

To examine the dynamical phase behavior of the system, we vary the basal excitability of the neurons and the size of their network – ΔV_{max} and N – while fixing the rest of the parameters. We study a range of network sizes $10 \leq N \leq 10^3$, using the smaller networks ($N \approx 10^2$) for their computational efficiency [1] and the larger networks ($N \approx 10^3$) to approach the size of the physiological preBötC. We find that our principal results: activity phase separation and phase boundary roughness appear in both small networks and larger ones. In section 8.6, we return to the question of the model's large N limit, where we demonstrate that one can explore arbitrarily large N networks via a scaling relation.

Typical results for dynamical phase diagrams of the networks are shown in Fig. 8.1 for three different choices of the fixed variables. We observe in Fig. 8.1A the numerically determined phase diagram for all-to-all coupled networks, which agrees with the mean field solution of the model shown in Appendix C. In general, we find that the numerically determined phase diagram agrees with the mean field approximation in all-to-all networks (for arbitrary initial conditions) as long as the transition in dendritic sensitivity is sufficiently smooth, *i.e.* $g_C \gtrsim 1$ (see Appendix E.2). In this limit we observe all five dynamical phases: Q (light blue, lightest gray), BTO (blue, lighter gray), ATO (purple, darker gray), TMA (green, middle gray) and HA (dark red, darkest gray).

[1] Simulation time scales as N^2 for a single network and as N^3 to map the phase diagram for a particular set of network parameters

There are two ways to invalidate the mean-field predictions. The first is to make the dendritic calcium adaptation more abrupt, *i.e.*, decrease $g_C \lesssim 1$ while retaining the all-to-all coupling. In that case, we encounter a much more complex phase space as shown in Fig. 8.1B where the phases mix on a small scale in the parameter space. We also observe a dependence upon initial conditions. We discuss the quasi-periodic pattern arising in this case in the Appendix E.4. In effect, the dynamical phase diagram is not only highly heterogeneous, but also the regions that we associate with a particular phase may depend on the choice of initial conditions. The mean-field analysis is non-predictive, and one may say that the even the introduction of a dynamical phase diagram is not as well defined as in the mean-field case.

The second way to invalidate the mean-field predictions is more interesting. We maintain the smooth neuronal sigmoids, but reduce the number of network connections. In that case, as shown in Fig. 8.1C, the phase behavior of the network is once again insensitive to initial conditions. Moreover, the general structure of the mean-field phase diagram is preserved, but the phase boundaries are distorted. Both the HA (dark red, darkest gray) and Q (light blue, lightest gray) phases expand, while the physiologically relevant TMA (green) phase shrinks. Both the TMA and BTO (blue, lighter gray) phase are now bounded, whereas they extended to arbitrarily large ΔV in the mean-field prediction. In this regime, we do not see chaotic dynamics unlike in the cases where g_C is small. Changing other parameters of the model changes the shape of the phase boundaries, but does not introduce new dynamical phases. Both routes to the breakdown of mean field theory (small g_C and more sparsely connected networks) are related to an inherent instability toward activity phase separation. We discuss this in more detail below.

Before discussing the phase separation, we note that the roughness of the phase

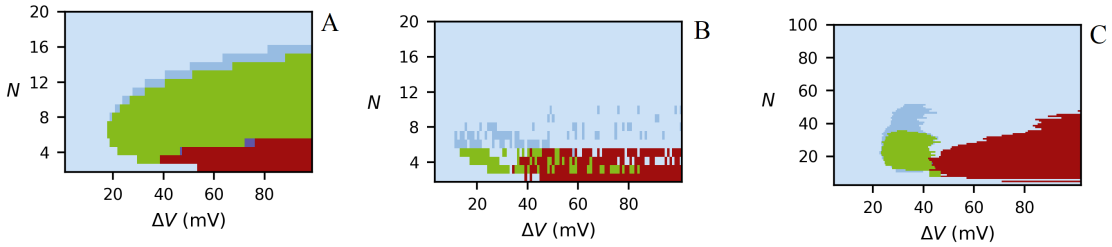

Figure 8.1: (Color online) Dynamical phase diagram of the model as a function of the size of the network N and basal neuronal excitability ΔV. (A) An all-to-all coupled network with large $g_C = 3$ produces phase behavior consistent with mean–field predictions, but (B) sharp sigmoids (small $g_C = 0.01$) produce a disordered diagram in which all dynamical phases are strongly mixed and the network dynamics is highly dependent on initial conditions. Finally, in (C) randomly connected networks ($p = 0.2$) with large $g_C = 3$, have initial-condition independent results with a modified dynamical phase diagram. In all three panels the phases are: Q (light blue, lightest gray), BTO (blue, lighter gray), HA (dark red, darkest gray), ATO (purple, darker gray), TMA (green, middle gray). All parameter values are listed in appendix E.5.

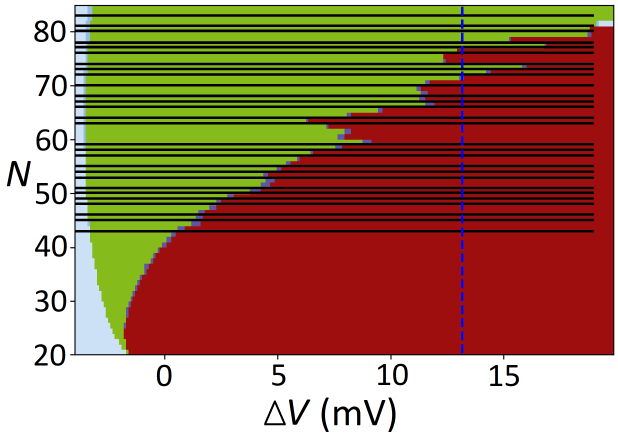

Figure 8.2: (Color online) Reentrant behavior along the of the TMA-HA phase boundary. k-cores transitions are shown as black lines, and colors are the same as at the previous figure.). All parameter values are listed in appendix E.5.

diagram in the non-mean-field regime, as shown in Fig. 8.1C, implies that the physiologically desirable stably oscillating phase (TMA) admits a type of reentrant behavior in which one can remove neurons (decrease N) from a network in the high activity state to render it in the stably oscillating TMA phase. In Fig. 8.2 we see examples of such possible transitions at $\Delta V = 18$mV (indicated by the vertical dashed line) where by decreasing the number of neurons from $N = 90$ to $N = 65$, one encounters transitions TMA-HA-TMA-HA, before remaining in the HA phase below $N = 72$. This suggests a specific experimental test of the fundamental model that can be made by looking for these reentrant dynamical transitions upon killing neurons in the network. In this figure we also show with black horizontal lines the values of N at which various k-cores of the network vanish. The positions of the tongues of extra stability of the oscillating TMA phase appear to be bounded by these k-core

transitions, suggesting that the disappearance high-k k-cores changes the stability of the oscillatory (TMA) phase. We return to this point in section 8.5, where we show that k-cores play a dominant role in the phase stability of a somewhat simplified version of the model.

The fact that removing neurons from the network can enhance its ability to maintain stable oscillations seems to be counter-intuitive. This reentrant behavior appears at many phase boundaries in the system, including the one between the high-activity (HA) and quiescent (Q) phases. An example of such reentrant behavior at this phase boundary is shown in Fig. 8.3. To understand how this behavior emerges, it is simpler to study this case where the neurons' dynamics reaches a fixed point rather than a limit cycle. Consider a fixed point of the system; setting the time derivatives on the left hand side of Eqs. 8.1, 8.2 equal to zero, we obtain

$$V_i = V_{eq} + \Delta V(C_i)\tau_V \sum_j M_{ij} r(V_j) \tag{8.6}$$

$$C_i = C_{eq} + \Delta C \tau_C \sum_j M_{ij} r(V_j) \tag{8.7}$$

For neuron i to be rapidly firing, it must receive a number of EPSPs consistent with both $V_i > V^*$ and $C_i < C^*$. In this way, its somatic voltage is maintained above the threshold, and it remains sensitive to EPSPs. Too many EPSPs will drive $C_i > C^*$, resulting in the neuron's somatic potential falling below that threshold, while too few EPSPs will allow $V_i < V^*$ even while maintaining dendritic sensitivity. As a result, the stable configuration of $V_i > V^*$ and $C_i < C^*$ can be destroyed by either adding or removing neurons that synapse on neuron i. We can see precisely how this works in an example of a small network of seventeen neurons poised near the HA-Q boundary.

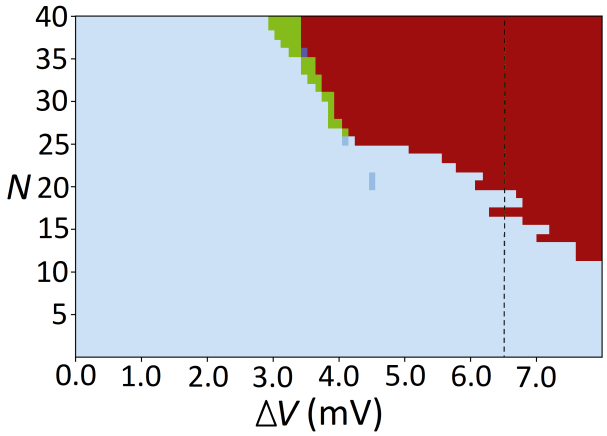

Figure 8.3: (Color online) Phase diagram showing reentrant behavior at the Q (light blue, lightest gray) HA (dark red, darkest gray) phase boundary. There are also small regions of the oscillatory phases: TMA (green, middle gray), ATO (purple, darker gray), BTO (blue, lighter gray). Black vertical dashed line shows reentrant behavior. The moving along this line is shown in Fig.8.4. All parameter values are listed in appendix E.5.

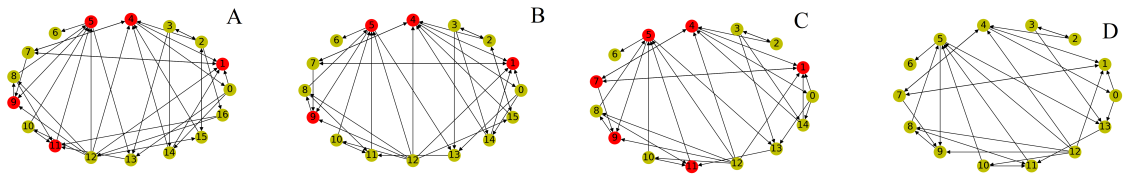

Figure 8.4: (Color online) Example of reentrant high activity on a small network. Red (dark gray) neurons have $V > V^*$ and dark yellow (light gray) $V < V^*$. The neurons are numbered and the last neuron in each network is removed when going $A \rightarrow B \rightarrow C \rightarrow D$. With the removal of neuron 16 (from A to B) , the somatic potential of neuron 11 drops below the threshold, as it has insufficient voltage input, and the average network voltage falls below V^*, too. Going from B to C neuron 15, which synapses to neuron 4, is removed, which lowers its calcium concentration. As a consequence, the somatic potential of the neuron 4 increases as well as its firing rate, resulting in increasing the firing rate and voltage input to neuron 7. The somatic potential of neuron 7 then goes above the threshold too. The increasing firing rate of neuron 4 also raises the somatic potential of neuron 0, which raises somatic potential of neuron 13, which in turn raises it for the neuron 11. Although somatic potentials of neurons 0 and 13 do not exceed V^*, for neuron 11 it does. As a result, the average voltage of the network rises above V^*. Finally, when neuron 14 is removed (from C to D), all neurons are deactivated and ΔV must increase to restore high activity. All parameter values are listed in appendix E.5.

In Fig. 8.4 we see that eliminating a low-firing rate neuron (number 16) from the network causes neuron 11 to change from high to low firing rate. Removing an excitatory neuron has the expected behavior of reducing the total activity of the network. But the subsequent removal of another low-firing rate neuron (neuron 15) results in neurons 7 and 11 once again returning to high firing rate. Finally, by removing the low-firing rate neuron 14, the entire network collapses into the quiescent state.

8.3 Spontaneous symmetry breaking on all-to-all networks

In this section we explore phase separation on all-to-all coupled networks, i.e., those having an adjacency matrix of the form $M_{ij} = 1$ for all $i \neq j$ and $M_{ii} = 0$ for all i. The steady-state of the system spontaneously breaks the permutation symmetry of the neurons. To explore this symmetry breaking, we first investigate the symmetry preserving solution, that is obtained from the pair of differential equations

$$\frac{dV}{dt} = \frac{1}{\tau_V}(V_{eq} - V) + (N-1)\Delta V(C) r(V) \tag{8.8}$$

$$\frac{dC}{dt} = \frac{1}{\tau_C}(C_{eq} - C) + (N-1)\Delta C r(V), \tag{8.9}$$

which results from setting $C_i = C(t)$ and $V_i = V(t)$ for all i in Eqs. 8.1, 8.2 and using the all-to-all adjacency matrix.

We demonstrated numerically that the dynamics of the full system Eqs. 8.1, 8.2 evolves towards this permutation symmetric solution for arbitrary initial conditions if the sigmoidal functions $P(V)$ and $\Delta V(C)$ are smooth enough (see Fig. 8.5C, D). If, on the other hand, these sigmoids are sharper, the system becomes unstable towards activity phase separation (breaking the original permutation symmetry of

the underlying network) into time-independent subnetworks of high and low firing rate neurons, when the initial conditions are not themselves identical across the network (see Fig. 8.5A, B). The phenomenon of activity phase separation in all-to-all biological networks has been observed in a model of cell regulatory networks [122, 151].

The symmetry broken state is, of course, not captured by the mean field analysis. To explore it, we need to analyze the full system of equations. Defining the sum of firing rates over the entire network as $R = \sum_i r(V_i)$, we rewrite the dynamical system as

$$\frac{dV_i}{dt} = \frac{1}{\tau_V}(V_{eq} - V_i) + \Delta V(C_i)\,[R - r(V_i)] \tag{8.10}$$

$$\frac{dC_i}{dt} = \frac{1}{\tau_C}(C_{eq} - C_i) + \Delta C\,[R - r(V_i)]\,. \tag{8.11}$$

Now we can look for a self-consistent solution of this system, *i.e.*, we find $V_i(R)$ such that $R = \sum_i r(V_i)$. Studying the nullclines of Eqs. 8.10, 8.11, we see that it can have one to three fixed points. The cases of one and three fixed points are shown in Fig. 8.6, where we see the intersections of the nullclines of Eqs. 8.10 and 8.11 in orange (light gray) and blue (dark gray) respectively.

Since we are looking for a self-consistent solution, we can not analyze its stability directly from the graph; however, we can find the fixed points and later analyze their stability. For neuronal parameters consistent with smooth sigmoids, there is only one fixed point (V_f, C_f) for a fixed value of R. This self-consistent solution is both permutation symmetric and consistent with our mean field prediction. In contrast, for sharp sigmoids, there is more than one fixed point, so it is possible to find some fraction of the network neurons at a high-voltage fixed point, while the remainder is at a low-voltage fixed point. The number of neurons in these two categories is

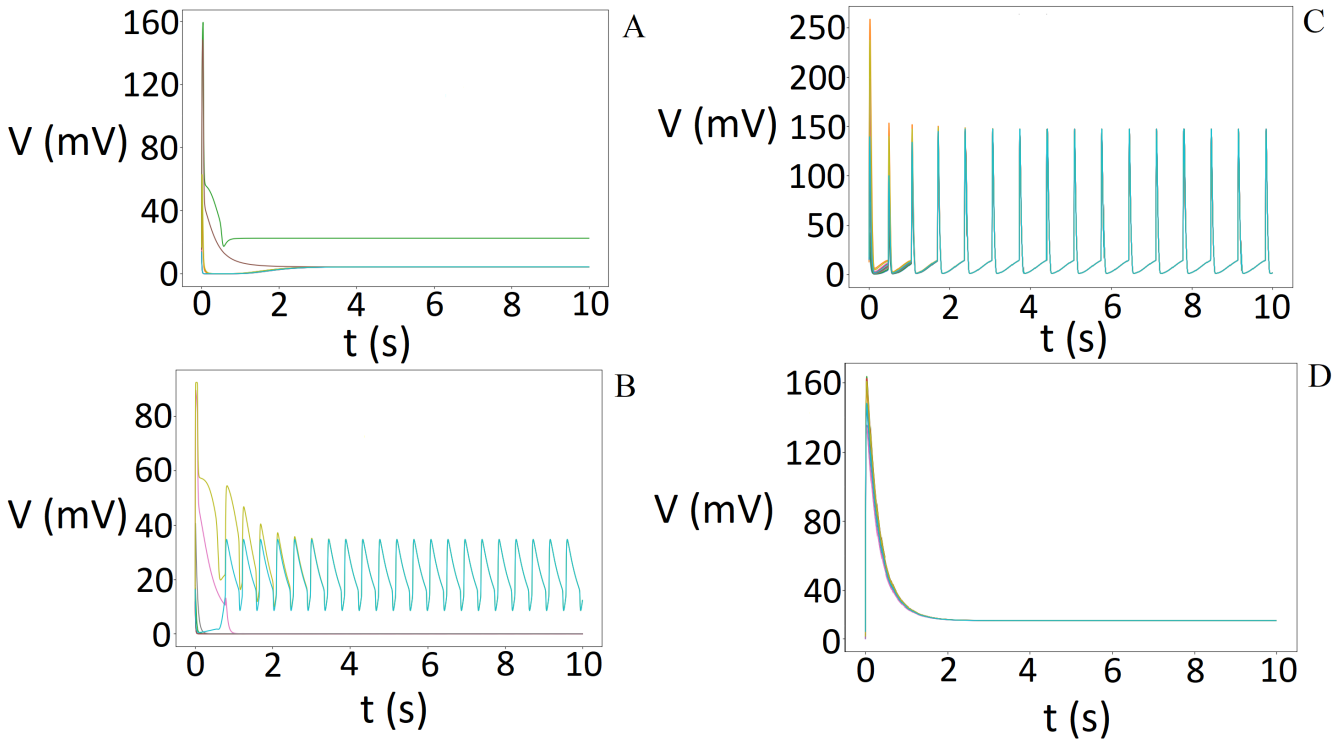

Figure 8.5: Activity phase separation on all-to-all connected network of $N = 10$ neurons. The traces show somatic potential of individual neurons as a function of time. (A) One neuron is at high voltage , nine are quiescent, $g_V = 0.3$ mV, $g_C = 0.5$. (B) Two neurons oscillate, eight are quiescent, $g_V = 0.3$ mV, $g_C = 0.5$. (C) Synchronous oscillations of all neurons, $g_V = 0.1$ mV, $g_C = 1.1$. (D) All neurons at high voltage, $g_V = 1.8$ mV, $g_C = 10.8$. All parameter values are listed in appendix E.5.

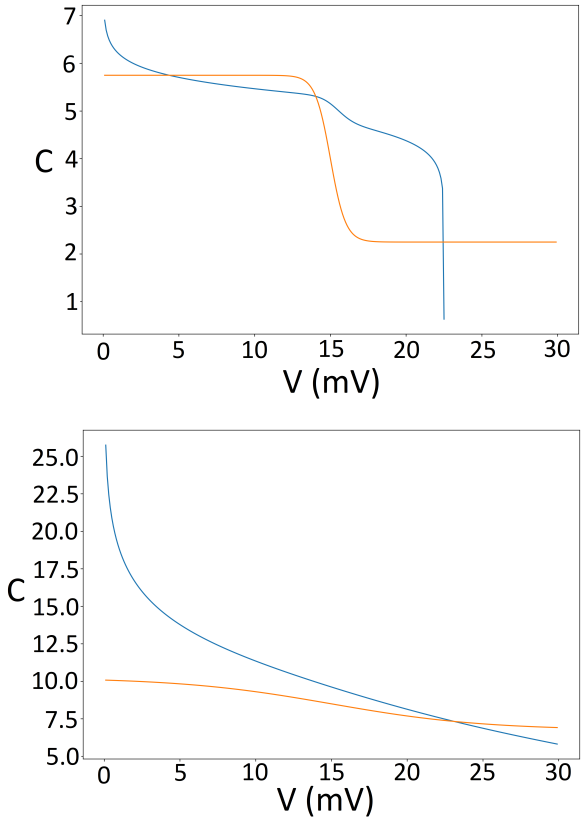

Figure 8.6: (Color online) Nullclines of the all-to-all $N = 10$ network described by Eqs. 8.10 (orange, light gray) and 8.11 (blue, dark gray) in the text. There are either three fixed points or one fixed point depending on parameters. Assuming R is constant (and not fixed self-consistently) two of the fixed points annihilate in a standard pitchfork bifurcation [173]. (A) $g_V = 0.5$ mV, $g_C = 0.3$, three fixed points. (B) $g_V = 5$ mV, $g_C = 3$, one fixed point. All parameter values are listed in appendix E.5.

determined by the condition $R = \sum_i r(V_i)$. There is also a range of parameters with $g_V > 0, g_C = 0$, such that the self-consistent solution does not exist.Therefore, there is no fixed point, and only oscillations are allowed. See Appendix E.4 for the details of the analytical calculation.

For the small values of g_C (sharp sigmoid), the phase separation into firing and quiescent neurons is the only stable state. For intermediate values of g_C we still observe this stable state shown in Fig. 8.5A. We also show activity separation into oscillating and quiescent subnetworks in Fig. 8.5B. Continuing to increase g_C we obtain synchronous oscillations of the whole network in Fig. 8.5C, and, finally, fixed point with constant uniform activity in Fig. 8.5D.

For the case of the large physiological-like network $N = 1000$ neurons we also observe phase separation in the case of the sharp sigmoid (Fig.8.7), which demonstrates that the separation is not the finite-size effect.

8.3.1 Step function limit: All-to-all networks

To better understand activity phase separation on the network, it is useful to consider a non-physiological limit of the model in which the sigmoidal functions describing both the firing rate and the dendritic adaptation are taken to be infinitely sharp, *i.e.*, step functions: $g_V = g_C = 0$. In this case, neurons with above-threshold voltage V^* fire at the maximal rate r_m, while neurons below that threshold voltage fire at the basal rate r_b. If the number of high and low firing rate neurons are n_h and n_l respectively ($n_h + n_l = N$) we find that

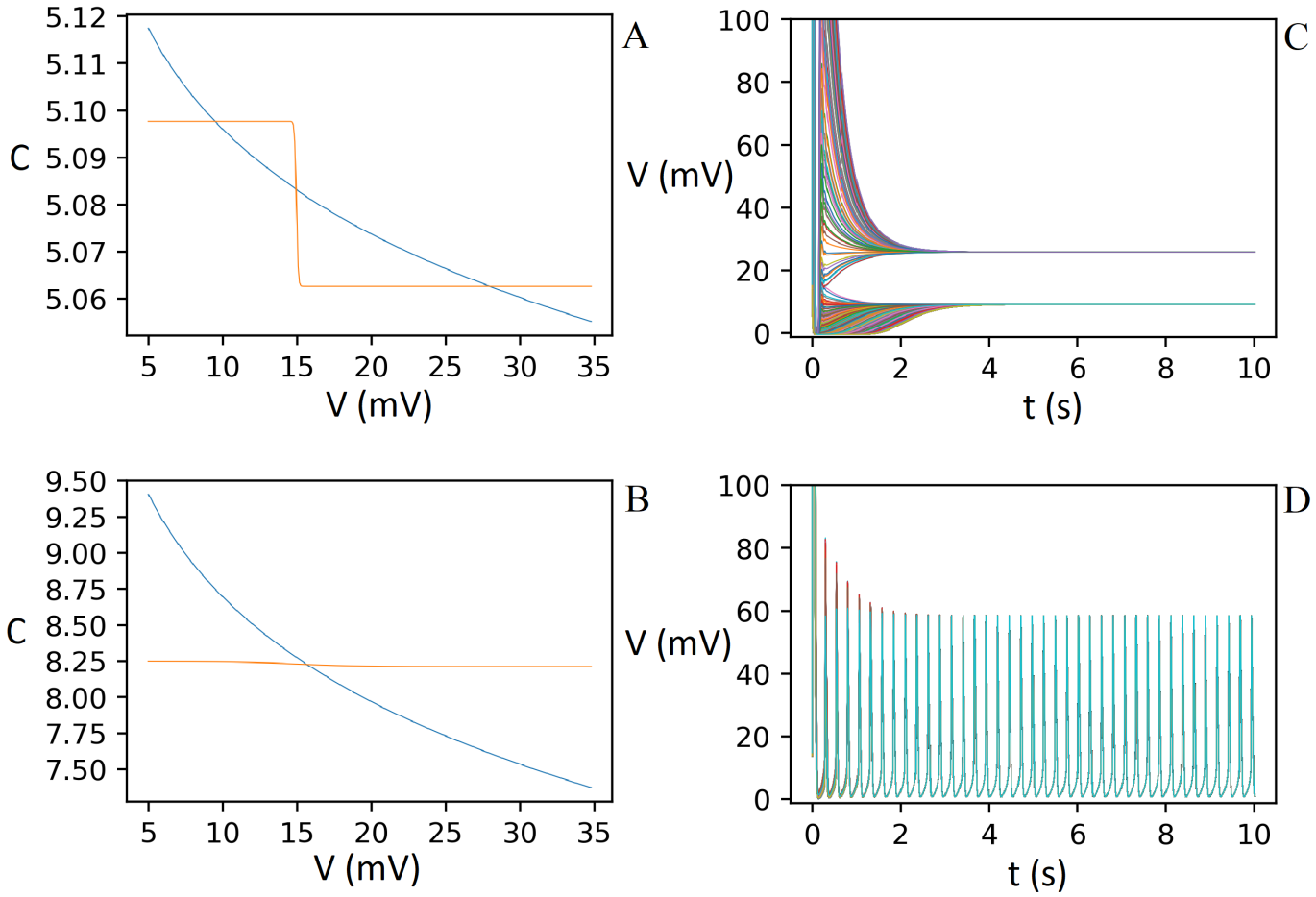

Figure 8.7: Activity phase separation on all-to-all connected network of $N = 1000$ neurons. The left panel shows nullclines as in Fig.8.6, the right panel shows corresponding traces of voltage versus time, as in Fig.8.5. The upper panel demonstrates activity separation for $g_V = 0.05$ mV, $g_C = 0.03$. The lower panel show no such phase separation but synchronous oscillation with $g_V = 2$ mV, $g_C = 1$. All parameter values are listed in appendix E.5.

$$V_h = V_{eq} + \Delta V(C_h)\tau_V \left[(n_h - 1)r_m + n_l r_b\right] \tag{8.12}$$

$$C_h = C_{eq} + \Delta C\tau_C \left[(n_h - 1)r_m + n_l r_b\right]. \tag{8.13}$$

Similarly, the low firing-rate neurons have

$$V_l = V_{eq} + \Delta V(C_l)\tau_V \left[(n_l - 1)r_b + n_h r_m\right] \tag{8.14}$$

$$C_l = C_{eq} + \Delta C\tau_C \left[(n_l - 1)r_b + n_h r_m\right]. \tag{8.15}$$

One can check that rate of spikes received by a high firing-rate neuron $R_{high} = [(n_h - 1)r_m + n_l r_b]$ is less than that received by a low firing-rate neuron $R_{low} = [(n_l - 1)r_b + n_h r_m]$. However, the condition for being at a high firing rate is $V^* < V_h$ and a low firing rate is $V^* > V_l$. For these inequalities to hold simultaneously with the result that $R_{high} < R_{low}$, one needs the high firing-rate neurons to be more sensitive to incoming spikes than the low firing-rate ones. Thus we conclude that this state requires $C_l > C^* > C_h$. From this conclusion, we find n_l, the number of low-firing rate neurons, to be

$$n_l = \left\lfloor \frac{(Nr_m - r_b)\Delta C\tau_C + C_{eq} - C^*}{\Delta C\tau_C(r_m - r_b)} \right\rfloor, \tag{8.16}$$

where we have introduced the *floor* function: $\lfloor x \rfloor$ = the integer part of the real number x.

To observe the phase separated state, we require that the high-firing rate neurons remain sufficiently sensitive to incoming spikes. The lower bound of their sensitivity $\Delta V(C_h)$ is given by

$$V^* - V_{eq} < \Delta V(C_h)\tau_V \left[(n_h - 1)r_m + n_l r_b\right]. \tag{8.17}$$

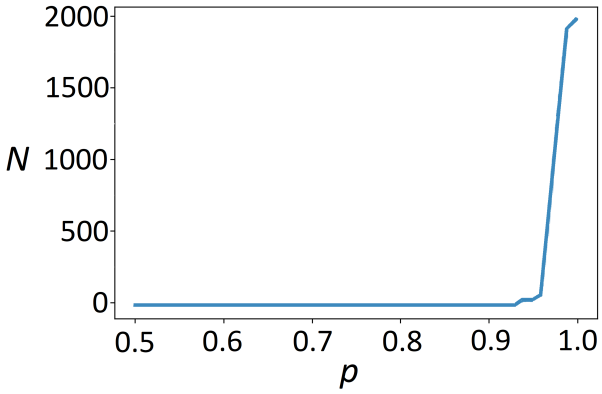

Figure 8.8: Number of stable fixed points as a function of the network connectivity probability p for $N = 100$ neurons. For $p = 1$ this number coincides with $\frac{n!}{n_l! n_h!}$, and rapidly falls to one or zero when $p \lesssim 0.9$. All parameter values are listed in appendix E.5.

While the number of neurons at low firing-rate neurons n_l is fixed by Eq. 8.16, the identity of these neurons is determined solely by the initial conditions on the all-to-all network. There are a large number $\frac{n!}{n_l! n_h!}$ of otherwise identical fixed points that are related by permutation symmetry of the network. If, however, the network is more sparsely connected and thus does not have this permutation symmetry, there are fewer fixed points, as is discussed in the following section.

8.4 Symmetry breaking on sparse networks

If we randomly remove edges from the all-to-all network, we break the permutation symmetry of the neurons, and produce an instance of a network selected from ensemble of ER networks with probability $p < 1$ of a directed connection between neurons.

This leads to a rapid reduction in the number of stable fixed points with decreasing p, as shown in Fig. 8.8.

Below $p \approx 0.9$ the number of stable fixed points drops to just one or vanishes entirely, resulting in only an oscillatory or approximately chaotic solution. For the case of the step function neurons, or for sufficiently sharp sigmoidal responses, we do not typically observe globally synchronized oscillations. The asynchronous firing of different neurons results in many self-crossing for the network averaged V vs. C graph, as shown in Fig. 8.9.

While for the smooth sigmoids the most common case when oscillations occur is an unstable fixed point, this is not possible when sigmoids are very sharp. Indeed, any fixed point that not exactly on the threshold in this case is stable, as shown in Appendix E.3. Therefore, the only opportunity for the oscillatory or approximately chaotic behavior is the absence of fixed point.

8.4.1 Oscillations on star networks

In order to understand how all fixed points vanish in sparser networks, we consider the special case of a star network, in which one central neuron is bidirectionally coupled to $N-1$ other neurons. Those other neurons are not coupled to each other. Such a network is shown in Fig. 8.10.

We choose parameters such that the range of the central neuron's firing rate is large enough to take the peripheral neurons across their firing-rate threshold:

$$\Delta V(0)\tau_V r_b < V^* < \Delta V(0)\tau_V r_m. \tag{8.18}$$

Furthermore, we require that all the peripheral neurons firing together at their basal

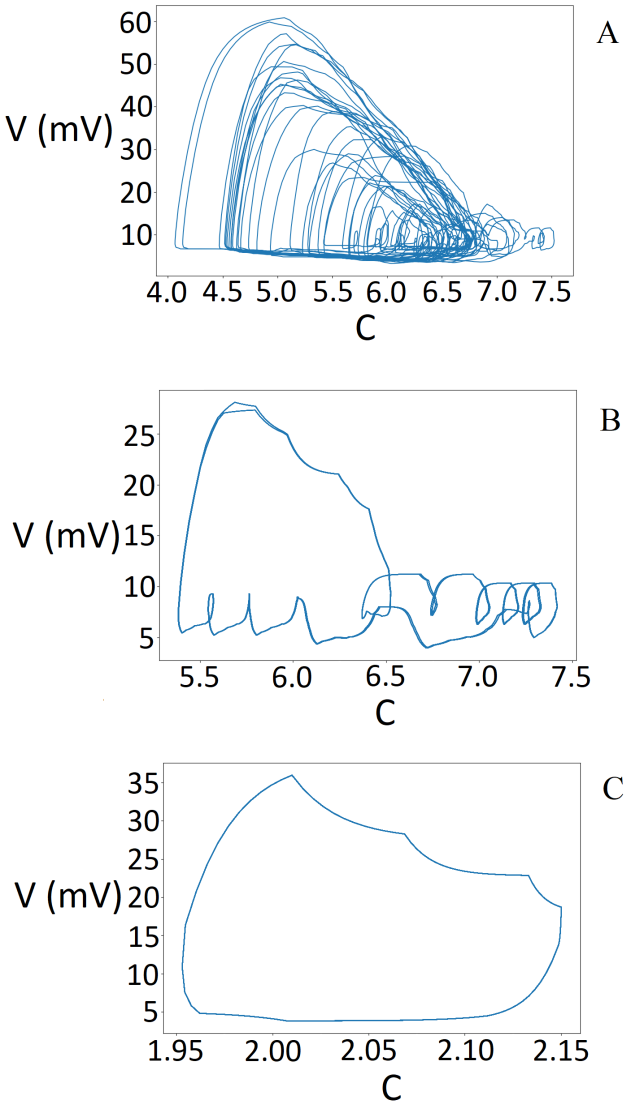

Figure 8.9: Phase trajectories in the averaged $V - C$ plane for networks with step–function neurons. (A) Almost chaotic behavior. True chaos is not observed since the number of possible states is finite, but the voltage varies wildly. (B) Limit cycle with self-intersections, indicating asynchronous firing. (C) Standard limit cycle with synchronous firing, corresponding to true metronomic activity (TMA), rarely observed in the step-function limit.

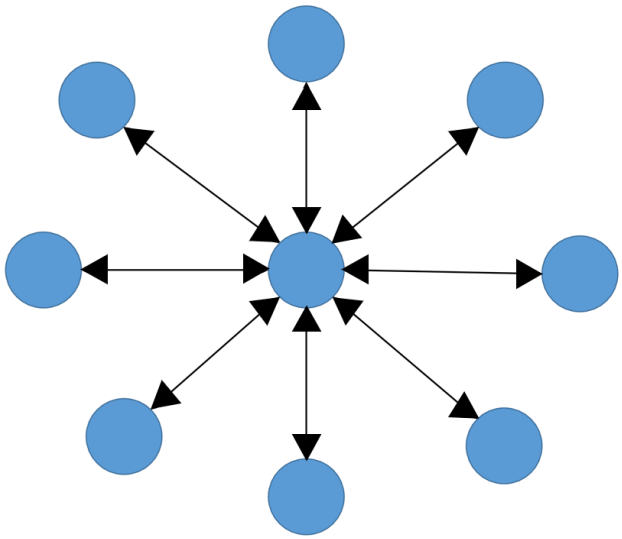

Figure 8.10: A star network with $N = 9$ neurons. The peripheral neurons are bidirectionally coupled to the central neuron, but not to each other.

rate are able to excite the central neuron over threshold. If, however, the central neuron's dendritic calcium is above threshold, then all the peripheral neurons firing at their maximal rate are collectively insufficient to excite the central neuron:

$$(N-1)\Delta V(C > C^*)\tau_V r_m < V^* < (N-1)\Delta V(0)\tau_V r_b. \tag{8.19}$$

We also demand two conditions on the calcium threshold. First, a single neuron cannot fire rapidly enough to push another neuron's dendritic calcium over threshold:

$$C^* > \Delta C \tau_C r_m. \tag{8.20}$$

$N-1$ neurons, however, firing at their maximal rate can induce calcium concentrations over threshold in the central neuron:

$$(N-1)\Delta C \tau_C r_b < C^* < (N-1)\Delta C \tau_C r_m, \tag{8.21}$$

but they cannot do so when they are all firing at their basal rate.

By obeying all of the above inequalities, the system cannot reach a fixed point. Instead the network with these step-function neurons oscillates. The central neuron excites the peripheral ones and then those neurons drive the central neuron's calcium concentration above threshold rendering it insensitive. As a result, the central neuron returns to its low firing state and then so do the peripheral ones. At this point, the cycle begins again.

Recall, however, that the step-function neurons on the all-to-all coupled network do not oscillate, instead they reach one of many fixed points characterized by activity phase separation. By breaking the permutation symmetry of the network, the star network admits a new synchronous oscillatory phase. This is reminiscent of an effect called converse symmetry breaking [132], where the necessary condition for synchronous activity of a coupled network of oscillators is an asymmetry of this system. We observe a similar stability of globally synchronous oscillations in random networks that break the permutation symmetry such as the ER graphs discussed above.

8.5 The effect of network heterogeneity on phase separation

We have established that the neuron model leads generically to activity phase separation. On permutation symmetric all-to-all networks, this phase separation is a form of a spontaneously broken symmetry, but it exists on more sparse networks too. This poses the question: how does the network topology modify phase separation? To address this, we consider another simplified limit of the model by setting $r_b = 0$ (i.e. a neuron is either firing or not), using a step function firing rate ($g_V \to 0$),

and eliminating dendritic adaptation by taking $C^* \to \infty$. The system in this limit is equivalent to coarse-grained neuronal network considered in [104] that based on mutualistic ecosystem network studied in [125]. It was shown that in such model k-core exactly coincides with the most stable part of the system (the active voxels in subliminal state in [104] and surviving species in [125]). We repeat below the derivation of this effect in terms of the system at hand based on [104, 125] demonstrating that, in this case, the cluster of firing neurons will be a k-core of the network with k determined by neuronal parameters.

Consider n_i actively firing input neurons synapsing on neuron i. From the fixed point condition $\dot{V}_i = 0$ we find

$$\frac{V_i}{\tau_V} = n_i \Delta V r_m. \tag{8.22}$$

For the i^{th} neuron to be part of the group of actively firing ones, $V_i > V^*$, which implies that number n_i of firing inputs exceeds a lower bound:

$$n_i \geq \frac{V^*}{\tau_V \Delta V r_{max}}. \tag{8.23}$$

We intend to relate the actively firing group with a topological feature of the network: a k-core. This structure is defined to be the maximal subnetwork, such that within it each neuron has k or more inputs from the other neurons in that subnetwork. k-cores have been discussed in a variety of applications in neuroscience, bioinformatics, ecology, and the study of social networks [125, 10, 157, 98]. The condition for a neuron to be in the actively firing group, Eq. 8.23, is equivalent to membership within a k-core with the integer k given by

$$k = \left\lfloor \frac{V^*}{\tau_V \Delta V r_{\max}} \right\rfloor. \tag{8.24}$$

If a k-core with some k given by Eq. 8.24 is absent from the network, the dynamical system on that network relaxes to the quiescent fixed point, but if such a k-core is present, the neurons making up the k-core become fixed in the HA phase. We note that for typical values of k, most of the network will be part of that k-core [37] because for $k > 2$ the probability of a neuron being part of the k-core has a discontinuous jump from zero to a significant value as a function of the density of synaptic connections (in the thermodynamic limit of large networks).

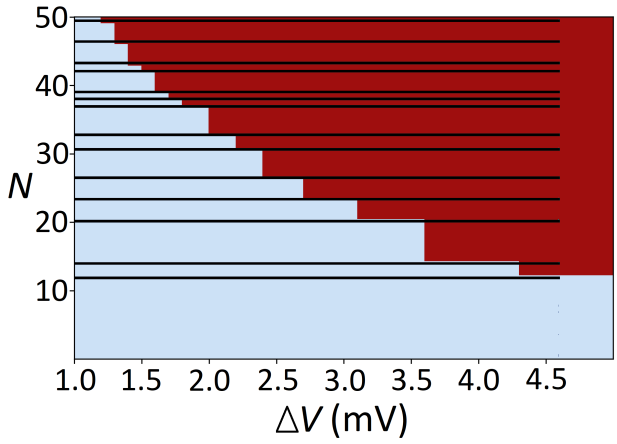

Figure 8.11: (Color online) The phase diagram for the simplified model discussed in section 8.5. There is no oscillatory phase, only quiescent (Q, light blue, lightest gray) and high activity (HA, dark red, darkest gray). Black horizontal lines correspond to k-core transitions. We see almost exact correspondence between k-cores transtions and steps on the phase boundary. Small deviations are due to the fact that the average voltage of the whole network can be below V^* even in the presence of the active k-core due to the averaging over all neurons including quiescent ones. All parameter values are listed in appendix E.5.

We compare our predicted phase boundary of the system and k-cores in Fig. 8.11. The predicted k value for a particular set of n and ΔV parameters corresponds exactly to the point in phase space where the HA phase gives way to the Q phase. For this restricted version of the Feldman Del Negro model, at least, there is a precise correspondence between the neuronal network's dynamical phase behavior and the prediction made purely from the topology of the underlying network. k-cores completely determine the dynamical phase transition of the neurons interacting on them, and how the network phase separates into groups of high and low activity neurons.

8.6 Discussion and applications to the preBötzinger complex

We have explored the FDN model of oscillations in the preBötC and found a form of dynamical phase separation on the network in which groups of neurons separate into high and low firing-rate fixed points. This firing-quiescent phase separation plays the crucial role in the termination of the TMA phase. One feature that emerges from this work is that the permutation-symmetric system (the all-to-all coupled network) admits a type of spontaneous symmetry breaking into these high and low activity phases. In more sparse networks such as in the physiological preBötC, this permutation symmetry is broken by the network. The details of network connectivity modify the inherent instability of the system toward phase separation into groups of high and low firing-rate neurons. In one particular limit of the model, we found that this interaction of neuronal dynamics and network topology is particularly simple. By examining only the k-core structure of the network, one can precisely predict both the dynamical phase diagram and which neurons will end up in the high and

low firing rate groups.

In the full model, the effect of the k-cores in determining the phase boundaries of the dynamical system remains, but no longer does it completely control these dynamics. The incomplete influence of k-cores was observed earlier [154]. Here we believe we have better elucidated the underlying mechanism and explained why their control of the dynamics is not complete.

To assess the importance of these observations for the physiological preBötC, we first present the numerically computed phase diagram for 1000 neurons using parameters consistent with physiological measurements. This is shown in Fig. 8.12. Please see appendix E.1 for a discussion of how the neuronal and network parameters were selected.

As discussed in the appendix, there is a remaining uncertainty in determining the value of ΔC. Moreover, the full preBötC has somewhere between two to three times as many neurons as used in the simulation. We note, however, a scaling argument, based on the mean-field analysis of the model, that allows us to shift ΔC as a way of effectively changing the network's size. In the mean-field theory, three parameters ΔC, ΔV, and pN appear in only two combinations $pN\Delta V$ and $pN\Delta C$. As a result, if we change $\Delta C \to \frac{\Delta C}{\lambda}$, $\Delta V \to \frac{\Delta V}{\lambda}$, and $pN \to pN\lambda$ the mean-field solutions are invariant. We can test this scaling hypothesis in the full model by comparing the phase diagram of the N=1000 network with $\Delta C = 2.5 \times 10^{-2}$, shown in Fig. 8.13, to a much smaller network of $N = 100$ and $\Delta C = 0.1$, shown in Fig. 8.1C. Their correspondence supports out exploration of larger networks using calcium scaling.

The scaling hypothesis suggests that, if we were able to expand the network size used in Fig. 8.12 to the preBötC's true physiological size, we would find that the

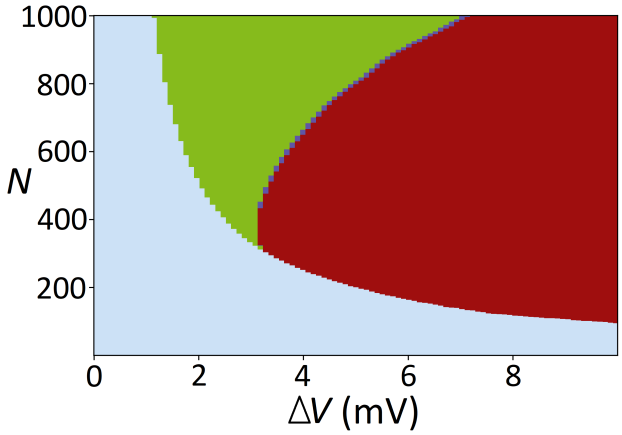

Figure 8.12: (Color online) Phase diagram of the network with physiologically relevant parameters. It shows three stable dynamical phases: true metronomic activity (TMA, green, middle gray) consistent with the preBöC's physiological dynamics, as well as a high activity (HA, dark red, darkest gray), and a quiescent (Q, light blue, lightest gray) regime. There is a narrow band of above threshold oscillations (ATO, purple, darker gray). The diagram corresponds to the part of the phase diagram in Fig.8.13 in the black frame under rescaling, thus does not have all the possible phases present. All parameter values are listed in appendix E.5.

region of stable oscillations is bounded from above as well as for high and low neuronal excitability. We see in Fig. 8.13 that the large N network has a rough phase boundary between the TMA and Q on the right side of the bounded TMA domain, which is incompatible with the mean-field analysis and reflects the role of dynamical phase separation on the network. This result makes an interesting prediction in that there are regions of the phase diagram in the physiological system where *increasing* neuronal excitability can actually produce globally quiescent networks, through

calcium inhibition. This feature cannot be reproduced by the mean-field model.

Another consequence of this large N phase diagram is that we can predict the robustness of the network to damage. From Fig. 8.13, we see that under optimal conditions, one can destroy about eighty percent of the network before causing the collapse of the oscillating phase. This agrees with experimental observations [57]. One may notice that the crucial condition for this robustness is the smoothness of the sigmoids. If we make sigmoids sharper, the system becomes highly sensitive not only to damage but also to the initial conditions (see Appendix E.2 for the influence of parameters g_V and g_C controlling the sharpness of sigmoids).

We propose three types of experimental tests of the above analysis. The first of these, alluded to above, is that the network should be able to be silenced by increasing neuronal excitability. Secondly we predict that the roughness of the phase boundaries, particularly when N is large, suggests presence of multiple reentrant transitions in which the network goes from being oscillatory to quiescent, and back to oscillatory as neurons are removed from it. Third, one should be able to directly observe dynamical phase separation in the system. In either the high activity or quiescent phase, one should be able to find neurons trapped at the other fixed point so that the globally quiescent state of the network should harbor some fixed fraction of high firing rate neurons. Conversely, the network in its globally highly active state should contain a subpopulation of neurons trapped in their low firing-rate state.

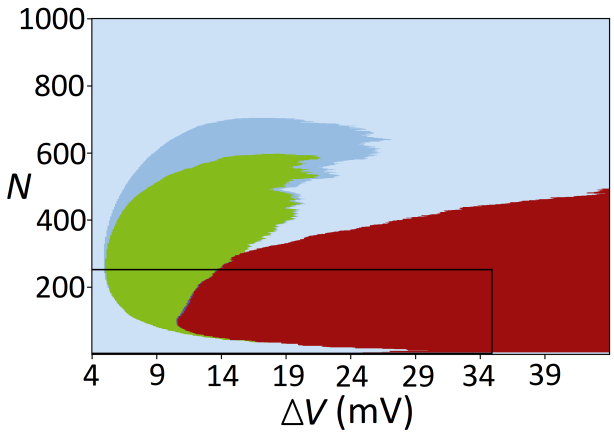

Figure 8.13: (Color online) Phase diagram of large networks with N up to 1000. All five phases are present: true metronomic activity (TMA) is green (middle gray), below threshold oscillations (BTO, blue, lighter gray), above threshold oscillations (ATO, purple, darker gray), high activity (HA, dark red, darkest gray), and quiescent (Q, light blue, lightest gray). The right TMA-BTO and BTO-Q boundaries demonstrate the reentrant behavior. In general, the pattern is approximately the same as in Fig. 8.1C, supporting the scaling argument. The black frame shows the part of the diagram that maps into the phase diagram in the Fig.8.12 under rescaling. All parameter values are listed in appendix E.5.

APPENDIX A

Appendix for "Topological defects produce kinks in biopolymer filament bundles"

A.1 Additional information for collagen experiments

A.1.1 Pepsin extracted collagen

We observed kinking only in pepsin-extracted collagen. Acid-extracted collagen (TeloCol 5225, Advanced BioMatrix) produces bundles with no observable kinks under confocal microscopy. Structural differences between acid- and protein-digested collagen have been previously described in literature [152]. It is possible that defects in the bundles are introduced during the reconstitution process with a higher probability when the covalent cross links between collagen molecules are removed during the pepsin digestion, which allows greater freedom to the collagen subfibrils during the early stage of collagen hydrogel reconstitution. However, this is not easy to explore experimentally. We reconstituted the collagen by adjusting the pH of the soluble collagen solution to 7 with NaOH followed by dilution in PBS (phosphate buffered saline, Gibco). We did not add any cross-linking enzymes or chemicals at any point. We estimated the range of number of filaments per bundle in our system from published SEM images of similarly reconstituted type-1 collagen bundles to be xxx -xxx.

([123, 60, 143]).

A.1.2 Work flow for measuring curvature of bundle from image using splines

We determined the curvature of the bundle in the four steps. First, we obtain the brightness of each pixel in the raw image of the bundle. Second, for each value of position X we consider the brightness of the pixel as the function of y. Third, for each x, we do a Gaussian fit of this function, obtaining the mean and standard deviation, which we consider to be y position of this piece of the bundle and the measurement error respectively. Fourth, we use MATLAB fit function in *smoothspline* mode to obtain the trace of the filament $y(x)$ before calculating the curvature to regularize non-physical, extremely large values of curvature that are just an artefact of data collection [3, 34, 35]. Finally, we repeat the last step with addition of the random errors, that have a uniform distribution on the interval ± 1 pixel to estimate propagation of error in position to error in curvature. See Fig. A.2 for the illustration of the work flow.

A.1.3 Angle of kink over time

We recorded 50 images of each bundles in total. However, the kinks are not visible in every frame due to movement of the bundle. The measured angle may vary – see Fig. A.1 for the measurement of the single kink angle in different frames using the angle tool in imageJ ([4]). For the general results, we measured the angle of the kink in at least three different images using imageJ and we reported the average of these angles – see results for all bundles in the Fig. 2.1 in main document.

A.1.4 Measured angle compared to true kink angle

The experimentally measured kink angle is actually the angle of the 2D projection of the kink onto the microscope's focal plane. To estimate the true kink angle distribution, we perform the following numerical algorithm. First, for each physical 3D kink angle ϕ in the interval $(0°, 180°)$ with $5°$ steps, we generate bundles (two straight line segments, each with length 3μm, joined at the specified angle ϕ) in 3D with random orientations distributed uniformly over the unit sphere. The centers of the kinks were also randomly positioned with respect to the focal plane. As a result, most physical kinked bundles have little overlap with the focal plane, having less than 3 microns of visible bundle length on either side of the kink. These bundles are rejected just as they were in experiment. The bundles that completely fit in the focal plane of thickness 1 μm are then projected onto this plane, and the angle of the projection is measured.

We gather 1000 such projections for each possible 3D kink angle ϕ. We thus obtain the distribution of the measured angles for each particular 3D angle. From these thousand cases, we construct a vector representing the frequency of kink angles lying within five-degree bins of observed kink angle in our two-dimensional projection d_2. Of course, this should correspond to the actual histogram data, which is shown in Fig. 1C of the main text. In actuality, we wish to solve the inverse problem: Given that we observe a particular distribution of projected kink angles onto the focal plane, what is physical distribution of those kink angles in three-dimensions? We call this latter distribution d_3 in analogy to the just introduced vector d_2. The error introduced by our two-dimensional projection of the three-dimensional kinks can be estimated by comparing these two vectors.

Taking the numerically obtained mapping of d_3 to d_2, we introduce the matrix M relating them:

$$d_2 = M d_3. \tag{A.1}$$

Inverting this, we obtain the desired information – how to relate the observed d_2 to the physical distribution of kink angles ds_3, namely

$$d_3 = M^{-1} d_2. \tag{A.2}$$

Using the experimentally observed distribution d_2, we obtain the most likely distribution of physical kink angles, which is shown in Fig. A.3A. The nonphysical negative frequency values at small kink angles are caused by the fact that we underestimated the number of small kinks in the data. We surmise that these low-angle kinks were rejected as being straight, or unkinked bundles. Artificially increasing the number of such weakly kinked bundles in the observed data – see Fig. A.3B – leads to positive frequencies for all the physical, three-dimensional kink angles.

The most likely physical kink distribution obtained from this data analysis does not dramatically differ from the observed kink angle distribution obtained from the focal plane projections. This can be understood simply because we required that one observe enough of the straight bundles on either side of the kink to ensure that the plane of physical, kinked bundle is nearly parallel to and lies within the focal plane of the instrument. Quantitatively, we observed less than ten percent differences between the relative frequency of the projected and inferred physical kink angle frequencies in the more highly populated bins around thirty degrees. The differences between these frequencies approached twenty percent for the smallest kink angle bins. For nearly vanishing kink angles, the projection effect introduced greater uncertainties since there are more orientations of a weakly kinked, nearly straight bundle that kept

the bundle within the focal plane.

A.1.5 Estimation of ζ for collagen bundles

The exact mechanism by which reconstituted collagen forms bundles from a soluble state is poorly understood [178, 183, 83, 55, 49, 23, 159]. Relevant to this manuscript, the stiffness of native collagen bundles has been measured for both dry and hydrated states, and scanning electron micrographs reveal network ultrastructure, including potential kinks. Importantly, while the aforementioned studies used predominantly native collagen bundles, we examine here samples of reconstituted fibrous collagen hydrogels, which have been depleted of telopeptides that form many of the intramolecular covalent cross links. Due to pepsin digestion and lack of cross-linking enzymes in the hydrogels, we infer that cross linking is driven by electrostatic interactions. Molecular simulations using a coarse-grained model provides estimates of parameters μ, a, and κ, where κ is derived from measurements of native collagen. This model includes an array of intramolecular interactions of strength $11.06\,\mathrm{kcal\,mol^{-1}}$, and effective spacing of 14.72 Å, and filament stiffness $14.98\ \mathrm{kcal\,mol^{-1}}$ (see Ref. [17, 33, 39]). These electrostatic interactions are reversible, a key feature of our model and simulations. ζ can be estimated from the course grain model as follows:

$$\mu = \frac{7.7 \times 10^{-20}\mathrm{J}}{1.4 \times 10^{-9}\mathrm{m}} \tag{A.3}$$

$$a = 1.47 \times 10^{-9}\mathrm{m} \tag{A.4}$$

$$\kappa = \left(1.381 \times 10^{-23}\mathrm{J/K}\right)(300K)\,(23.4\mathrm{nm}) = 9.695 \times 10^{-29}\mathrm{m\ J}. \tag{A.5}$$

These values lead to an estimate of ζ for collagen filament bundles of:

$$\zeta \approx 1.2. \tag{A.6}$$

A.2 Further information about the numerical model and the setup of the computational experiments

A.2.1 Setup of the computational experiments

Initially, all filaments were chosen to be straight and parallel without any cross links, as mentioned in the main article. The number of filaments in the bundle was varied between $N = 2$ and $N = 225$. In the plane perpendicular to the initial direction of the filaments, the filaments were arranged on a hexagonal grid with spacing $d = d_0 = 100$nm between the filaments. We also conducted simulations using a square grid and did not observe any noticeable influence of this initial lateral arrangement of the filaments on our results. Unless otherwise stated, the filaments were free to move in 3D. In the minimal setup of two filaments in 2D, the two parallel filaments were constrained to move only in the plane by means of Dirichlet boundary conditions on all beam nodes. Upon beginning the simulation at time $t = 0$s, the stochastic thermal forces acted on the filaments in combination with the random binding and unbinding of cross links give rise to the self-assembly of the bundles. The bundle shapes, including, for instance, the curvature of the bundle centerline along its length, as well as the distribution of cross links were analyzed over the entire simulation time of up to 1000s.

A.2.2 Filament model

As mentioned in the article, each filament is described by means of nonlinear, geometrically exact, 3D Simo-Reissner beam theory [145, 160]. In terms of the structural rigidity of the filament, we thus account for axial, torsional, bending, and shear deformation. All filaments are chosen to be initially straight with a length of $L_0 = 20\mu\text{m}$ and persistence length $L_p \approx 7\mu\text{m}$. The geometrical and material parameters resemble F-actin, which is a key constituent of the cytoskeleton. A complete specification is given by the cross-section area $A = 1.9 \times 10^{-5}\mu\text{m}^2$, area moment of inertia $I = 2.85{\times}10^{-11}\mu\text{m}^4$, polar moment of inertia $I_p = 5.7{\times}10^{-11}\mu\text{m}^4$, Young's modulus $E = 10^9\text{pN}/\mu\text{m}^2$, Poisson ratio $\nu = 0.3$, and shear correction factor $\kappa_s = 0.75$. By default, we discretized each filament with 100 beam finite elements using linear Lagrange shape functions for the centerline discretization [74]. Alternatively, we used 20 beam finite elements with cubic Hermite polynomials for the centerline interpolation [118].

A.2.3 Brownian dynamics model

As mentioned in the article, we account for the Brownian dynamics of the filaments by including stochastic thermal forces and viscous drag forces acting as line loads along the beam axis [28, 29]. Viscous forces and moments are computed assuming a quiescent background fluid and individual damping coefficients for translations parallel and perpendicular to the filament axis, as well as rotation around the filament axis. Thermal forces are determined from the stochastic Wiener process in accordance with the fluctuation-dissipation theorem. Finally, an implicit Euler scheme is used to discretize in time and a Newton-Raphson algorithm solves the result-

ing nonlinear system of equations. In our simulations, the temperature is set to $T = 293\text{K}$ and the dynamic viscosity of the quiescent background fluid is assumed to be $\eta = 10^{-3}\,\text{Pa}\,\text{s}$. We applied a base time step size of $\Delta t = 0.01\text{s}$ and an adaptive time stepping scheme, which iteratively reduces the time step size if needed.

A.2.4 Cross-link model

All details on the applied cross-link model can be found in Reference [129]. This numerical model tracks linker molecules explicitly as they switch between three possible states: free, singly bound, or doubly bound. Free linker molecules experience Brownian motion until eventually all binding criteria are met and they establish a first, and later possibly a second, connection to a filament. In the doubly bound state, i.e., a cross-link spanning two filament binding spots on different filaments, each linker is treated as an additional, very short beam element, which can transmit forces and moments between the filaments. The binding decision is made based on a given binding rate k_{on} and a distance criterion that takes into account the spatial extent $L_\ell \pm \Delta L_\ell$ and thus action range of the linker molecule. Moreover, the linker molecule is assumed to have a preferred orientation with respect to the filaments, which is expressed in terms of two scalar angles. The first angle α_f denotes the mutual angle of the filament tangents at the binding spots. The second angle α_ℓ describes the angle between the cross-linker axis and (either one of) the filament tangents. Finally, the orientation preference of a linker molecule is specified as the allowed range of angles $\alpha_f \pm \Delta\alpha_f$ and $\alpha_\ell \pm \Delta\alpha_\ell$. In order to establish a cross-link, all angle criteria, as well as the aforementioned distance criterion and the probability criterion based on the binding rate need to be met.

The length of the linker is chosen to be $L_\ell = 100\text{nm}$ (with a tolerance of $\Delta L_\ell = 2\text{nm}$) and the angle preferences are set to $\alpha_f = 0\text{rad}$ (i.e. parallel filament axes, with a tolerance of $\Delta\alpha_f = \pi/100\text{rad}$) and $\alpha_\ell = \pi/2\text{rad}$ (i.e. perpendicular cross-linker and filament axes, with a tolerance of $\Delta\alpha_\ell = \pi/4\text{rad}$. For all 3D simulations, the total number of linker molecules has been set to $N_\ell = 20000$. This results in a volume number density of $\rho_\ell \approx 36\mu\text{m}^{-3}$, because the size of the periodic simulation box has been chosen to be $22 \times 5 \times 5\mu\text{m}$. In the special case of the two-filament bundle in (pseudo) 2D, the linker density ρ_ℓ has been kept constant and the total number of linker molecules has been set to $N_\ell = 20000$ for a reduced box size of $22 \times 5 \times 1\mu\text{m}$. The binding spots along the filament are assumed to be located equidistantly with a spacing of $\Delta s_{\text{bs}} = 0.02\mu\text{m}$, resulting in 1000 binding spots per filament. It is important to note that each binding spot can be occupied by at most one cross linker. Unless otherwise stated, the binding and unbinding rates specifying the reaction kinetics are set to $k_{\text{on}} = 90\text{s}^{-1}$ and $k_{\text{off}} = 3\text{s}^{-1}$. Only for the experiments studying the dynamics of defects, an increased unbinding rate of $k_{\text{off}} = 6\text{s}^{-1}$ has been applied to speed up the reorganization of cross-links and be able to observe, for instance, the dynamics and interaction of braids within feasible simulation times. These parameter values are chosen based on experimentally measured rate constants of F-actin crosslinker proteins. Typical values reported for different species such as alpha-actinin [53, 121], filamin [53], myosin [116], and fascin [177] lie in the range of $10 < k_{\text{on}} < 100\,\text{s}^{-1}$ for binding and $0.1 < k_{\text{off}} < 10\,\text{s}^{-1}$ for unbinding. Note, however, that the measured chemical reaction rate for binding depends on the reactants' concentrations and therefore needs to be converted to the binding rate of a *single* linker in our numerical model based on its effective reaction volume. More details can be found in our previous article [30].

The material specification of the cross links, which are thought to be short, stiff rods, is given as follows. Each cross link is included as one additional beam element with cross-section area $A = 4.75 \times 10^{-6}\mu\text{m}^2$, area moment of inertia $I = 4.5\times10^{-11}\mu\text{m}^4$, polar moment of inertia $I_p = 9.0\times10^{-11}\mu\text{m}^4$, Young's modulus $E = 10^{10}\text{pN}/\mu\text{m}^2$, Poisson ratio $\nu = 0.3$, and shear correction factor $\kappa_s = 0.75$. These parameter values aim to mimic the properties of actin binding proteins, which are another key constituent of the cytoskeleton, and is thus in accordance with the F-actin-like filaments described above.

A.2.5 Additional plots of simulation results

Figs. A.4 and A.5 provide additional plots of simulation results. In Fig. A.4 we show the time evolution of the number of cross linkers within the bundle (left) and the number of braids (right). In the former, we observe the rapid quench to a fully cross linked bundle in about 20s of simulated time in all five runs shown. In the latter, we see the initial quenching of braids. Typically there are a number of such defects, but their number is rapidly reduced over time due to either braid annihilation or diffusion off the edges. Typically, one or more of these braids become a long-lived defect on the bundle.

In Fig. A.5B-D we plot the curvature of the bundle's centerline at three different points in time. The configuration of the two-filament bundle shown in Fig. A.5A corresponds to the curvature data plotted in D. This complements the plot of the mean (black) and standard deviation range (red) of the curvature shown in Fig. 2.1E of the main manuscript, which is reproduced here in Fig. A.5E for the reader's convenience. In summary, Fig. A.5 illustrates the connection between the braids in

the bundle and the peaks in the curvature as well as the curvature fluctuations at these locations.

A.3 Details of theoretical calculations

A.3.1 Loops

We consider the case of two-filament bundle, where uncross-linked segments of the first and second filaments with lengths L_1 and L_2 respectively are trapped between two cross links. The extra trapped length makes the filaments bend, resulting in a kink - see Fig. A.8. We assume here for simplicity that the cross-links are of zero length. These cross-links completely fix both the angle and position of the filaments at the point of binding so that they are parallel. If we parametrize the conformation of i^{th} filament by the angle its local tangent makes with respect to a fixed coordinate axis as a function of arc length s, $\alpha(s)$, the energy of the two-filament bundle (shown in Fig. A.8) is given by

$$E = \mu L + \frac{\kappa_1}{2}\int_{-L_1/2}^{L_1/2} ds\alpha_1'^2(s) + \frac{\kappa_2}{2}\int_{-L_2/2}^{L_2/2} ds\alpha_2'^2(s), \tag{A.7}$$

where $\kappa_{1,2}$ are bending moduli of the two filaments, $L_{1,2}$, is the trapped length of the two filaments in the loop, and μ is binding energy of the cross-links per unit length. $L = \max(L_1, L_2)$ is the uncross-linked part of the bundle, which incurs an energy increase of μL due to the absence of cross linker binding energy within the loop. At the ends of this uncross-linked region, we impose boundary conditions on the x and

y coordinates of the position of the filament ends

$$\int_{-L_1/2}^{L_1/2} ds \sin\alpha_1(s) = \int_{-L_2/2}^{L_2/2} ds \sin\alpha_2(s) \tag{A.8}$$

$$\int_{-L_1/2}^{L_1/2} ds \cos\alpha_1(s) = \int_{-L_2/2}^{L_2/2} ds \cos\alpha_2(s), \tag{A.9}$$

and on the angles at the ends of the loop

$$\alpha_1\left(\pm\frac{L_1}{2}\right) = \alpha_2\left(\pm\frac{L_2}{2}\right). \tag{A.10}$$

We rescale the integration variable $ds = L_i dz$ to have the same integration limits over both filaments in Eqs. A.8, A.9.

$$E = \mu L + \int_{-1/2}^{1/2} dz \left[\frac{\kappa_1 \alpha_1'^2}{2L_1} + \frac{\kappa_2 \alpha_2'^2}{2L_2}\right]. \tag{A.11}$$

Renaming the tangent angles at the ends of the loop $\phi = 2\alpha_i\left(-\frac{1}{2}\right)$ and $\psi = 2\alpha_i\left(\frac{1}{2}\right)$, and gathering the boundary conditions into the rescaled loop energy integral Eq. A.7 using delta functions (where necessary) and six Lagrange multipliers ($\lambda_i^{\pm}$ and $\lambda_{c,s}$) to impose the various boundary constraints, we write:

$$\begin{aligned} E &= \mu L + \int_{-1/2}^{1/2} dz \Bigg\{ \frac{\kappa_1 \alpha_1'^2}{2L_1} + \frac{\kappa_2 \alpha_2'^2}{2L_2} + . \\ &+ \lambda_s \left(L_1 \sin\alpha_1 - L_2 \sin\alpha_2\right) + \lambda_c \left(L_1 \cos\alpha_1 - L_2 \cos\alpha_2\right) + \\ &+ \lambda_1^+ \left(\delta\left(s - \frac{1}{2}\right)\alpha_1 - \frac{\phi}{2}\right) + \lambda_1^- \left(\delta\left(s + \frac{1}{2}\right)\alpha_1 + \frac{\psi}{2}\right) + \\ &+ \lambda_2^+ \left(\delta\left(s - \frac{1}{2}\right)\alpha_2 - \frac{\phi}{2}\right) + \lambda_2^- \left(\delta\left(s + \frac{1}{2}\right)\alpha_2 + \frac{\psi}{2}\right) \Bigg\}. \end{aligned}$$

Minimizing this energy with respect to $\alpha_{1,2}(s)$ we obtain

$$\frac{\kappa_1 \alpha_1''}{L_1} = \lambda_s L_1 \cos\alpha_1 - \lambda_c L_1 \sin\alpha_1 + \lambda_1^+ \delta\left(s - \frac{1}{2}\right) + \lambda_1^- \delta\left(s + \frac{1}{2}\right) \tag{A.12}$$

$$\frac{\kappa_2 \alpha_2''}{L_2} = -\lambda_s L_2 \cos\alpha_2 + \lambda_c L_2 \sin\alpha_2 + \lambda_2^+ \delta\left(s - \frac{1}{2}\right) + \lambda_2^- \delta\left(s + \frac{1}{2}\right). \tag{A.13}$$

To satisfy these equations, we need to impose four boundary conditions at the filament ends $s_i/L_i = \pm 1/2$

$$\frac{\kappa_i}{L_i}\alpha_i'\left(\mp\frac{1}{2}\right) = \pm\lambda_i^{\mp}, \tag{A.14}$$

and demand that the tangent angles $\alpha_{1,2}(s)$ obey the differential equations

$$\frac{\kappa_1}{L_1}\alpha_1'' = \lambda_s L_1 \cos\alpha_1 - \lambda_c L_1 \sin\alpha_1 \tag{A.15}$$

$$\frac{\kappa_2}{L_2}\alpha_2'' = -\lambda_s L_2 \cos\alpha_2 + \lambda_c L_2 \sin\alpha_2. \tag{A.16}$$

in the interior.

Eqs. A.15, A.16 are familiar in that their express the equation of static equilibrium for a beam subject to forces appplied at their ends. These forces are exerted by the filaments on each other via the cross links at the ends of the loop. We choose our coordinates so that the $\hat{x}$ axis passes through the first cross link on each side of the loop shown as black circles in Fig. A.8. These forces are equal and opposite; to ensure that there is no unbalanced torque on the loop, they must lie in the $\hat{x}$ direction. This leads to $\lambda_s = 0$. So

$$\frac{\kappa_1}{L_1}\alpha_1'' = -\lambda_c L_1 \sin\alpha_1 \tag{A.17}$$

$$\frac{\kappa_2}{L_2}\alpha_2'' = \lambda_c L_2 \sin\alpha_2. \tag{A.18}$$

Minimizing the energy with respect to the angles ϕ and ψ, we obtain

$$\lambda_1^+ + \lambda_2^+ = 0 \tag{A.19}$$

$$\lambda_1^- + \lambda_2^- = 0, \tag{A.20}$$

which leads to

$$\frac{\kappa_1\alpha_1'\left(\frac{1}{2}\right)}{L_1} + \frac{\kappa_2\alpha_2'\left(\frac{1}{2}\right)}{L_2} = 0 \tag{A.21}$$

$$\frac{\kappa_1\alpha_1'\left(-\frac{1}{2}\right)}{L_1} + \frac{\kappa_2\alpha_2'\left(-\frac{1}{2}\right)}{L_2} = 0 \tag{A.22}$$

using Eqs. A.14. Due to the symmetry of the problem, the solution should have $\phi = \psi$ so both $\alpha_i(s)$ are odd functions. Using these solutions for the Lagrange multipliers in the force balance equations Eqs. A.17,A.18 and returning to the dimensionful arc length independent variable we find the conditions for force balance

$$\kappa_1 \alpha_1'' - F \sin \alpha_1 = 0 \tag{A.23}$$

$$\kappa_2 \alpha_2'' + F \sin \alpha_2 = 0, \tag{A.24}$$

where $F = \lambda_c$ is the force acting on the end. The conditions for torque balance at the ends of the loop are

$$\kappa_1 \alpha_1' \left(\pm \frac{L_1}{2} \right) = \tau \tag{A.25}$$

$$\kappa_2 \alpha_2' \left(\pm \frac{L_2}{2} \right) = -\tau \tag{A.26}$$

using Eqs. A.21 and A.22 and observing that $\tau = \lambda_1^+$ is the torque.

Let us consider the limit of small angles between the filaments' tangents and the $\hat{x}$ axis, $\alpha_i(s) \ll 1$. Then for nearly straight filaments Eqs. A.23,A.24 can be linearized:

$$\kappa_1 \alpha_1'' - F \alpha_1 = 0 \tag{A.27}$$

$$\kappa_2 \alpha_2'' + F \alpha_2 = 0. \tag{A.28}$$

The solution of Eqs. A.27,A.28 with boundary conditions Eqs. A.25,A.26 is

$$\alpha_i(s) = (-1)^{i+1} \frac{\tau}{\kappa_i \omega_i \cosh\left(\frac{\omega_i L}{2}\right)} \sinh\left(\omega_i s\right) \tag{A.29}$$

with $\omega_1^2 = F/\kappa_1$ and $\omega_2^2 = -F/\kappa_2$. The boundary conditions Eqs. A.8,A.10 then give

$$L_1 - \frac{\tau^2 L_1}{4\kappa_1^2 \omega_1^2} \left(\frac{2 \tanh\left(\frac{\omega_1 L_1}{2}\right)}{\omega_1 L_1} - 1 + \tanh\left(\frac{\omega_1 L_1}{2}\right)^2 \right) = L_2 - \frac{\tau^2 L_2}{4\kappa_2^2 \omega_2^2} \left(\frac{2 \tanh\left(\frac{\omega_2 L_2}{2}\right)}{\omega_2 L_2} - 1 + \tanh\left(\frac{\omega_2 L_2}{2}\right)^2 \right) \tag{A.30}$$

and

$$\frac{\tau}{\kappa_1\omega_1\cosh\left(\frac{\omega_1 L_1}{2}\right)}\sinh\left(\frac{\omega_1 L_1}{2}\right) = -\frac{\tau}{\kappa_2\omega_2\cosh\left(\frac{\omega_2 L_2}{2}\right)}\sinh\left(\frac{\omega_2 L_2}{2}\right) \tag{A.31}$$

respectively. Eq. A.9 is automatically satisfied since $\alpha_i(s)$ are odd functions. To obtain a simple solution of these equations, consider the case where $\kappa_1 = \kappa_2 = \kappa$. Then $\omega_1 = i\omega_2 = i\omega$. We simplify Eq. A.31 to

$$\tan\left(\frac{\omega_1 L_1}{2}\right) = -\tanh\left(\frac{\omega_2 L_2}{2}\right) \tag{A.32}$$

If we further assume that the trapped length is approximately the same for both filaments, i.e., $\Delta L = L_2 - L_1 \ll L_1$. Then we find from Eq. A.32 that

$$\omega L_1 \approx \omega L_2 \approx 2x \tag{A.33}$$

where $x \approx 2.365$, which is the first nonzero solution of $\tan x = -\tanh x$. Then Eq. A.30 gives

$$\tau = \sqrt{\frac{2\Delta L}{L}}\frac{2\kappa x}{L} \tag{A.34}$$

The bundle's energy is

$$E = \mu L + \frac{4\Delta L \kappa x^2}{L^2} \tag{A.35}$$

This energy is still subject to minimization with respect to the length of the loop L. Doing so we obtain

$$L = 2\left(\frac{\Delta L \kappa x^2}{\mu}\right)^{1/3} \tag{A.36}$$

Finally, we obtain the kink angle by substituting into Eq. A.29:

$$\phi = 2\frac{\Delta L^{1/3}\mu^{1/6}}{\kappa^{1/6}x^{1/3}}\tanh(x). \tag{A.37}$$

The kink angle grows continuously as $\Delta L^{1/3}$. This analytic result is graphed in Fig. 2.6A of the main manuscript.

A.3.2 Braiding

In this subsection, we explore the energetics of braided bundle configurations with three filaments. We consider first the limit of stiff filaments, which allows us to make certain mathematical approximations detailed in the next subsection.

A.3.2.1 Stiff filaments

When filaments are stiff, i.e., $\frac{a^2\mu}{\kappa_{1,2}} \ll 1$, we use two ansätze: the small slope approximation and $\frac{L^2\mu}{\kappa_{1,2}} \ll 1$. The small slope approximation requires that the filaments' tangents always lie near to the $\hat{x}$ the direction parallel to the tangent of the bundle in its undeformed, mechanical ground state. In that case, it is useful to characterize the conformation of the i^{th} filament by its contour $y(x)$. Note that we have replaced arc length s by the x position as the independent variable. In the small angle approximation, the difference between these independent variables is small and contributes only at higher than quadratic order in the filament's Hamiltonian. We may write the energy of the filament in this approximation as

$$E = \sum_{i=1,2} \int_{-b/2}^{b/2} dx \left\{ \frac{\kappa_i}{2}(y_i'')^2 + \mu(1 + \frac{1}{2}y_i'^2) \right\}, \tag{A.38}$$

where b is the length of the braided region where the cross linking density vanishes. This will be determined later by energy minimization. Once again, μ is the binding energy per unit length of the filament. This term indicates the energy loss associated with the fact that there is no cross-links coupled to the filament in the braid. The boundary conditions are $y_i(\pm b) = \pm a_i \cos\phi$, $y'(\pm b_i) = \pm \tan\phi$ with $a_1 + a_2 = a$, the size of the cross link. After we minimize the energy Eq. A.38 of the bundle filament

with respect to the conformations of the filament $y(x)$ we obtain

$$E_i = b\mu + 2\kappa_i\omega\left(\frac{a_i^2\omega_i^2\cos^2\left(\frac{\phi}{2}\right)}{-\tanh\left(\frac{\omega_i b}{2}\right)+\frac{\omega_i b}{2}} + \frac{\tan^2\left(\frac{\phi}{2}\right)}{\sinh\left(\frac{\omega_i b}{2}\right)}\cosh\left(\frac{\omega_i b}{2}\right)\right) \tag{A.39}$$

where $i = 1, 2$ and $\omega_i = \sqrt{\frac{\kappa_i}{\mu}}$.

The second ansatz is equivalent to $\omega_i b \ll 1$ once we assume small slopes. Then the bundle energy is

$$E = b\mu + 4\sum_{i=1,2}\left(\frac{12\kappa_i a_i^2\cos^2\left(\frac{\phi}{2}\right)}{b^3} + \frac{\kappa_i\tan^2\left(\frac{\phi}{2}\right)}{b}\right). \tag{A.40}$$

Minimization of the energy Eq. A.40 with respect to a_i leads to

$$E = b\mu + 4\left(\frac{12a^2\kappa_1\kappa_2\cos^2\left(\frac{\phi}{2}\right)}{(\kappa_1+\kappa_2)b^3} + \frac{(\kappa_1+\kappa_2)\tan^2\left(\frac{\phi}{2}\right)}{b}\right). \tag{A.41}$$

Minimization of Eq. A.41 with respect to b gives an equation for b:

$$\mu b^4 - 4(\kappa_1+\kappa_2)\tan^2\left(\frac{\phi}{2}\right)b^2 - 144a^2\frac{\kappa_1\kappa_2}{\kappa_1+\kappa_2}\cos^2\left(\frac{\phi}{2}\right) = 0 \tag{A.42}$$

with solution

$$b^2 = 2\frac{(\kappa_1+\kappa_2)\tan^2\left(\frac{\phi}{2}\right) \pm \sqrt{\left((\kappa_1+\kappa_2)\tan^2\left(\frac{\phi}{2}\right)\right)^2 + 36\mu a^2\frac{\kappa_1\kappa_2}{\kappa_1+\kappa_2}\cos^2\left(\frac{\phi}{2}\right)}}{\mu}. \tag{A.43}$$

From Eq. A.43 we obtain

$$\omega_i^2 b^2 = 2\left(\frac{(\kappa_1+\kappa_2)}{\kappa_i}\tan^2\left(\frac{\phi}{2}\right) \pm \sqrt{\left(\frac{(\kappa_1+\kappa_2)}{\kappa_i}\tan^2\left(\frac{\phi}{2}\right)\right)^2 + 36(\omega_i a)^2\frac{\kappa_1\kappa_2}{(\kappa_1+\kappa_2)\kappa_i}\cos^2\left(\frac{\phi}{2}\right)}\right). \tag{A.44}$$

Since both $\omega_i a \ll 1$ and $\tan\phi \ll 1$, all terms in Eq. A.44 are small, thus validating the ansatz $\omega_i b \ll 1$ as long as the small slope approximation ($\phi \ll 1$) holds. We also

check that $\frac{b}{a} \gg 1$ what is necessary for the small slope approximation:

$$\frac{b^2}{a^2} = 2\frac{(\kappa_1+\kappa_2)\tan^2\left(\frac{\phi}{2}\right) \pm \sqrt{\left((\kappa_1+\kappa_2)\tan^2\left(\frac{\phi}{2}\right)\right)^2 + 36\mu a^2 \frac{\kappa_1\kappa_2}{\kappa_1+\kappa_2}\cos^2\left(\frac{\phi}{2}\right)}}{\mu a^2} > \\ > \frac{12\sqrt{\frac{\kappa_1\kappa_2}{\kappa_i\kappa_1+\kappa_2}\cos^2(\phi/2)}}{\omega_i a} \gg 1 \quad \text{(A.45)}$$

To perform the minimization of energy Eq. A.41 with respect to the kink angle ϕ, we introduce a change of variable $u = 1/\cos^2\left(\frac{\phi}{2}\right)$, which makes calculations more transparent. Then $\tan^2\left(\frac{\phi}{2}\right) = u - 1$, $\cos^2\left(\frac{\phi}{2}\right) = 1/u$, and the energy Eq. A.41 can be rewritten as

$$E = b\mu + \left(\frac{48a^2\kappa_1\kappa_2}{(\kappa_1+\kappa_2)ub^3} + 4\frac{(\kappa_1+\kappa_2)(u-1)}{b}\right). \quad \text{(A.46)}$$

Then the minimization of the energy Eq. A.46 determines u at the minimum, which is

$$u_{min} = \sqrt{\frac{12a^2\frac{\kappa_1\kappa_2}{\kappa_1+\kappa_2}}{(\kappa_1+\kappa_2)b^2}} \quad \text{(A.47)}$$

By definition $u > 1$. This means that, unless $u_{min} > 1$, the only possible solution is $u = 1$. Since $a \ll b$ (see Eq. A.45), we have $u_{min} < 1$ so minimum energy occurs at $u = 1$, which implies a zero kink angle $\phi = 0$. As a result, braids in stiff filaments do not lead to kinks; the braided configuration has a region lacking cross linkers, but the average contour of the braided bundle is straight.

A.3.2.2 More flexible filaments

In the case of more flexible filaments, we can no longer use the small slope approximation; we return to the description of the bundle in terms of angles $\alpha_i(s)$. The

boundary conditions in this notation are

$$\alpha_i\left(\pm\frac{L_i}{2}\right)=\pm\frac{\phi}{2} \tag{A.48}$$

and

$$\int_{-L_1/2}^{L_1/2} ds\sin(\alpha_1(s)) = \int_{-L_2/2}^{L_2/2} ds\sin(\alpha_2(s))+2a\cos\left(\frac{\phi}{2}\right) \tag{A.49}$$

$$\int_{-L_1/2}^{L_1/2} ds\cos(\alpha_1(s)) = \int_{-L_2/2}^{L_2/2} ds\cos(\alpha_2(s)), \tag{A.50}$$

where a is the size of the cross link, which becomes relevant in this case. We can use Lagrange multipliers to incorporate the boundary conditions Eqs. A.49,A.50 into the integral form of the bundle's energy:

$$\begin{aligned} E &= \lambda_c\left[\int_{-L_1/2}^{L_1/2} ds\cos(\alpha_1(s))-\int_{-L_2/2}^{L_2/2} ds\cos(\alpha_2(s))\right]+ \\ &+ \lambda_s\left[\int_{-L_1/2}^{L_1/2} ds\sin(\alpha_1(s))-\int_{-L_2/2}^{L_2/2} ds\sin(\alpha_2(s))-2a\cos\left(\frac{\phi}{2}\right)\right]+ \\ &+ \int_{-L_i/2}^{L_i/2} ds\kappa_i\frac{\alpha_i'^2}{2}+\tilde{\lambda_i}\left[\delta\left(s+\frac{L_i}{2}\right)\alpha_i+\frac{\phi}{2L_i}\right]+\lambda_i^\dagger\left[\delta\left(s-\frac{L_i}{2}\right)\alpha_i-\frac{\phi}{2L_i}\right]+\mu L \end{aligned} \tag{A.51}$$

where λ_i, $\tilde{\lambda_i}$,$\lambda_i^\dagger$, λ_s and λ_c are Lagrange multipliers. We vary the energy Eq. A.51 with respect to α, obtaining the equation of state:

$$\kappa_1\alpha_1'' = \lambda_s\cos\alpha_1-\lambda_c\sin\alpha_1+\tilde{\lambda_1}\delta\left(s+\frac{L_1}{2}\right)+\lambda_1^\dagger\delta\left(s-\frac{L_1}{2}\right) \tag{A.52}$$

$$\kappa_2\alpha_2'' = -\lambda_s\cos\alpha_2+\lambda_c\sin\alpha_2+\tilde{\lambda_2}\delta\left(s+\frac{L_2}{2}\right)+\lambda_2^\dagger\delta\left(s-\frac{L_2}{2}\right). \tag{A.53}$$

Eqs. A.52,A.53 give us $\tilde{\lambda_i}=\kappa_i\alpha_i'\left(-\frac{L_i}{2}\right)$ and $\lambda_i^\dagger=-\kappa\alpha_i'\left(\frac{L_i}{2}\right)$. Easy to see that $\lambda_s=0$ cannot simultaneously satisfy Eqs. A.52,A.53, boundary conditions,and the integral condition. If $\lambda_s=0$ the solution $\alpha(s)$ must be an odd function, which immediately

causes the boundary condition integral to vanish since it is the integral of an odd function $\sin(\alpha(s))$ over symmetric limits. Thus, we cannot satisfy the boundary condition Eq. A.49 . If we consider to be a continuous function of its arguments $\lambda_s = \lambda_s(\mu, a, \kappa)$, we note that it cannot change its sign - otherwise it would be zero somewhere, according to Bolzano's theorem. Therefore, since, for small $a^2\mu/\kappa_i$, $\lambda_s < 0$, then λ_s must be negative everywhere.

Minimizing the energy Eq. A.51 with respect to L_i we obtain equations

$$\int_{-L_1/2}^{L_1/2} ds \left(-\frac{\kappa_1}{2}\alpha_1'^2 + \mu + \lambda_c \cos\alpha_1 + \lambda_s \sin\alpha_1\right) = 0 \tag{A.54}$$

$$\int_{-L_2/2}^{L_2/2} ds \left(-\frac{\kappa_2}{2}\alpha_2'^2 + \mu - \lambda_c \cos\alpha_2 - \lambda_s \sin\alpha_2\right) = 0. \tag{A.55}$$

Using the Eqs. (A.52 , A.53), we obtain two conserved quantities (the analog of first integrals of a dynamical system) I_i, $dI_i/ds = 0$

$$I_1 = \frac{\kappa_1}{2}\alpha_1'^2 - \lambda_s \sin\alpha_1 - \lambda_c \cos\alpha_1 \tag{A.56}$$

$$I_2 = \frac{\kappa_2}{2}\alpha_2'^2 + \lambda_s \sin\alpha_2 + \lambda_c \cos\alpha_2. \tag{A.57}$$

Comparing Eqs. A.56,A.57 and Eqs. A.54,A.55 we get

$$I_1 = I_2 = \mu. \tag{A.58}$$

Substituting Eqs. A.56,A.57 into Eq. A.58 we obtain

$$\frac{4\lambda_s \sin\left(\frac{\phi}{2}\right)}{\alpha_1'\left(\frac{L_1}{2}\right) - \alpha_1'\left(-\frac{L_1}{2}\right)} = \kappa_1 \left[\alpha_1'\left(\frac{L_1}{2}\right) + \alpha_1'\left(-\frac{L_1}{2}\right)\right] \tag{A.59}$$

$$-\frac{4\lambda_s \sin\left(\frac{\phi}{2}\right)}{\alpha_2'\left(\frac{L_2}{2}\right) - \alpha_2'\left(-\frac{L_2}{2}\right)} = \kappa_2 \left[\alpha_2'\left(\frac{L_2}{2}\right) + \alpha_2'\left(-\frac{L_2}{2}\right)\right]. \tag{A.60}$$

Finally, the variation of the total energy Eq. A.51 with respect to ϕ gives

$$\frac{\partial E}{\partial \phi} = 4\lambda_s a \sin\left(\frac{\phi}{2}\right) + \tilde{\lambda_1} + \tilde{\lambda_2} - \lambda_1^\dagger - \lambda_2^\dagger. \tag{A.61}$$

Using boundary conditions Eqs. A.52,A.53 we simplify Eq. A.61 to

$$\frac{\partial E}{\partial \phi} = 4\lambda_s a \sin\left(\frac{\phi}{2}\right) + \kappa_1 \alpha_1'\left(-\frac{L_1}{2}\right) + \kappa_2 \alpha_2'\left(-\frac{L_2}{2}\right) + \kappa_1 \alpha_1'\left(\frac{L_1}{2}\right) + \kappa_2 \alpha_2'\left(\frac{L_2}{2}\right). \tag{A.62}$$

Substituting Eqs. A.59, A.60 into Eq. A.62 we find

$$\frac{\partial E}{\partial \phi} = 4\lambda_s \sin\left(\frac{\phi}{2}\right)\left[a + \frac{2}{\alpha_1'\left(\frac{L_1}{2}\right) - \alpha_1'\left(-\frac{L_1}{2}\right)} - \frac{2}{\alpha_2'\left(\frac{L_2}{2}\right) - \alpha_2'\left(-\frac{L_2}{2}\right)}\right]. \tag{A.63}$$

Eq. A.63 shows that $\phi = 0$ is an extremum. To decide whether it is a maximum or minimum, we must determine the sign of the term in square brackets above. From the small slope analysis, we observed that when $a^2\mu/\kappa \ll 1$, the zero angle (no kink) is a minimum so in that in case, the term in brackets is negative there. The transition from minimum to maximum occurs when the expression in square brackets increases to zero:

$$a + \frac{2}{\alpha_1'\left(\frac{L_1}{2}\right) - \alpha_1'\left(-\frac{L_1}{2}\right)} - \frac{2}{\alpha_2'\left(\frac{L_2}{2}\right) - \alpha_2'\left(-\frac{L_2}{2}\right)} = 0. \tag{A.64}$$

The terms α_i' are the signed curvatures of their respective filaments. At the kinking transition where $\phi = 0$, we can determine the signs of the these curvatures introducing positive radii of curvature $R_{1,2}(\pm L_{1,2}/2)$:

$$R_1\left(\pm\frac{L_1}{2}\right) = \mp\frac{1}{\alpha_1'\left(\pm\frac{L_1}{2}\right)} \tag{A.65}$$

$$R_2\left(\pm\frac{L_2}{2}\right) = \pm\frac{1}{\alpha_2'\left(\pm\frac{L_2}{2}\right)}. \tag{A.66}$$

Writing down Eq. A.64 in terms of these absolute radii of curvature, we obtain the condition for the kinking transition

$$a = \frac{2}{\frac{1}{R_1\left(\frac{L_1}{2}\right)} + \frac{1}{R_1\left(-\frac{L_1}{2}\right)}} + \frac{2}{\frac{1}{R_2\left(\frac{L_2}{2}\right)} + \frac{1}{R_2\left(-\frac{L_2}{2}\right)}}. \tag{A.67}$$

Because of Eqs. A.56,A.57, the radii of curvature at the ends of the two filaments are equal: $R_{1,2} = R_{1,2}\left(\frac{L_{1,2}}{2}\right) = R_{1,2}\left(-\frac{L_{1,2}}{2}\right)$. Then we simplify Eq. A.67

$$a = R_1 + R_2. \tag{A.68}$$

For stiff filaments $R_{1,2} \gg a$ as can be seen from the small slope analysis. For more flexible filaments, however, the length of the uncross-linked region should as small as possible, e.g., $\frac{L-a}{a} \ll 1$ since loss in length is prohibited by large μ, while sharp bends are feasible since κ is small. This leads to size of the braid $b \ll a$, that inevitably leads to $R_{1,2} \ll a$. Between these cases of very flexible and very stiff filaments we should have an intermediate result where Eq. A.68 is satisfied, and transition occurs.

For further analysis of this transition let us explore the case $\kappa_1 = \kappa_2 = \kappa$. To investigate the behavior of kink angle near the critical point, we introduce a symmetry ansatz, namely, $\alpha_1(s) = -\alpha_2(-s)$. This ansatz obviously solves equation of state Eqs. A.52,A.53. We have numerically checked that this symmetric solution indeed provides the global energy minimum – see Fig. 2.6B in the main document. Using the symmetric approach, we obtain from Eqs. A.56 and A.57

$$I = \kappa\frac{\alpha'^2}{2} - \lambda_s \sin\alpha - \lambda_c \cos\alpha \tag{A.69}$$

$$I = \kappa\frac{\alpha'^2}{2} - \lambda_s \sin\alpha + \lambda_c \cos\alpha. \tag{A.70}$$

Eqs. A.69,A.70 require $\lambda_c = 0$, so the conserved quantity I simplifies to

$$I = \kappa\frac{\alpha'^2}{2} - \lambda_s \sin\alpha. \tag{A.71}$$

Using Eq. A.71 and the fact that $I = \mu$ (see Eq. A.58), we obtain

$$\alpha'\left(\pm\frac{L}{2}\right)^2 = 2\left(\frac{\mu}{\kappa} \pm \lambda_s \sin\left(\frac{\phi}{2}\right)\right). \tag{A.72}$$

Using the same symmetry, we also simplify Eq. A.64 to

$$a + \frac{4}{\alpha'\left(\frac{L}{2}\right) - \alpha'\left(-\frac{L}{2}\right)} = 0. \tag{A.73}$$

We transform Eq. A.73 and obtain

$$\alpha'\left(\frac{L}{2}\right)^2 - 2\alpha'\left(\frac{L}{2}\right)\alpha'\left(-\frac{L}{2}\right) + \alpha'\left(-\frac{L}{2}\right)^2 = \frac{16}{a^2}. \tag{A.74}$$

We substitute Eq. A.72 to Eq. A.74, finding

$$-\alpha'\left(\frac{L}{2}\right)\alpha'\left(-\frac{L}{2}\right) = \frac{8}{a^2} - \frac{\mu}{\kappa}. \tag{A.75}$$

After taking the square of Eq. A.75 and substituting into it Eq. A.72, we obtain

$$\lambda_s^2 \sin^2(\phi/2) = \frac{8\kappa^2}{a^4}\left(\frac{\mu a^2}{\kappa} - 2\right) \tag{A.76}$$

Eq. A.76 has a solution for ϕ only if $\frac{\mu a^2}{\kappa} \geq 2$. Therefore, the critical point is $\frac{\mu a^2}{\kappa} = 2$. Near this critical point we expect square-root like behavior of ϕ.

A.3.3 Braid group and knot theory for our model

We start with a brief review of the mathematical apparatus of the braid group for a braid with three filaments Br_3 . When we refer to the filaments by their label (1,2,3), in the discussion related to the braid group we refer to that filament's position in the bundle cross section and not to its physical identity. The most left filament is always filament 1, the most right is filament 3, and the filament 2 is in the middle. After each swap, when one filament passes above another filament, in the next cross section we correspondingly swap their indices. The braid group has two generators: σ_1, corresponding to passing filament 2 over the filament 3, and σ_2, corresponding to passing filament 3 over filament 1. These operators are not their own inverses.

For example $\sigma_1^{-1} \neq \sigma_1$ corresponds to passing filament 3 over filament 2. We also introduce an operator σ_3, corresponding to passing filament 1 over filament 2, which can be written in terms of the two generators: $\sigma_3 = \sigma_1\sigma_2^{-1}\sigma_1^{-1}$. Finally, there is braid group relation, equivalent to the third Reidemeister move in knot theory

$$\sigma_3\sigma_1\sigma_3 = \sigma_1\sigma_3\sigma_1. \tag{A.77}$$

Note that the first Reidemeister move (looping) is not allowed for braids, and the second is just the definition of the inverse operator.

We apply this mathematical apparatus to a three-filament bundle. Consider a projection of that bundle onto the plane containing filaments 1 and 3 in a segment of the bundle. Filament 2 can either be above or below this plane, which we denote as Δ- or ∇-states respectively. All braids and twists of the bundle can be expressed in terms of these group operators of the tensor product of the braid group and the permutation group of two elements Z_2: $\mathrm{Br}_3 \otimes Z_2$. The Z_2 group takes into account whether the bundle segment is in the Δ or ∇ state.

We introduce operators b_i, corresponding to the braiding of the ith filament, and $r_\pm$, corresponding to the twist of the bundle by $\pm\frac{\pi}{3}$. We write down the elements of the group $\mathrm{Br}_3 \otimes Z_2$ as two-component vectors, where first and second components correspond to the states Δ and ∇ respectively. Then the operators b_i and $r_\pm$ can be

written as (see Fig. A.10):

$$b_1 = \begin{pmatrix} 0 & \sigma_1^{-1}\sigma_3 \\ \sigma_1\sigma_3^{-1} & 0 \end{pmatrix} \tag{A.78}$$

$$b_2 = \begin{pmatrix} 0 & 1 \\ 1 & 0 \end{pmatrix} \tag{A.79}$$

$$b_3 = \begin{pmatrix} 0 & \sigma_3\sigma_1^{-1} \\ \sigma_3^{-1}\sigma_1 & 0 \end{pmatrix} \tag{A.80}$$

$$r_+ = \begin{pmatrix} 0 & \sigma_1^{-1} \\ \sigma_3^{-1} & 0 \end{pmatrix} \tag{A.81}$$

$$r_- = \begin{pmatrix} 0 & \sigma_3 \\ \sigma_1 & 0 \end{pmatrix}. \tag{A.82}$$

It can be shown that $b_2b_2 = b_1b_3 = r_+r_- = 1$. There are two different subgroups in $\mathrm{Br}_3 \otimes Z_2$ – one generated by braids $b_{1,2,3}$ and the other generated by rotations $r_\pm$. These two subgroups do not have common elements except 1. This is easy to prove by introducing the weight of a group element as follows. We write every element in terms of σ_1, σ_3 and their inverses, as we have already done above. Using this decomposition of the group elements, we define the weight of an element as the number of σ_1s plus the number of σ_3s minus number of their inverses. The identity Eq. A.77 does not change the weight. Moreover, the weight is additive under the action of the group. Every element of the braid group has weight 0, but all elements of the rotation group other than the identity have a nonzero weight. Hence, 1 is the only common element.

The complete description of the possible states of the bundle also requires that one studies the case when we rotate the segment of the bundle while fixing its endpoints.

For example, consider a bundle segment containing a b_2 braid and apply a clockwise rotation to the bundle while fixing the triangles of filament cross sections at both end. That clockwise rotation or twist leads to the insertion of operators r_+ and r_- at the ends and changes the nature of the braid: $b_2 \to b_3$ for Δ state and $b_2 \to b_1$ for ∇ state. After direct substitution of definitions of $b_{1,2,3}$ – see Eqs. A.78, A.79, A.80, A.82,A.81 – and using the Reidemeister move Eq. A.77, we see that the resulting operator is still b_2. Therefore, the rotation does not change the group structure of the bundle segment. If instead we have a braid and then apply equal and opposite twists to the ends of bundle segment containing that braid (applying the operators r_+ and r_- on either side of the braid), then the braid turns into different braid. This resulting braid depends on whether the bundle was originally in the Δ state and ∇ state. As a result of this reasoning, any combination of braids and rotations acting on either the Δ or ∇ state can be written as a rotation times some combination of braids. Since rotations are continuous transformations that can be relaxed at the end of the bundle, these rotations are not relevant to our analysis. We are interested only in the interactions of braids so we may concentrate on the structure of the subgroup of $\mathrm{Br}_3 \otimes Z_2$ generated by $b_{1,2,3}$.

To simplify the further calculations, we introduce $A = \sigma_1\sigma_3^{-1}$, $B = \sigma_1^{-1}\sigma_3$, $C =$

$\sigma_1\sigma_3$, and $D = \sigma_3\sigma_1$. Then we can rewrite the braid operators b_i as

$$b_1 = \begin{pmatrix} 0 & B \\ A & 0 \end{pmatrix} \tag{A.83}$$

$$b_2 = \begin{pmatrix} 0 & 1 \\ 1 & 0 \end{pmatrix} \tag{A.84}$$

$$b_3 = \begin{pmatrix} 0 & A^{-1} \\ B^{-1} & 0 \end{pmatrix}. \tag{A.85}$$

The Reidemeister condition written in terms of A, B, C, D is

$$D = CA = BC. \tag{A.86}$$

Using Eq. A.86 we rewrite b_i as

$$b_1 = \begin{pmatrix} 0 & CAC^{-1} \\ A & 0 \end{pmatrix} \tag{A.87}$$

$$b_2 = \begin{pmatrix} 0 & 1 \\ 1 & 0 \end{pmatrix} \tag{A.88}$$

$$b_3 = \begin{pmatrix} 0 & A^{-1} \\ CA^{-1}C^{-1} & 0 \end{pmatrix}. \tag{A.89}$$

There are no additional conditions on A and C akin to the Reidemeister condition so that they form a free group – all distinct sequences of A's and C's are unequal. We can reduce products of b_i only by using $AA^{-1} = CC^{-1} = 1$. Combinations of braids can be simplified only by the three contractions $b_1b_3 = 1$, $b_3b_1 = 1$, and $b_2b_2 = 1$. As a result, braid dynamics on a three-filament bundle are defined solely by these relations for braid combination. Assuming that braids b_1, b_2, b_3 are distributed with

equal probability along the bundle, we ran Monte-Carlo simulations of braid dynamics using the following rules. Braids diffuse locally along the filament as required by translational invariance. We note that there are no long-range interactions either between braids or between a braid and the edge of the bundle because the configuration of the filaments near to the braid as already returned to that of the undeformed bundle. When two braids collide during their diffusion, they merge into one braid because, by putting the two braids together, the bundle recovers more cross linkers. If they pair of braids form a braid - antibraid couple, then they annihilate through a local rearrangment of the filaments so that all of the lost cross linkers are regained by the bundle. Finally, if a braid reaches the end of the bundle, it vanishes by diffusing off the end. The number of braids as the function of time for a single run of the simulation is shown in Fig. A.6.

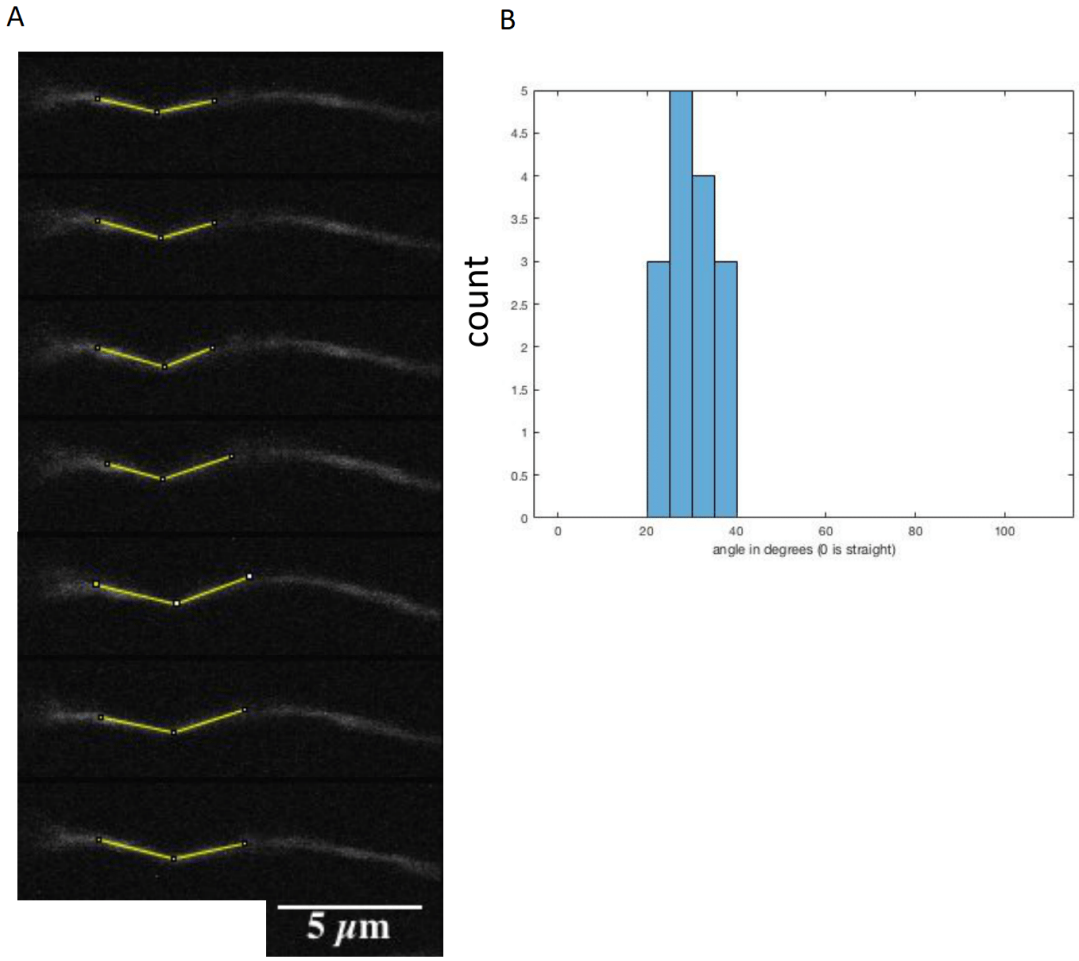

Figure A.1: Measurements of a single kink over time. A) Multiple images of a bundle with a kink. Not all snapshots of the bundle are shown in this figure. Yellow lines overlaid on the bundle are from the angle measurement tool in ImageJ. B) Histogram showing the measured angles for this single kink.

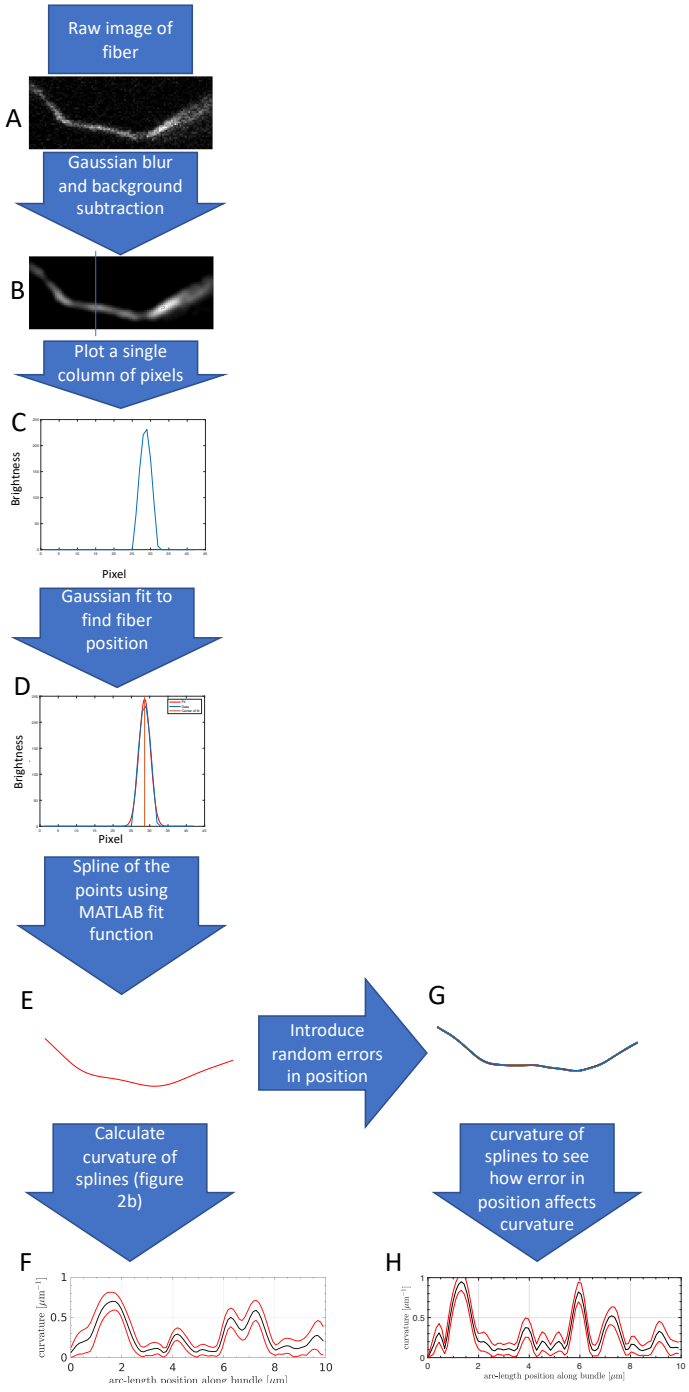

Figure A.2: Process of determining curvature of the bundles from the images. (A)Fluorescence confocal image of a bundle. (B) Blurred and background subtracted image. (C) Line intensity profile across the bundle. (D) Gaussian fit of the line intensity profile is used to determine the y axis location of the bundle at the x position of the line profile. (E) Cubic spline of the points generated from the Gaussian fit. (F) Summary of all the curvatures of the spines. (G) 50 splines with errors introduced in the position (uniformly distributed between 0.5 and -0.5) from which the spline is cal-

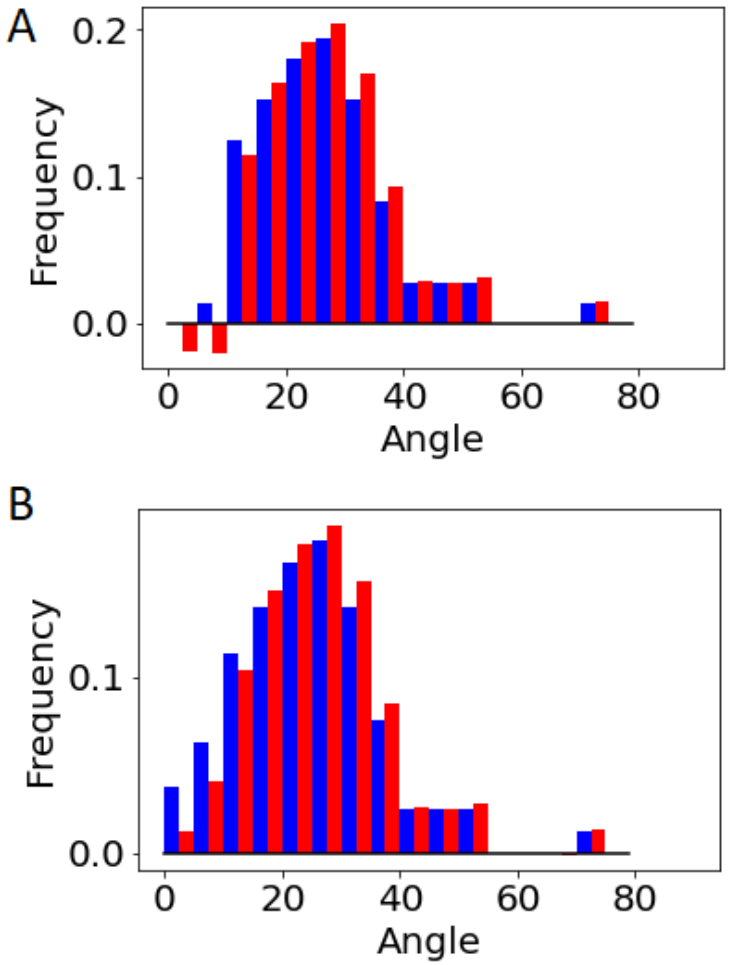

Figure A.3: Distribution of the measured 2D projected kink angles (blue) and of 3D kinks angles inferred from measured distribution using Eq. A.2 (red). (A) The distribution for the observed angles is taken from the experiment. Negative values for inferred kinks angles are caused by underestimation of the observed number of kinks with small angles. (B) Artificially increasing the amount of small angle kinks from the experimental data leads to disappearance of negative frequency values at small kinks.

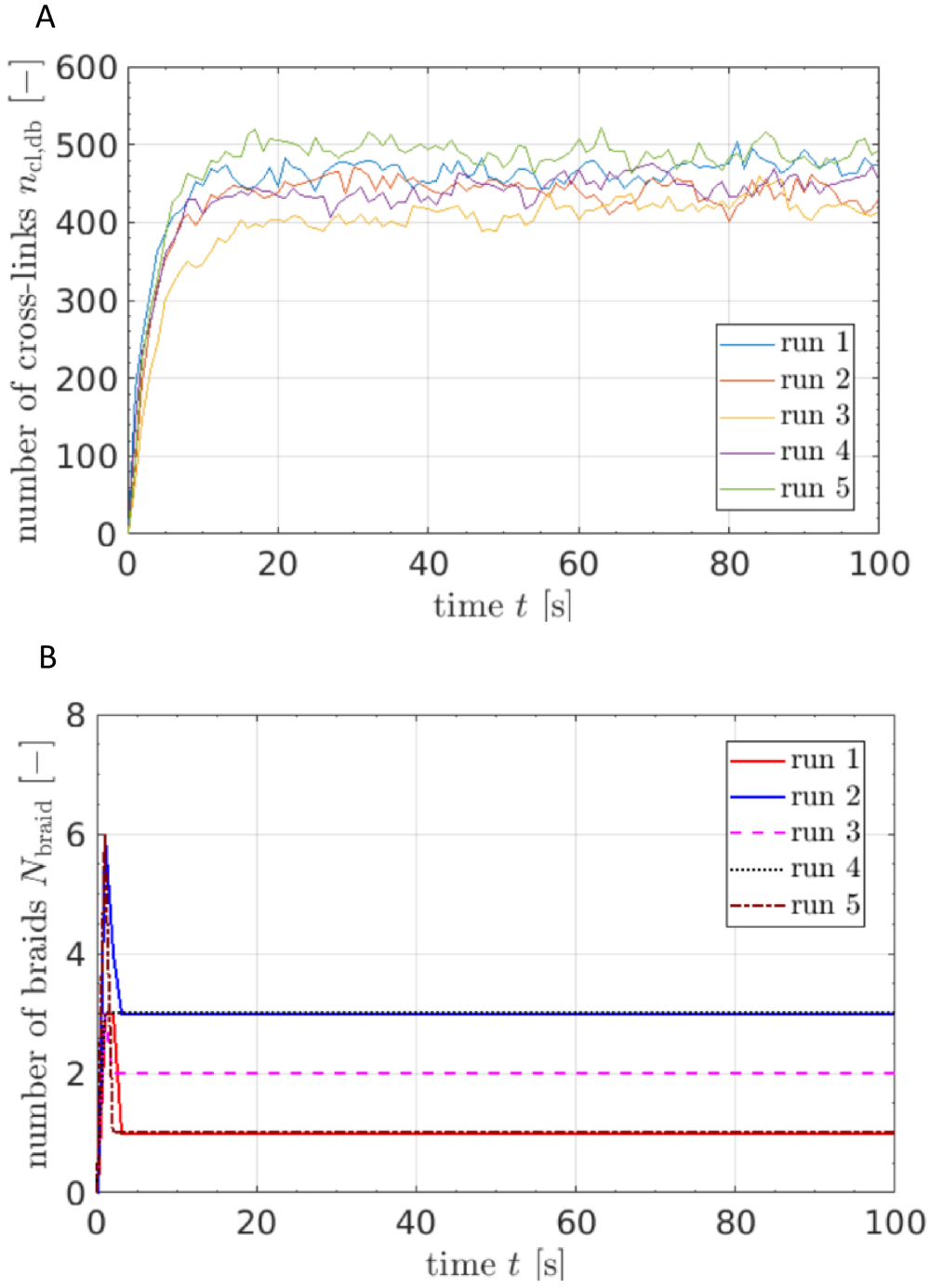

Figure A.4: Number of cross-links (A) and number of braids (B) over time, observed in five independent simulation runs.

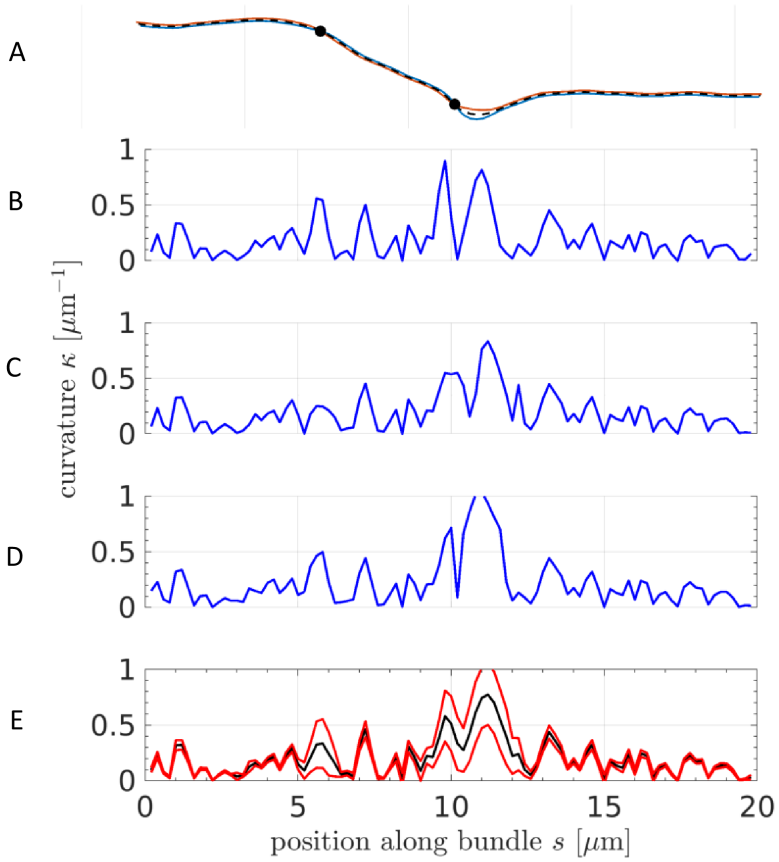

Figure A.5: Curvature of the bundle centerline observed in 2D simulations. (A) Bundle centerline (black dashed line), individual filaments (blue and red) and braids (black dots) for the configuration plotted in (D). (B)-(D) Curvature of the bundle centerline at three different points in time. (E) Mean of the curvature (black) over 100 configurations with a time interval of 1s each. Red lines indicate one standard deviation.

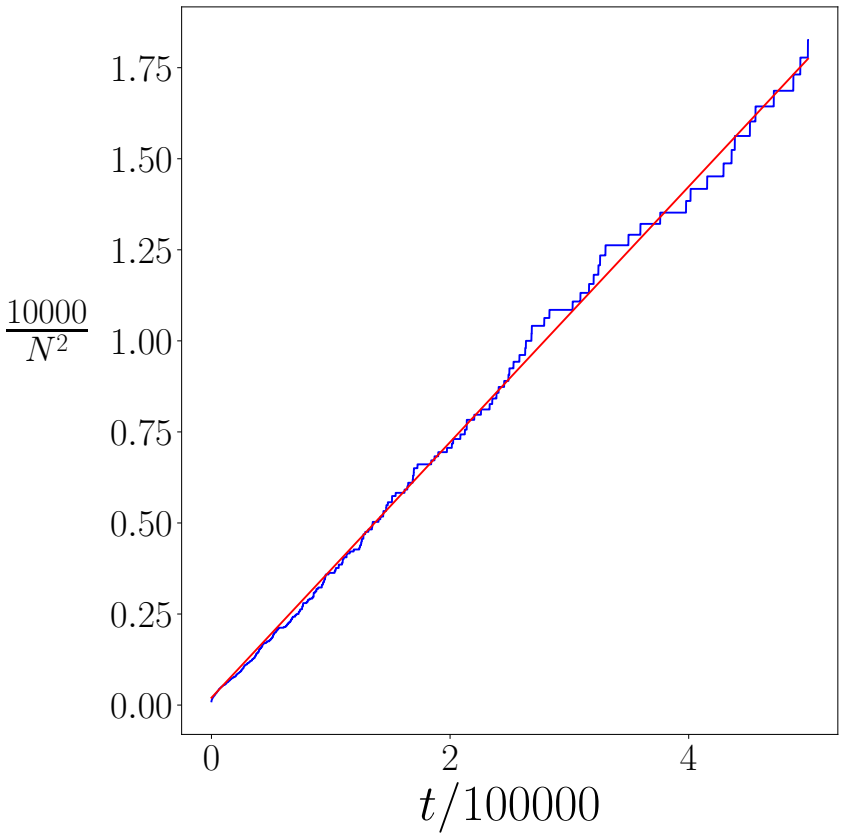

Figure A.6: (Blue) Inverted square of the number of kinks as the function of time as the result of the single run of Monte-Carlo simulation. (Red) linear fit of obtained data. In spite of sticking events, the trend is linear, supporting the analysis in Sec. 3D of the main document.

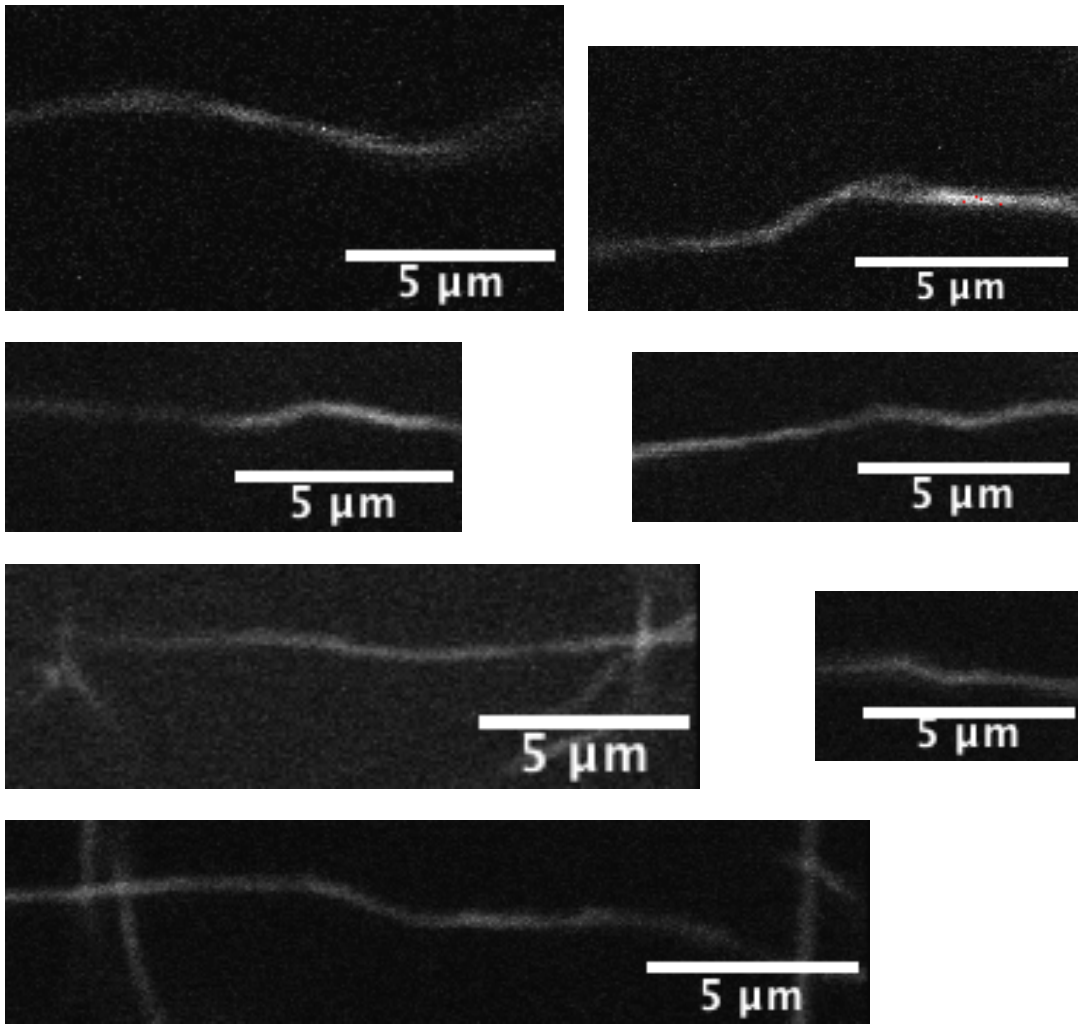

Figure A.7: Several examples of bundles exhibiting z shaped kinks. This shape may be due to 2 loop defects forming as 2 filaments slide in opposite directions. Only a single snapshot is shown here, but these kinks persisted over the observation time.

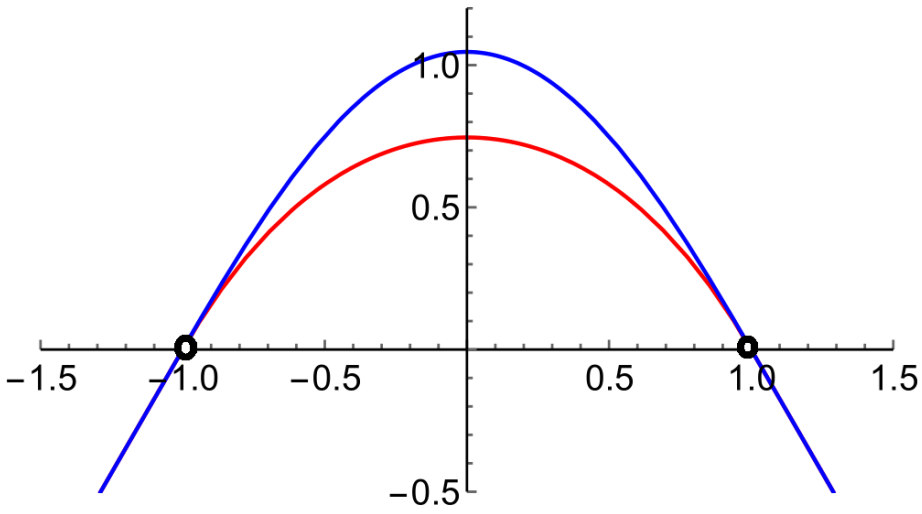

Figure A.8: A schematic diagram of a loop made by two filaments. There is an excess of length between the cross links (black circles) of the blue filament as compared to the red one. This length mismatch generates a localized bend (kink) in the energy-minimized structure.

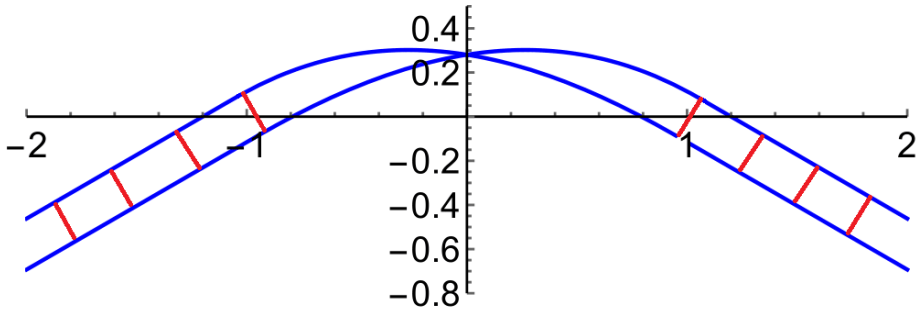

Figure A.9: Schematic description of the 2D braid used for the analytic calculations. The blue lines are filaments, and red lines represent cross links.

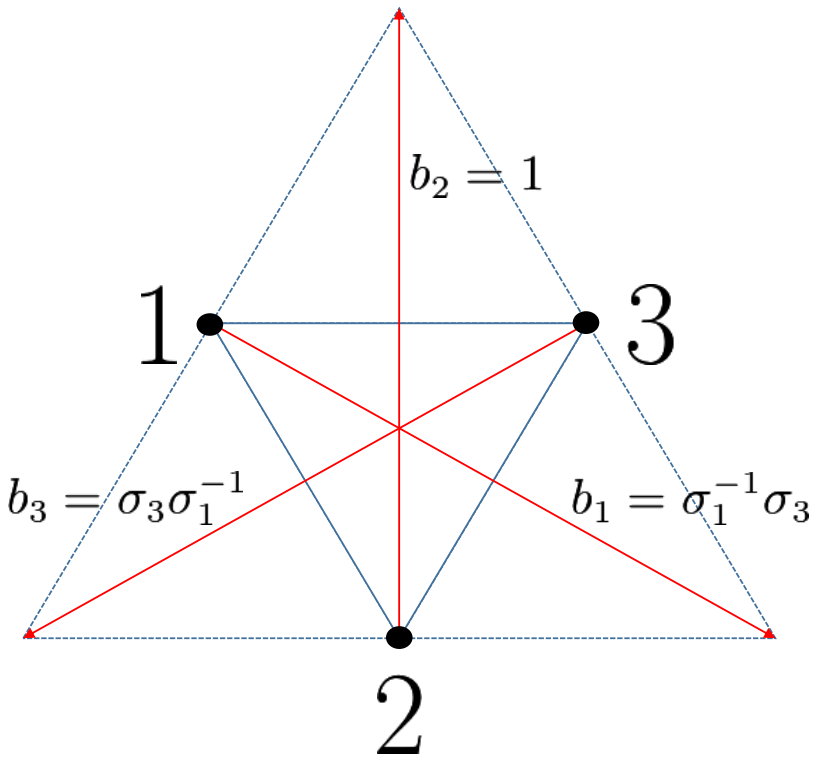

Figure A.10: Illustration of the braid group generators $b_{1,2,3}$ acting on a bundle in ∇-state with filaments 1,2,3. For example, b_1 corresponds to first passing filament 1 *over* filament 2, which is done by operator σ_3. After that, the former filament 1 is now filament 2, and vice versa. The second and final step in the braid operation is passing the new filament 2 (i.e., old filament 1) *under* filament 3, which is performed by operator σ_1^{-1}. We obtain the formulae for other operators in the same way.

APPENDIX B

Appendix for "Thermal Schwinger Effect: Defect Production in Compressed Filament Bundles"

B.1 Loops Generation as a Kramers' escape problem

B.1.1 Forming a z-bend: The Energetics of a Loop Pair Production

We considered the energetics of a loop in the absence of the external force in Ref. [163]. There I found that, for a particular amount of excess trapped length ΔL, the angle of the loop that minimizes the energy is

$$\phi = 2\frac{\Delta L^{1/3}\mu^{1/6}}{\kappa^{1/6}x^{1/3}}\tanh(x), \tag{B.1}$$

where $x \approx 2.365$ is a first non-zero solution of the equation $\tan x = -\tanh x$. We can also express the minimum energy E of the loop and its size L (the length of the shorter filament(s) that is not cross linked to the looping filament) as the function of the trapped length:

$$E = 3\mu^{2/3}\Delta L^{1/3}\kappa^{1/3}x^{2/3} \tag{B.2}$$

and

$$L = \Delta L^{1/3}\frac{2\kappa^{1/3}x^{2/3}}{\mu^{1/3}}. \tag{B.3}$$

From Eqs. B.1,B.2, and B.3 I observe that amount of the trapped excess length ΔL fully controls the kinking angle ϕ, the energy of the defect E and the length of the defected region L. As a result, if the trapped length is equal and opposite for two loops (the excess length on one set of filaments in the first defect compensates for the length deficit on the same filaments in the second defect), the angles ϕ of the two defects will also be equal and opposite. Similarly, the loop sizes L and energies E of the two defects will be equal. If the total size of the uncross-linked region is ℓ (comprising two loop defects), then $L = \ell/2$, and I can express ϕ and E in terms of ℓ:

$$\phi = \frac{\ell \mu^{1/2}}{2\kappa^{1/2} x} \tanh(x) = \frac{1}{g_2} \sqrt{\frac{\mu}{\kappa}} \ell \tag{B.4}$$

and

$$E = 3\mu \frac{\ell}{4} \tanh(x)^{2/3} = g_1 \mu \ell / 2. \tag{B.5}$$

These are easily obtained from Eqs. B.1 and B.2 above using ℓ appropriately. This pair of length-compensating loops together constitute a single z-bend, as discussed in the main text.

If I now assume that the compression force F is small enough, I may ignore the finite-force corrections to the angle. Then, for a given compressive load F acting on a bundle containing a pair of length-compensating loop defects that produce a z-bend where a length R separates the two loops, the decrease of the bundle's energy is the work done by the compressive load in shortening it: $-FR(1 - \cos\phi)$. Taking this into account, I obtain the total energy of the z-bend as the sum of this work and energy cost of the formation of the two defects

$$E_{tot} = g_1 \mu \ell - FR(1 - \cos\phi). \tag{B.6}$$

As long as $F \ll \mu$, changes in R of the order of ℓ produce small changes to the

energy when compared to the first term in Eq. B.6. Thus, in this limit it does not matter whether I define R to be the distance between the defect centers or the defect edges. For consistency, I consider R to be the distance between the closest edges of the defects, i.e., when the defects are starting to separate, R grows from 0.

B.1.2 The Thermal Production of Loop Pairs as a Kramers' Escape Process

We now consider the process of z-bend formation as the thermally activated production of two loops. This process has two essentially distinct steps. In the first, two loops are created on the bundle. To conserve the length of filaments involved, the excess trapped length in one loop is compensated by an equal amount of trapped length in the other loop but now associated with the other filament. In short, one can look at this process as the exchange of a conserved amount of length trapped between cross links in two overlapping structures, forming a loop pair. In the second part of this process, the two loops diffusively separate to form the z-bend. During the first part of this process, the two loops can easily continue to exchange length so that the trapped length within in the loops changes. Once the loops separate, such exchanges of length would require the reconfiguration of the all the cross links in the bundle section between the two loops. This is energetically prohibitive so the loop sizes are now fixed.

These two distinct processes can be combined into a single one using a particular reaction coordinate, which represents the changing amount of trapped length in the first part and then the inter-loop separation in the second part. The effect potential

associated with this single reaction coordinate can be written as follows:

$$U(x) = \begin{cases} g_1\mu x, x < \ell_0 \\ g_1\mu\ell_0 - F(1-\cos\phi)(x-\ell_0), x > \ell_0. \end{cases} \tag{B.7}$$

In the following it is helpful to define $A = g_1\mu$ and $B = F(1-\cos\phi)$. Then, for a loop pair containing excess length equal to ℓ_0, the effective potential for the reaction coordinate may be written simply as an initially linearly increasing function with slope A connected to a linearly decreasing function with slope $-B$. These two sections are joined at the point of loop pair separation where the reaction coordinate is equal to ℓ_0. For reference, the potential is

$$U(x) = \begin{cases} Ax, x < \ell_0 \\ A\ell_0 - B(x-\ell_0), x > \ell_0. \end{cases} \tag{B.8}$$

The average escape time $\langle T\rangle$ for a loop pair of a given size ℓ_0 is then given by the mean first passage time to escape this potential well at $x = 0$. Using standard results for this problem, I may write

$$\langle T\rangle = \frac{1}{D}\int_0^{x_0} dy e^{\beta U(y)} \int_0^y dz e^{-\beta U(z)}. \tag{B.9}$$

The first integral is taken from initial state of the system at $x = 0$ (no loops at all) where the potential vanishes $U(0) = 0$, to the point $x_0 > 0$, where the potential is again zero $U(x_0) = 0$. This condition is satisfied at $x_0 = (A+B)\ell_0/B$. Substituting the potential $U(x)$ from Eq. B.8 into Eq. B.9 I find that I must perform the integrals

$$\langle T\rangle = \frac{1}{D}\left(\int_0^{\ell_0} dy \int_0^y dz e^{\beta A(y-z)} + \int_{\ell_0}^{x_0} dy \int_0^{\ell_0} dz e^{\beta(A\ell_0 - B(y-\ell_0) - Az)} + \int_{\ell_0}^{x_0} dy \int_{\ell_0}^y dz e^{\beta B(z-y)}\right). \tag{B.10}$$

Doing so, I obtain

$$\langle T\rangle = \frac{1}{D}\Bigg[\frac{1}{\beta A}(\frac{1}{\beta A}(e^{\beta A\ell_0}-1)-\ell_0) \tag{B.11}$$
$$+\frac{1}{\beta A}\frac{1}{\beta B}(e^{\beta A\ell_0}-1)(1-e^{-\beta B(x_0-\ell_0)})$$
$$+\frac{1}{\beta B}(x_0-\ell_0-\frac{1}{\beta B}(1-e^{-\beta B(x_0-\ell_0)})\Bigg].$$

We substitute x_0 to get

$$\langle T\rangle = \frac{1}{D}\Bigg[\frac{1}{\beta A}\frac{1}{\beta A}e^{\beta A\ell_0}-\frac{1}{\beta A}\frac{1}{\beta A}-\frac{1}{\beta A}\ell_0+ \tag{B.12}$$
$$+\frac{1}{\beta A}\frac{1}{\beta B}e^{\beta A\ell_0}-2\frac{1}{\beta A}\frac{1}{\beta B}+e^{-\beta A\ell_0}\frac{1}{\beta A}\frac{1}{\beta B}+$$
$$+\frac{1}{\beta B}A\ell_0/B-\frac{1}{\beta B}\frac{1}{\beta B}+e^{-\beta A\ell_0}\frac{1}{\beta B}\frac{1}{\beta B}\Bigg].$$

We now further assume that $B \ll A$, which implies that the compressive force driving the loops apart is small compared to the work per unit length necessary to create a loop of a specific size. In this limit, I investigate the case in which the thermal activation of loop pairs should be rather rare. The opposite limit of large compressive force implies that loops rapidly proliferate so that the rapid collapse of the bundle becomes a different and complex dynamical problem. In this marginal case of weak forces being just able to generate loop pairs, I simplify the mean escape time to

$$\langle T\rangle = \frac{1}{D}\Bigg[\frac{1}{\beta^2 AB}e^{\beta A\ell_0}+\frac{1}{\beta^2 B^2}(\beta A\ell_0-1+e^{-\beta A\ell_0})\Bigg]. \tag{B.13}$$

Furthermore, in limit of small angular bends of the loops ϕ (consistent with small amounts of excess trapped length) I approximate: $1-\cos\phi \approx \phi^2/2$. Substituting

A, B and expressing the total size of the uncross-linked region ℓ_0 in terms of the loop angle using Eq. B.4 I obtain

$$\langle T \rangle = \frac{1}{D} \frac{4}{\beta^2 F^2 \phi^4} \left(\frac{\tau \phi^2}{2 g_1} e^{\eta \phi} + \eta \phi - 1 + e^{-\eta \phi} \right) \tag{B.14}$$

with $\eta = g_1 g_2 \beta \kappa^{1/2} \mu^{1/2}$ and $\tau = F/\mu$.

To find the angle produced with maximal rate (minimal escape time $r = \frac{1}{\langle T \rangle}$), I introduce an auxiliary variable $\psi = \eta \phi$ in order to write

$$\langle T \rangle = \frac{1}{D} \frac{4 \eta^4}{\beta^2 F^2} f(\psi), \tag{B.15}$$

with

$$f(\psi) = C \psi^{-2} e^{\psi} + \psi^{-3} + (e^{-\psi} - 1) \psi^{-4}, \tag{B.16}$$

where $C = \frac{\tau}{2 g_1 \eta^2}$. For $C \ll 1$ I look for $\psi^\star$ such that $f'(\psi^\star) = 0$ in order to extremize the mean escape time. Using the ansatz $\psi \gg 1$, I find that

$$f'(\psi) \approx C \psi^{-2} e^{\psi} - 3 \psi^{-4}. \tag{B.17}$$

From this result, I find the condition for the minimum escape time to be

$$C \psi^2 e^{\psi} = 3, \tag{B.18}$$

which in the limit $C \ll 1$ has the approximate solution

$$\psi^\star = \log \frac{3}{C} \gg 1. \tag{B.19}$$

Using the above result for $\psi^\star$, I calculate the minimum escape time

$$f(\psi^\star) \approx 3 \log \left(\frac{3}{C} \right)^{-2}, \tag{B.20}$$

working in the same approximation $C \ll 1$. Leading to our estimate for the maximal loop pair production rate

$$r_{\max} = \frac{1}{\langle T \rangle_{\min}} = \frac{D}{3} \left[\frac{\tau \log\left(\frac{6 g_1 \eta^2}{\tau}\right)}{2\beta\kappa} \right]^2 . \tag{B.21}$$

B.2 Braids

B.2.1 Forming a u-bend: Energetics of Braid Pair Production

We first consider the energetics of a braid under the compression, using the same approach as in Ref. [163]. There I showed that the energy of the most simple braid of three filaments can be mapped onto a two-dimensional projection of the 3D braid onto the plane. The 2D pseudobraid consists of only two filaments. This simplification results from the observation that in a torsion-free braid of filaments in 3D, two of the three filaments take identical paths (have identical conformations) through the defect and maintain their cross linking within that pair, while the third takes a different path and loses cross links to the other two. As a result, I can lump the energetics of the two identical filaments into one in the analysis of the 2D pseudobraid. We characterize the conformation of the filament by the angle $\alpha(s)$ between its local tangent and a fixed axis, which I take to be the x-axis, as a function of arc length s

To analyze the pseudobraid, one should consider the case in which the two filaments have differing bending moduli. This makes the analytical solution problematic. For simplicity, in this analytical part I focus only on the case of the equal bending moduli of two filaments in the projection $\kappa_1 = \kappa_2 = \kappa$, that presumably results in the symmetric u-bend - two braids with equal angle. We address the case of differing bending moduli by direct numerical minimization. Finally, following Ref. [163], I

introduce a symmetry ansatz: $\alpha_1(s) = -\alpha_2(-s) = \alpha(s)$, which is justified by later comparing the results with numerical minimization of the energy.

The boundary conditions are the same as in Ref. [163]

$$\alpha\left(\pm\frac{L}{2}\right) = \pm\frac{\phi}{2} \tag{B.22}$$

and

$$\int_{-L/2}^{L/2} ds \sin(\alpha(s)) \;\; = \;\; -\int_{-L/2}^{L/2} ds \sin(\alpha(s)) + 2a\cos\left(\frac{\phi}{2}\right). \tag{B.23}$$

The first of these requires the filaments to once again be parallel at the ends of the braid defect and ensure that the tangent rotates through the full kink angle as the arc length variables moves through the braid defect. The second enforces their normal separation of a as fixed by the cross-linking molecules at each end of the braid defect.

In addition to this previous analysis of braids in bundles with free ends, the energy from Ref. [163] now needs a contribution from the compression $FR\cos\phi$:

$$\begin{aligned} E &= 2\left[\lambda_s\left[\int_{-L/2}^{L/2} ds \sin(\alpha(s)) - a\cos\left(\frac{\phi}{2}\right)\right] + \right. \\ &+ \int_{-L/2}^{L/2} ds\kappa\frac{\alpha'^2}{2} + \tilde{\lambda}\left[\delta\left(s+\frac{L}{2}\right)\alpha + \frac{\phi}{2L}\right] + \lambda^\dagger\left[\delta\left(s-\frac{L}{2}\right)\alpha - \frac{\phi}{2L}\right]\Bigg] \\ &+ \mu L + FR\cos\phi, \end{aligned} \tag{B.24}$$

where λ, $\tilde{\lambda}$,$\lambda^\dagger$, and λ_s are Lagrange multipliers fixing boundary conditions given in Eqs. B.22 and B.23.

We vary the energy Eq. B.24 with respect to $\alpha(s)$, obtaining the equation of elastic equilibrium, which is the same as the one obtained in Ref. [163] for the braid with free boundaries:

$$\kappa\alpha \;\; = \;\; \lambda_s\cos\alpha_1 + \tilde{\lambda}_1\delta\left(s+\frac{L_1}{2}\right) + \lambda_1^\dagger\delta\left(s-\frac{L_1}{2}\right). \tag{B.25}$$

Eq. B.25 requires us to impose the equalities: $\tilde{\lambda} = \kappa\alpha'\left(-\frac{L}{2}\right)$ and $\lambda^{\dagger} = -\kappa\alpha'\left(\frac{L}{2}\right)$. Repeating arguments from [163] I show that λ_s must be negative everywhere. Minimizing the energy Eq. B.24 with respect to the length of the defect L I obtain

$$\int_{-L/2}^{L/2} ds \left(-\frac{\kappa}{2}\alpha'^2 + \mu + \lambda_c \cos\alpha + \lambda_s \sin\alpha\right) \quad = \quad 0. \tag{B.26}$$

$$\tag{B.27}$$

Using Eq. B.25, I find a conserved quantity (the analog of first integrals of a dynamical system) I such that $dI/ds = 0$. This first integral is given by

$$I \quad = \quad \frac{\kappa}{2}\alpha'^2 - \lambda_s \sin\alpha. \tag{B.28}$$

Comparing Eq. B.28 and Eq. B.26 I find the value of this first integral, which is the binding energy per unit length of the cross linkers:

$$\frac{\kappa}{2}\alpha'^2 - \lambda_s \sin\alpha = \mu. \tag{B.29}$$

From the result the rate of change of the tangent angle at the ends of the braid defect are fixed. I find

$$\alpha'^2\left(\pm\frac{L}{2}\right) = 2\left[\frac{\mu}{\kappa} \pm \lambda_s \sin\left(\frac{\phi}{2}\right)\right]. \tag{B.30}$$

Subtracting in the Eq. B.30 the upper sign equation from the lower sign one, I obtain a helpful expression for later use:

$$\frac{4\lambda_s \sin\left(\frac{\phi}{2}\right)}{\alpha'\left(\frac{L}{2}\right) - \alpha'\left(-\frac{L}{2}\right)} = \kappa\left[\alpha'\left(\frac{L}{2}\right) + \alpha'\left(-\frac{L}{2}\right)\right]. \tag{B.31}$$

Finally, the variation of the total energy Eq. B.24 with respect to ϕ gives

$$\frac{\partial E}{\partial \phi} = 4\lambda_s a \sin\left(\frac{\phi}{2}\right) + 2\tilde{\lambda} - 2\lambda^{\dagger} - FR\sin(\phi). \tag{B.32}$$

Using boundary condition Eq. B.25, I simplify Eq. B.32 to

$$\frac{\partial E}{\partial \phi} = 4\lambda_s a \sin\left(\frac{\phi}{2}\right) + \kappa\alpha'\left(-\frac{L}{2}\right) + \kappa\alpha'\left(-\frac{L}{2}\right) + \kappa\alpha'\left(\frac{L}{2}\right) + \kappa\alpha'\left(\frac{L}{2}\right) - FR\sin(\phi)\,. \tag{B.33}$$

Substituting Eqs. B.31 into Eq. B.33 I find

$$\frac{\partial E}{\partial \phi} = 4\lambda_s \sin\left(\frac{\phi}{2}\right)\left[a + \frac{4}{\alpha'\left(\frac{L}{2}\right) - \alpha'\left(-\frac{L}{2}\right)} + \frac{FR}{2\lambda_s}\cos(\phi/2)\right]. \tag{B.34}$$

Eq. B.34 shows that $\phi = 0$ is an extremum.The transition from minimum to maximum occurs when the expression in square brackets is zero:

$$a + \frac{4}{\alpha'\left(\frac{L}{2}\right) - \alpha'\left(-\frac{L}{2}\right)} - \frac{FR}{2\lambda_s}\cos(\phi/2) = 0. \tag{B.35}$$

While this transition from minimum to maximum indicates the second order phase transition, I also may have a situation in which there is another potential minimum at $\phi \neq 0$. If, at some value of system parameters, this minimum becomes deeper than the minimum at $\phi = 0$ (even when it is still minimum, not maximum), I obtain a first order phase transition instead of the second order one. As I see using numerical energy minimization, the symmetric case corresponds to the second order phase transition, while the asymmetric produces a first-order kinking transition. Here I continue to study the symmetric case to analytically explore the second order phase transition.

Let us consider the critical point at which the braided bundle transitions from an unkinked state with $\phi = 0$ to one with finite kinking angles. Assuming the transition is second order so that the kinking angle grows continuously from zero at the transition, I may study this point by first setting $\phi = 0$. Eq. B.30 then transforms to

$$\alpha'\left(\pm\frac{L}{2}\right) = \pm\sqrt{2\frac{\mu}{\kappa}}. \tag{B.36}$$

Using it, I simplify Eq. B.35 to

$$a - \frac{2}{\sqrt{2\mu/\kappa}} = \frac{FR}{2\lambda_s}. \tag{B.37}$$

As I move through the braid, α increases from 0 to its maximal value $\alpha_{\max}$ and then decreases back to 0. $\alpha_{\max}$ is determined by $\alpha'_{\max} = 0$, so Eq. B.29 gives

$$\mu = -\lambda_s \sin \alpha_{\max}, \tag{B.38}$$

and

$$\alpha_{\max} = \arcsin(-\mu/\lambda_s). \tag{B.39}$$

Due to symmetry of the problem the maximum angle occurs at the origin of the arc length variable: $\alpha_{\max} = \alpha(0)$. The integral condition Eq. B.23 for $\phi = 0$ gives

$$\int_{-L/2}^{L/2} ds \sin \alpha = a. \tag{B.40}$$

Due to symmetry, the integral can be transformed to

$$\int_{-L/2}^{0} ds \sin \alpha = a/2, \tag{B.41}$$

where α grows from 0 to $\alpha_{\max}$. Denoting $z = \sin \alpha(s)$ so that $\alpha(s) = \arcsin z$, and

$$\alpha'(s) ds = \frac{dz}{\sqrt{1 - z^2}}. \tag{B.42}$$

Then Eq. B.29 gives

$$\alpha' = \pm\sqrt{2(\mu + \lambda_s z)/\kappa}. \tag{B.43}$$

Then on the interval under consideration, α grows so

$$ds = \frac{dz}{\sqrt{1 - z^2}\sqrt{2(\mu + \lambda_s z)/\kappa}}. \tag{B.44}$$

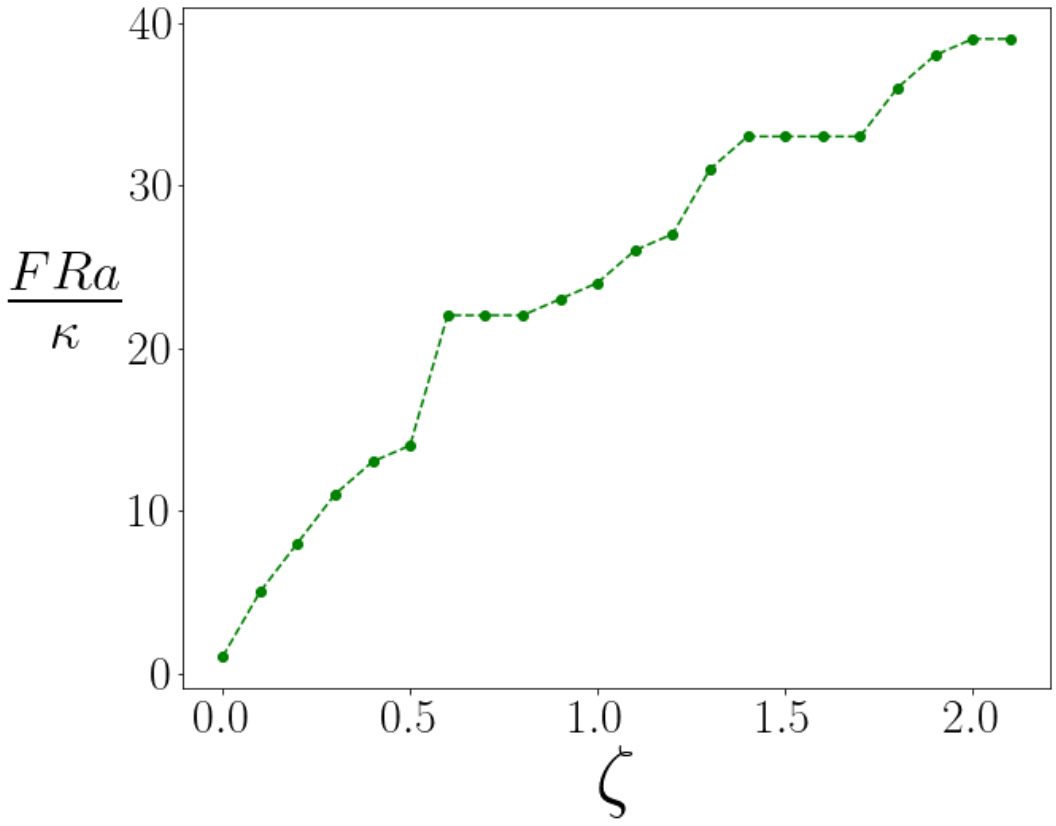

Figure B.1: The compressive load required to produce Euler buckling in a three-filament bundle as a function of ζ. Green dots - results of numerical minimization of the energy. Dashed line - guide for the eye.

Substituting this identity into the integral in Eq. B.41 I may write

$$\int_0^{-\mu/\lambda_s} \frac{zdz}{\sqrt{1-z^2}\sqrt{2(\mu+\lambda_s z)/\kappa}} = a/2. \tag{B.45}$$

Finally, I use Eq. B.37 to determine λ_s and after some some algebra, I obtain an equation relating compressive load and ζ at critical point

$$\int_0^1 \frac{\left(\left(\sqrt{2\zeta}-\zeta\right)\frac{2\kappa}{FRa}\right)^2 tdt}{\sqrt{1-\left(\left(\sqrt{2\zeta}-\zeta\right)\frac{2\kappa}{FRa}\right)^2 t^2}\sqrt{1-t)}} = \sqrt{\zeta/2}. \tag{B.46}$$

This implicit relation between between ζ and the critical compressive load $F^\star = F^\star(\zeta)$ can be solved numerically. The results are shown in Fig.3 of the main text.

B.3 Euler buckling of the bundle

We determine the critical force for buckling of a three-filament bundle by numerically minimizing its energy:

$$E = -F\Delta L + \mu\ell + \sum_{i=1}^{N} \int ds \frac{\kappa_i}{2} \left(\partial_s \hat{t}_i\right)^2. \tag{B.47}$$

In this minimization, I do not insert either braid or loop defects, but the bundle when bent does loose cross linkers. This uncross-linked region may be viewed as some sort of localized defect, but it is not one of the defects whose annealing requires a system-sized rearrangement of cross links.

We observe that, for a strong enough compression, the state where the central part of the bundle bends has less energy than the straight bundle. The size of the bent part ℓ is determined by the minimization of the energy Eq. B.47. We find the threshold compression value at which bundles transform from straight to bent, as a function of ζ (see Fig. B.1 SI). We observe that this value is significantly bigger

than the braid-induced kinking threshold (see Fig. 3 main document), showing that defect production occurs before buckling upon increasing force.

APPENDIX C

Appendix for "The conformation of a semiflexible filament in a quenched random potential"

C.1 Calculating the traces

In this appendix we discuss the calculation of the trace of the operator $\mathcal{O}^{-1}\mathcal{G}^{-1}$ obtained in Eq. 6.16. The operators $\mathcal{O}$ and $\mathcal{G}$ were introduced in Eqs. 6.8 and 6.14 respectively. To calculate the traces, we need the complete spectrum of the two differential operators in question. In other words, we must solve

$$\mathcal{O}\Psi = E_n\Psi \tag{C.1}$$

subject to the fixed-end boundary conditions $\Psi(0) = \Psi(L_0)$. The solution is a constant and the set of standing waves satisfying the boundary conditions: $\Psi(y) = A\sin(z_n y)$, where, as discussed in the main text, $z_n = n\pi/L_0$ for nonnegative integer n. Defining $\omega = \sqrt{\frac{k}{m}}$ we may write the trace as

$$\mathrm{Tr}G^{-1} = 2\xi\sum_{n=0}^{\infty}\frac{1}{z_n^2}. \tag{C.2}$$

Since both operators can be simultaneously diagonalized, it is also possible to write

$$\mathrm{Tr}(\mathcal{O}^{-1}G^{-1}) = \frac{4\xi}{k}\sum_{n=0}^{\infty}\frac{1}{z_n^2}\frac{1}{z_n^2+\omega^2} \tag{C.3}$$

Using the above results and Eq. 6.16, one finds directly that

$$\Delta F = \frac{m\xi}{2} \sum_{n=0}^{\infty} \frac{1}{z_n^2} \left(1 - \frac{\omega^2}{z_n^2 + \omega^2} \right). \tag{C.4}$$

The second term in the product occurring in the summand removes the singularity associated with the $n = 0$ term.

$$\Delta F = \frac{k\xi}{2} \sum_{n=0}^{\infty} \frac{1}{z_n^2 + \omega^2} \tag{C.5}$$

The summation can be done in closed form leading to the disorder-averaged free energy:

$$[F] = F_{SHO} + \frac{k\xi}{4} \frac{1 + \omega L_0 \coth(\omega L_0)}{\omega^2} \tag{C.6}$$

C.2 The Modified Harmonic Oscillator

In this appendix we review the partition function of the modified harmonic oscillator. The modified harmonic oscillator Hamiltonian has an addition p^4 where $p \to -i\partial$ is the momentum operator. This leads to a time-independent Schrödinger operator of the form $\mathcal{O}_\kappa$ introduced to discuss the semiflexible filament in the text. A more complete exposition of this problem can be found in Refs. [89] and [45]. We begin by factoring the differential operator $\mathcal{O}_\kappa$, defined in Eq. 6.23 into a product of two commuting second order differential operators as shown in Eq. 6.27:

$$\mathcal{O}_\kappa = \mathcal{O}_1 \mathcal{O}_2, \tag{C.7}$$

where

$$\mathcal{O}_j = \partial^2 + \omega_j^2. \tag{C.8}$$

It immediately follows that the partition sum for the modified harmonic oscillator is given by a product of the partition functions of two separate harmonic oscillators Z_1

and Z_2,

$$Z_{MHO} = \frac{1}{\sqrt{\det \mathcal{O}_1}} \frac{1}{\sqrt{\det \mathcal{O}_2}} = Z_1 Z_2, \tag{C.9}$$

with frequencies ω_1 and ω_2 respectively. The free energy immediately follows. From Eq. C.9, it is the sum of the free energies of the two harmonic oscillators introduced above in Eq. C.7,

$$F_{MHO} = F_1 + F_2 = T \ln(2 \sinh(\omega_1 L_0/2)) + T \ln(2 \sinh(\omega_2 L_0/2)). \tag{C.10}$$

The remainder of this appendix uses the above result.

We first compute the free energy of the filament in a confining potential (finite k). Since the mass term in the equation of motion represents tension $m = \tau/T$ – see Eq. 6.8– and since tension is conjugate to arclength in the Hamiltonian, the derivative of the free energy with respect to mass gives us mean arclength that we seek.

$$\langle L \rangle = \frac{1}{T} \partial_m F. \tag{C.11}$$

There is one complication. The free energy is divergent in the limit that $k \to 0$. We require the arclength of the unconfined filament in order to compute ΔL, as defined in Eq. 6.19. To address this problem, we compute the mean arclength at finite k, take the necessary derivative, and then take the limit $k \to 0$, which then provides a finite result.

We first recall the (possibly complex) frequencies $\omega_{1,2}$ and use them to compute derivatives of the free energy in Eq. C.10.

$$\frac{\partial_m F_{MHO}}{T} = \frac{\partial_m \omega_1 L_0 \cosh(\omega_1 L_0/2)}{2 \sinh(\omega_1 L_0/2)} + \frac{\partial_m \omega_2 L_0 \cosh(\omega_2 L_0/2)}{2 \sinh(\omega_2 L_0/2)} \tag{C.12}$$

We know that $\omega_1^2 + \omega_2^2 = \frac{m}{\ell_P}$ and that $\omega_1 \omega_2 = \sqrt{\frac{k}{\ell_P}}$. When there is no confining potential $k = 0$, one frequency vanishes. This implies that the spectrum of the

corresponding operator includes a zero eigenvalue, which, as discussed above, will be problematic for the analysis. In preparation for taking the $k \to 0$ limit we keep only the lowest terms in k here. Expanding to lowest order in k we find that

$$\omega_1^2 + \omega_2^2 \pm 2\omega_1\omega_2 = \frac{m}{\ell_{\rm P}} \pm 2\sqrt{\frac{k}{\ell_{\rm P}}}, \tag{C.13}$$

which means

$$\omega_1 \pm \omega_2 = \sqrt{\frac{m}{\ell_{\rm P}} \pm 2\sqrt{\frac{k}{\ell_{\rm P}}}} \tag{C.14}$$

Solving for $\omega_{1,2}$ we find that

$$\omega_1 = \sqrt{\frac{m}{\ell_{\rm P}}} \tag{C.15}$$

$$\omega_2 = \sqrt{\frac{k}{m}}. \tag{C.16}$$

These results allow us to take the appropriate m derivatives:

$$\partial_m\omega_1 = \frac{1}{2}\sqrt{\frac{1}{m\ell_{\rm P}}} \tag{C.17}$$

$$\partial_m\omega_2 = -\frac{1}{2}\sqrt{\frac{k}{m^3}}. \tag{C.18}$$

By assuming that the filament is long we may take $\omega_1 L_0 \gg 1$. We also assume that k may be sufficiently small so that $\omega_2 L_0 \ll 1$ (we will take it to zero shortly). The free energy of the filament is then

$$F_{MHO} = T\omega_1 L_0/2 + T\ln\left(\omega_2 L_0\right). \tag{C.19}$$

Taking the derivative as shown in Eq. C.11, we obtain the mean length

$$\langle L\rangle|_{k=0} = \frac{1}{4}\sqrt{\frac{1}{m\ell_{\rm P}}}L_0 - \frac{1}{2m}. \tag{C.20}$$

For large L_0 the last term can be ignored, leaving us with the $k = 0$ result.

We now turn to the case where k remains finite. Then for long filaments we have $\omega_1 L \gg 1$ and $\omega_2 L \gg 1$, allowing us to write F_{MHO}, defined in Eq. C.10 as

$$F_{MHO} = T(\omega_1 + \omega_2)\frac{L_0}{2} = \frac{TL_0}{2}\sqrt{\frac{m}{\ell_{\mathrm{P}}}} + 2\sqrt{\frac{k}{\ell_{\mathrm{P}}}}. \tag{C.21}$$

Then, taking the m derivative as above, we obtain the mean arclength of the filament with a confining potential $k \neq 0$:

$$\langle L \rangle_{MHO} = \frac{1}{\sqrt{m\ell_{\mathrm{P}}}}\frac{1}{\sqrt{1+2\phi}}\frac{L_0}{4} \tag{C.22}$$

Subtracting the equivalent quantity for the $k = 0$ case, shown in Eq. C.20, we obtain an expression for the change in excess mean arclength due to the presence of the confining potential

$$\Delta L_{MHO} = \frac{1}{\sqrt{mb}}\frac{1}{\sqrt{1+2\phi}}\frac{L_0}{4} - \frac{1}{4}\sqrt{\frac{1}{m\ell_{\mathrm{P}}}}L_0 \tag{C.23}$$

Returning the original, physical parameters of the semiflexible filament model, this expression becomes

$$\Delta L_{MHO} = \frac{1}{\beta\sqrt{\tau\kappa}}\left(\frac{1}{\sqrt{1+2\phi}} - 1\right)\frac{L_0}{4}. \tag{C.24}$$

C.3 Replica Trick

The core idea of the replica trick is the following. We want to find $[\ln Z]$ where the average is over the ensemble of quenched potentials. We may rewrite this in the following form

$$[\ln Z] = \lim_{R\to 0}\left[\frac{Z^R - 1}{R}\right] \tag{C.25}$$

In many cases the straightforward calculation of the left hand side is intractable, while it is possible to compute on the right hand side for positive integer R and

then take the limit. The reader is referred to Ref. [119] for further details of this approach. We first demonstrate the utility of the replica method in a simplified model. We assume a Gaussian Hamiltonian so that the partition function has the form

$$Z = \int \mathcal{D}y(x) e^{-\int yAy + 2y_0 By} \tag{C.26}$$

where A,B are operators acting on the variable y. The variable y is affected by a quenched potential, y_0 whose statistics are fixed by the Gaussian distribution

$$\mathcal{P}(V) \propto e^{-\int y_0 C y_0}, \tag{C.27}$$

controlled by another operator C. This problem is designed to be sufficiently simple that it can be solved without the replica trick. It is also directly related to valley approximation, as the reader may confirm. A straightforward calculation of the partition function, followed by taking the logarithm and then averaging the resulting free energy over the quenched potential distribution leads to

$$[\ln Z] = \ln \frac{1}{\sqrt{\det A}} - \frac{1}{2}\mathrm{tr}(C^{-1}BA^{-1}B). \tag{C.28}$$

If we now repeat the calculation using the replica trick, we first replicate the Hamiltonian to form Z^R:

$$Z^R = \int \mathcal{D}y_r(x) e^{-\int \sum_{r=1}^{R} y_r A y_r + 2y_0 B y_r}, \tag{C.29}$$

where the replicated variables are indexed by r: y_r, $r = 1, \ldots, R$. We now average the replicated partition sum over the quenched potential (notice we are swapping the order of the two averages) to obtain

$$\left[Z^R\right] = \frac{\int \mathcal{D}y_r(x)\mathcal{D}y_0(x) e^{-\int \sum_{r=1}^{R} y_r A y_r + 2y_0 B y_r + y_0 C y_0}}{\int D y_0(x) e^{-\int y_0 C y_0}}. \tag{C.30}$$

Introducing $\vec{y} = (y_0, y_1 ... y_R)$ we can write Eq. C.30 in the form

$$\left[Z^R\right] = \frac{\int \mathcal{D}\vec{y}(x) e^{-\int_0^T \vec{y}\mathcal{A}\vec{y}}}{\int Dy_0(x) e^{-\int y_0 C y_0}} \tag{C.31}$$

where the matrix $\mathcal{A}$ can be written in the block form

$$\mathcal{A} = \begin{pmatrix} C & \tilde{B}^T \\ \tilde{B} & \tilde{A} \end{pmatrix}. \tag{C.32}$$

The $\tilde{A}$ block is the $R \times R$ matrix coupling the replicated variables. The $\tilde{B}$ block is an $R \times 1$ matrix coupling the R replicated variables to the quenched disorder y_0. The remaining calculation involves performing the Gaussian integrals over $\vec{y}$. We find

$$[Z^R] = \left(\frac{\det \mathcal{A}}{\det C}\right)^{-1/2} \tag{C.33}$$

The determinant of the block matrix can be written as

$$\det \mathcal{A} = \det \tilde{A} \det \left(C - \tilde{B}^T \tilde{A}^{-1} \tilde{B}\right), \tag{C.34}$$

and we observe that, in our model, the variables y_r, $r = 1, \ldots, R$ are noninteracting so that the $\det \tilde{A} = \det A^R$. As a consequence,

$$[Z^R] = \left\{\det A^R \det(1 - RB^T A^{-1} B C^{-1})\right\}^{-1/2}. \tag{C.35}$$

By taking the $R \to 0$, we reproduce the exact result, Eq. C.28.

Now, we consider using the replica trick for the problem at hand. Specifically, we examine a flexible polymer at temperature T interacting with a quenched delta-correlated random potential. The polymer has tension τ and length L. We will examine the average potential energy of the filament in the pinning potential. For later computational convenience, we introduce a coupling constant α controlling the interaction of the polymer with pinning potential.

The partition function is

$$Z_\alpha = \int \mathcal{D}y(x) e^{-\beta \int_0^L dx \frac{\tau}{2}\dot{y}^2 + \alpha V(x,y)} \tag{C.36}$$

We can calculate the average potential energy as

$$\left.\frac{\partial F}{\partial \alpha}\right|_{\alpha=1} = \left\langle \int V(x, y(x)) dx \right\rangle . \tag{C.37}$$

After this thermal average, we take the average of the potential over the ensemble of pinning potentials

$$\left.\frac{\partial [F]}{\partial \alpha}\right|_{\alpha=1} = \left[\left\langle \int V(x, y(x)) dx \right\rangle \right] \tag{C.38}$$

We assume that averaging and differentiation commute. We expect that the mean potential energy should be negative. Indeed, the random potential will pick negative and positive values with the same probability. The polymer, however, will prefer the negative regions to the positive.

We now perform the necessary averages using the replica trick with, as before, the replica index being $r = 1..R$. The replicated partition sum is now

$$Z_\alpha^R = \int \mathcal{D}y_i(x) e^{-\beta \int_0^L dx \sum_{i=1}^R \frac{\tau}{2}\dot{y}_r^2 + \alpha V(x, y_r(x))} . \tag{C.39}$$

The average over the pinning potential, once again, couples the replicas. We first write that average over the distribution of $V(x, y)$,

$$\left[Z_\alpha^R\right] = \int \mathcal{D}y_r e^{-\beta \frac{\tau}{2} \int_0^L dx \sum_{i=1}^R \dot{y}_r^2} \int \mathcal{D}V \mathcal{P}(V) e^{-\beta \int_0^L dx \int dy \sum_{i=1}^R \alpha V(x,y)\delta(y - y_r(x))} \tag{C.40}$$

Since $\mathcal{P}(V)$ is a Gaussian with fixed variance σ we can directly perform the Gaussian integral over V. We also notice that the delta functions $\delta(y - y_r(x))$ allow us to do the integral over y in the exponent. Doing both steps we obtain

$$\left[Z_\alpha^R\right] = \int \mathcal{D}y_r e^{-\beta(\int_0^L dx \sum_{i=1}^R \frac{\tau}{2}\dot{y}_r^2 - \sigma\beta\alpha^2 \sum_{i,j=1}^R \delta(y_i(x)-y_j(x))}. \tag{C.41}$$

Eq. C.41 now appears to be the partition function of R particles interacting through a delta-potential. It can be written in the form

$$[Z_\alpha^n] = \int \mathcal{D}y_r e^{-L_0 H(y_1(x),\ldots,y_R(x))} \tag{C.42}$$

where the multi-particle Hamiltonian is

$$H = \sum_{r=1}^R \frac{1}{2\beta\tau} p_r^2 - \sigma\beta^2 \sum_{i,j=1}^R \alpha^2 \delta(y_j(x) - y_i(x)). \tag{C.43}$$

Notice that in Eq. C.42 that the length of the polymer L_0 plays the role of inverse temperature $1/T$ for the fictitious particles. Of course, $L_0 \neq \beta$, which is the inverse temperature of the polymer. We also note that x plays the role of time in this dynamical system of interacting particles.

Since the sum contains the term $i = j$, there is a positive infinite constant C in the Hamiltonian. Separating these terms explicitly we rewrite the Hamiltonian as

$$H = \sum_{i=1}^R \frac{1}{2\beta\tau} p_i^2 - 2\sigma\beta^2 \sum_{i<j} \tau^2\alpha^2 \delta(y_j(x) - y_i(x)) - C\sigma\beta^2\tau^2\alpha^2. \tag{C.44}$$

Reflecting on the fact that the path integral in Eq. C.42 is analogous to the quantum transition amplitude for the system of fictitious particles [140] and that the long polymer limit $L_0 \to \infty$ corresponds to the zero temperature limit for that system, we may focus on the ground state wavefunction [85, 84]. To find the ground state wavefunction, we use the Bethe ansatz:

$$\Psi_0 = C_0 \exp\left(-\kappa \sum_{\alpha<\beta} |y_\alpha - y_\beta|\right). \tag{C.45}$$

The constant C_0 is chosen to satisfy the normalization condition. The constant κ is set so that the discontinuity of the first derivative cancels the delta-function, i.e., $\frac{2}{\beta\tau}\kappa = 2\sigma\beta^2\alpha^2$.

We transform the sum by choosing a particular ordering of the R particles on the y line: $y_1 < y_2 < \ldots < y_R$. In this ordering the sum in Eq. C.45 is particularly simple:

$$\sum_{\alpha<\beta} |y_\alpha - y_\beta| = \sum_\alpha (2\alpha - n - 1) y_\alpha. \tag{C.46}$$

From this we obtain the ground state energy

$$E_R = RC\sigma\beta^2\tau^2\alpha^2 - \frac{1}{2\beta\tau}\kappa^2 \frac{R(R+1)(R-1)}{3} \tag{C.47}$$

Then the partition function is

$$Z^R = e^{-\beta E_R} \tag{C.48}$$

and the free energy is

$$\beta F = -[\log Z] = -\lim_{R\to 0}[\frac{Z^R - 1}{n}] = \beta \lim_{R\to 0} \frac{E_R}{R}. \tag{C.49}$$

Taking the limit we get

$$F = C\sigma\beta\tau^2\alpha^2 + \frac{1}{6}\sigma^2\beta^4\alpha^4\tau. \tag{C.50}$$

Using Eq. C.38, we obtain the potential energy of the thermalized polymer in the random pinning potential, averaged over an ensemble of such potentials:

$$\left[\left\langle \int V(x, y(x))dx \right\rangle\right] = 2C\sigma\beta\tau^2 + \frac{2}{3}\sigma^2\beta^4\tau \tag{C.51}$$

This potential energy is positive definite, which is clearly unphysical. The result shows that the replica trick fails to find the averaged potential energy of the polymer

in the pinning potential. The problem may lie in either the introduction of the infinite constant C, or in the replica trick itself.

We conjecture that the failure of the replica trick in this case is related to the failure of the analytical continuation inherent in the method. To expand on this idea we consider an example related to directed polymers (without a bending energy) in a complex random potential with zero correlation length ($\xi \to 0$), as explored by Zhang [190]. In that work [Eq. (11) of that article] the author asserts that

$$\int dF P(F) e^{-nF} = e^{-t(nF_0 - an^3)}, \tag{C.52}$$

where $P(F)$ is the probability distribution of free energies of the directed polymer due to the statistical ensemble of quenched potentials in its environment and n is the replica index. The left hand side of this expression is $[Z^n]$. Now $P(F)$ should decay exponentially or faster for negative F, otherwise the integral will be divergent. The result on the right hand side, arrived at through a saddle point evaluation of the integral, is exact for all positive integer n in the limit of large t. The goal (as in our case too) is to examine the $n \to 0$ limit.

To examine this point let us perform the integration in Eq. C.52 by first Taylor expanding the exponential and then integrating term by term.

$$\int dF P(F) \sum_{k=0}^{\infty} \frac{(-nF)^k}{k!} = \sum_{k=0}^{\infty} \frac{(-(nF_0 - n^\beta))^k}{k!}. \tag{C.53}$$

From Ref. [93] we know that the large positive F behavior of $P(F)$ is $\sim \exp(-F^{\frac{5}{2}})$, ensuring the convergence of these integral and justifying the swapping of the order of summation and integration. The sum on the right hand side can be reorganized in terms of powers of the replica index n so that each term in the summand takes the form $d_k n^k$. In this form that sum can be combined with integral on the left to

write an infinite sum that is now equal to zero.

$$\sum_{k=0}^{\infty} c_k n^k = 0 \tag{C.54}$$

where

$$c_k = \int dF P(F) \frac{(-F)^k}{k!} - d_k. \tag{C.55}$$

If we were allowed to assert that each term in the sum Eq. C.54 separately vanished, then we would be able to calculate all moments of the free energy directly from the known coefficients d_k. This process for $k = 1$ is the essence of the replica trick as used to compute the mean free energy. Unfortunately, this conclusion is not necessarily valid. A simple counter example can be obtain from the Taylor expansion of the function $F(z) = f(z)\sin(\pi z)$, where $f(z)$ is an analytic function. Let a_k be Taylor expansion coefficients for $F(z)$. Then it is easy to see that if we choose $c_k = \frac{a_k}{k!}$ we will get Eq. C.54, but not all c_k are zero. The same issue appears in Ref. [85].

APPENDIX D

Appendix for "Microcircuit synchronization and heavy tailed synaptic weight distribution in preBötzinger Complex contribute to generation of breathing rhythm"

D.1 Choice of the physiological parameters

While Δt_{ij} can be taken directly from the experimental data [148], we need to fit parameters τ_{m}, τ_{s}, and W_{ij} obtain approximately the same EPSP profile as observed experimentally. The EPSP decay time constant 20 is almost τ_{m} ($\tau_{\mathrm{m}} \gg \tau_{\mathrm{s}}$). We then chose τ_{s} to fit the EPSP rise time. The lognormal distribution for EPSP amplitudes was determined from published parameters[148]. Specifically, the unitary EPSP amplitude of inputs from putative rhythmogenic neurons was distributed as 2.8 $\pm$1.5 mV (mean$\pm$SD). The high variance of EPSP amplitude requires a heavy tailed distribution in order to capture the entire range of EPSPs without incurring negative values, i.e., assuming a symmetric normal distribution 99.75% (mean$\pm$3SD) range of EPSPs would be -1.7 mV to 7.3 mV. Furthermore, this EPSP distribution of preBötC rhythmogenic neurons is consistent with the notion that biologically plausible, log-normal distributions of unitary EPSP amplitudes seen in several brain regions 22 are

essential to explain their behavior. Thus, we modeled EPSP amplitudes by fitting the parameters of a lognormal distribution for synaptic weightsW_{ij} to reflect the experimental range of unitary EPSP amplitudes. In terms of the model parameters, an EPSP amplitude of 2.8 mV required a synaptic weight of $W_{ij} = 300$ mV/ms.

D.1.1 Simulations for stimulation of 1-10 neurons

Stimulation (by holographic photolysis of caged glutamate [80] of 4 - 9 of preBötC neurons induces inspiratory bursts (I-burst) through synchronization of preBötC rhythmogenic neurons with a $\geq$ 80% success rate, with latencies ranging from 57 ms - 360 ms that are inversely related to the number of stimulated neurons (Figure 7.1G-I). Specifically, the minimum number of co-stimulated neurons that induced an I-burst (henceforth referred to as the threshold number of neurons) ranged from 4 - 9 with the latency to I-burst generation ranging from 170 ms – 370 ms (255±43 ms; mean±SEM) (Figure 1H). For experiments with suprathreshold number of stimulated neurons, consisting of 1 - 3 additional neurons, the latency to induce I-burst ranged from 57 ms – 160 ms (125±23 m; mean±SEM; Figure 1I)[80]. We simulated the effects of experimental photostimulation of preBötC neurons by "depolarizing" chosen neurons to produce a similar spiking pattern [80]. We characterized the spiking pattern by the time between activation and the first spike τ_{delay}, average period of spiking of the laser stimulated neurons, T_{laser}, the standard deviation, ΔT, of the spiking period distribution, and the number of spikes produced n_{spikes}, all based on experimental measurements [80]. The parameters used for the model are listed Supplementary Table S1. To model the experimental conditions in a connected population of 1000 LIF point neurons (the same order as the number of preBötC

rhythmogenic neurons), we mimicked the effect of 9 mM [K^+] in the extracellular bathing solution on neuronal excitability by incorporating a constant depolarizing potential that put $V_{\text{rest}} \sim -60$ mV while keeping the threshold for spikes at –48 mV; for the purposes of the model, this was represented by a 12 mV depolarization from baseline potential, defined as 0 mV. To simulate the holographic photolysis experiments [80], we initiated spiking in 1 - 9 neurons in a connected population[148] of 1000 LIF neurons, q.v., MODEL section, at 25±3 Hz per their experimentally characterized firing behavior [80] (Figure 7.1 E-F).

D.1.2 Seeding neurons with low-frequency uncorrelatied firing for burst initiation

The preBötC Type I inspiratory neurons, which are putatively rhythmogenic [7, 58, 147, 137] start firing at very low frequencies (∼0.5-1 Hz) in the late interburst interval, referred to as the preinspiratory (preI) period. Their activity leads to progressive network synchronization in the preI period that culminates in an inspiratory burst. We modeled this preI activity by initializing the neurons in the network to fire randomly at Poisson-distributed frequencies (mean range: 0.5 to 2.0 Hz), to "seed" the network with low levels of uncorrelated activity, as observed, preceding each burst, in experiments [7, 58, 147, 137]. After this initialization of neuronal activity, we computed the network firing rate in 5 ms bins as a measure of instantaneous synchrony in the network [149]. We chose this temporal window to capture correlated firing, i.e., synchrony, among neurons as this window (of coincidence) was too short for any neuron to spike more than once (their refractory period was set to 3 ms in all the models, a reasonable boundary condition based on experimental data,

Supplementary Table S1). Next, we computed average network activity from the firing rate computed in 5 ms bins, as a two-pass moving average, with a 25 ms moving window and 5 ms steps size.

D.2 On-off model for ER network

To acquire more general understanding of the processes during the burst formation in the preBötC, we consider the simplified version of the neuron model, namely on-off. In such model, the neuron can be either in "on" state, or in "off" state. When neuron has q or more "on" neighbors that synapse onto it, it also transits to the "on" state on the next step of the simulation. This model is a drastic simplification of the LIF model. Basically, one may think about it as LIF model where all synaptic weights are equal and initially chosen neurons were activated in an ideal synchrony.

The model then resembles the disease spreading dynamics [63] in which the on and off states of the neurons are analogous to the infected and susceptible states of individuals. The principal difference is that firing-quiescent model is deterministic, while the disease spreading model includes stochastic transitions between susceptible and infected individuals. We discuss this analogy below.

Since the class of ER networks is the only one found that gives physiologically relevant results, we concentrate on this type of network hereafter. We first estimate the probability that an arbitrary chosen neuron A be activated in the on-off model. We introduce the quantity $p_{i,m}$, the probability that exactly i neurons out of the m initially activated neurons synapse onto any particular neuron A. This probability is clearly independent of the choice of neuron A. From the definition of an ER graph

we have $p_{1,1} = p$. More generally, we note that

$$p_{i,m} = \binom{m}{i} p^i (1-p)^{m-i} \tag{D.1}$$

where $\binom{m}{i} = \frac{m!}{i!(m-i)!}$ is the number of ways to take i elements out of n. This results relies on the fact that there are no correlations between network connections in an ER network. The probability to be connected to not less than q neurons out of n neurons is simply determined by the appropriate sum of $p_{i,m}$ since the different numbers of connections are mutually exclusive events. We may write that probability as

$$p_{>q,m} = \sum_{i=q}^{m} \binom{m}{i} p^i (1-p)^{m-i}. \tag{D.2}$$

By setting the lower limit to q, we have computed the probability that the m activated neurons activate the neuron in question, A.

It then follows that the average number of the neurons that will switch to the synchronized firing state on the next time step is

$$n_1 = N p_{>q,m}, \tag{D.3}$$

where N is the total number of the neurons in the network, and the averaging is over the ensemble of ER graphs. Clearly there are three cases of interest. First, if $n_1 \ll 1$ with high probability we may assert that no neuron switches to the firing state at the next step. As a result synchronization does not spread. In contrast, if $n \gg 1$ then typically a large number of neurons are activated at the next step and global network synchronization is essentially assured. Between these two limits there is a transition at the threshold of $n_1 \approx 1$. This point is the most interesting and complicated to study, but understanding the synchronization dynamics at the threshold is vital for understanding the slow growth of synchronization in the ER

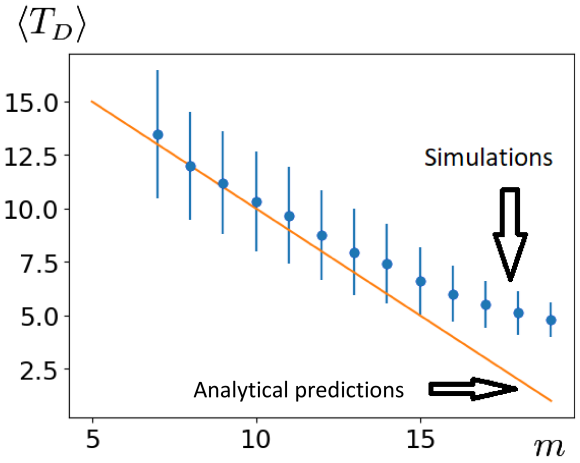

Figure D.1: (color online) Comparing the mean-field theory and simulations of the firing-quiescent model for a small network of 100 neurons. We observe a wide range of minimal growth rate for small m above the synchronization threshold. The error bars show the standard deviation of the mean for each data point.

network near the synchronization threshold. This slow growth underlies the strong dependence of the mean time delay for synchronization with increasing m, observed in our simulations.

Not all ER networks admit these threshold dynamics. Within the space of all random network ensembles, parameterized by network size and connection probability $\{N, p\}$, only some support $n_1 \approx 1$. In the other ER network ensembles, synchronization is either immediate or impossible as discussed above. In particular, finite size effects are essential: $N \to \infty$ results in either $n_1 = 0$ for $m < q$ or $n_1 \to \infty$ for $m \geq q$. Neither option is consistent with experiment. We note that the maximum N that supports the observed variations of mean time delay with the number of initially stimulated neurons is given by

$$N_{\max} = p^{-q} \tag{D.4}$$

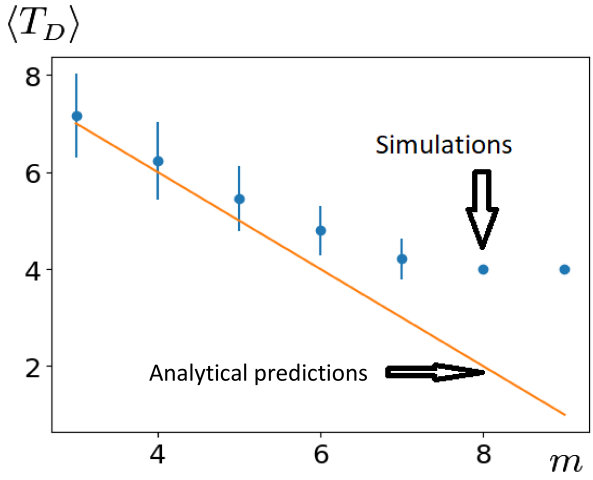

Figure D.2: (color online) Comparing the mean-field theory and simulations of the firing-quiescent model for a large network of 1000 neurons. We observe a much smaller range of minimal growth rate at small m above the synchronization threshold as compared to that of smaller networks. The error bars show the standard deviation of the mean for each data point.

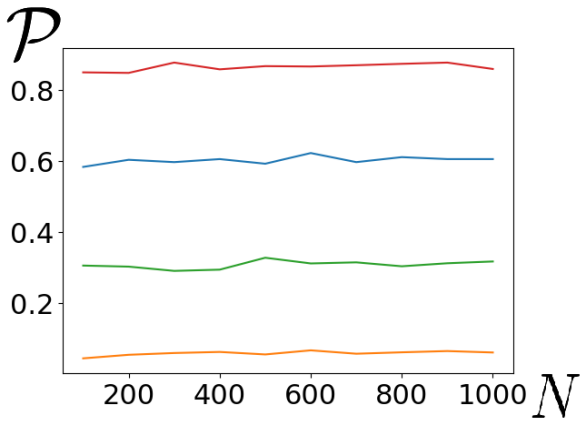

Figure D.3: (color online) The probability to synchronize as function of N under keeping α to be constant. The curves from top to bottom correspond to $\alpha = 2.0, 1.0, 0.5, 0.2$

easily obtained from setting n_1 to unity in Eq. D.3. The best current estimates for these quantities in the burstlet forming preBötC are $N \sim 10^3$ and $p \sim 0.065$ while the number of coincident neuronal spikes necessary to activate the postsynaptic neuron is $q = 3$. Thus we estimate from Eq. D.4 that $N_{max} \approx 3.6 \times 10^3$, which is indeed bigger than the estimated number of neurons involved. It may be noted that the value of q is critical: If q were reduced to two, the maximum network size capable of sustaining a threshold regime of slow synchronization growth would be reduced to about two hundred, much smaller than the physiological system. Measurements of q are perhaps the best way to invalidate our model.

We further explore how the process of synchronization depends on the parameters N, p, q, m by rewriting our model as a moving of the agent along the interval with obstacles, with coordinates of obstacles given by Eq. (D.2)with $m = m_{initial}, m_{initial}+1...N$ and neurons as points uniformly distributed along this interval (see subsection D.3 for the details and the proof of equivalence). In this representation we can prove that the average time of synchronization as function of the number of activated neurons approximately obeys the relation $\langle T_D(m)\rangle = 1 + \langle T_D(m+1)\rangle$ in the range of m where the probability of synchronization is small (which can be the case only when $N < N_{max}$). Physically this statement corresponds for the activation of only one neuron per step. Numerical simulations validate this theoretical prediction (see Fig. D.1, D.2)

Second, we explore the probability to synchronize as a function of N, p, q, m and prove that for large N it is a homogeneous function on N and p with critical exponent q:

$$\mathcal{P}(N, p, q, m) = f(Np^q, m, q) = f(\alpha, m, q) \tag{D.5}$$

with $\alpha = Np^q$. Easy to see that the criticality condition is simply $\alpha = 1$. We numerically check this statement by calculating the synchronization probability for different N but varying p correspondingly to keep α the same. Fig. D.3 demonstrates that probability as function of N for different α is constant.

D.3 Analytical description

D.3.1 Transformation of the model

To make more predictions using the firing-quiescent model it is convenient to make a few transformations of it, that does not change any of the probability distributions and averages we are interested in.

The first simplification comes from the fact that for all the runs of the simulations we studied the doubling of the initial number of neurons always eventually leaded to the burst. Moreover, the time from the initiation to the burst was essentially defined by the time from initiation to the doubling. Therefore, we do not have to run our simulation till we reach $0.6N$ active neurons threshold, but we can stop at $2m$ neurons.

Second simplification follows from the fact that initially activated neurons are chosen randomly from ER network without any correlation with its connectivity. Therefore, we do not have to generate the whole ER network beforehand, but can define only the neighbors of the neurons that are already active (in the same way as we do for the whole network). Since $m \ll N$ we can safely assume that the

activation of already active neurons does not happen. This way we do not need $N \times N$ connectivity matrix, but only $2m \times N$. We start with its first half $m \times N$, and we add $m+i$th row if previous matrix $(m+i-1) \times N$ has i or more columns with not less than q ones (which is equivalent to adding newly activated neurons to the set of active).

This procedure is equivalent to the motion of the agent along the interval [0,1] with obstacles in points $p_{>q,m+i}$ defined by Eq. (D.2) and uniformly distributed along the interval N bonus points. Each time the agent meets the bonus point it collects it, and the agent loses one bonus point at each obstacle. If the agent does not have bonus points he can not pass the obstacle.

Indeed, the probability that given column with $i+m-1$ neurons has not less than q ones is given by $p_{>q,i+m}$ from Eq. (D.2) . For the motion of the agent, the probability that given bonus point is before the ith ostacle, is $p_{>q,i+m}$ too. We add $m+i$th row if the number of columns with $i+m-1$ neurons is i or more. The agent passes ith obstacle if the number of bonus points before it is i or more. Therefore, the transitions and their probabilities are the same. Hence, these two models describe the same dynamics.

D.3.2 Homogenity of the probability finction and critical exponents. Average time delay.

The description of the process as the moving of the agent can give us a few insights about the behavior of this system. First, let us consider the probability of the burst as the function $\mathcal{P}(N,p,q,m)$. In the thermodynamical limit $N \to \infty$, $p \to 0$ such that $Np^q \approx$ const we have $p_{>q,m} \approx \binom{m}{q} p^q$. The probability to have exactly n bonus

points out of total N at the subinterval $[0, p_{>q,m}]$ is $\binom{N}{n}(p_{>q,m})^n \approx \frac{(\binom{m}{q})^n}{n!}(Np^q)^n$. We see that N and p enter this value only as a combination Np^q. Therefore, after the summation over all possible distributions that lead to the burst we obtain that the probability of the burst is a homogeneous function on N and p with critical exponent q:

$$\mathcal{P}(N, p, q, m) = f(Np^q, m, q) = f(\alpha, m, q) \tag{D.6}$$

where we introduced the new variable $\alpha = Np^q$.

We can also make a prediction about the slope of the function $\langle T_D(m) \rangle$ near the threshold. First we would like to demonstrate that the dominant scenario of the burst for the case when we are close to the threshold will be one when we activate only one neuron at the first step. To do it we need to introduce a few new probabilities. First,

$$p_i = \begin{cases} p_{>q,i+m-1} \text{ for } i = 1 \\ p_{>q,i+m-1} - p_{>q,i+m-2} \text{ else} \end{cases} \tag{D.7}$$

is a probability for the particular bonus point to be in the ith subinterval.

The probability exactly for n bonus points to be in the ith subinterval is

$$P_{i,n} = \binom{N}{n} p_i^n (1 - p_i)^{N-n} \tag{D.8}$$

Rewriting them using α in the limit $N \to \infty$ we have $p_{>q,m} \approx \binom{m}{q}\frac{\alpha}{N}$. Hence

$$p_i = \begin{cases} \binom{i}{q} \frac{\alpha}{N} \text{ for } i = m \\ \left(\binom{i}{q} - \binom{i-1}{q} \right) \frac{\alpha}{N} \text{ else} \end{cases} \tag{D.9}$$

or we can rewrite it

$$p_i = \begin{cases} \binom{i}{q} \frac{\alpha}{N} \text{ for } i = m \\ \binom{i-1}{q-1} \frac{\alpha}{N} \text{ else} \end{cases} \tag{D.10}$$

Let us simply write

$$p_i = g(q, i) \frac{\alpha}{N} \tag{D.11}$$

where we incorporated both cases to the definition of $g(q, i)$ In the limit $N \to \infty$ we also rewrite $P_{i,n}$

$$P_{i,n} = \binom{N}{n} p_i^n (1 - p_i)^{N-n} = \frac{N^n}{n!} p_i^n (1 - p_i)^{N-n} \tag{D.12}$$

or, substituting the definition, we get

$$P_{i,n} = \frac{g(q, i)^n}{n!} \alpha^n (1 - p_i)^{N-n} \tag{D.13}$$

Near the threshold we assume the probability of the burst to be close to zero. Therefore, we assume α to be small. Then we get

$$P_{i,n} = \frac{g(q, i)^n}{n!} \alpha^n \tag{D.14}$$

Let us compare the probabilities that two bonus points will go to the first subinterval with the probability that one will go to the first and one to the second. The first probability is

$$P_{i,2} = \frac{g(q,i)^2}{2}\alpha^2 \tag{D.15}$$

The second is

$$P_{i,1}P_{i+1,1} = g(q,i)g(q,i+1)\alpha^2 \tag{D.16}$$

Their ratio is

$$\frac{P_{i,1}P_{i+1,1}}{P_{i,2}} = \frac{2g(q,i+1)}{g(q,i)} \tag{D.17}$$

For $i = m$ we have

$$\frac{P_{m,1}P_{m+1,1}}{P_{m,2}} = \frac{2\binom{m}{q-1}}{\binom{m}{q}} \tag{D.18}$$

That is

$$\frac{P_{m,1}P_{m+1,1}}{P_{m,2}} = \frac{2q}{m-q+1} \tag{D.19}$$

We see that near the threshold, $q \gg m - q$, the dominant term for the passage time and probability will be the one that starts with one bonus point at the first subinterval (i.e., one neuron activated at the first step). Already from this we can qualitatively predict that near the threshold increasing m by one should lead to decreasing delay time by one step. Let us obtain it more precisely.

Let us find $\langle T_D(m)\rangle$ in this approximation. We have

$$\langle T_D(m)\rangle = 1 + P_{m,1}\frac{\tilde{\mathcal{P}}_{m+1}}{\mathcal{P}_m}\langle \tilde{T}_D(m+1)\rangle + ... \tag{D.20}$$

where $\tilde{\mathcal{P}}_{m+k}$ and $\langle \tilde{T}_D(m+k)\rangle$ are probability and time to pass starting from the kth obstacle (assuming we just passed it). We can write

$$\mathcal{P}_m = P_{m,1}\tilde{\mathcal{P}}_{m+1} + P_{m,2}\tilde{\mathcal{P}}_{m+2} + ... \tag{D.21}$$

$$\langle \tilde{T}_D(m+1)\rangle = 1 + P_{m,2}\frac{\tilde{\mathcal{P}}_{m+2}}{\tilde{\mathcal{P}}_{m+1}}\langle \tilde{T}_D(m+2)\rangle + ... \tag{D.22}$$

and

$$\langle T_D(m+1)\rangle = 1 + P_{m,2}\frac{\tilde{\mathcal{P}}_{m+2}}{\mathcal{P}_{m+1}}\langle \tilde{T}_D(m+2)\rangle ... \tag{D.23}$$

Leaving only dominant terms we get

$$\mathcal{P}_m = P_{m,1}\tilde{\mathcal{P}}_{m+1} \tag{D.24}$$

$$\tilde{\mathcal{P}}_{m+1} = P_{m,2}\tilde{\mathcal{P}}_{m+2} \tag{D.25}$$

$$\mathcal{P}_{m+1} = P_{m,2}\tilde{\mathcal{P}}_{m+2} \tag{D.26}$$

$$\langle \tilde{T}_D(m+1)\rangle = 1 + P_{m,2}\frac{\tilde{\mathcal{P}}_{m+2}}{P_{m,2}\tilde{\mathcal{P}}_{m+2}}\langle \tilde{T}_D(m+2)\rangle = 1 + \langle \tilde{T}_D(m+2)\rangle \tag{D.27}$$

and

$$\langle T_D(m+1)\rangle = 1 + \langle \tilde{T}_D(m+2)\rangle ... \tag{D.28}$$

That gives

$$\langle T_D(m)\rangle = 1 + \langle T_D(m+1)\rangle + ... \tag{D.29}$$

what we wanted to demonstrate.

APPENDIX E

Appendix for "Dynamical phase separation on rhythmogenic neuronal networks"

E.1 Determining physiological parameters for the model

To prepare Fig. 8.12 we must address the current understanding of the physiological parameters of the neurons as well as the network connectivity parameters. Most of them can be fixed using experimental data shown in Table 8.1. (To obtain value for p from [146] we use the fact that out of 23 pairs of neurons, three were unidirectionally connected, which gives 3/23 probability for the connection in any of two direction, and twice less for the connection in the particular direction). The exception is the set of parameters related to the dendritic calcium concentration, that are not currently as well known. We chose them to reproduce the observed dynamics of the system.

Specifically, we set τ_C to reproduce the observed period of stable oscillation. Taking into account that, for us, the units for the calcium concentration are arbitrary as is the choice of the zero for that concentration, we are left with only two independent parameters: g_C and ΔC. g_C is chosen to be large enough that we have reproducible phase behavior, avoiding highly heterogeneous and initial-condition dependent results as shown in Fig. 8.1B. We also require it to be small enough to produce a true

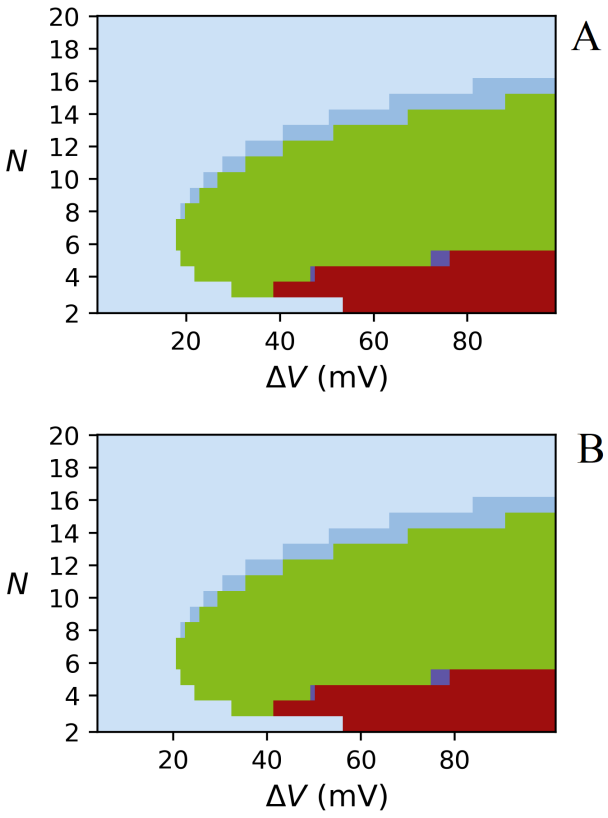

Figure E.1: (Color online) (A) Phase diagram for the all-to-all coupled network, using arbitrary initial conditions and smooth sigmoids. It is identical to (B), the mean-field phase diagram. Phases are: Q (light blue, lightest gray), BTO (blue, lighter gray), HA (dark red, darkest gray), ATO (purple, darker gray), TMA (green, middle gray). All parameter values are listed in appendix E.5.

Table E.1: Parameters used in the simulation

Fig.	g_C	g_V	C^*	$V^* - V_{eq}$	τ_C	τ_V	r_m	r_b	ΔC	ΔV_{max}	p	N
Units	-	mV	-	mV	ms	ms	Hz	Hz	-	mV	-	-
8.1A	3	5	5	15	500	10	75	5	0.1	0-100	1	2-20
8.1B	0.01	5	5	15	500	10	75	5	0.1	0-100	1	2-20
8.1C	3	5	5	15	500	10	75	5	0.1	0-100	0.2	2-100
8.2	5	5	15	15	500	10	75	5	0.035	0-25	0.75	2-100
8.3	0	0	15	15	500	10	75	5	0.1	5-30	0.5	2-20
8.4	0	0	15	15	500	10	75	5	0.1	10	0.5	6-9
8.6A	0.3	0.5	5	15	500	10	75	5	0.1	50	1	10
8.6B	3	5	5	15	500	10	75	5	0.1	50	1	10
8.5A	0.3	0.5	5	15	500	10	75	5	0.1	50	1	10
8.5B	0.3	0.5	5	15	500	10	75	5	0.1	50	1	10
8.5C	1.1	0.1	5	15	500	10	75	5	0.1	50	1	10
8.5D	10.8	1.8	5	15	500	10	75	5	0.1	50	1	10
8.7A,C	0.03	0.05	5	15	500	10	75	5	0.001	2.5	1	1000
8.7B,D	1.0	2.0	5	15	500	10	75	5	0.001	2.5	1	1000
8.8	0	0	20	15	500	10	70	5	0.015	7.3	0.5-1	100
8.11	0	0	∞	15	500	10	70	5	0.1	1-5	0.5	1-50
8.13	3	5	5	15	500	10	75	5	0.025	1-50	0.083	1-1000
8.12	3	5	5	15	500	20	40	0.1	0.007	1-10	0.065	1-1000
E.1	3	5	5	15	500	10	75	5	0.1	0-100	1	2-20
E.2	0-3	0-20	5	15	500	10	75	5	0.1	0-100	1	2-20
E.3	0	5	5	15	500	10	75	5	0.025	0-15	1	2-50

threshold for calcium inactivation of the dendrite, *i.e.*, $\frac{C_{eq}-C^*}{g_C} > 1$. The last parameter to be fixed is ΔC. The proper choice of ΔC is facilitated by scaling behavior observed in the mean-field approximation of the model.

Indeed, consider Fig. 8.1C. To quantitatively fit the *in vitro* data, the network must support stable oscillations when $\Delta V \approx 2.8$ mV, which is the average magnitude of an EPSP [146]. To do that, we choose $\Delta C = 0.007$ and find, with no remaining fitting parameters, that stable oscillations occur for networks $N \approx 10^3$ neurons – see Fig. 8.12. It is computationally difficult to study networks with $N > 2000$, but we can use the rescaling property, observed in the mean-field approximation, to qualitatively predict the behavior for larger N. If we choose $\Delta C = 0.025, p = 0.083$, we obtain the phase diagram, shown in Fig. 8.13. The result is quite similar to that shown in Fig. 8.1C, which describes on a much smaller system.

E.2 Mean-field solution

The mean field solution is obtained by assuming that somatic potentials and dendritic calcium concentrations of all the neurons are the same: $V_i = V, C_i = C$. Another assumption is that the network is on average homogeneously connected, *i.e.* each neuron on average has pN inputs and outputs, with N the total number of neurons and p the connection probability. Then Eqs. 8.1, 8.2 are rewritten as pair of equations for V and C

$$\frac{dV}{dt} = \frac{1}{\tau_V}(V_{eq} - V) + \Delta V(C)p(N-1)r(V) \tag{E.1}$$

$$\frac{dC}{dt} = \frac{1}{\tau_C}(C_{eq} - C) + \Delta C p(N-1)r(V), \tag{E.2}$$

The phase diagram for such system is shown in Fig. E.1B. One may see that it is identical to the phase diagram for the all-to-all coupled network in Fig. E.1A in case of smooth transition in dendritic sensitivity. The mean-field approximation is valid for large g_V and g_C but breaks down when they become smaller. More detailed results are shown in Fig. E.2.

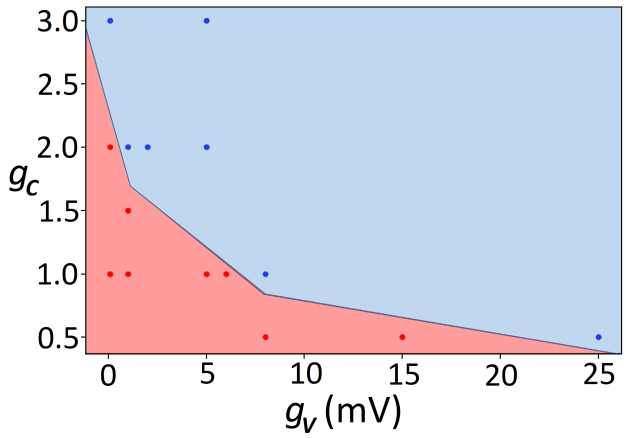

Figure E.2: (Color online) The results of the simulations for different g_V and g_C. Blue, light region (red, dark region) points correspond to the case where the dynamics agree (disagree) with mean field predictions, as determined by a visual inspection of the numerically obtained phase diagrams. The blue region exhibits both insensitivity to initial conditions and robustness in the face of damage. Conversely, the red region is highly sensitive to both initial condition and damage. All parameter values are listed in appendix E.5.

E.3 Stability of fixed points on sparse networks

For the smooth-sigmoid neurons, we found in section 8.3 that there was only a single fixed point – see Fig. 8.6. When that fixed point is unstable, the system executes limit cycle oscillations. To determine the parameter range of these oscillations, here we investigate the stability of that fixed point. Expanding the equations of motion near the fixed point $\{V_i^f, C_i^f\}$ in the $2N$ dimensional space of V_i, C_i, we define $v_i = V_i - V_i^f, c_i = C_i - C_i^f$ and obtain

$$\begin{aligned} \frac{dv_i}{dt} &= -\frac{v_i}{\tau_V} + \Delta V'(C_i^f) c_i \sum_j M_{ij} r(V_j^f) + \\ &\quad + \Delta V(C_i^f) \sum_j M_{ij} r'(V_j^f) v_j \end{aligned} \tag{E.3}$$

$$\frac{dc_i}{dt} = -\frac{c_i}{\tau_C} + \Delta C \sum_j M_{ij} r'(V_j^f) v_j \tag{E.4}$$

Using $r(V)$ and $\Delta V(C)$ from Eqs. 8.3, 8.4, we find

$$\begin{aligned} \frac{dv_i}{dt} &= -\frac{v_i}{\tau_V} - \frac{1}{g_C} \Delta V_{max} \sigma'\left(\frac{C^* - C_i^f}{g_C}\right) c_i \sum_j M_{ij} r(V_j^f) + \\ &\quad + \frac{1}{g_V} (r_m - r_b) \Delta V(C_i^f) \sum_j M_{ij} \sigma'\left(\frac{V_j^f - V^*}{g_V}\right) v_j, \end{aligned} \tag{E.5}$$

and

$$\frac{dc_i}{dt} = -\frac{c_i}{\tau_C} + \Delta C (r_m - r_b) \sum_j M_{ij} \sigma'\left(\frac{V_j^f - V^*}{g_V}\right) v_j. \tag{E.6}$$

Dynamical phase separation requires that neither $C^* - C_i^f$ nor $V^* - V_i^f$ vanish. Therefore, if g_V and g_C are small, the terms with sigmoids are exponentially suppressed. Neglecting these, we see that only the first term on the right hand side of Eqs. E.5

and E.6 remains. This implies the stability of the fixed point. For large g_C and g_V, however, we cannot ignore the terms proportional to σ', which destabilize the phase-separated fixed point.

E.4 Quasi-periodic phase diagrams

We consider the case $g_C = 0, g_V > 0$, where quasi-periodic phase diagram can emerge. Following subsection 8.3.1 by assuming activity phase separation to n_h neurons with V_h, C_h and n_l neurons with V_l, C_l we write equations for the fixed point:

$$V_h - V_{eq} = \Delta V(C_h)\tau_V \left[(n_h - 1)r(V_h) + n_l r(V_l)\right] \tag{E.7}$$

$$C_h - C_{eq} = \Delta C\tau_C \left[(n_h - 1)r(V_h) + n_l r(V_l)\right]. \tag{E.8}$$

and

$$V_l - V_{eq} = \Delta V(C_l)\tau_V \left[(n_l - 1)r(V_l) + n_h r(V_h)\right] \tag{E.9}$$

$$C_l - C_{eq} = \Delta C\tau_C \left[(n_l - 1)r(V_l) + n_h r(V_h)\right]. \tag{E.10}$$

In the case where $g_C = 0$, we have $\Delta V(C_l) = 0, \Delta V(C_h) = \Delta V_{max}$ (for $C_h < C^*, C_l > C^*$. Then as in section 8.3.1, we obtain the number of neurons firing at low rate

$$n_l = \left\lfloor \frac{(Nr(V_h) - r(V_l))\Delta C\tau_C + C_{eq} - C^*}{\Delta C\tau_C(r(V_h) - r(V_l))} \right\rfloor, \tag{E.11}$$

and simplify the equations for the somatic potentials to get $V_l = V_{eq}$ and

$$\frac{V_h - V_{eq}}{\Delta V_{max}\tau_V} = Nr(V_l) - r(V_h) + \left\lceil \frac{\frac{C^*}{\Delta C \tau_C} - (N-1)r(V_l)}{r(V_h) - r(V_l)} \right\rceil \tag{E.12}$$

where the *ceil* function $\lceil x \rceil$ is the smallest integer that is larger or equal to x.

Eq. E.12 does not have a solution for V_h for some parameters. Due to the ceil function on the right hand side, the changes happen when its argument is incremented by one, what causes quasi-periodic structure of the phase diagram (see Fig. E.3).

E.5 Simulation details

The code is published at https://github.com/mbibireata/Networks. We use the parameters for all figures from Table E.1

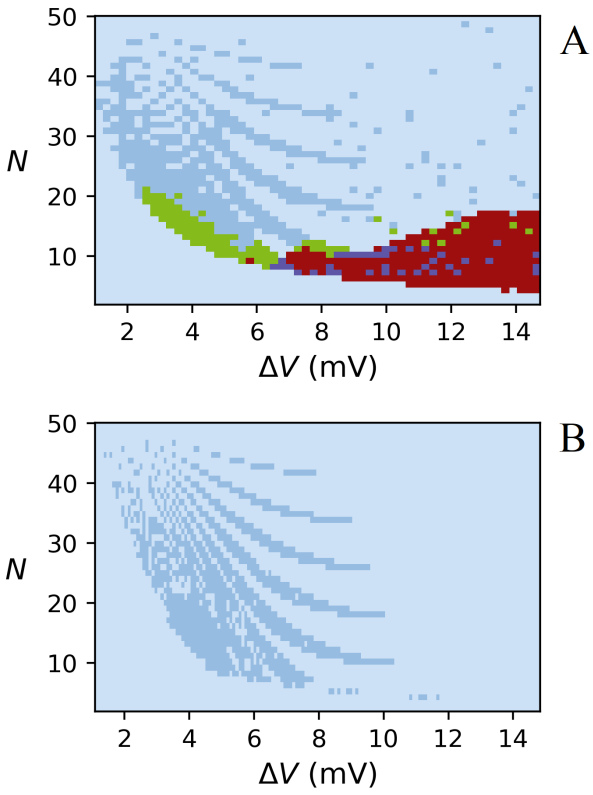

Figure E.3: (Color online) (A) Phase diagram for the all-to-all coupled network, $g_C = 0, g_V > 0$. All five previously mentioned phases are present. There is a quasi-periodical pattern on the BTO (blue, lighter gray) - Q (light blue, lightest gray) boundary. This phase diagram fits the theoretical prediction (B) where blue (lightest gray) corresponds to the case that Eq. E.12 has a solution and dark red (darkest gray) to the case that it does not. All parameter values are listed in appendix E.5.

Bibliography

[1] Actin crosslinking. https://www.mechanobio.info/cytoskeleton-dynamics/actin-crosslinking/. Accessed: 2021-06-04.

[2] BACI: A Comprehensive Multi-Physics Simulation Framework, https://baci.pages.gitlab.lrz.de/website, 2020.

[3] Smoothing splines (https://www.mathworks.com/help/curvefit/smoothing-splines.html), 2020.

[4] Michael D Abràmoff, Paulo J Magalhães, and Sunanda J Ram. Image processing with imagej. *Biophotonics international*, 11(7):36–42, 2004.

[5] Sadjad Arzash, Jordan L Shivers, Albert J Licup, Abhinav Sharma, and Fred C MacKintosh. Stress-stabilized subisostatic fiber networks in a ropelike limit. *Physical Review E*, 99(4):42412, apr 2019.

[6] Sadjad Arzash, Jordan L Shivers, and Fred C MacKintosh. Finite size effects in critical fiber networks. *Soft Matter*, 16(29):6784–6793, 2020.

[7] Sufyan Ashhad and Jack L Feldman. Emergent elements of inspiratory rhythmogenesis: network synchronization and synchrony propagation. *Neuron*, 106(3):482–497, 2020.

[8] Jessica Ausborn, Hidehiko Koizumi, William H Barnett, Tibin T John, Ruli Zhang, Yaroslav I Molkov, Jeffrey C Smith, and Ilya A Rybak. Organization of the core respiratory network: Insights from optogenetic and modeling studies. *PLOS Computational Biology*, 14(4):e1006148, 2018.

[9] Bartholomew J Bacak, Taegyo Kim, Jeffrey C Smith, Jonathan E Rubin, and Ilya A Rybak. Mixed-mode oscillations and population bursting in the pre-bötzinger complex. *eLife*, 5:e13403, 2016.

[10] Gary D. Bader and Christopher WV Hogue. An automated method for finding molecular complexes in large protein interaction networks. *BMC Bioinformatics*, 4(1):2, 2003.

[11] Mark Bathe, Claus Heussinger, Mireille Claessens, Andreas Bausch, and Erwin Frey. Cytoskeletal bundle bending, buckling, and stretching behavior, 2006.

[12] Öjvind Bernander, Christof Koch, and Marius Usher. The effect of synchronized inputs at the single neuron level. *Neural Computation*, 6(4):622–641, 1994.

[13] Mihai Bibireata, Valentin M Slepukhin, and Alex J Levine. Dynamical phase separation on rhythmogenic neuronal networks. *Physical Review E*, 101(6):062307, 2020.

[14] Chase P. Broedersz, Martin Depken, Normal Y. Yao, Martin R. Pollak, David A. Weitz, and Frederick C. MacKintosh. Rheology of Semiflexible Bundle Networks with Transient Linkers. *Phys. Rev. Lett.*, 105:238101, 2010.

[15] Chase P. Broedersz, Martin Depken, Norman Y. Yao, Martin R. Pollak, David A. Weitz, and Frederick C. MacKintosh. Cross-link-governed dynamics of biopolymer networks. *Phys. Rev. Lett.*, 105:238101, Nov 2010.

[16] Nicolas Brunel and Simone Sergi. Firing frequency of leaky intergrate-and-fire neurons with synaptic current dynamics. *Journal of Theoretical Biology*, 195(1):87–95, 1998.

[17] Markus J Buehler. Atomistic and continuum modeling of mechanical properties of collagen: elasticity, fracture, and self-assembly. *Journal of Materials Research*, 21(8):1947–1961, 2006.

[18] Markus J Buehler. Nature designs tough collagen: explaining the nanostructure of collagen fibrils. *Proceedings of the National Academy of Sciences*, 103(33):12285–12290, 2006.

[19] Predrag Bursac, Guillaume Lenormand, Ben Fabry, Madavi Oliver, David A. Weitz, Virgile Viasnoff, James P. Butler, and Jeffery J. Fredberg. Rheology of Semiflexible Bundle Networks with Transient Linkers. *Nature Materials*, 4:557–561, 2005.

[20] John Cardy and Uwe C. Täuber. Theory of branching and annihilating random walks. *Phys. Rev. Lett.*, 77:4780–4783, Dec 1996.

[21] M. E. Cates, J. P. Wittmer, J.-P. Bouchaud, and P. Claudin. Jamming, force chains, and fragile matter. *Phys. Rev. Lett.*, 81:1841–1844, Aug 1998.

[22] P. M. Chaikin and T. C. Lubensky. *Principles of Condensed Matter Physics*. Cambridge University Press, 1995.

[23] Shu-Wei Chang and Markus J Buehler. Molecular biomechanics of collagen molecules. *Materials Today*, 17(2):70–76, 2014.

[24] Elisabeth E. Charrier and Paul A. Janmey. Mechanical properties of intermediate filament proteins. *Methods in enzymology*, 568:35–57, 2016. 26795466[pmid].

[25] SN Coppersmith, C-h Liu, Satya Majumdar, Onuttom Narayan, and TA Witten. Model for force fluctuations in bead packs. *Physical Review E*, 53(5):4673, 1996.

[26] Yan Cui, Kaiwen Kam, David Sherman, Wiktor A Janczewski, Yu Zheng, and Jack L Feldman. Defining prebötzinger complex rhythm-and pattern-generating neural microcircuits in vivo. *Neuron*, 91(3):602–614, 2016.

[27] C. J. Cyron, K. W. Müller, K. M. Schmoller, A. R. Bausch, W. A. Wall, and R. F. Bruinsma. Equilibrium phase diagram of semi-flexible polymer networks with linkers. *Europhysics Letters*, 102(3):38003, 2013.

[28] C J Cyron and W A Wall. Consistent finite-element approach to Brownian polymer dynamics with anisotropic friction. *Physical Review E*, 82:66705, 2010.

[29] C. J. Cyron and W. A. Wall. Numerical method for the simulation of the brownian dynamics of rod-like microstructures with three-dimensional nonlinear beam elements. *Int. J. Numer. Meth. Engng*, 90:955–987, 2012.

[30] Christian J. Cyron, Kei W. Müller, Andreas R. Bausch, and Wolfgang A. Wall. Micromechanical simulations of biopolymer networks with finite elements. *Journal of Computational Physics*, 244:236–251, jul 2013.

[31] Christopher A Del Negro, Gregory D Funk, and Jack L Feldman. Breathing matters. *Nature Reviews Neuroscience*, 19(6):351–367, 2018.

[32] Christopher A Del Negro, Christopher G Wilson, Robert J Butera, Henrique Rigatto, and Jeffrey C Smith. Periodicity, mixed-mode oscillations, and quasiperiodicityin a rhythm-generating neural network. *Biophysical Journal*, 82(1):206–214, 2002.

[33] Baptiste Depalle, Zhao Qin, Sandra J Shefelbine, and Markus J Buehler. Influence of cross-link structure, density and mechanical properties in the mesoscale deformation mechanisms of collagen fibrils. *Journal of the mechanical behavior of biomedical materials*, 52:1–13, 2015.

[34] John D'Errico. arclength (https://www.mathworks.com/matlabcentral/fileexchange/34871-arclength), matlab central file exchange. retrieved november 10, 2020., 2020.

[35] John D'Errico. interparc (https://www.mathworks.com/matlabcentral/fileexchange/34874-interparc), matlab central file exchange. retrieved november 10, 2020., 2020.

[36] Markus Diesmann, Marc-Oliver Gewaltig, and Ad Aertsen. Stable propagation of synchronous spiking in cortical neural networks. *Nature*, 402(6761):529–533, 1999.

[37] S. N. Dorogovtsev, A. V. Goltsev, and J. F. F. Mendes. k-core organization of complex networks. *Phys. Rev. Lett.*, 96:040601, Feb 2006.

[38] Andrew D. Doyle. Generation of 3d collagen gels with controlled diverse architectures. *Current Protocols in Cell Biology*, 72(1):10.20.1–10.20.16, 2016.

[39] Pavel Dutov, Olga Antipova, Sameer Varma, Joseph PRO Orgel, and Jay D Schieber. Measurement of elastic modulus of collagen type i single fiber. *PloS one*, 11(1):e0145711, 2016.

[40] P Erdös and A Rényi. On random graphs i. *Publicationes Mathematicae Debrecen*, 6:290–297, 1959.

[41] Bard Ermentrout. Neural networks as spatio-temporal pattern-forming systems. *Reports on Progress in Physics*, 61(4):353, 1998.

[42] Deniz Ertaş and Mehran Kardar. Rheology of Semiflexible Bundle Networks with Transient Linkers. *Physical Review Letters*, 73:1703, 1994.

[43] Jack L. Feldman and Christopher A. Del Negro. Looking for inspiration: new perspectives on respiratory rhythm. *Nature Reviews Neuroscience*, 7(3):232–241, 2006.

[44] Jack L Feldman and Kaiwen Kam. Facing the challenge of mammalian neural microcircuits: taking a few breaths may help. *The Journal of Physiology*, 593(1):3–23, 2015.

[45] R. P. Feynman and A.R. Hibbs. *Quantum Mechanics and Path Integrals*. Dover, New York, 1965.

[46] Dieter Forster. *Hydrodynamics fluctuations, broken symmetry, and correlation functions*. Addison-Wesley Publishing Co., Inc., Reading, MA., 1983.

[47] LC Foucard, JK Price, WS Klug, and AJ Levine. Cooperative buckling and the nonlinear mechanics of nematic semiflexible networks. *Nonlinearity*, 28(9):R89, 2015.

[48] Marco Franchi, Vittoria Ottani, Rita Stagni, and Alessandro Ruggeri. Tendon and ligament fibrillar crimps give rise to left-handed helices of collagen fibrils in both planar and helical crimps. *Journal of anatomy*, 216(3):301–309, 2010.

[49] Uwe Freudenberg, Sven H Behrens, Petra B Welzel, Martin Müller, Milauscha Grimmer, Katrin Salchert, Tilman Taeger, Kati Schmidt, Wolfgang Pompe, and Carsten Werner. Electrostatic interactions modulate the conformation of collagen i. *Biophysical journal*, 92(6):2108–2119, 2007.

[50] Eyal Gal, Rodrigo Perin, Henry Markram, Michael London, and Idan Segev. Neuron geometry underlies a universal local architecture in neuronal networks. *bioRxiv*, page 656058, 2019.

[51] Wulfram Gerstner. Time structure of the activity in neural network models. *Physical Review E*, 51(1):738, 1995.

[52] Edgar N Gilbert. Random graphs. *The Annals of Mathematical Statistics*, 30(4):1141–1144, 1959.

[53] W H Goldmann and G Isenberg. Analysis of filamin and α-actinin binding to actin by the stopped flow method. *FEBS Letters*, 336(3):408–410, dec 1993.

[54] Leonardo Golubović, Dorel Moldovan, and Anatoli Peredera. Dynamics of the euler buckling instability. *Physical Review Letters*, 81(16):3387, 1998.

[55] Colin A Grant, David J Brockwell, Sheena E Radford, and Neil H Thomson. Tuning the elastic modulus of hydrated collagen fibrils. *Biophysical journal*, 97(11):2985–2992, 2009.

[56] Gregory M. Grason. Braided bundles and compact coils: The structure and thermodynamics of hexagonally packed chiral filament assemblies. *Phys. Rev. E*, 79:041919, Apr 2009.

[57] P. A. Gray, W. A. Janczewski, N. Mellen, D. R. McCrimmon, and J. L. Feldman. Normal breathing requires prebã¶tzinger complex neurokinin-1

receptor-expressing neurons. *Nature neuroscience*, 4(9):927–930, Sep 2001. 11528424[pmid].

[58] Paul A Gray, Jens C Rekling, Christopher M Bocchiaro, and Jack L Feldman. Modulation of respiratory frequency by peptidergic input to rhythmogenic neurons in the prebötzinger complex. *Science*, 286(5444):1566–1568, 1999.

[59] Maximilian J Grill, Jonathan Kernes, Valentin M Slepukhin, Wolfgang A Wall, and Alex J Levine. Directed force propagation in semiflexible networks. *Soft Matter*, 2020.

[60] Thomas Gutsmann, Georg E Fantner, Manuela Venturoni, Axel Ekani-Nkodo, James B Thompson, Johannes H Kindt, Daniel E Morse, Deborah Kuchnir Fygenson, and Paul K Hansma. Evidence that collagen fibrils in tendons are inhomogeneously structured in a tubelike manner. *Biophysical Journal*, 84(4):2593–2598, 2003.

[61] Ehud Haimov, Reinhard Windoffer, Rudolf E. Leube, Michael Urbakh, and Michael M. Kozlov. Model for bundling of keratin intermediate filaments. *Biophysical Journal*, 119(1):65 – 74, 2020.

[62] Xinyu Hao, Shuangming Yang, Bin Deng, Jiang Wang, Xile Wei, and Yanqiu Che. A cordic based real-time implementation and analysis of a respiratory central pattern generator. *Neurocomputing*, 423:373–388, 2021.

[63] M. B. Hastings. Mean-field and anomalous behavior on a small-world network. *Phys. Rev. Lett.*, 91:098701, Aug 2003.

[64] DA Head, AJ Levine, and FC MacKintosh. Distinct regimes of elastic response and deformation modes of cross-linked cytoskeletal and semiflexible polymer networks. *Physical Review E*, 68(6):061907, 2003.

[65] DA Head, AJ Levine, and FC MacKintosh. Mechanical response of semiflexible networks to localized perturbations. *Physical Review E*, 72(6):061914, 2005.

[66] David A Head, Alex J Levine, and FC MacKintosh. Deformation of cross-linked semiflexible polymer networks. *Physical review letters*, 91(10):108102, 2003.

[67] C. Heussinger and E. Frey. Force distributions and force chains in random stiff fiber networks. *The European Physical Journal E*, 24(1):47–53, Sep 2007.

[68] Claus Heussinger, Mark Bathe, and Erwin Frey. Statistical mechanics of semiflexible bundles of wormlike polymer chains. *Phys. Rev. Lett.*, 99:048101, Jul 2007.

[69] Claus Heussinger and Erwin Frey. Floppy modes and nonaffine deformations in random fiber networks. *Phys. Rev. Lett.*, 97:105501, Sep 2006.

[70] Qingda Hu, Tessa Altair Morris, Anna Grosberg, Alex J. Levine, and E.L. Botvinick. Actively driven fluctuations in a fibrin network. *Submitted*, 2020.

[71] EM Huisman, T Van Dillen, PR Onck, and E Van der Giessen. Three-dimensional cross-linked f-actin networks: relation between network architecture and mechanical behavior. *Physical review letters*, 99(20):208103, 2007.

[72] R. C. Hurley, S. A. Hall, J. E. Andrade, and J. Wright. Quantifying interparticle forces and heterogeneity in 3d granular materials. *Phys. Rev. Lett.*, 117:098005, Aug 2016.

[73] Terence Hwa, David R. Nelson, and Valerii M. Vinokur. Rheology of Semiflexible Bundle Networks with Transient Linkers. *Physical Review B*, 48:1167, 1993.

[74] G. Jelenic and M. A. Crisfield. Geometrically exact 3d beam theory: implementation of a strain-invariant finite element for statics and dynamics. *Computer Methods in Applied Mechanics and Engineering*, 171(1-2):141–171, March 1999.

[75] Eric Jones, Travis Oliphant, Pearu Peterson, et al. SciPy: Open source scientific tools for Python, 2001–.

[76] Devin Kachan, Robijn Bruinsma, and Alex J. Levine. Casimir interactions in semiflexible polymers. *Phys. Rev. E*, 87:032719, Mar 2013.

[77] Devin Kachan, Kei W. Müller, Wolfgang A. Wall, and Alex J. Levine. Discontinuous bundling transition in semiflexible polymer networks induced by casimir interactions. *Phys. Rev. E*, 94:032505, Sep 2016.

[78] Devin Kachan, Kei W. Müller, Wolfgang A. Wall, and Alex J. Levine. Discontinuous bundling transition in semiflexible polymer networks induced by Casimir interactions. *Physical Review E*, 94(3):032505, sep 2016.

[79] Kaiwen Kam, Jason W Worrell, Wiktor A Janczewski, Yan Cui, and Jack L Feldman. Distinct inspiratory rhythm and pattern generating mechanisms in the prebötzinger complex. *Journal of Neuroscience*, 33(22):9235–9245, 2013.

[80] Kaiwen Kam, Jason W Worrell, Cathie Ventalon, Valentina Emiliani, and Jack L Feldman. Emergence of population bursts from simultaneous activation of small subsets of prebötzinger complex inspiratory neurons. *Journal of Neuroscience*, 33(8):3332–3338, 2013.

[81] NG Van Kampen. *Stochastic processes in physics and chemistry*. North Holland, 2007.

[82] CL Kane and TC Lubensky. Topological boundary modes in isostatic lattices. *Nature Physics*, 10(1):39–45, 2014.

[83] Pekka Kannus. Structure of the tendon connective tissue. *Scandinavian journal of medicine & science in sports*, 10(6):312–320, 2000.

[84] M Kardar. *Statistical Physics of Fields*. Cambridge University Press, New York, 2007.

[85] Mehran Kardar. Replica bethe ansatz studies of two-dimensional interfaces with quenched random impurities. *Nuclear Physics B*, 290:582 – 602, 1987.

[86] KE Kasza, CP Broedersz, GH Koenderink, YC Lin, W Messner, EA Millman, F Nakamura, TP Stossel, FC MacKintosh, and DA Weitz. Actin filament length tunes elasticity of flexibly cross-linked actin networks. *Biophysical journal*, 99(4):1091–1100, 2010.

[87] M Keating, A Kurup, M Alvarez-Elizondo, AJ Levine, and E Botvinick. Spatial distributions of pericellular stiffness in natural extracellular matrices are dependent on cell-mediated proteolysis and contractility. *Acta biomaterialia*, 57:304–312, 2017.

[88] Kitware Inc. Paraview 5.8.0, 2020.

[89] H. Kleinert. Path integral for second-derivative lagrangian. *Journal of Mathematical Physics*, 27:3003, 1986.

[90] Hagen Kleinert. *Path Integrals in Quantum Mechanics, Statistics, and Polymer Physics*. World Scientific, Singapore, 1995.

[91] Maurice Kleman. *The Topological Classification of Defects*. Springer US, Boston, MA, 1995.

[92] Christof Koch. *Biophysics of Computation: Information Processing in Single Neurons (Computational Neuroscience Series)*. Oxford University Press, Inc., New York, NY, USA, 2004.

[93] I. V. Kolokolov and S. E. Korshunov. Explicit solution of the optimal fluctuation problem for an elastic string in a random medium. *Phys. Rev. E*, 80:031107, Sep 2009.

[94] Maxwell A Kotlarchyk, Samir G Shreim, Martha B Alvarez-Elizondo, Laura C Estrada, Rahul Singh, Lorenzo Valdevit, Ekaterina Kniazeva, Enrico Gratton, Andrew J Putnam, and Elliot L Botvinick. Concentration independent modulation of local micromechanics in a fibrin gel. *PloS one*, 6(5):1–12, 2011.

[95] Hendrik Anthony Kramers. Brownian motion in a field of force and the diffusion model of chemical reactions. *Physica*, 7(4):284–304, 1940.

[96] Arvind Kumar, Stefan Rotter, and Ad Aertsen. Spiking activity propagation in neuronal networks: reconciling different perspectives on neural coding. *Nature Reviews Neuroscience*, 11(9):615–627, 2010.

[97] Matthew C. Kuntz and James P. Sethna. Rheology of Semiflexible Bundle Networks with Transient Linkers. *Physical Review B*, 62:11699, 2000.

[98] Nir Lahav, Baruch Ksherim, Eti Ben-Simon, Adi Maron-Katz, Reuven Cohen, and Shlomo Havlin. K-shell decomposition reveals hierarchical cortical organization of the human brain. *New Journal of Physics*, 18(8):083013, Aug 2016.

[99] L D Landau and E M Lifshitz. *Theory of Elasticity 3rd edition*. Oxford, 1986.

[100] Guillaume Lenormand, Emil Millet, Ben Fabry, James P. Butler, and Jeffery J. Fredberg. Rheology of Semiflexible Bundle Networks with Transient Linkers. *Journal of the Royal Society Interface*, 1:91–97, 2004.

[101] O Lieleg, KM Schmoller, Mireille MAE Claessens, and Andreas R Bausch. Cytoskeletal polymer networks: viscoelastic properties are determined by the microscopic interaction potential of cross-links. *Biophysical journal*, 96(11):4725–4732, 2009.

[102] BG Lindsey, KF Morris, LS Segers, and R Shannon. Respiratory neuronal assemblies. *Respiration physiology*, 122(2-3):183–196, 2000.

[103] C-h Liu, Sydney R Nagel, DA Schecter, SN Coppersmith, Satya Majumdar, Onuttom Narayan, and TA Witten. Force fluctuations in bead packs. *Science*, 269(5223):513–515, 1995.

[104] Francesca Arese Lucini, Gino Del Ferraro, Mariano Sigman, and Hernán A. Makse. How the brain transitions from conscious to subliminal perception. *Neuroscience*, 411:280 – 290, 2019.

[105] X. Ma, M.E. Schickel, M.D. Stevenson, A.L. Sarang-Sieminski, K.J. Gooch, S.N. Ghadiali, and R. T. Hart. Fibers in the extracellular matrix enable long-range stress transmission between cells. *Biophysical Journal*, 104(7):1410–1418, 2013.

[106] F. C. MacKintosh, J. Käs, and P. A. Janmey. Elasticity of semiflexible biopolymer networks. *Phys. Rev. Lett.*, 75:4425–4428, Dec 1995.

[107] F. C. MacKintosh, Josef Käs, and P. A. Janmey. Elasticity of semiflexible biopolymer networks. *Physical review letters*, 75(24):4425, 1995.

[108] F.C. MacKintosh, J. Käs, and P.A. Janmey. Rheology of Semiflexible Bundle Networks with Transient Linkers. *Phys. Rev. Lett.*, 75:4425, 1995.

[109] M. Maier, K. W. Müller, C. Heussinger, S. Köhler, W. A. Wall, A. R. Bausch, and O. Lieleg. A single charge in the actin binding domain of fascin can independently tune the linear and non-linear response of an actin bundle network. *European Physical Journal E*, 38(5):1–7, may 2015.

[110] Sayantan Majumdar, Louis C Foucard, Alex J Levine, and Margaret L Gardel. Mechanical hysteresis in actin networks. *Soft matter*, 14(11):2052–2058, 2018.

[111] Gerald S. Manning. The persistence length of dna is reached from the persistence length of its null isomer through an internal electrostatic stretching force. *Biophysical journal*, 91(10):3607–3616, Nov 2006. 16935960[pmid].

[112] Xiaoming Mao, Olaf Stenull, and Thomas C Lubensky. Effective-medium theory of a filamentous triangular lattice. *Physical Review E*, 87(4):042601, 2013.

[113] Xiaoming Mao, Olaf Stenull, and Thomas C Lubensky. Elasticity of a filamentous kagome lattice. *Physical Review E*, 87(4):042602, 2013.

[114] Xiaoming Mao, Ning Xu, and T. C. Lubensky. Soft modes and elasticity of nearly isostatic lattices: Randomness and dissipation. *Phys. Rev. Lett.*, 104:085504, Feb 2010.

[115] M. Cristina Marchetti and David R. Nelson. Rheology of Semiflexible Bundle Networks with Transient Linkers. *Physical Review B*, 42:9938, 1990.

[116] S B Marston. The rates of formation and dissociation of actin-myosin complexes. Effects of solvent, temperature, nucleotide binding and head-head interactions. *Biochemical Journal*, 203(2):453–460, may 1982.

[117] Paul Matsudaira. Actin crosslinking proteins at the leading edge. *Seminars in Cell Biology*, 5(3):165–174, 1994.

[118] Christoph Meier, Maximilian J Grill, Wolfgang A Wall, and Alexander Popp. Geometrically exact beam elements and smooth contact schemes for the modeling of fiber-based materials and structures. *International Journal of Solids and Structures*, 154:124–146, nov 2018.

[119] M. Mezard, G. Parisi, and M.A. Virasoro. *Spin Glass Theory and Beyond*. World Scientific, Singapore, 1987.

[120] Andrew R. Missel, Mo Bai, William S. Klug, and Alex J. Levine. Affine-nonaffine transition in networks of nematically ordered semiflexible polymers. *Phys. Rev. E*, 82:041907, Oct 2010.

[121] Hidetake Miyata, Ryohei Yasuda, and Kazuhiko Kinosita. Strength and lifetime of the bond between actin and skeletal muscle α-actinin studied with an optical trapping technique. *Biochimica et Biophysica Acta (BBA) - General Subjects*, 1290(1):83–88, 1996.

[122] Tsuyoshi Mizuguchi and Masaki Sano. Proportion regulation of biological cells in globally coupled nonlinear systems. *Phys. Rev. Lett.*, 75:966–969, Jul 1995.

[123] Oihana Moreno-Arotzena, Johann G Meier, Cristina Del Amo, and José Manuel García-Aznar. Characterization of fibrin and collagen gels for engineering wound healing models. *Materials*, 8(4):1636–1651, 2015.

[124] Consuelo Morgado-Valle, Luis Beltran-Parrazal, Marino DiFranco, Julio L. Vergara, and Jack L. Feldman. Somatic ca2+ transients do not contribute to inspiratory drive in prebã¶tzinger complex neurons. *The Journal of physiology*, 586(18):4531–4540, Sep 2008. 18635649[pmid].

[125] Flaviano Morone, Gino Del Ferraro, and HernÃ¡n A. Makse. The k-core as a predictor of structural collapse in mutualistic ecosystems. *Nature Physics*, 15(1):95–102, 2019.

[126] K W Müller, R F Bruinsma, O Lieleg, A R Bausch, W A Wall, and A J Levine. Rheology of Semiflexible Bundle Networks with Transient Linkers. *Physical Review Letters*, 112(23):238102, 2014.

[127] Kei W. Müller, Robijn F. Bruinsma, Oliver Lieleg, Andreas R. Bausch, Wolfgang A. Wall, and Alex J. Levine. Rheology of Semiflexible Bundle Networks with Transient Linkers. *Phys. Rev. Lett.*, 113:049901, 2014.

[128] Kei W. Müller, Robijn F. Bruinsma, Oliver Lieleg, Andreas R. Bausch, Wolfgang A. Wall, and Alex J. Levine. Rheology of semiflexible bundle networks with transient linkers. *Phys. Rev. Lett.*, 112(23):238102–, June 2014.

[129] Kei W. Müller, Christoph Meier, and Wolfgang A. Wall. Resolution of subelement length scales in Brownian dynamics simulations of biopolymer networks with geometrically exact beam finite elements. *Journal of Computational Physics*, 303:185–202, 2015.

[130] Onuttom Narayan and Daniel S. Fisher. Rheology of Semiflexible Bundle Networks with Transient Linkers. *Physical Review B*, 48:7030, 1993.

[131] David R. Nelson. *Defects and geometry in condensed matter physics*. Cambridge University Press, 2002.

[132] Takashi Nishikawa and Adilson E. Motter. Symmetric states requiring system asymmetry. *Phys. Rev. Lett.*, 117:114101, Sep 2016.

[133] Ryland W Pace, Devin D Mackay, Jack L Feldman, and Christopher A Del Negro. Inspiratory bursts in the prebötzinger complex depend on a calcium-activated non-specific cation current linked to glutamate receptors in neonatal mice. *The Journal of Physiology*, 582(1):113–125, 2007.

[134] Ryland W Pace, Devin D Mackay, Jack L Feldman, and Christopher A Del Negro. Role of persistent sodium current in mouse prebötzinger complex neurons and respiratory rhythm generation. *The Journal of Physiology*, 580(2):485–496, 2007.

[135] Jeong-Man Park and TC Lubensky. Topological defects on fluctuating surfaces: General properties and the kosterlitz-thouless transition. *Physical Review E*, 53(3):2648, 1996.

[136] Rodrigo Perin, Thomas K Berger, and Henry Markram. A synaptic organizing principle for cortical neuronal groups. *Proceedings of the National Academy of Sciences*, 108(13):5419–5424, 2011.

[137] Maria Cristina D Picardo, Krishanthi TH Weragalaarachchi, Victoria T Akins, and Christopher A Del Negro. Physiological and morphological properties of dbx1-derived respiratory neurons in the pre-bötzinger complex of neonatal mice. *The Journal of Physiology*, 591(10):2687–2703, 2013.

[138] P. Pincus. Excluded volume effects and stretched polymer chains. *Macromolecules*, 9:386–388, 1976.

[139] Thomas D Pollard. Actin and Actin-Binding Proteins. *Cold Spring Harbor Perspectives in Biology*, 8(8), aug 2016.

[140] A.M. Polyakov. *Gauge Fields and Strings*. Harwood Academic Publishers, London, 1987.

[141] Liudmila Prokhorenkova, Gleb Gusev, Aleksandr Vorobev, Anna Veronika Dorogush, and Andrey Gulin. Catboost: unbiased boosting with categorical features. *arXiv preprint arXiv:1706.09516*, 2017.

[142] E. Raspaud, M. Olvera de la Cruz, J.-L. Sikorav, and F. Livolant. Precipitation of dna by polyamines: A polyelectrolyte behavior. *Biophysical Journal*, 74(1):381 – 393, 1998.

[143] Christopher B Raub, Vinod Suresh, Tatiana Krasieva, Julia Lyubovitsky, Justin D Mih, Andrew J Putnam, Bruce J Tromberg, and Steven C George. Noninvasive assessment of collagen gel microstructure and mechanics using multiphoton microscopy. *Biophysical journal*, 92(6):2212–2222, 2007.

[144] Shawn P Reese, Niloofar Farhang, Randy Poulson, Gennie Parkman, and Jeffrey A Weiss. Nanoscale imaging of collagen gels with focused ion beam milling and scanning electron microscopy. *Biophysical Journal*, 111(8):1797–1804, 2016.

[145] E Reissner. On finite deformations of space-curved beams. *Zeitschrift für Angewandte Mathematik und Physik (ZAMP)*, 32(6):734–744, 1981.

[146] J. C. Rekling, X. M. Shao, and J. L. Feldman. Electrical coupling and excitatory synaptic transmission between rhythmogenic respiratory neurons in the

prebã¶tzinger complex. *The Journal of neuroscience : the official journal of the Society for Neuroscience*, 20(23):RC113–RC113, Dec 2000. 11090613[pmid].

[147] JENS C Rekling, JEAN Champagnat, and M Denavit-Saubié. Electroresponsive properties and membrane potential trajectories of three types of inspiratory neurons in the newborn mouse brain stem in vitro. *Journal of Neurophysiology*, 75(2):795–810, 1996.

[148] Jens C Rekling, Xuesi M Shao, and Jack L Feldman. Electrical coupling and excitatory synaptic transmission between rhythmogenic respiratory neurons in the prebötzinger complex. *Journal of Neuroscience*, 20(23):RC113–RC113, 2000.

[149] Alexa Riehle, Sonja Grün, Markus Diesmann, and Ad Aertsen. Spike synchronization and rate modulation differentially involved in motor cortical function. *Science*, 278(5345):1950–1953, 1997.

[150] Mathilda S Rudnicki, Heather A Cirka, Maziar Aghvami, Edward A Sander, Qi Wen, and Kristen L Billiar. Nonlinear strain stiffening is not sufficient to explain how far cells can feel on fibrous protein gels. *Biophysical journal*, 105(1):11–20, 2013.

[151] Hidetsugu Sakaguchi. Domain-size control by global feedback in bistable systems. *Phys. Rev. E*, 64:047101, Sep 2001.

[152] Kaori Sato, Tetsuya Ebihara, Eijiro Adachi, Seiichi Kawashima, Shunji Hattori, and Shinkichi Irie. Possible involvement of aminotelopeptide in self-assembly and thermal stability of collagen i as revealed by its removal with proteases. *Journal of Biological Chemistry*, 275(33):25870–25875, 2000.

[153] Erik Schäffer and Po-Zen Wong. Rheology of Semiflexible Bundle Networks with Transient Linkers. *Physical Review E*, 61:5257, 2000.

[154] David J Schwab, Robijn F Bruinsma, Jack L Feldman, and Alex J Levine. Rhythmogenic neuronal networks, emergent leaders, and k-cores. *Physical Review E*, 82(5):051911, 2010.

[155] Julian Schwinger. On gauge invariance and vacuum polarization. *Physical Review*, 82(5):664, 1951.

[156] Julian Schwinger. The theory of quantized fields. v. *Physical Review*, 93(3):615, 1954.

[157] Stephen B. Seidman. Network structure and minimum degree. *Social Networks*, 5(3):269 – 287, 1983.

[158] Jordan L Shivers, Sadjad Arzash, Abhinav Sharma, and Fred C MacKintosh. Scaling Theory for Mechanical Critical Behavior in Fiber Networks. *Physical Review Letters*, 122(18):188003, may 2019.

[159] Matthew D Shoulders and Ronald T Raines. Collagen structure and stability. *Annual review of biochemistry*, 78:929–958, 2009.

[160] J C Simo. A Finite Strain Beam Formulation. The Three-Dimensional Dynamic Problem. Part I. *Computer Methods in Applied Mechanics and Engineering*, 49:55–70, 1985.

[161] Valentin M. Slepukhin, Sufyan Ashhad, Jack L. Feldman, and Alex J. Levine. Microcircuit synchronization and heavy tailed synaptic weight distribution in prebötzinger complex contribute to generation of breathing rhythm, 2020.

[162] Valentin M Slepukhin, Maximilian J Grill, Qingda Hu, Elliot L Botvinick, Wolfgang A Wall, and Alex J Levine. Topological defects produce kinks in biopolymer filament bundles. *Proceedings of the National Academy of Sciences*, 118(15), 2021.

[163] Valentin M Slepukhin, Maximilian J Grill, Qingda Hu, Elliot L Botvinick, Wolfgang A Wall, and Alex J Levine. Topological defects produce kinks in biopolymer filament bundles. *Proceedings of the National Academy of Sciences*, 118(15), 2021.

[164] Valentin M. Slepukhin, Maximilian J. Grill, Kei W. Müller, Wolfgang A. Wall, and Alex J. Levine. Conformation of a semiflexible filament in a quenched random potential. *Physical Review E*, 99(4):042501, apr 2019.

[165] Valentin M. Slepukhin and Alex J. Levine. Braiding dynamics in semiflexible filament bundles under oscillatory forcing. *Polymers*, 13(13), 2021.

[166] Valentin M Slepukhin and Alex J Levine. Thermal schwinger effect: Defect production in compressed filament bundles. *arXiv preprint arXiv:2103.08832*, 2021.

[167] D A Smith. Path-integral theory of an axially confined worm-like chain. *Journal of Physics A: Mathematical and General*, 34(21):4507, 2001.

[168] Jeffrey Smith, Howard Ellenberger, Klaus Ballanyi, Diethelm Richter, and Jack Feldman. Pre-botzinger complex - a brain-stem region that may generate respiratory rhythm in mammals. *Science (New York, N.Y.)*, 254:726–9, 12 1991.

[169] Peter Sollich, François Lequeux, Pascal Hébraud, and Michael E. Cates. Rheology of Semiflexible Bundle Networks with Transient Linkers. *Phys. Rev. Lett.*, 78:2020, 1997.

[170] Anton Souslov, Andrea J. Liu, and T. C. Lubensky. Elasticity and response in nearly isostatic periodic lattices. *Phys. Rev. Lett.*, 103:205503, Nov 2009.

[171] Dan Strehle, Paul Mollenkopf, Martin Glaser, Tom Golde, Carsten Schuldt, Josef A. Käs, and Jörg Schnauß. Single actin bundle rheology. *Molecules*, 22(10), 2017.

[172] Jonathan Stricker, Tobias Falzone, and Margaret L Gardel. Mechanics of the f-actin cytoskeleton. *Journal of biomechanics*, 43(1):9–14, 2010.

[173] Steven H. Strogatz. *Nonlinear Dynamics and Chaos: With Applications to Physics, Biology, Chemistry and Engineering*. Westview Press, 2000.

[174] The MathWorks Inc. MATLAB R2017b, 2017.

[175] Sameer Varma, Joseph PRO Orgel, and Jay D Schieber. Nanomechanics of type i collagen. *Biophysical journal*, 111(1):50–56, 2016.

[176] Mathijs F J Vermeulen, Anwesha Bose, Cornelis Storm, and Wouter G Ellenbroek. Geometry and the onset of rigidity in a disordered network. *Physical Review E*, 96(5):53003, nov 2017.

[177] Danijela Vignjevic, Shin-ichiro Kojima, Yvonne Aratyn, Oana Danciu, Tatyana Svitkina, and Gary G Borisy. Role of fascin in filopodial protrusion. *Journal of Cell Biology*, 174(6):863–875, sep 2006.

[178] Yuka Wakuda, Shohei Nishimoto, Shin-ichiro Suye, and Satoshi Fujita. Native collagen hydrogel nanofibres with anisotropic structure using core-shell electrospinning. *Scientific reports*, 8(1):1–10, 2018.

[179] Min Wang, Lin Guo, and Haoran Sun. Manufacture of biomaterials. In Roger Narayan, editor, *Encyclopedia of Biomedical Engineering*, pages 116–134. Elsevier, Oxford, 2019.

[180] Xiao-Jing Wang and György Buzsáki. Gamma oscillation by synaptic inhibition in a hippocampal interneuronal network model. *Journal of Neuroscience*, 16(20):6402–6413, 1996.

[181] Xueying Wang, John A Hayes, Ann L Revill, Hanbing Song, Andrew Kottick, Nikolas C Vann, M Drew LaMar, Maria Cristina D Picardo, Victoria T Akins, Gregory D Funk, et al. Laser ablation of dbx1 neurons in the pre-bötzinger complex stops inspiratory rhythm and impairs output in neonatal mice. *eLife*, 3:e03427, 2014.

[182] Duncan J Watts and Steven H Strogatz. Collective dynamics of 'small-world'networks. *Nature*, 393(6684):440–442, 1998.

[183] Marco P.E. Wenger, Laurent Bozec, Michael A. Horton, and Patrick Mesquida. Mechanical behavior of individual type i collagen fibrils. *Biophysical Journal*, 93(4):1255–1263, 2007.

[184] Wikipedia Contributor. . https://commons.wikimedia.org/w/index.php?curid=8882110, 2009. [Online; accessed 2021-06-04].

[185] Wikipedia Contributor. The eukariotic cytoskeleton. https://commons.wikimedia.org/w/index.php?curid=655748, 2013. [Online; accessed 2021-06-04].

[186] Wikipedia Contributor Solitchka on fr.wikipedia. Translated by GKFXtalk. . https://commons.wikimedia.org/w/index.php?curid=38255260, 2005. [Online; accessed 2021-06-04].

[187] Jan Wilhelm and Erwin Frey. Elasticity of stiff polymer networks. *Phys. Rev. Lett.*, 91:108103, Sep 2003.

[188] Steven J Winder and Kathryn R Ayscough. Actin-binding proteins. *Journal of Cell Science*, 118(4):651 LP – 654, feb 2005.

[189] Lanti Yang. *Mechanical properties of collagen fibrils and elastic fibers explored by AFM*. PhD thesis, University of Twente, Enschede, The Netherlands, 2 2008.

[190] Y.-C. Zhang. Rheology of Semiflexible Bundle Networks with Transient Linkers. *Europhys. Lett.*, 9:113, 1989.

[191] Di Zhou, Leyou Zhang, and Xiaoming Mao. Topological edge floppy modes in disordered fiber networks. *Physical review letters*, 120(6):068003, 2018.